QUANTITATIVE THERMAL DESORPTION SPECTROMETRY OF NOBLE GASES IN SOLIDS

QUANTITATIVE THERMAL DESORPTION SPECTROMETRY OF NOBLE GASES IN SOLIDS

PROEFSCHRIFT ter verkrijging van
de graad van doctor in de
technische wetenschappen
aan de Technische Hogeschool Delft
op gezag van de rector magnificus,
prof. ir. B.P.Th. Veltman,
voor een commissie aangewezen
door het college van dekanen
te verdedigen op
donderdag 12 februari 1981
te 14.00 uur door
AART ADRIANUS VAN GORKUM
natuurkundig ingenieur
geboren te Hazerswoude

Delft University Press/1981

Dit proefschrift is goedgekeurd door de promotor
prof. dr. ir. H. van Dam

dr. E.V. Kornelsen, copromotor

Probeer het maar met mijn menu, gij eter
Morgen smaakt het u al beter
En overmorgen al zeer goed!
En wilt gij dan nog meer - de negen
Hoofdstukken die ik nu al heb geschreven
Geven mij beslist tot negen nieuwe moed.

vrij naar Nietzsche's "De vrolijke Wetenschap"
in de vertaling van Pé Hawinkels

to all friends

Preface

The study as described in this thesis was conducted in close cooperation with Dr. E.V. Kornelsen in his laboratory at the National Research Council in Ottawa, Canada. I had acquainted myself with the technique of thermal desorption spectrometry during my study for the degree of engineering physics in the group of Drs. H. van Dam, L.M. Caspers and A. van Veen at Delft University of Technology, The Netherlands. During my 2 1/2 year stay in Canada, we developed a theoretical background for the thermal desorption technique, enabling us to make this technique quantitative. Applications in new fields (channeling, bubble nucleation) came about. My still fresh mathematical memory combined with Dr. Kornelsen's excellent experimental experience formed a fertile ground for the generation and subsequent testing of ideas. A great improvement was the computer-aided data taking and handling, resulting in the automatic analysis of desorption spectra.

The chapters of this thesis are all in the form of papers, with the usual advantages and disadvantages: easy to read as separate chapters, difficult to read the thesis as a whole. I have placed all chapters in a logical order, beginning with the more general chapters. Since the papers have now lost their generic order, references to subsequent chapters will occur.

The work described in this thesis gives the final products of my 'Canadian period'. In fabricating these products we had much help from Dave Blair, for whom 'small repairs take a minute, impossible ones an hour', from Diane Dabrowski and Anne Statham who $(re)^n$ - typed (with $n \geq 2$) our papers, and from Roger Côté and Ray Stewart with technical assistance. Paul Amirault, George Walker, Rob Vallières and Leslie Cameron are acknowledged for making the drawings and Alf Castellano for converting them to photographs. I would like to thank the National Research Council, and the members of the Electron Physics Section of the Division of Electrical Engineering in particular, for their hospitality. Special thanks to Dr. J.P. Hobson for allowing me to (mis)use his secretary.

My stay in Canada was made possible by a grant from the Canada Council, a grant/loan from the Dutch Ministry of Education, a Research Associateship from the National Research Council and a grant from the Netherlands Organization for the Advancement of Pure Research (ZWO).

Chapter 2 Accepted by Vacuum
Chapter 3 Accepted by Vacuum
Chapter 4 Journal of Applied Physics 51 (1980) 2594-2602
Chapter 5 Radiation Effects 42 (1979) 93-111
Chapter 6 Radiation Effects 42 (1979) 113-124
Chapter 7 Nuclear Instruments and Methods 170 (1980) 161-170
Chapter 8 Physics Letters 75A (1979) 134-136
Chapter 9 Radiation Effects 52 (1980) 25-34
Chapter 10 Journal of Nuclear Materials 92 (1980) 79-88

Introduction

The phenomena of ion trapping and subsequent release upon heating have been observed as early as 1858 in gas discharge tubes.[1] It lasted until about 1950 that much interest was devoted to these phenomena, then in connection with the ionic pumping effect in ultra high vacuum gauges and ion pumps.[2] The technique of flash desorption as the thermal heating method was called,[3] made possible the measurement (at least approximately) of the binding energy of the desorbing gas to the sample.[4]

Thermal desorption spectra using polycrystalline materials were very complicated in structure,[5] and it was soon discovered that the use of clean single crystals in an ultra high vacuum environment produced spectra with 'clean' resolvable peaks.[6] This meant a major step forward for the thermal desorption technique, and systematic studies were undertaken to identify peaks in the spectra for different noble gases implanted in metals.[7] Most studies were performed on tungsten, and it was found that the noble gases, except helium, desorbed via two mechanisms: first order release for gas desorbing from binding sites close to the surface and socalled diffusional release from gas desorbing via a (vacancy) diffusion process.

Helium showed a different behaviour: only first order release peaks were present. This was explained by the postulate of high interstitial mobility at room temperature of helium in tungsten.[8] This postulate was confirmed independently by recent low temperature experiments using the FIM atom probe technique.[9]

The special role of helium was exploited in experiments in which helium was used as a probe for lattice damage introduced by other ions.[10] Helium was found to bind to defects produced by these ions, with in general different binding energies for different types of defects. Moreover, it was found that in general the binding energy of the helium was different when more than one helium atom occupies a trap. Since the number of helium atoms desorbing in a certain binding state can be measured, it is known how many traps were occupied by one, two, etc. helium atoms. Based on statistical arguments, the number of traps can then be derived.[11] This was the beginning of the Quantitative Thermal Desorption Spectrometry (QTDS). It was soon realized that special requirements had to be

imposed on the conditions under which QTDS could be performed unambiguously. In general low helium doses are required, making sensitive equipment necessary. This is the subject of the chapters 2 and 3,[12] in which theoretical arguments for the experimental requirements as well as the technical aspects to fulfill these requirements are given.

In chapter 4 a new method to extract the kinetic parameters (activation energy, frequency factor, reaction order) from a single desorption peak is described.[13]

Chapter 5 gives the full mathematical theory that forms the basis of QTDS. In it the methods to measure the number of traps and their average depth, the trapping radius for the trapping of helium, the average depth of injected helium and its entrance probability are given. In the next chapters this theory is used to measure some of the mentioned quantities.

All experiments described in this thesis were carried out using a tungsten (100) crystal. Much information was already available on this particular material, making comparisons possible. QTDS measurements are of course not restricted to this material.

In chapter 6 the multiple trapping of helium at xenon traps in tungsten is described.[15] An excellent correspondence with the theory was found and the trapping radius of the xenon traps was measured as a function of the number of helium atoms in the trap. The experiments showed that at least 100 helium atoms can be trapped at a single trap. The binding energy of the helium to the trap was found to increase monotonically with the number of helium atoms present in the trap.

Chapter 7 contains the measurements of the channeling effect of helium in W <100>: the product of average range and entrance probability of the helium was measured as a function of incident angle and energy.[16] Strong enhancement was found in the <100> direction. The half angle $\psi_{\frac{1}{2}}$ was derived as a function of energy from 25 to 5000 eV. This angle $\psi_{\frac{1}{2}}$ was found to depart from the Lindhard theory below 1000 eV, to reach a maximum at ~ 200 eV and to drop below this energy. This effect was confirmed by computer simulations of the channeling effect at these low energies, as reported in the letter in chapter 8.[17] A qualitative correspondence was found with the $\psi_{\frac{1}{2}}$ vs energy relation as found in the experiments.

The entrance probability (= 1 - reflection coefficient) is the subject of chapter 9.[18] It was measured for helium on W(100) and combined with previous measurements (chapter 7) to yield the true average range of injected helium in W(100) for a normal and random direction of incidence.

The last chapter describes the study of helium bubble nucleation in tungsten using vacancies, annealed helium, neon, argon, krypton and xenon atoms as trapping centers.[19] As was found for xenon (chapter 6), all traps accept at least 100 helium atoms with no sign of saturation. The binding energy of the helium to the trap increases monotonically with the number of helium atoms present in the traps. The traps show an identical behaviour when the number of helium atoms trapped is greater than about 10: the character of the original trapping center is then lost. It is thus shown that helium bubbles can form at room temperature, creating very stable clusters.

Most of the data in this thesis are, besides being of fundamental interest, of importance to problems in future fusion reactors. The interaction of low energy (< 20 keV) helium from the plasma with the wall of the reactor is an important parameter in the performance of such a reactor. Useful data for reflection coefficient and range of helium on tungsten, and crystallografic dependence of these quantities are given. Moreover, the study of the last chapter, in which it is shown that helium atoms cluster around impurities in metals, is of great importance for studies of blistering and bubble nucleation.

References

[1] J. Plücker, Pogg. Ann. 105 (1858) 67

[2] For a review see: W.A. Grant, G. Carter, Vacuum 15 (1965) 477

[3] G. Ehrlich, J. Appl. Phys. 32 (1961) 4

[4] (a) P.A. Redhead, Vacuum 12 (1962) 203
(b) G. Carter, Vacuum 12 (1962) 245

[5] (a) E. V. Kornelsen, Can. J. Phys. 42 (1964) 364
(b) K. Erents, G. Carter, Vacuum 16 (1966) 523
(c) K. J. Close and J. Yarwood, Brit. J. Appl. Phys. 18 (1966) 1165

[6] E. V. Kornelsen, J. Appl. Phys. 39 (1968) 4546

[7] (a) E. V. Kornelsen and M.K. Sinha, J. Appl. Phys. 40 (1969) 2888
(b) E. V. Kornelsen, Can. J. Phys. 48 (1970) 2812

[8] K. Erents, G. Carter, Vacuum 17 (1967) 215
see also ref. 7b

[9] A. Wagner and D.N. Seidman, Phys. Rev. Lett. 42 (1979) 515

[10] (a) E. V. Kornelsen, Rad. Eff. 13 (1972) 227
(b) A. van Veen, A. A. van Gorkum, L. M. Caspers, J. Nihoul, L. Stals, J. Cornelis, Phys. Stat. Sol. (a) 32 (1975) K 123
[11] (a) D. Edwards Jr. and E. V. Kornelsen, Rad. Eff. 26 (1975) 155
(b) A. van Veen, L. M. Caspers, E. V. Kornelsen, R.H.J. Fastenau, A. A. van Gorkum, A. Warnaar, Phys. Stat. Sol. (a) 40 (1977) 235
[12] (a) A. A. van Gorkum and E. V. Kornelsen, to be published
(b) E. V. Kornelsen and A. A. van Gorkum. to be published
[13] Aart A. van Gorkum, J. Appl. Phys. 51 (1980) 2594-2602
[14] A. A. van Gorkum and E. V. Kornelsen, Rad. Eff. 42 (1979) 93
[15] E. V. Kornelsen and A. A. van Gorkum, Rad. Eff. 42 (1979) 113
[16] E. V. Kornelsen and A. A. van Gorkum, Nucl Instr. Meth. 170 (1980) 161
[17] A. A. van Gorkum, Phys. Lett. 75A (1979) 134
[18] A. A. van Gorkum and E. V. Kornelsen, Rad. Eff. 52 (1980) 25-34
[19] E. V. Kornelsen and A. A. van Gorkum, J. Nucl. Mat. 92 (1980) 79-88

QUANTITATIVE THERMAL DESORPTION SPECTROMETRY OF IONICALLY IMPLANTED INERT GASES
I. FUNDAMENTAL ASPECTS

A.A. van Gorkum and E.V. Kornelsen

Division of Electrical Engineering
National Research Council of Canada
Ottawa, Canada K1A 0R8

ABSTRACT

Quantitative thermal desorption spectrometry can be carried out if the doses are below limits to avoid (1) the creation of surface disorder, (2) the interaction of gas atoms during the desorption cycle, (3) the retrapping of helium during the desorption cycle, and (4) the multiple occupation of traps by helium. These limits are quantified, and it is shown that in general small amounts of gas have to be detected. The accuracy with which the energy E and frequency factor ν can be extracted from a measured 1st order desorption peak is ultimately limited by shot noise in the mass spectrometer. This noise is quantified for both the static and dynamic modes of operation. For the dynamic case, the noise is minimized if $\Delta t/\tau \approx \sqrt{2}$ with Δt the sample time and τ the vacuum time constant. In both modes, the error in the derived value of E has the form $\Delta E/E = C/N_0 \cdot (L/S)^{\frac{1}{2}} \cdot (1+\beta/\beta_c)^{\frac{1}{2}}$, *with* N_0 *the total number of particles in the peak,* L *the background leak rate,* S *the (new concept of) system sensitivity and* β_c *dependent on background pressure, peak temperature,* L *and* N_0. *For the dynamic mode,* C *is much smaller (10 to 67 times) than for the static mode. The error in* E *thus decreases monotonically with* β *and reaches a plateau value for* $\beta \ll \beta_c$. *Some examples are given showing that accuracies of ~1% can be obtained for peaks with* $N_0 \sim 10^8$ *particles for practically achievable values of* L *and* S.

1 Introduction

Thermal desorption spectrometry (TDS) of inert gases implanted in metals has proven to be a valuable tool for the study of intrinsic and extrinsic defects and the interaction between them.[1-6] It has been shown recently that additional quantitative information, e.g. the range of the implanted gases[7], the number of traps in the metal[8,9] as well as their trapping radii for trapping of helium[10] can also be extracted from TDS data. A theory describing these possibilities has been developed.[11] The TDS technique may be defined as consisting of the following steps:

1. Inert gas ions are implanted into a carefully prepared solid sample where they are bound in well defined trapping configurations within ~ 1 - 100 nm of its surface.
2. The sample is heated in a known profile with time (usually linear) and the release rate of the implanted gas determined by measuring its partial pressure with a mass spectrometer (MS) to yield a thermal desorption spectrum.
3. The kinetic parameters: binding energy E, frequency factor ν, reaction order i, and bound population N_0 are derived for the binding states that can be distinguished in the spectrum.

The desorption rate of the monitored gas, as appearing in the gas phase, is simply related to the detrapping rate of this gas from the traps in the sample only when the concentrations of the traps are so low that a gas atom released from a trap has a negligible probability of interaction with another trap or gas atom during its random walk migration to the surface.

It has been shown, mainly for tungsten and molybdenum as sample materials, that the noble gases Ne, Ar, Kr and Xe show the following desorption spectra features[10,11,26]

- *At implantation energies just above the entrance threshold, the desorption spectra consist of a number of 1st order peaks. These are thought to originate from gas atoms desorbing from sites very close ($\leq$ 10 Å) to the surface.*
- *At energies about a factor 3 above the entrance threshold, a peak having the characteristics of a diffusion peak appears. The gas desorbing in this peak was originally bound at sites further ($\geq$ 10 Å) from the surface, and had to diffuse via a vacancy mechanism to the surface.*

Helium behaves very differently, due to its high mobility at room temperature in the metals studied[14,15]. At incident energies below the threshold energy for displacement of lattice atoms, the helium atoms will diffuse until they desorb or are trapped by traps. Vacancies[4] and the inert gas atoms Ne, Ar, Kr and Xe, possibly associated with vacancies[4,10,16] act as traps. All of these traps can accommodate more than one helium atom[4,16]. Upon heating, the helium is released from the traps in distinct peaks, corresponding to a 1st order release process (provided again that the trap concentration is so low that no retrapping occurs). In general, the binding energy E of the helium to the trap depends on the number i of helium atoms in the trap. New peaks corresponding to different values of E thus appear when i increases. The simplest spectra result for low helium doses where no multiple occupation of the traps results.

The limit to the concentration of traps below which no retrapping occurs, as well as the limit to the helium dose to avoid multiple occupation of the traps are discussed in Section 2. Below these limits, the desorbed quantities of gas are very small, making an apparatus of high sensitivity, as described recently[17], necessary. In Section 3 of the present paper, quantitative requirements for a thermal desorption system capable of carrying out experiments in the low dose region will be given. The properties of the system are defined in terms of the system sensitivity S (see Eq. (11)) and the background leak rate L of the desorbing gas. The accuracy $\frac{\Delta E}{E}$ with which one can derive the binding energy E from the data is ultimately limited by shotnoise in the mass spectrometer, and will be used as a quantitative assessment of the system. In Section 4, it is shown that for a peak whose size is limited by the conditions from Section 2, a high value of S and a low value of L are needed to achieve reasonable accuracy ($\sim$ 1%) in E. The following paper[18] (to be called paper II) will discuss the technical parameters that determine L and S, other aspects of the apparatus required to do quantitative TDS and the acquisition, manipulation and analysis of the data.

2 Limits to concentrations and doses

In this section, four limits to fulfill the conditions mentioned in the introduction will be discussed (see Table I).

i. A first requirement relates to the surface disorder created by the bombardment of the single crystal samples. To avoid this disorder, the bombardment doses have to be kept below about 10^{13} cm^{-2} (see also paper II).

Table I *Limits to concentrations and doses*

	condition	maximum trapped conc. (cm^{-2})	$r_G = r_0 = 3$ Å
i	heavy gas (Ne, Ar, Kr, Xe) agglomeration	$C_G \leq \frac{0.1}{4\pi r_G \bar{d}_G}$	$\frac{2.6 \times 10^{13}}{\bar{d}_G(\text{Å})}$
ii	He retrapping	$C_T \leq \frac{0.1}{4\pi r_0 \bar{d}_T}$	$\frac{2.6 \times 10^{13}}{\bar{d}_T(\text{Å})}$
iii	multiple trap occupation	$C_{He} \leq \frac{0.01}{4\pi r_0 \bar{d}_T}$	$\frac{2.6 \times 10^{12}}{\bar{d}_T(\text{Å})}$

ii. A second requirement relates to the interaction of the heavy gas atoms (Ne, Ar, Kr, Xe) during the desorption cycle. When the depth of the gases is $\gtrsim 10$ Å, a diffusional release process occurs. The chance of one encountering another during this random walk has to be much smaller than that of reaching the surface. Based on the theory in reference 9, the concentration C_G of gas atoms is limited to:

$$C_G << \frac{1}{4\pi r_G \bar{d}_G} \qquad (1)$$

with C_G = concentration of the gas atoms (cm^{-2})

r_G = trapping radius for gas-gas trapping (cm)

$\bar{d}_G$ = average depth of the gas atoms (cm)

The trapping radius r is the radius of an ideal sphere, that traps whenever a particle comes within a distance r. The value of r is such that it yields the same trapping rate as the real trap[19]. The value of r_G is expected to be about 3 Å [16], so that condition (1) becomes

$$C_G \leq \frac{0.1}{4\pi r_G \bar{d}_G} = \frac{2.6 \times 10^{13}}{\bar{d}_G(\text{Å})} \quad (cm^{-2}) \qquad (2)$$

Condition (2) is a very severe restriction to the dose for normally used ions, energies and crystals: for 1500 eV Xe incident on W(100), $\bar{d}_G \approx 18$ Å, limiting C_G to $\sim 1.5 \times 10^{12}$ cm^{-2}. We have indeed found substantial Xe clustering effects at values of $C_G \approx 4 \times 10^{12}$ cm^{-2}.

Some experiments involve annealing of the implanted gas atoms. At high enough temperature ($\sim$ 1600 K for W) the gas atoms that occupy positions

far enough ($\gtrsim$ 10 Å) from the surface will start to diffuse. In this diffusion process, some atoms desorb while others diffuse deeper into the crystal, so that the concentration C_G is reduced while the average depth $\bar{d}_G$ of the remaining atoms increases. As mentioned in a previous paper[10], diffusion calculations have shown that the product $C_G * \bar{d}_G$ is about constant, so that if condition (2) is not met before the anneal, neither will it be met after.

iii. To avoid retrapping of helium in experiments in which the release of helium from traps is measured, the concentration of the traps C_T is limited by the condition:

$$C_T << \frac{1}{4\pi r_0 \bar{d}_T} \tag{3}$$

in which r_0 is now the interaction radius for helium with the trap and $\bar{d}_T$ the average depth of the traps. Since r_0 and r_G are expected to be about the same, condition (3) is very similar to condition (2).

iv. The helium spectra become simpler when the helium doses are so low that the average number of helium atoms trapped per trap is ~ 0.1 [4,10]. The fraction of the traps occupied by 2 helium atoms is then much smaller than that occupied by 1 atom. The concentration of the trapped helium is then equal to

$$C_{He} \leq 0.1\, C_T \ . \tag{4}$$

Since C_T is limited by equation (3)

$$C_{He} << \frac{1}{40\pi r_0 \bar{d}_T} \tag{5}$$

or $$C_{He} \leq \frac{1}{400\pi r_0 \bar{d}_T} \tag{6}$$

The trapping radius r_0 is expected to be ≈ 3 Å. The depth $\bar{d}_T$ depends on many parameters (type of ion, ion energy, crystal type, incident direction, etc.). Some experiments require $\bar{d}_T$ to be larger than the range of the helium[11], in which case $\bar{d}_T$ may have to be as large as 1000 Å,[7] leading to

$$C_{He} \lesssim 2.5 \times 10^9 \text{ cm}^{-2} \ .$$

In the low dose region, as given by equation (6), the number of helium atoms desorbing can be as low as 2.5×10^9 cm^{-2}. Since areas are ~ 0.1 cm^2, only $\sim 2.5 \times 10^8$ atoms desorb in a peak, from which both the energy E and frequency factor ν have to be derived. The system parameters required to derive E and ν with a specified accuracy will be given in the next section.

3 Principles and accuracy of TDS

3.1 *Principles of the measurement*

The desorptions are carried out in a UHV environment, and the partial pressure p of the desorbing gas is measured with a mass spectrometer (MS) (see paper II for a more extensive discussion). The desorption rate is then given by

$$\frac{dN}{dt} = n_0 V \left[\frac{dp}{dt} + \frac{p}{\tau} \right] - L \qquad (7)$$

N = number of particles that have not yet desorbed
p = partial pressure of the desorbing gas
n_0 = 3.27×10^{19} (mol torr^{-1} ℓ^{-1})
τ = pumping time constant (s) (= V/pumping speed)
V = desorption volume (ℓ)
L = background leak rate of monitored gas (mol s^{-1})

assuming that the MS and the sample are in the same volume V (see paper II for corrections if this condition is not fulfilled).

There are basically 2 modes of operation:

1. *Static* ($\tau \to \infty$) with no (deliberate) pumping of the monitored gas*.
   The desorption rate is then equal to

$$\frac{dN}{dt} \approx n_0 V \frac{dp}{dt} - L \qquad (8)$$

   so that the derivative of the pressure is proportional to the desorption rate.

2. *Dynamic* $\left[\frac{dp}{dt} << \frac{p}{\tau} \right]$
   In this case, deliberate pumping is present and the desorption rate is approximately given by

*Pumping will, however, always occur: the MS itself is a pump (see paper II).

$$\frac{dN}{dt} \approx n_0 V \frac{p}{\tau} - L \qquad (9)$$

so that the measured pressure is directly proportional to $\frac{dN}{dt}$. This equation shows that p is proportional to τ in this dynamic mode. In Section 3.3, the optimum value of τ will be given.

All helium desorption peaks measured in the low dose region up to now conform well to the first order form given by the equation

$$\frac{dN}{dt} = -N\nu \exp\left(-\frac{E}{kT}\right) \qquad (10)$$

where ν = frequency factor (s^{-1})

E = activation energy (eV)

k = Boltzmann constant (eV K^{-1})

T = absolute temperature (K)

Since for most samples the diffusion time of the helium to the surface is very short compared to the peak width, the detrapping rate defined by equation (10) can be equated to the desorption rate of equations (7-9). The initial population N_0 is found by integration of the peak. The parameters E and ν can be derived independently from the peak using a new method based on the concept of "characteristic time" as described in Ref. 20. This new method uses all measured data points in a peak as long as no neighbouring peak contributes to the desorption rate at that point.

The properties of the detection system can be expressed in terms of the system sensitivity S:

$$S = \frac{G}{n_0 V e} \qquad (11)$$

where G = ion current per unit of pressure (i^+/p) of the MS ionizer (A $torr^{-1}$)†

V = desorption volume

e = electron charge

S is the number of ions detected per second in the MS per molecule in the gas phase (volume V). Using an electron multiplier, the ions are either counted

†When an electron multiplier is used, a conversion factor < 1 has to be included since not all ions necessarily lead to a charge pulse at the output of the multiplier[17].

or measured as a current. In both cases, a *shot noise* is present in the measured signal. This shot noise is the basic parameter limiting the accuracy of the measured values of N_0, E and ν.

3.2 *Shot noise analysis*

A simple relation exists between the shot noise introduced when the output pulses are counted directly and that introduced when the current is measured. If the analogue signal is put through a filter with a unity passband up to the cut-off frequency $f_c = \frac{1}{2\Delta t}$ and is subsequently sampled via an A/D converter at intervals Δt, then the shot noise is a factor m greater then when direct counting had taken place with counting intervals Δt. The factor m can be shown to be[25]

$$m = \left[\frac{M_2 M_0}{M_1^2}\right]^{\frac{1}{2}} \tag{12}$$

where M_0, M_1 and M_2 are the respective moments of the pulse height distribution. It ranges from $\sqrt{4/3} = 1.15$ for a uniform to $\sqrt{2} = 1.41$ for an exponential distribution.

For the present analysis it will be assumed that the counting mode is used. The number of counts per channel is

$$Q = S\Delta t\, n_0\, Vp, \tag{13}$$

so that the desorption rate is given by

$$\frac{dN}{dt} = \frac{1}{S\Delta t}\left(\frac{\Delta Q}{\Delta t} + \frac{Q}{\tau}\right) - L \tag{14}$$

where ΔQ is the change in Q for adjacent channels. The standard deviation (s.d.) in Q is given by $\sqrt{Q}$, and consequently the s.d. in $\frac{dN}{dt}$:

$$\left(\sigma_{\frac{dN}{dt}}\right)^2 = \left(\frac{1}{S\Delta t}\right)^2\left[\left(\frac{\sigma_{\Delta Q}}{\Delta t}\right)^2 + \left[\frac{\sigma_Q}{\tau}\right]^2\right] \tag{15}$$

and since $(\sigma_{\Delta Q})^2 \approx 2.(\sigma_Q)^2$

$$\sigma_{\frac{dN}{dt}} = \frac{Q^{\frac{1}{2}}}{S(\Delta t)^2}\left[2 + \left(\frac{\Delta t}{\tau}\right)^2\right]^{\frac{1}{2}} . \tag{16}$$

3.3 *Optimum choice of* $\Delta t/\tau$

For the dynamic case, τ can still be chosen at will. It can be used to minimize the 'noise' in the resulting value of $\frac{dN}{dt}$: since Q is proportional to Δt and τ (equations (13) and (9)):

$$\sigma_{\frac{dN}{dt}} \propto \left[\frac{\tau}{\Delta t}\right]^{\frac{1}{2}} \left[2 + \left[\frac{\Delta t}{\tau}\right]^2\right]^{\frac{1}{2}} \qquad (17)$$

This function is plotted, normalized to 1 at its minimum, in Figure 1. It reaches a minimum for $\Delta t/\tau = \sqrt{2}$ which is very broad and symmetrical in $\log\left[\frac{\Delta t}{\tau}\right]$ †. The noise is within a factor 2 of the minimum for $0.18 \leq \Delta t/\tau \leq 11.1$.

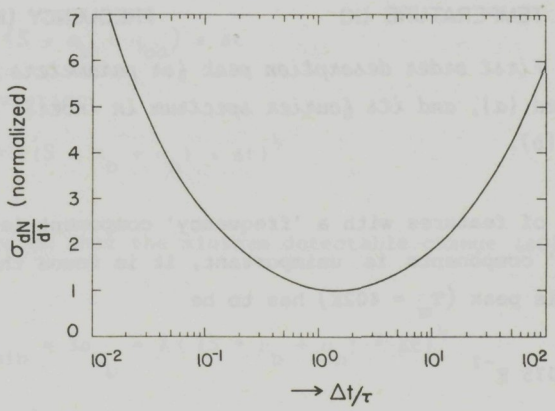

Fig. 1 *Normalized standard deviation in the desorption rate* $\frac{dN}{dt}$ *as a function of the ratio of sample time* Δt *and pumping time constant* τ.

3.4 *Minimum number of points per peak*

The determination of E and ν is critically dependent on the form of the peak (1st and 2nd order, diffusion-like). Here again we will focus on a first order peak, but mainly as an example. In order to decide how many points over the whole peak adequately represent the form of this peak, a fourier transformation of a theoretical 1st order peak was made. Figure 2 shows the original desorption peak (E = 1 eV, $\nu = 10^{13}$ s^{-1}, β = 40 Ks^{-1}) and its fourier transformation in K^{-1}. The scale of the fourier transformation is in (degrees

† A similar value for the optimum was suggested by Edwards[21] based on somewhat different arguments.

Kelvin)$^{-1}$ rather than in s^{-1} since the form of the peak on a temperature scale is almost independent of β. The fourier transform is thus also nearly independent of β, and the 'frequency' scale proportional to $1/T_m$. Assuming

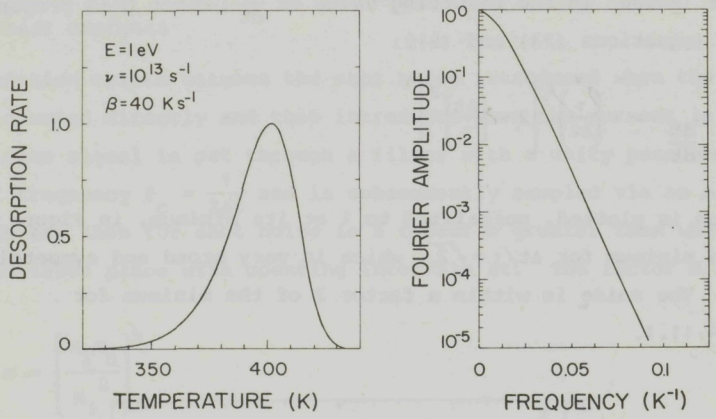

Fig. 2 *First order desorption peak for parameters as indicated (a), and its fourier spectrum in inverse degrees Kelvin (b).*

that the inclusion of features with a 'frequency' component less than 10^{-4} of the low 'frequency' components is unimportant, it is found that the Nyquist 'frequency' for this peak (T_m = 402K) has to be

$$f_N \sim 0.075\ K^{-1}$$

or in general

$$f_N \approx \frac{30}{T_m} . \tag{18}$$

Samples are thus required at intervals

$$\Delta T = \frac{1}{2f_N} = \frac{T_m}{60} \tag{19}$$

or

$$\frac{\Delta T}{T_m} \approx \frac{1}{60} = 1.67 \times 10^{-2}. \tag{20}$$

Since the full width at 10% of the maximum is about 0.15 T_m for this peak, a minimum of about *10 points* over this width are needed to sufficiently represent the form of this peak. This conclusion is rather insensitive to variations in E, ν, or β, or even the form (order) of the peak. If more than 10 points are

available, they can without loss of information about the form of the peak, be condensed to 10 smoothed values by means of a digital filter.

3.5 *Minimum detectable desorption peak*

A background number of molecules n_b will be present in the gas phase producing a signal with noise. The minimum detectable desorption peak will be taken equal to 3 times the standard deviation of the noisy signal. In the *dynamic* case, the background molecules are present due to the background leak rate, so that $n_b = L * \tau$. In the *static* case, they are either present upon closing off the desorption volume from the pumps, or from previously desorbed peaks in the same desorption cycle. In both the dynamic and static modes, the background counting rate q_{bd} of the detector itself contributes to the total background counting rate. The total background number of counts per channel is

$$Q_b = (S * n_b + q_{bd}) * \Delta t \tag{21}$$

with standard deviation

$$\sigma_{Q_b} = \{(S * n_b + q_b) * \Delta t\}^{\frac{1}{2}} \tag{22}$$

Using the assumption that the minimum detectable change $(\Delta Q)_{min}$ in Q is three time the s.d.

$$(\Delta Q)_{min} = 3\sigma_{Q_b} = 3\{(S * n_b + q_b) * \Delta t\}^{\frac{1}{2}} \tag{23}$$

(since $(\Delta Q)_{min} << Q$), corresponding to a desorption of

$$(\Delta n)_{min} = \frac{(\Delta Q)_{min}}{S\Delta t} = 3\left(\frac{n_b + q_b/S}{S\Delta t}\right)^{\frac{1}{2}} = \frac{3}{S\Delta t}\sqrt{Q_b} \tag{24}$$

in one channel.

If Δt is chosen such that it includes the whole peak, then $(\Delta n)_{min}$ is the minimum detectable desorption peak. It should be pointed out that only the total number in the peak can be determined. No information about the form of the peak is obtained since it appears in a single channel. The next section will focus on the question of extracting E and ν from a noisy peak.

3.6 *Shot noise errors in* E *and* ν

The errors in E and ν due to shot noise will be different for the static and dynamic mode. For the dynamic mode, the analysis will be based on the optimum choice of the ratio of sample time and pumping time constant of $\Delta t/\tau = \sqrt{2}$.

In both modes, a background leak rate L will be assumed. For the static mode, an additional number n_b of molecules is included in the background, either from desorption of previous peaks in the spectrum or already present at the start of the desorption cycle.

The energy E (and the frequency factor ν) can be extracted using a new method based on the concept of "characteristic time" as described in Reference 20. In this method, all data points from a single peak that have no contribution from neighbouring peaks are used. An estimate can also be made of the error in the deduced values of E and ν. Equations for the error in E will be derived. It can easily be shown from the 1st order rate equation that the error in ν is related to that in E by:

$$\Delta_{\ln\nu} \approx \frac{E}{kT_m} \cdot \frac{\Delta E}{E} \tag{25}$$

with T_m the temperature of the peak maximum. Since $\frac{E}{kT_m} \approx 30$, a relative error of 1% in E yields an error in ν of a factor 1.35.

In Appendix II, it is shown that for the *static* case, the relative error in E, using the mentioned method, is approximately given by

$$\frac{\Delta E}{E} \approx \frac{0.48}{\sqrt{\delta * \Delta Q_m}} \left(1 + 10\, \frac{n_b + Lt_{0.3}}{N_0}\right)^{\frac{1}{2}} \tag{26}$$

where

$$\delta = \frac{w\beta\Delta t}{T_m}, \text{ the width of the peak over which the data points extend as a fraction of } T_m \tag{27}$$

w = number of sample points over the peak

β = heating rate ($K\ s^{-1}$)

ΔQ_m = change in counts per channel at the maximum of the desorption rate, excluding the background leak rate

$$= S(\Delta t)(\Delta t) \cdot \left.\frac{dN}{dt}\right|_{max} \tag{28}$$

$t_{0.3}$ † = time from closing off the system to the time where the desorption rate reaches 0.3 of the maximum rate

N_0 = total number of particles desorbing in the peak

For the *dynamic* case: (see Appendix I)

† As is shown in the Appendix, this time enters since the error reaches a minimum if all points above 0.3 of the maximum are used (see Appendix I & II).

$$\frac{\Delta E}{E} \approx \frac{2.2}{\sqrt{wQ_m}} \left(1 + 3.3 \frac{L}{\left.\frac{dN}{dt}\right|_m}\right)^{\frac{1}{2}} \tag{29}$$

where Q_m = number of counts per channel at the maximum of the desorption rate, excluding the background leak rate = $S\Delta t \left.\frac{dN}{dt}\right|_m * \tau$ (30)

$\left.\frac{dN}{dt}\right|_m$ = desorption rate maximum

The desorption rate at the maximum can be shown to be given approximately by (easily derived from equation (10))

$$\left.\frac{dN}{dt}\right|_m \approx 10\ N_0 \beta / T_m \ . \tag{31}$$

Using this expression, including equations (28) and (30) for ΔQ_m and Q_m, equations (26) and (29) can be rewritten as:

static $$\frac{\Delta E}{E} \approx \frac{0.48}{\left\{\frac{\delta^3}{10}\right\}^{\frac{1}{2}}} \left(\frac{\beta}{S T_m N_0}\right)^{\frac{1}{2}} \left(1 + 10 \frac{n_b + Lt_{0.3}}{N_0}\right)^{\frac{1}{2}} \tag{32}$$

dynamic $$\frac{\Delta E}{E} \approx \frac{2.2}{\left\{\frac{\delta^2}{\sqrt{2}}\right\}^{\frac{1}{2}}} \left(\frac{\beta}{S T_m N_0}\right)^{\frac{1}{2}} \left(1 + 3.3 \frac{L}{\left.\frac{dN}{dt}\right|_m}\right)^{\frac{1}{2}} \tag{33}$$

If it is assumed that points over the full width at 10% height are included, than $\delta = \frac{w * \Delta T}{T_m} \approx 0.15$ for a 1^{st} order peak. Using this value,

static $$\frac{\Delta E}{E} \approx 26 \left(\frac{\beta}{S T_m N_0}\right)^{\frac{1}{2}} \left(1 + 10 \frac{n_b + Lt_{0.3}}{N_0}\right)^{\frac{1}{2}} \tag{34}$$

dynamic $$\frac{\Delta E}{E} \approx 17 \left(\frac{\beta}{S T_m N_0}\right)^{\frac{1}{2}} \left(1 + 3.3 \frac{L}{\left.\frac{dN}{dt}\right|_m}\right)^{\frac{1}{2}} \tag{35}$$

The last two equations show that when the background is insignificant, (for the static case, $n_b + Lt_{0.3} << 0.1\ N_0$ and for the dynamic case $L << 0.3 \left.\frac{dN}{dt}\right|_m$)

the error for the static case is a factor 26/17 ≈ 1.5 higher than for the (optimum) dynamic case, independent of all other parameters.

In both cases, the error decreases monotonically with decreasing heating rate β, and reaches a limiting value for $\beta \to 0$ of (see Figure 3 and Table II)

Table II *Relative errors in energies*

quantity	mode	
	static	dynamic
$\frac{\Delta E}{E}$	$26\left[\frac{\beta}{S T_m N_0}\right]^{\frac{1}{2}} \cdot \left[1 + 10\,\frac{n_b + L t_{0.3}}{N_0}\right]^{\frac{1}{2}}$	$17\left[\frac{\beta}{S T_m N_0}\right]^{\frac{1}{2}} \cdot \left[1 + 3.3\,\frac{L}{\frac{dN}{dt}\Big\|_m}\right]^{\frac{1}{2}}$
$\frac{\Delta E}{E}$ for $\beta \to 0$	$\frac{82}{N_0}\left[\frac{T_{0.3} - T_0}{T_m}\right]^{\frac{1}{2}} \cdot \left[\frac{L}{S}\right]^{\frac{1}{2}}$	$\frac{10}{N_0} \cdot \left[\frac{L}{S}\right]^{\frac{1}{2}}$
$\frac{\frac{\Delta E}{E}}{\left[\frac{\Delta E}{E}\right]_{\beta=0}}$	$\left[1 + \frac{\beta}{\beta_c}\right]^{\frac{1}{2}}$	$\left[1 + \frac{\beta}{\beta_c}\right]^{\frac{1}{2}}$
β_c	$\frac{L(T_{0.3} - T_0)}{n_b + 0.1 N_0}$	$\frac{L T_m}{3 N_0}$

static
$$\frac{\Delta E}{E} = \frac{82}{N_0}\left[\frac{T_{0.3} - T_0}{T_m}\right]^{\frac{1}{2}}\left[\frac{L}{S}\right]^{\frac{1}{2}} \tag{36}$$

dynamic
$$\frac{\Delta E}{E} = \frac{10}{N_0}\left[\frac{L}{S}\right]^{\frac{1}{2}} \tag{37}$$

where T_0 is the starting temperature, assuming that the desorption cycle is started upon closing off the desorption volume. With the introduction of the heating rate β_c according to (see Table II)

static
$$\beta_c = \frac{L(T_{0.3} - T_0)}{n_b + 0.1 N_0} \tag{38}$$

dynamic
$$\beta_c = \frac{L T_m}{3 N_0} \tag{39}$$

equations (34) and (35) can be written in normalized form as

$$\frac{\frac{\Delta E}{E}}{\left(\frac{\Delta E}{E}\right)_{\beta=0}} = \left[1 + \frac{\beta}{\beta_c}\right]^{\frac{1}{2}} \tag{40}$$

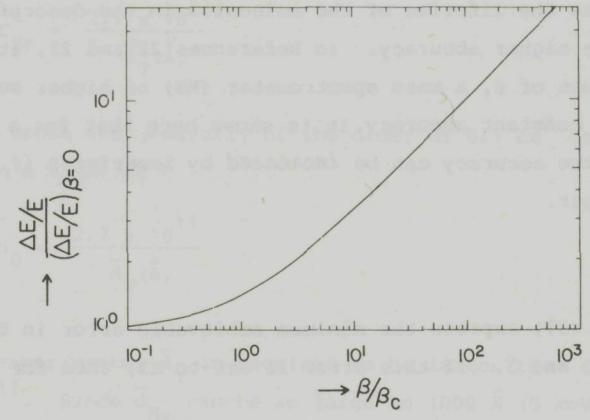

Fig. 3 *Relative error in energy* E, *normalized to the value for a heating rate* $\beta=0$, *as a function of the heating rate* β *relative to the critical heating rate* β_c *as defined in Eqs. (38) and (39).*

This function is plotted in Figure 3 and shows that the minimum error is reached within 14% for $\beta/\beta_c = 0.3$. The values of β below which the increase in accuracy in E is minimal mean

static $$Lt_{0.3} = 3.3(n_b + 0.1N_0) \tag{41}$$

dynamic $$L = \left.\frac{dN}{dt}\right|_m . \tag{42}$$

It is thus seen that it only pays off to go lower in β until $\left.\frac{dN}{dt}\right|_m$ (proportional to β, equation (31)) reaches L for the dynamic case. In the static case, it pays off to decrease β until the buildup of the background due to the

background leak rate over a time $t_{0.3}$ is equal to $3.3(n_b + 0.1N_0)$.

One has to realize that a decreasing value of β should be accompanied by an increasing value of Δt. For the analogue mode of current measurement, a decreasing cut-off frequency in the filter just before the A/D converter is necessary. Alternately, one could sample at a much higher rate than the minimum of $\frac{1}{\Delta t} \approx 60 \frac{\beta}{T_m}$ required (see equation (20)), and use the extra values to obtain smoothed values of the desorption rate at intervals $\Delta t \approx \frac{T_m}{60\beta}$, thus numerically simulating the low frequency filter. In the dynamic mode, lowering β also requires increasing τ, since $\Delta t/\tau$ has to stay constant. The increasing value of τ increases the lifetime of the molecules in the desorption volume, contributing to the higher accuracy. In references 22 and 23, it was stated that for lower values of β, a mass spectrometer (MS) of higher sensitivity is needed to maintain constant accuracy. It is shown here that for a constant sensitivity of the MS, the accuracy can be *increased* by lowering β if τ is made proportionally larger.

4 Discussion

Equations (36) and (37) express the minimum achievable error in E for the system parameters L and S. If this error is set to x%, then for the *dynamic* mode

$$\frac{L}{S} \leq 10^{-6} x^2 N_0^2 \tag{43}$$

where N_0 is the total number of atoms desorbing in a peak. For the *static* mode

$$\frac{L}{S} \leq 1.5 \times 10^{-8} x^2 N_0^2 \left(\frac{T_m}{T_{0.3} - T_0}\right) \tag{44}$$

In an experiment especially set up to measure E accurately in the static mode, one could choose T_0 close to the starting temperature of the peak. This way, $(T_{0.3} - T_0)/T_m$ could be reduced to ~ 0.15. Equation (44) then becomes

$$\frac{L}{S} \leq 1.0 \times 10^{-7} x^2 N_0^2 \tag{45}$$

When $T_0 << T_{0.3}$, the static mode requires a value of $\frac{L}{S}$ 67 times smaller than the dynamic mode. For the conditions leading to equation (45), this ratio reduces to 10.

As mentioned in Section 2, the number of particles desorbing in a peak (N_0) can be small. The most stringent requirement was related to the desorption of helium from traps, when (1) no retrapping effects occur and (2) the number of helium atoms per trap is smaller than 0.1, leading to equation (6)

$$C_{He} \leq \frac{1}{400\pi r_0 \bar{d}_T}$$

and since $r_0 \approx 3$ Å, the number of helium atoms per cm^2 has a maximum of

$$C_{He} = \frac{2.7 \times 10^{12}}{\bar{d}_T(\text{Å})} \quad .$$

Bombardment areas are generally of the order of 0.1 cm^2 (see paper II) resulting in a value of

$$N_0 = \frac{2.7 \times 10^{11}}{\bar{d}_T(\text{Å})} \quad .$$

In certain experiments, $\bar{d}_T$ is required to be larger than the range $\bar{d}_{He}$ of the helium[7,10,11]. Since $\bar{d}_{He}$ can be as large as 1000 Å (5 keV helium along the <100> channel in tungsten[24], values of N_0 as low as $\sim 2.5 \times 10^8$ atoms are encountered. If the energy E has to be derived with an accuracy x = 1%, then for the dynamic mode the requirement is

$$\frac{L}{S} \leq 6.3 \times 10^{10},$$

and for the static mode, a factor 67 ($T_0 \ll T_{0.3}$) or 10 (for $(T_{0.3}-T_0)/T_m \sim 0.15$) times smaller.

For the system described in Reference 14 (with $L \approx 5 \times 10^6$ s^{-1} for routine operating conditions, $G_{eff} = 6.4 \times 10^{-3}$ A $torr^{-1}$ for He, V = 2.27 ℓ), operating in the static mode,

$$\frac{L}{S} = \frac{L}{\left(\frac{G}{n_0 Ve}\right)} = \frac{5 \times 10^6}{5.4 \times 10^{-4}} = 9.3 \times 10^9 \quad .$$

This system is thus capable of measuring the energy E of a peak with a total population of 2.5×10^8 with an accuracy of ~ 3% (for $(T_{0.3} - T_0)/T_m \approx 1$ and 1.2% for the special designed experiment where $(T_{0.3} - T_0)/T_m \approx 0.15$. The

heating rate required to yield an error within 14% of the minimum was given in Section 3 as 0.3 β_c or

$$\beta \approx 0.3 \frac{L(T_{0.3} - T_0)}{(n_b + 0.1N_0)} .$$

For the mentioned system, $n_b \approx 5 \times 10^8$. Assuming $T_{0.3} - T_0 = 1000$ K, a β of ~ 3 K s^{-1} is required. Since the relative span over wich the points are taken is equal to

$$\frac{w*\beta*\Delta t}{T_m} \approx 0.15$$

and $m \approx 10$, the sample time Δt has to be equal to ~ 5 seconds for a peak at $T_m = 1000$ K.

If the discussed system were operated dynamically, the minimum achievable error for a peak of $N_0 = 2.5 \times 10^8$ helium atoms would be

$$\frac{\Delta E}{E} = \frac{10}{N_0} \left(\frac{L}{S}\right)^{\frac{1}{2}} = 0.39\%.$$

Since $\beta_c = 6.7$ K s^{-1}, an accuracy of 0.45% is reached for $\beta = 0.3\ \beta_c = 2$ K s^{-1} and 1% for $\beta = 11$ K s^{-1}. Sample times Δt of $15/\beta = 7.5$ sec resp 1.4 sec are required, while the vacuum time constants τ have to be $\frac{\Delta t}{\sqrt{2}} = 5.3$ sec resp 1 sec. The background partial helium pressure in this dynamic mode would be

$$p = \frac{L\tau}{n_0 V} \approx 6.7 \times 10^{-14}\ \tau \text{ torr}$$

or 3.5×10^{-13} resp 6.7×10^{-14} torr.

5 Summary and conclusions

Quantitative thermal desorption spectrometry can yield valuable information when doses are limited to maxima as given in equations (1-6). When helium is used to probe defects, doses as low as 10^9 cm^{-2} result for traps at 1000 Å. Since bombarded areas are ~ 0.1 cm^{-2}, the desorption peak due to $\sim 10^8$ helium atoms has to be measured. The energy E and frequency factor ν have to be extracted independently. This can be done by a new method described in Reference 20. The accuracy with which E (and ν) can be extracted is limited by shot noise in the detector. This noise has been quantified (equation (16))

and it is shown that the optimum ratio of sample time Δt to pumping time constant τ is $\Delta t/\tau \approx \sqrt{2}$. In the static mode ($\tau \to \infty$), the accuracy with which one can derive E and ν is lower, as shown by equations (34) and (35) that express the relative errors in E for both the static and dynamic mode as a function of the newly introduced concept of system sensitivity S, the background leak rate L and the heating rate β. It was shown that $\frac{\Delta E}{E}$ decreases monotonically with decreasing β, and reaches a plateau value for $\beta \to 0$. The value of β for which $\frac{\Delta E}{E}$ is within 14% of this limiting value was calculated. For moderate values of L and S, accurate values of E and ν can be derived for a peak with a population as low as $\sim 10^8$ helium atoms.

Acknowledgements

One of us (AAvG) would like to thank the Dutch Ministery of Education and the Netherlands Organization for the Advancement of Pure Research (ZWO) for research grants during the course of this work.

Appendix I

In this appendix, an approximate expression for the error in E will be derived for the dynamic mode. The standard deviation in the derived value of $\frac{dN}{dt}$ was given as (equation (16))

$$\sigma_{\frac{dN}{dt}} = \frac{Q^{\frac{1}{2}}}{S(\Delta t)^2}\left\{2 + \left[\frac{\Delta t}{\tau}\right]^2\right\}^{\frac{1}{2}} \qquad \text{(A-1)}$$

For the optimum value of $\frac{\Delta t}{\tau} = \sqrt{2}$

$$\sigma_{\frac{dN}{dt}} = \frac{2Q^{\frac{1}{2}}}{S(\Delta t)^2} \cdot \qquad \text{(A-2)}$$

The number of counts Q per channel is

$$Q = S*\Delta t*n_g$$

with n_g the number of particles in the gas phase. The result for Q is thus

$$Q = S*\Delta t*\left(\tau*\left(L + \frac{dN}{dt}\right)\right) = S\,\frac{(\Delta t)^2}{\sqrt{2}}\left(L + \frac{dN}{dt}\right) \quad . \tag{A-3}$$

Equation (A-2) becomes

$$\sigma_{\frac{dN}{dt}} = \frac{2\,S^{\frac{1}{2}}(\Delta t)\left(L + \frac{dN}{dt}\right)^{\frac{1}{2}}}{S(\Delta t)^2\,2^{\frac{1}{4}}} = \frac{2^{\frac{3}{4}}}{S^{\frac{1}{2}}\Delta t}\left(L + \frac{dN}{dt}\right)^{\frac{1}{2}} \tag{A-4}$$

or in relative terms

$$\frac{\text{noise}}{\text{signal}} = \frac{\sigma_{\frac{dN}{dt}}}{\frac{dN}{dt}} = \frac{2^{\frac{3}{4}}\left(L + \frac{dN}{dt}\right)^{\frac{1}{2}}}{S^{\frac{1}{2}}\Delta t\,\frac{dN}{dt}} \quad . \tag{A-5}$$

The new method to derive E and ν involves plotting the values $\frac{1}{T_i}$ vs $\ln\left\{\frac{T_i^2}{\psi_i}\right\}$ where T_i is the temperature at which the desorption rate is a fraction i of the maximum rate, and ψ_i the "characteristic time" (see Ref. 20) corresponding to that fractional rate. The slope of the straight line through these points yields the value of $\frac{E}{k}$. Due to the uncertainty in $\frac{dN}{dt}$, an error in T_i results. The relation between these errors can be calculated from the theoretical 1st order rate equation

$$\frac{dN}{dt} = -N\nu \exp -\left(\frac{E}{kT}\right) \quad . \tag{A-6}$$

The solution of this equation is[20]

$$\frac{dN}{dt} = -N_0\nu \exp -\left(\frac{E}{kT}\right) \exp(-\psi) \tag{A-7}$$

with ψ (the "characteristic time") equal to

$$\psi = \frac{\nu kT^2}{\beta E}\, g\left(\frac{E}{kT}\right) \exp\left(-\frac{E}{kT}\right)$$

$$g(z) = ze^z E_2(z) \approx 1 \quad \text{for} \quad z > 20$$

$E_2(z)$ = incomplete Γ function of the 2nd kind.

Since

$$\Delta T_i \approx \frac{\Delta \frac{dN}{dt}}{\frac{d^2N}{dt^2}} \cdot \frac{\Delta T_i}{\Delta t} = \beta \frac{\Delta \frac{dN}{dt}}{\frac{dN}{dt}} * \frac{\frac{dN}{dt}}{\frac{d^2N}{dt^2}} \qquad \text{(A-8)}$$

and

$$\frac{\frac{dN}{dt}}{\frac{d^2N}{dt^2}} = \frac{1}{\frac{E\beta}{kT^2}(1 - \psi/g)} \qquad \text{(A-9)}$$

it follows that

$$\frac{\Delta T_i}{T_i} = \frac{1}{\frac{E}{kT_i}(1 - \psi_i/g_i)} * \frac{\Delta \frac{dN}{dt}}{\frac{dN}{dt}} \qquad \text{(A-10)}$$

The error in E (the slope of the line drawn through the points) is related to the errors in the temperatures T_i. The errors in $\ln\left\{\frac{T_i^2}{\psi}\right\}$ (x-axis) are small compared to the ones in $\frac{1}{T_i}$ (y-axis). It is thus assumed that only errors in the y-coordinate exist. Moreover, it will be assumed that all points have an error equal to the largest error present (this procedure thus overestimates the error in E). It can be shown that the largest error occurs in the point corresponding to the lowest temperature T_r.

Based on these assumptions, the error in E is given by

$$\Delta E = \left(\frac{w}{w\sum x_i^2 - (\sum x_i)^2}\right)^{\frac{1}{2}} \cdot \Delta\left(\frac{1}{T_i}\right) = F(w)\,\frac{\Delta_1}{T_i} = F(w) * \frac{E}{kT_i} \cdot \frac{\Delta T_i}{T_i} \qquad \text{(A-11)}$$

where w is the number of points and x_i the values of $\ln\left\{\frac{T_i^2}{\psi_i}\right\}$. F(w) is a function of both the number of points w and the span of the points (the total range of x-values). For w > 10, as is needed to represent the total form of the desorption peak, (see section 3.4)

$$F(w) \approx \frac{1}{\Delta x}\left(\frac{10}{w}\right)^{\frac{1}{2}} \tag{A-12}$$

with Δx the total span of x-values:

$$\Delta x = \ln\left\{\frac{T_s^2}{\psi_s}\right\} - \ln\left\{\frac{T_r^2}{\psi_r}\right\} = \ln\left\{\frac{T_s^2}{T_r^2}\cdot\frac{\psi_r}{\psi_s}\right\}. \tag{A-13}$$

T_r and T_s are the lowest and highest used temperatures in the peak. It will be assumed that the highest temperature is at the same fractional amplitude as the lowest temperature ($r = -s$). The relative error in E can be related to the relative error in $\frac{dN}{dt}$ by equations (A-10), (A-11), (A-12) and (A-13):

$$\frac{\Delta E}{E} = \frac{1}{\ln\left\{\frac{T_s^2}{T_r^2}\cdot\frac{\psi_r}{\psi_s}\right\}}\left|\frac{10}{w}\right|^{\frac{1}{2}}\cdot\frac{1}{1-\frac{\psi_r}{g_r}}\cdot\left[\frac{\Delta\frac{dN}{dt}}{\frac{dN}{dt}}\right]_r \tag{A-14}$$

$$= \frac{10^{\frac{1}{2}} * 2^{\frac{3}{4}} * \left[\left.\frac{dN}{dt}\right|_r + L\right]^{\frac{1}{2}}}{\left(1-\frac{\psi_r}{g_r}\right)\ln\left\{\frac{T_s^2}{T_r^2}\cdot\frac{\psi_r}{\psi_s}\right\} w^{\frac{1}{2}} S^{\frac{1}{2}} \Delta t \left.\frac{dN}{dt}\right|_r}. \tag{A-15}$$

By definition

$$\left.\frac{dN}{dt}\right|_r = r\left.\frac{dN}{dt}\right|_m \tag{A-16}$$

$$\frac{\Delta E}{E} = \frac{2^{\frac{3}{4}}}{\Delta t\left[S\left.\frac{dN}{dt}\right|_m\right]^{\frac{1}{2}}} * \left[\frac{\left[\frac{10}{w}\right]^{\frac{1}{2}}\left(1+\frac{L}{r\left.\frac{dN}{dt}\right|_m}\right)^{\frac{1}{2}}}{r^{\frac{1}{2}}\left(1-\frac{\psi_r}{g_r}\right)\ln\left\{\frac{T_s^2}{T_r^2}\cdot\frac{\psi_r}{\psi_s}\right\}}\right] \tag{A-17}$$

The function in square brackets is plotted in Figure 4 as a function of r,

Fig. 4 *Relative error in the energy E (large brackets of Eq.(A-17)) assuming points above a fraction r of the maximum amplitude are used. Parameter is the ratio of background desorption rate L and maximum desorption rate of the peak* $\left.\frac{dN}{dt}\right|_m$.

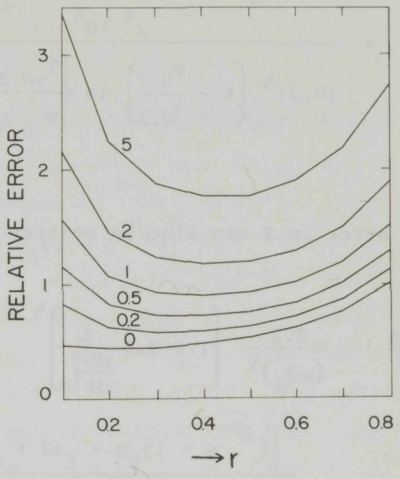

with $\frac{L}{\left.\frac{dN}{dt}\right|_m}$ as parameter. It is assumed that desorption rates at temperatures T_r, $T_{r+0.1}$, $T_{r+0.2}$, ..., $T_{m+0.1}$, ..., T_s are used. It is seen that this function reaches a minimum for $r \approx 0.3$ for $\frac{L}{\left.\frac{dN}{dt}\right|_m} < 1$, and for $r \approx 0.4$ if $\frac{L}{\left.\frac{dN}{dt}\right|_m} > 1$. In practical measurements, L will never be much greater than $\left.\frac{dN}{dt}\right|_m$, so that the optimum value of r = 0.3 will be assumed.

The optimum arises since for r < 0.3, the errors in the lowest temperatures become larger, while for r > 0.3, the number of points starts to decrease, increasing the error. Assuming r = 0.3 thus yields

$$\frac{\Delta E}{E} = \frac{C\left[1 + 3.3\,\frac{L}{\left.\frac{dN}{dt}\right|_m}\right]^{\frac{1}{2}}}{\Delta t\left[w\,S\left.\frac{dN}{dt}\right|_m\right]^{\frac{1}{2}}} \qquad \text{(A-18)}$$

with

$$C = \frac{2^{\frac{1}{4}}\, 10^{\frac{1}{2}}}{(0.3)^{\frac{1}{2}} \left(1 - \frac{\psi_{0.3}}{g_{0.3}}\right) \ln \left\{ \frac{T_{+0.3}^{\,2}}{T_{-0.3}^{\,2}} \cdot \frac{\psi_{-0.3}}{\psi_{+0.3}} \right\}} \approx 3.1 \qquad \text{(A-19)}$$

The relative error in E can also be written as

$$\frac{\Delta E}{E} = \frac{2.2}{(wQ_m)^{\frac{1}{2}}} \left(1 + 3.3 \frac{L}{\left.\frac{dN}{dt}\right|_m} \right)^{\frac{1}{2}} \qquad \text{(A-20)}$$

with $$Q_m = S\Delta t * \left.\frac{dN}{dt}\right|_m * \tau = \frac{S(\Delta t)^2}{\sqrt{2}} \left.\frac{dN}{dt}\right|_m$$

the number of counts at the peak maximum due to the net desorption rate (excluding the background desorption rate L).

Appendix II

The derivation of equation (26) for the relative error in E in the static mode goes along similar lines as in Appendix I for the dynamic mode. Equation (A-1) now becomes, since $\tau \to \infty$

$$\sigma_{\frac{dN}{dt}} = \frac{(2Q)^{\frac{1}{2}}}{S(\Delta t)^2} \; . \qquad \text{(A-21)}$$

The number of particles in the gas phase n_g is equal to

$$n_g = n_b + \int_0^{t_i} \left(\frac{dN}{dt} + L \right) dt = n_b + Lt_i - (N(t_i) - N_0) \qquad \text{(A-22)}$$

where t_i = time from closing off the system and starting the desorption. For a first order peak,

$$N(t_i) - N_0 = -N_0\left(1 - e^{-\psi_i}\right) \tag{A-23}$$

with ψ the "characteristic time" (see Ref. 20 and equation (A-7)). The number of counts per channel, Q_i, is equal to

$$Q_i = S\Delta t * \left[n_b + Lt_i + N_0\left(1 - e^{-\psi_i}\right)\right] \tag{A-24}$$

and the noise/signal ratio

$$\frac{\text{noise}}{\text{signal}} = \frac{\sigma_{\frac{dN}{dt}}}{\frac{dN}{dt}} = \frac{2^{\frac{1}{2}}\left[n_b + Lt_i + N_0\left(1 - e^{-\psi_i}\right)\right]^{\frac{1}{2}}}{S^{\frac{1}{2}}(\Delta t)^{3/2}\,\frac{dN}{dt}} \tag{A-25}$$

The same considerations as leading to equation (A-14) apply, resulting in

$$\frac{\Delta E}{E} = \frac{1}{\ln\left\{\frac{T_s^2}{T_r^2}\cdot\frac{\psi_r}{\psi_s}\right\}}\left[\frac{10}{w}\right]^{\frac{1}{2}}\cdot\frac{1}{\left[1 - \frac{\psi_r}{g_r}\right]}\cdot\frac{2^{\frac{1}{2}}\left[n_b + Lt_i + N_0\left(1 - e^{-\psi_i}\right)\right]^{\frac{1}{2}}}{S^{\frac{1}{2}}(\Delta t)^{3/2}\,\frac{dN}{dt}}$$

$$= \frac{2^{\frac{1}{2}}\,N_0^{\frac{1}{2}}}{(\Delta t)^{3/2}\,S^{\frac{1}{2}}\left.\frac{dN}{dt}\right|_m} * \left[\frac{\left[\left(\frac{10}{w}\right)^{\frac{1}{2}}\left[1 - e^{-\psi_r} + \frac{\left(n_b + Lt_r\right)}{N_0}\right]^{\frac{1}{2}}\right]}{r\left[1 - \frac{\psi_r}{g_r}\right]\ln\left\{\frac{T_s^2}{T_r^2}\cdot\frac{\psi_r}{\psi_s}\right\}}\right] \tag{A-26}$$

The term in square brackets reaches again a minimum for $r \approx 0.3$, so that

$$\frac{\Delta E}{E} \approx \frac{C\,N_0^{\frac{1}{2}}}{\Delta t(wS\Delta t)^{\frac{1}{2}}\left.\frac{dN}{dt}\right|_m}\left[1 - e^{-\psi_{0.3}} + \frac{n_b + Lt_{0.3}}{N_0}\right]^{\frac{1}{2}} \tag{A-27}$$

with

$$C = \frac{10^{\frac{1}{2}}\, 2^{\frac{1}{2}}}{0.3\left(1 - \frac{\psi_{0.3}}{g_{0.3}}\right) \ln\left\{\frac{T_{+0.3}^{\,2}}{T_{-0.3}^{\,2}} \cdot \frac{\psi_{-0.3}}{\psi_{+0.3}}\right\}} \approx 3.4\sqrt{2} = 4.8. \quad \text{(A-28)}$$

Since

$$\left.\frac{dN}{dt}\right|_m \approx 10\, N_0 \beta / T_m ,$$

$$\delta = \frac{w \beta \Delta t}{T_m}$$

and

$$\psi_{0.3} \approx 0.1$$

$$\frac{\Delta E}{E} = \frac{0.48}{(\delta \Delta Q_m)^{\frac{1}{2}}} \left(1 + 10\, \frac{n_b + Lt_{0.3}}{N_0}\right)^{1/2} \quad \text{(A-29)}$$

with $\Delta Q_m = S(\Delta t)^2 \left.\frac{dN}{dt}\right|_m$ = change in counts/channel at maximum of desorption peak due to net desorption (excluding background).

References

[1] E.V. Kornelsen, Phys. Rev. 136 (1964) A849.

[2] K.J. Close, J. Yarwood, Brit. J. Appl. Phys. 18 (1967) 1593.

[3] K. Erents, G. Farrell, G. Carter, Proc. 4th Int. Vac. Congr. 1968, Inst. Phys. Conf. Ser. #5, p. 145.

[4] E.V. Kornelsen, Rad. Eff. 13 (1972) 227.

[5] D.E. Edwards Jr., J. Appl. Phys. 46 (1975) 1437.

[6] L.M. Caspers, A. van Veen, A.A. van Gorkum, A. van den Beukel, C.M. van Baal, Phys. Stat. Sol. (A) 37 (1976) 371.
[7] E.V. Kornelsen, A.A. van Gorkum, Nucl. Instr. Meth. 170 (1980) 161.(ch.7)
[8] D.E. Edwards Jr., E.V. Kornelsen, Rad. Eff. 26 (1975) 155.
[9] A. van Veen, L.M. Caspers, E.V. Kornelsen, R.H.J. Fastenau, A.A. van Gorkum, A. Warnaar, Phys. Stat. Sol. (A) 40 (1977) 235.
[10] E.V. Kornelsen, A.A. van Gorkum, Rad. Eff. 42 (1979) 113.(ch.6)
[11] A.A. van Gorkum, E.V. Kornelsen, Rad. Eff. 42 (1979) 93.(ch.5)
[12] E.V. Kornelsen, M.K. Sinha, J. Appl. Phys. 39 (1968) 4546.
[13] E.V. Kornelsen, M.K. Sinha, J. Appl. Phys. 40 (1969) 2888.
[14] A. Wagner, D.N. Seidman, Phys. Rev. Lett. 42 (1979) 515.
[15] E.V. Kornelsen, Can. J. Phys. 48 (1970) 2812.
[16] E.V. Kornelsen, A.A. van Gorkum, submitted to J. Nucl. Mat.(ch.10)
[17] E.V. Kornelsen, D.L. Blair, J. Vac. Sc. Techn. 14 (1977) 1299.
[18] E.V. Kornelsen, A.A. van Gorkum, following paper(ch.3)
[19] Point defects in metals, A.C. Damask, G.J. Dienes, Gordon and Breach, New York and London, 1963.
[20] A.A. van Gorkum, J. Appl. Phys. 51 (1980) 2594.(ch.4)
[21] D.E. Edwards Jr., Vacuum 26 (1976) 91.
[22] G. Carter, Vacuum 12 (1962) 245.
[23] S.E. Donnelly, D.C. Ingram, R.P. Webb, D.G. Armour, Vacuum 29 (1979) 303.
[24] A.A. van Gorkum, E.V. Kornelsen, to be published in Rad. Eff.(ch.9)
[25] R.K. Swank, J. Appl. Phys. 44 (1973) 4199.
[26] E.V. Kornelsen, A.A. van Gorkum, unpublished results.

QUANTITATIVE THERMAL DESORPTION SPECTROMETRY OF IONICALLY IMPLANTED INERT GASES
II. TECHNICAL REQUIREMENTS

E.V. Kornelsen and A.A. van Gorkum

Division of Electrical Engineering
National Research Council of Canada
Ottawa, Canada K1A 0R8

ABSTRACT

Experimentally, quantitative thermal desorption spectrometry requires that a well characterized sample be subjected to specified ion bombardments, heated in an accurately defined temperature-time profile, and the resulting gas desorption rate measured with the highest available sensitivity. This paper discusses the main considerations affecting the design of the sample, its heating equipment, the ion gun and the partial pressure detector to meet these requirements.

It was shown in the preceding paper that the system sensitivity and background leak rate are the only apparatus parameters affecting the accuracy with which kinetic parameters (binding energy, frequency factor, reaction order) can be derived from the data. Approximate limits to the achievable values of these two parameters are given. The required properties of the data acquisition system and the data treatment and analysis procedures are also outlined. Some experimental examples are given to illustrate the quantitative accuracies that can be attained.

1 Introduction

The experimental technique of thermal desorption spectrometry (TDS) has been applied for many years to the study of chemisorbed gases and ionically implanted inert gases. Although both involve (or should involve) well-characterized surfaces in ultrahigh vacuum systems, these two applications have rather different technical requirements: In the former, the number of desorbed molecules is relatively large ($\sim 10^{12} - 10^{15}$) since coverages $\sim 10^{-3}$ - 1 monolayer and surface areas ~ 1 cm^2 are usually of interest. The required sensitivity of mass spectrometers for detection of the desorbing gas is in this case quite modest and can be met by commercially available instruments. It is, in fact, feasible to use line-of-sight geometry, allowing the desorption of non-gaseous species as well as gases to be studied[1]. For implanted inert gases, the number of desorbed molecules is in general much smaller. Two distinct kinds of thermal desorption spectra are of interest:

a. *that of heavy gases (Ne, Ar, Kr, Xe) which either desorb by a first order process from surface related sites or diffuse from deeper sites as substitutional impurities before desorbing,*
b. *that of helium released from "traps" (either impurity atoms or vacancies, or clusters of these in some combination) which undergoes rapid interstitial diffusion to the surface and gives desorption rates showing the first order kinetics of the detrapping.*

In case a) the implanted concentrations must be so low that the probability of two gas atoms encountering one another during their diffusion is small, since otherwise clusters of the atoms may form. In case b) an even more stringent requirement arises: to establish the number of traps and their fundamental binding properties for helium, it is necessary to measure helium spectra when only a small fraction of the already small number of traps is occupied, since multiple occupation otherwise complicates their interpretation.

Approximate limits to the permissible concentrations and doses which result from the above considerations are derived in section 2 of the companion paper to this[2], referred to hereafter as I. It turns out that the number of desorbed atoms of interest is $\sim 10^7$ to 10^{13}. A mass spectrometer of somewhat specialized design is required to detect such small quantities of gas, and care must be taken to minimize background gas sources which might obscure the desorption signal.

In paper I, quantitative criteria for the required mass spectrometer sensitivity and background leak rate are derived. It is shown that for a single desorption peak, once an allowed error ΔE in the binding energy E is specified, the important characteristics of the apparatus necessary to do adequate TDS measurements can be approximated by a single fairly simple equation. For the two basic modes of measurement, this equation can be written as follows:

a. for the *static mode*, in which the desorbing gas accumulates in an isolated volume containing no significant pumps

$$\frac{\Delta E}{E} \simeq 26\left[\frac{\beta}{S T_m N_0}\right]^{\frac{1}{2}}\left[1 + 10\,\frac{n_b + L t_{0.3}}{N_0}\right]^{\frac{1}{2}} \qquad (1)$$

b. for the *dynamic mode*, in which the desorbed gas is continuously removed by a pump of constant relatively high speed

$$\frac{\Delta E}{E} \simeq 17\left[\frac{\beta}{S T_m N_0}\right]^{\frac{1}{2}}\left[1 + 3.3\,\frac{L}{\left.\frac{dN}{dt}\right|_m}\right]^{\frac{1}{2}} \qquad (2)$$

where β = temperature rise rate ($K\ s^{-1}$)

S = the system sensitivity, $\frac{G}{n_0 eV}$

G = MS sensitivity i^+/p ($A\ torr^{-1}$)

V = desorption volume (ℓ)

$n_0 = 3.27 \times 10^{19}$ molecules $torr^{-1}\ \ell^{-1}$ (at 300 K)

$e = 1.602 \times 10^{-19}$ C

T_m = the peak temperature (K)

N_0 = the initial number of bound molecules

$\left.\frac{dN}{dt}\right|_m$ = maximum desorption rate ($mol\ s^{-1}$)

L = background leak rate of the gas being desorbed ($mol\ s^{-1}$)

n_b = number of molecules in the desorption volume at the start of the desorption sweep (static mode only)

$t_{0.3}$ = time from isolation of desorption volume to time at which desorption rate is $0.3 \times \left.\frac{dN}{dt}\right|_m$ (static mode only).

In the dynamic mode, the optimum ratio $\frac{\Delta t}{\tau} = \sqrt{2}$ of the sampling time Δt to the pumping time constant τ must be preserved for Eq. (2) to hold.

The present paper deals with the design and operation of ultrahigh vacuum apparatus for TDS and outlines a number of technical conditions which must be met if data of adequate quality is to be obtained and analyzed.

Section 2 gives the required characteristics of the sample itself and of the ion gun used to bombard it. In section 3, the apparatus related parameters in eqs. (1) and (2) and the system components most important in determining their magnitudes are discussed. Section 4 presents some relevant aspects of sample heating.

It will be assumed from the outset that some form of digital data equipment is being used for the acquisition and manipulation of the data, since quantitative measurement is otherwise nearly, if not completely, impossible. The general requirements of the acquisition system are discussed in section 5, and the corrections which must be applied to the measured data to obtain the desorption rate spectrum in section 6.

Finally, certain aspects of peak deconvolution are discussed in section 7. In particular, the use of a computer to optimize the fit of a theoretically generated desorption spectrum to the experimental data is discussed and some observations are made on the advantages and limitations of this technique for the analysis of multi-peak spectra.

In the sub-sections of sections 2, 3 and 4, the discussion of general requirements is augmented by examples of characteristics and conditions that have been achieved in an operating system[3,4] in our laboratory. To illustrate the acquisition, treatment and deconvolution of data using this same apparatus in conjunction with a small computer-based acquisition system, a selection of thermal desorption spectra are presented as examples in section 8.

2 Sample and bombardment considerations

The requirement that well-defined trapping states must be generated in the sample in a controlled and repeatable way, and that the temperature of its bombarded region must be uniform during the desorption cycle determine the main characteristics of both the sample being studied and the ion gun used for the implantations. These characteristics are the subject of the present section.

2.1 The sample

To avoid the complexities introduced by grain boundaries, uncontrolled surface orientations and impurities, the sample must be a single crystal with a flat surface of known (usually low-index) orientation, and with surface impurity levels not exceeding a few % of a monolayer. The ultrahigh vacuum, sample preparation and analysis techniques familiar in surface science experiments are thus mandatory for TDS as well.

The analysis of TDS data (see I) depends critically on the shape of the desorption peak. A non-uniform temperature of the bombarded area of the sample during desorption would cause the peaks to broaden, leading to errors in the deduced kinetic parameters. A change in peak width of 5% is sufficient to lead to measurable changes in the parameters, so that since the peaks are $\sim 0.08\ T_m$ wide, non-uniformities of $\frac{0.08T_m}{20}$ or $0.004\ T_m$ should not be exceeded. This requirement favours thick samples (≥ 1 mm) heated by electron bombardment rather than thin ribbons heated resistively. The thermal conductance of the crystal mounting structure must be relatively low as well to avoid radial temperature gradients, but it must be mechanically stable under repeated heating $\sim 0.75\ T_{melt}$ since such treatment is required for complete removal of the implanted gas in some cases. It is also important that the mount allow the orientation of the crystal relative to the incident ion beam to be varied.

The choice of the sample size requires a compromise. The available signal amplitude is proportional to the number of atoms desorbed and therefore, at a given concentration, proportional to the bombarded area, calling for a large size. Fabrication, surface preparation, characterization and heating on the other hand all become more difficult with increasing size. Furthermore, to maintain well defined incident ion directions on the crystal, the ion beam length and therefore the ion gun size must increase with increasing sample size. Taken together, these considerations (which are common to many types of apparatus used in surface science) normally lead to samples with a bombarded area $\leq 0.2\ cm^2$ and overall diameters $d \leq 0.7$ cm. Only rarely are diameters > 1.0 cm used.

The samples used in our apparatus are compatible with a vacuum transfer device[5] which allows them to be inserted and removed with a minimum of disturbance to the system vacuum conditions and the sample surface state. Sizes up to 1.0 cm in diameter and 0.3 cm in thickness can be accommodated. They are mounted on standard molybdenum rings via three 0.05 cm diam. tungsten pins which enter holes in the cylindrical edge as illustrated in Fig. 1a. The

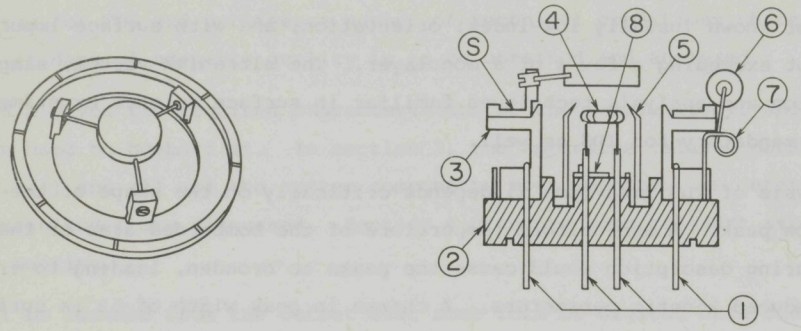

Fig. 1 (a) *crystal mounted by tungsten pins on molybdenum ring. The marks are azimuth identifiers.* (b) *crystal bombarder, consisting of* (1) *Pt pins;* (2) Al_2O_3 *mounting block;* (3) *Mo platform;* (4) *W filament* (ϕ = 0.125 mm); (5) *Mo shield electrode;* (6) *Mo roller with* Al_2O_3 *insert;* (7) *W springs* (ϕ = 0.375 mm); (8) *Mo insulator shield;* (S) *Mo ring* (see (a))

rings are deposited by the transfer device onto a mount where they are held in place by a centering cone and three roller-tipped springs. A cross section of the mount with a sample in place is shown in Fig. 1b. The mount contains an electron bombardment heater which directs 1 kV electrons onto the back surface of the sample. The maximum available power is 120 W.

To avoid the difficult problem of making removable thermocouple connections to the transferable samples, temperatures have to-date been measured with a calibrated infra-red pyrometer (see section 4).

2.2 *The ion gun*

Trapping states characteristic of both the crystal surface and the bulk crystalline material are of interest in TDS experiments. There is evidence to suggest that the former are within ~ 10 Å of the crystal surface, so that implantation depths, even for the study of bulk traps, can be quite small ($\lesssim$ 200 Å) and the ion energies correspondingly low ($\lesssim 10^4$ eV). It was, in fact, shown in I that for larger depths, lower concentrations of implanted gas, and thus a higher mass spectrometer sensitivity is required. The low maximum energy allows the ion gun to be made relatively small ($\lesssim$ 1 m in overall length)

and compatible with only modest interelectrode potentials and fields.

The threshold energy for entrance of ions into solids is ~ 4 - 8 eV for He^+ [6] and ~ 20 - 200 eV for the heavier ions $Ne^+ - Xe^+$ [7,8]. The threshold for producing surface damage by heavy ion impact is comparable to the sputtering threshold, ~ 15 - 25 eV. To cover the entire range of energies of interest, the ion gun should thus be capable of providing beams from a few eV to ~ 10^4 eV.

Since the extraction of beams from ion sources is inefficient at very low energies due to ion space charge, it is advisable to design the ion gun to operate with lenses able to decelerate the beam between extraction and sample impact. The same lenses can be used to accelerate the beam for the highest required energies, so that the range of extraction voltages used in the ion source is further reduced. As an example, one might use 40 V to 1000 V for beam extraction from the source, a unipotential lens to transport the beam at the extracted energy, and a lens able to accelerate or decelerate the beam by a factor of 10 to cover the extremes of the energy range of interest. The gun would then operate in one of three distinct modes requiring different arrangements of the various electrode potentials.

Two aspects of the experiments make it desirable to have ion beam lengths (measured from the last focussing or deflecting electrode to the sample) of ~ 25 cm or more. Firstly, the ion source should be situated outside of the desorption volume to avoid excessive background leak rates L (see section 3.2). This requires that the beam be directed through an in-line ultrahigh vacuum valve which will normally be of substantial axial length. Secondly, the angle of ion incidence on the sample must be well defined because directional effects (channeling) can be prominent even at these low energies[9]. This angle definition is most easily satisfied by having the beam length from the final lens much larger than the diameter d_B of the bombarded area. For d_B = 0.5 cm (see section 2.1), a beam length of 25 cm will define the incident angle to within about $\pm 0.5^\circ$. This is barely adequate since characteristic channeling angles at the energies of interest are ~ 5 - 10° [9].

Provisions must also be made in the ion gun to mass analyse the beam so that the bombarding ion species is known. This is particularly important when He^+ beams are used, since the presence of even a small fraction of heavy ions in the beam could cause extensive lattice disorder while the He^+ ions produced little or none[6]. If inert gas beams are to be used exclusively, a very modest resolving power ($M/\Delta M \approx 10$) is adequate, and this makes it possible to design a mass analyser with transmission approaching unity so that the full intensity

of the extracted beam can be retained.

The ion beam currents needed for TDS are determined primarily by the required sample ion doses n^+ (ions cm^{-2}). As outlined in I, these are in most cases necessarily small, rarely exceeding a few times 10^{14} ions cm^{-2}. Since the bombarded area is nominally $A_b \lesssim 0.2$ cm^2, the maximum time required for a bombardment is

$$t_m = \frac{e A_b n^+}{i^+} \approx (3 \times 10^{-20}) \frac{n^+}{i^+} \quad s. \tag{3}$$

If a bombarding time $t_m \approx 10^3$ s is acceptable, then for an upper limiting value $n^+ \approx 5 \times 10^{14}$ cm^{-2} a beam current $i^+ \approx 1.5 \times 10^{-8}$ A is sufficient.

It has been shown[3] that highly efficient ion sources can yield such beam currents at relatively low working pressures ($\lesssim 2 \times 10^{-6}$ torr). It is thus not necessary to resort to differentially pumped sources and their attendant additional pumping requirements.

It may be noted that since sputtering yields for many materials are ~1 for energies of some hundreds of eV, the ion dose to sputter a monolayer from the bombarded surface is ~ 1×10^{15} ions cm^{-2}. The ion beam can thus be used to sputter-clean the crystal provided that the adsorption monolayer time is $t_m >> 2 \times 10^3$ sec, i.e. that the partial pressure of adsorbable gas is $p_a << 5 \times 10^{-10}$ torr. For convenience, somewhat higher beam currents are, of course, desirable.

Ion space charge spreading limits the beam current to values lower than the above requirement for the lowest energies of interest. The space charge limited current is

$$I_{max} = (3.62 \times 10^{-6}) \frac{d^2}{\ell^2 M^{\frac{1}{2}}} V^{3/2} = KV^{3/2} \text{ A} \tag{4}$$

where
- ℓ = beam length (cm)
- d = beam diameter at the two ends (cm)
- M = mass number of the beam ions
- V = beam voltage (V)

For ℓ = 25 cm and d = 0.5 cm, as used in this section, $K = 7.2 \times 10^{-10}$ for He^+, and $K = 1.26 \times 10^{-10}$ for Xe^+. For these two ions the limiting beam current falls to 1.5×10^{-8} A at ~ 8 V and ~ 24 V respectively.

Quantitative analysis of TDS data requires that the concentrations of the trapped particles and (in the case of He) of the traps must be fairly well defined. For the heavy gas implantations and for helium injections leading to only a small number $i < 0.2$ of He atoms per trap, concentration variations of ± 10% are generally tolerable. For higher values of i, the tolerable variations become progressively smaller. The ion beam must therefore be spread out to ensure the uniformity of current density over the bombarded area, and as a result the actual total current that must be supplied by the gun is larger than the estimates made above. If the beam is simply defocussed, then its profile is roughly Gaussian, and to achieve a dose variation limit of x% it can be shown that only a fraction f = x of the beam is actually used, the rest being incident on the beam stop, the final electrode whose aperture defines the bombarded area on the sample. A somewhat larger fraction f can be utilized if the beam is raster-scanned over the aperture. This proves to be advantageous only if the beam diameter d_b can be made less than about the aperture diameter d_a. For $d_b/d_a = 0.25$, f can be shown to be ~ 0.45, and for $d_b/d_a \to 0$, $f \to \pi/4$ because of the square shape of the scanned area. Whether defocussing or scanning is used, some means of probing the current density distribution at the sample is highly desirable to verify that uniformity criteria have been met.

Another problem which arises at low ion beam energies is the curvature of the beam due to stray magnetic fields. If a field of B (Oersted) exists over the whole length ℓ (cm) of a beam, an ion of mass number M and energy E (eV) will suffer an angular deflection of

$$\theta = \frac{\ell}{R} = \frac{0.4\ell B}{\sqrt{ME}} \text{ degrees.} \qquad (5)$$

For static fields, errors in incident directions of ~ θ/2 will result when electrostatic deflectors are used to adjust the beam position on the sample. In a related way, an oscillating magnetic field of peak amplitude B will lead to a "spot splitting" of

$$\Delta = \frac{\ell^2 B}{144\sqrt{ME}} \text{ cm.} \qquad (6)$$

This makes the time-average beam depart from circular symmetry and can complicate the uniformity, beam utilization and incident angle considerations

discussed above. As a typical example, a 100 eV He^+ beam of length ℓ = 25 cm will have, for B = 1 Oe, $\theta = 0.5°$ and Δ = 0.22 cm.

Finally, consideration should be given to the outgassing properties of the ion gun, particularly of the ion source. It was mentioned earlier that bombarding times ~ 10^3 sec are commonly used. In order to limit the contamination of the crystal by background gas adsorption during this time to, say 0.05 monolayer, the partial pressure of chemisorbable gases at the crystal while exposed to the operating ion gun must be $p \leq 5 \times 10^{-11}$ torr. The choice of structural materials compatible with high temperature degassing and thorough bake-out procedures is essential, and verification of the surface contamination state mandatory. An ion gun which satisfies the above criteria reasonably well in actual operation has been reported in an earlier publication[3], and its detailed specifications will not be repeated here.

3 Factors affecting the system sensitivity and background

The defining equations (1) and (2) contain only five parameters that depend on the experimental apparatus itself: these are the mass spectrometer sensitivity G, the desorption volume V, the background leak rate L, the initial number of gas phase molecules n_b, and the background current in the MS multiplier, which can be expressed as an equivalent leak rate L_d or number of molecules n_{bd} to be added to L and/or n_b (see section 1).

The form of equations (1) and (2) show that to minimize $\Delta E/E$, the system sensitivity S should be maximized (G maximized, V minimized), and L and n_b should be minimized. In this section, the technical aspects of accomplishing this will be discussed.

3.1 MS sensitivity G

The total ion current produced in an electron impact ionizer is

$$i^+ = i^- s \bar{\ell} p \quad A \tag{7}$$

where
- i^- = the ionizing electron current (A)
- s = the ionization coefficient (ion electron^{-1} cm^{-1} torr^{-1})
- $\bar{\ell}$ = mean electron path in ionizer (cm)
- p = gas pressure (torr)

The highest sensitivity is achieved when all of the produced ions reach the MS collector: $G_{max} = i^+/p = i^-\bar{\ell}s$ A torr^{-1}. The maximum in s occurs at

electron energies in the range 50 eV to 120 eV for most common gases. It reaches values ranging from $s_{max} \approx 1$ cm^{-1} torr^{-1} for He to $s_{max} \approx 15$ cm^{-1} torr^{-1} for Xe. Practical limits to the achievable values of the product $i^- \bar{\ell}$ can be estimated by considering the space charge limited current density that can be transmitted across a space of length d:

$$J_{max} = 9.32 \times 10^{-6} \frac{E_e^{3/2}}{d^2} \text{ A cm}^{-2} \qquad (8)$$

where E_e is the electron energy in eV.

If we approximate the ionizer by a cube with side $\bar{\ell}$, then

$$\bar{\ell}\, i^-_{max} = \bar{\ell}^3 J_{max} = 9.32 \times 10^{-6} E_e^{3/2} \bar{\ell} \text{ A cm}$$

which for $E_e \approx 100$ eV is $\approx 10^{-2} \bar{\ell}$ A cm. Even if ion trapping is used to minimize the electron space charge, instabilities in the ion production rate begin to occur at currents not much greater than i^-_{max}, say $\sim 2i^-_{max}$. The values of $\bar{\ell}$ also have practical limits. At $\bar{\ell} \gtrsim 2$ cm, it becomes increasingly difficult to extract all of the produced ions into a beam suitable for mass analysis, and G approaches a limiting value due to the increasing losses.

The foregoing considerations lead to the following very approximate upper limits to G:

$$G_{max}(\text{He}) \sim 4 \times 10^{-2} \text{ A torr}^{-1}$$
$$G_{max}(\text{Xe}) \sim 6 \times 10^{-1} \text{ A torr}^{-1}$$

In the 90° magnetic sector mass spectrometer used in our apparatus[4], experimental values G(He) = 1.6×10^{-2} A torr^{-1} and G(Ar) = 1.3×10^{-1} A torr^{-1} have been achieved using an electron current of 15 mA in a cylindrical ionizer 2 cm in diameter and 2 cm in length.

3.2 The background leak rate L

Two sources contribute to the background leak rate L of the molecules to be detected. The first is the diffusive emission of gas from the bulk of the materials present (electrodes, insulators, structural parts, and the vacuum envelope), and the second is the reemission of near-surface gas ionically pumped earlier by the operation of ionizing devices (ion gun, mass

spectrometer, electron bombardment heater, ionization gauges, ion pumps).

The first gives a more or less constant leak rate L_m related to the overall heat-treatment history of the materials and, for the case of helium, to the permeation constant of envelope materials such as borosilicate glass and some ceramics (L_p). It has been found that, aside from permeation, it is possible to achieve extremely small source rates of all the inert gases ($L_m \leq 1 \times 10^6$ molecules s^{-1} or 3×10^{-13} torr ℓ s^{-1}). A borosilicate glass envelope, on the other hand, is known to transmit $\sim 1 \times 10^5$ molecules $s^{-1}cm^{-2}$ of atmospheric helium[10]. For a nominal envelope area of 1000 cm^2, this would lead to $L_p \approx 1 \times 10^8$ molecules s^{-1}, some 100 times larger than L_m.

The reemission rate L_i of inert gas previously pumped ionically has been found[11] to obey the equation

$$L_i = \frac{An_p}{t_p} \text{ molecules } s^{-1} \qquad (9)$$

where n_p = the number of gas atoms (molecules) pumped

t_p = time since they were pumped (s)

A = a constant dependent on the ion species, ion energy, target material and temperature, and ranging from 10^{-3} to 10^{-1}.

The constant A can be established for any given ionizing device by pumping some measured number of molecules $n_p = n_0 V \Delta p$ and observing the leak rate as a function of time thereafter. It is usually more convenient, however, to relate L_i to some easily measurable operating parameter which is proportional to n_p such as the ion dose to the sample, n^+, in the case of the ion gun or the exposure $p\Delta t$ (torr s) in the case of the MS ionizer. This method is used in the example described below.

The background pressure and leak rate of the ^3He were found to be immeasurably small in our apparatus ($p < 1 \times 10^{-15}$ torr, $L < 1 \times 10^3$ molecules s^{-1}). To establish the reemission constant associated with the ion beam impingement therefore, the sample was bombarded with $n^+ = 1 \times 10^{11}$ $^3He^+$ ions at 250 eV - a nominal "low dose" bombardment. Because of deliberate defocussing to achieve uniform current density (see section 2.2) an additional $\sim 2 \times 10^{11}$ ions (not measured) struck the beam stop. Subsequent measurements of the ^3He leak rate yielded the relation

$$L_i = (1.4 \times 10^{-2}) \frac{n^+}{t} \text{ molecules } s^{-1}.$$

The proportionality constant $A_1 = 1.4 \times 10^{-2}$ can be used to predict L_i from this source for any dose and time following a 250 eV He^+ bombardment. In a similar way, after exposing the operating MS to 5×10^{-10} torr of ^3He for 200 seconds ($p\Delta t = 1 \times 10^{-7}$ torr s) it was found that

$$L_i = \frac{A_2(p\Delta t)}{t} = \frac{(1.1 \times 10^{16})(p\Delta t)}{t} \text{ molecules } s^{-1}$$

The above relationships were found to be reasonably well obeyed up to at least $t = 10^6$ s. Even three weeks after the MS exposure, the ^3He leak rate, although small, was still easily measurable at 1.8×10^3 molecules s^{-1}. At this time, the ^3He partial pressure with the magnetron ion pump operating was $\sim 6 \times 10^{-15}$ torr. The mass spectrometer signal including a leak-up upon isolating from the pump, is illustrated in Fig. 2.

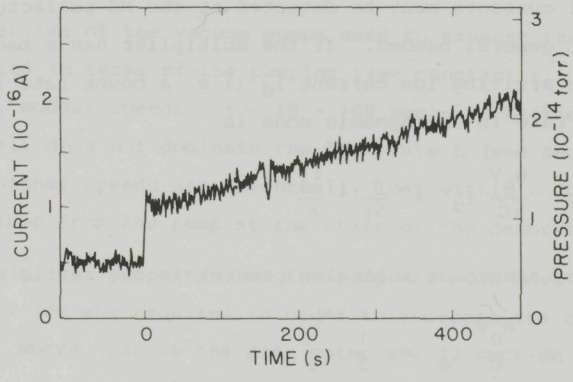

Fig. 2 *The ^3He current at the input of the electron multiplier and corresponding ^3He partial pressure before and after isolating the desorption chamber from the magnetron pump. The multiplier background current of 2.4×10^{-16} A has been subtracted.*

The above example indicates that under normal operating conditions, when several bombardments and/or exposures are likely to occur per day, practical limits to L_i are likely to be $\sim 10^6$ molecules s^{-1}. Using ^3He for only the lowest doses, and relatively infrequently, values perhaps one order of magnitude lower might be attainable. It is clear that helium permeable materials should not be used in the desorption volume envelope, and that the MS should be operated only at pressures near the lowest attainable.

In the static mode of TDS measurements, the number of molecules in the desorption volume at the start of the desorption sweep, n_b, is also of importance. n_b is related to the leak rate L and the pumping time constant τ at the background pressure: $n_b = L\tau$ molecules. In this regard, two points should be made concerning uhv pumps. Firstly, ion pumps tend to have increasingly large τ at low total pressures ($< 5 \times 10^{-11}$ torr) and even the best have negligible speed ($\tau \to \infty$) at pressures $p_u \sim 10^{-12}$ torr. In a V liter volume, if the gas of interest comprises a fraction α of the residual gas, $n_b = n_0 V p_u \alpha \sim 3 \times 10^7\ \alpha\ V$ molecules will be the lowest value attainable. Secondly, a pump may have a back-flow rate L_{bf} of the gas in question depending on its type, construction and pumping history. This may greatly exceed the desorption rate L discussed above, resulting in an unexpectedly large value of n_b. A careful evaluation of the pump at its lowest attainable pressure is advisable before including it in a TDS system.

Some additional aspects of pumps for TDS systems are discussed in section 3.5.

3.3 MS detector background

Since very small currents must be detected at the MS collector, an electron multiplier is in general needed. If the multiplier has a background current equivalent to an arriving ion current i_d (i.e. a count rate i_d/e), the equivalent leak rate in the dynamic mode is

$$L_d = \frac{n_0 V}{\tau G} i_d = \frac{1}{S\tau} \cdot \frac{i_d}{e} \qquad (10)$$

and the equivalent number of molecules present in the static mode is

$$n_{bd} = \frac{n_0 V}{G} i_d = \frac{1}{S} \frac{i_d}{e} \qquad (11)$$

These must be added to the values of L and n_b discussed earlier (section 3.2).

It will be shown in section 5, that the maximum ion currents that will be encountered in acquiring high quality data are too large to allow pulse counting techniques to be used. The advantage gained by discriminating against smaller background pulses is therefore not available, and the *total* multiplier background current must be considered as contributing to i_d. Using a Cu-Be dynode 10-stage multiplier, the detector in our apparatus had an equivalent input current of 2.4×10^{-16} A independent of net gain between 10^2 and 5×10^4. The resulting equivalent n_{bd} was $\sim 1 \times 10^6$ molecules. As can be seen in equation (10), in the dynamic mode L_d can be made small by making τ large.

3.4 Desorption volume

The desorption volume V will normally contain the sample, its mount, manipulator and heater, and the detecting mass spectrometer MS. As a practical lower limit, it could be arranged to contain only the crystal, its mount and heater and the ionizer volume of the MS. In this case, operating in the dynamic mode, the ion exit aperture from the MS source would be used as the pump-out aperture defining τ, and a desorption volume $V \sim 0.1 - 0.2$ ℓ might be feasible. This arrangement would at the same time minimize L by excluding all ion gun components including the beam stop from the desorption volume. It would however, be necessary to use a moveable "capping" device to connect the crystal to the MS ionizer between bombardment and desorption.[19]

In the static mode, the entire mass spectrometer, including the analyzer and detector, forms part of the desorption volume, and $V < 1$ litre is difficult to achieve. Our system has a desorption volume of 2.27 ℓ.

3.5 Pumps

The required properties of the vacuum pumps used to exhaust the desorption volume can be stated in terms of the pumping time constant τ. For the static mode of operation, modest speeds ($\tau \sim 10 - 100$ sec) are sufficient provided that the pump itself does not dominate the leak rate L (see section 3.2). The advantage of higher speeds are essentially lost within $\sim 3\tau$ of isolating the desorption volume from the pump at the start of the desorption cycle.

For the dynamic mode, the properties of the pump are much more important. Values $\tau \sim 1$ to 0.1 sec are required in order to approach the optimum condition $\Delta t/\tau \approx \sqrt{2}$ where $1/\Delta t$ is the data rate (see I, section 3.3). Furthermore, τ must be accurately known and constant to extremely low pressures. As a typical example, if $L = 10^6$ molecules s^{-1} and $\tau = 0.1$ s, the equilibrium partial pressure is

$$\frac{L\tau}{n_0} = 3 \times 10^{-15} \text{ torr.}$$

In addition, the pump must introduce no additional leak rate L, especially one which is time or pressure dependent (see section 3.2).

Inert gases are pumped in our system by a single-cell magnetron pump. It has a speed for helium of $\sim 3 \times 10^{-2}$ ℓs^{-1} at $p \geq 1 \times 10^{-10}$ torr. Its effective speed at $3\text{-}4 \times 10^{-12}$ torr of He, however, is $\sim 7 \times 10^{-3}$ ℓs^{-1} and at 2×10^{-12} torr it is near zero.

4 Sample heating and temperature measurement

It has already been mentioned in section 2.1 that the temperature of the bombarded area on the crystal must remain uniform to within ~ 0.4% throughout the desorption sweep. To achieve this condition, it is most practical to electron bombard the back face of the thick samples. Heat flow estimates show that for a thickness-to-diameter ratio of 0.2 and a thermal conduction loss through the mounting structure of 10^{-2} watt K^{-1}, the uniformity criterion should be met for metallic samples of 0.5 to 1.0 cm in diameter.

The temperature measurement accuracy available from properly mounted thermocouples is usually acceptable (ΔT ~ 2K at 1000 K, ~ 10 K at 2000 K). By storing the thermocouple output as well as the partial pressure (MS) signal, smoothed temperature profiles can be computed to yield both the temperature and its rate of change at any point on the sweep (see section 6 for utilization). Depending on the thermal properties of the crystal and its dimensions, corrections may be necessary to obtain the true temperature of the bombarded area from that indicated by the thermocouple.

Pyrometric measurement of the sample temperature has the following disadvantages:

a. Radiant flux decreases very rapidly with temperature and becomes too small for accurate measurements below ~ 900 K.

b. The transmission coefficient of the viewing window may change due to evaporated deposits or other contamination, causing errors which are difficult to correct.

Nevertheless, we have used a recording infra-red pyrometer for temperature measurements to-date to avoid the problems of making thermocouple connections to the transferable samples. We estimate the errors to be ± 10 K at 1000 K, and ± 20 K at 2000 K. Below 1000 K, interpolations based on the crystal thermal capacity, radiation loss, conduction loss and supplied power have been used to deduce the temperature profile.

The acquisition system can also be used to advantage to control the crystal heating power so that the temperature follows fairly closely the desired variation with time (usually linear). This can be done either by supplying an amount of power calculated to match the sample heat capacity, conductive loss and radiation loss, or by utilizing the temperature signal in a feedback loop.

Three undesirable side effects result from the crystal heating:

a. Heating of the sample surroundings by conduction and radiation may cause them to emit additional molecules giving an additional and time dependent L term. This is particularly serious if electrodes surrounding the crystal have been struck by the ion beam. Heating of the beam stop (see section 3.2) especially must be avoided. This effect will be most serious when the temperature rise rate β is made low to minimize the noise/signal ratio (see I, section 3.6).

b. The desorption of chemisorbed gases from the sample and its surrounding can cause anomalies in the MS signal by changing the ionization rate in its source and/or the ion transmission efficiency. Even 0.01 monolayer of desorbing gas causes pressure variations orders of magnitude larger than those produced by the desorbing inert gas (see section 1) and the resulting transient changes in inert gas signals are often easily visible. This effect can be reduced somewhat by interposing getter-coated baffles between the crystal and the MS source to attenuate the pressure transients[4]. Hydrogen desorption appears to be most serious since it is usually the most prevalent background gas and in addition is most difficult to attenuate because of its rather low sticking coefficient on getter surfaces.

c. The bombarding electron current used to heat the crystal produces ions of the desorbing gas, creating a time varying ionic pump which must be corrected for (see section 6). The gas pumped by this mechanism is, furthermore, available for later re-emission, contributing to the effect mentioned above in a.

5 Data acquisition and experiment control

From the point of view of the digital data system, the problem is one of:

a. measuring and storing an adequate number of samples of the gas partial pressure and crystal temperature signals of sufficient precision to permit quantitative analysis,

b. providing a driving signal to the crystal heating circuits which results in at least approximately the desired crystal temperature profile.

In this section, some general aspects of the required data acquisition and control parameters will be discussed.

Desorption sweeps will cover temperature intervals ranging from a few hundred K to ~ 2000 K depending on the crystal material and the particular experiment. Maximum temperatures will not usually exceed ~ 2/3 of the crystal melting point. In paper I, it was shown by Fourier analysis that 10 data points over a single desorption peak are sufficient for accurate analysis. Since the total width of the peaks is ~ 0.15 T_m, where T_m is the peak temperature, the "channel width" should be $\Delta T \approx 0.015\ T_m$. For the lowest T_m encountered in room temperature experiments ($\approx$ 350 K), ΔT = 5 K is therefore adequate. The total number of data points in a desorption spectrum is thus not likely to exceed ~ 400 $(2000/\Delta T)$.

It was also shown in I that errors in the parameters derived from the data decrease monotonically with decreasing temperature rise rate β. Limiting values are approached when $\left.\frac{dN}{dt}\right|_m \sim L$ for the dynamic mode, or $3.3(n_b + 0.1\ N_0) \sim L t_{0.3}$ for the static mode (see I, section 3.6). For large peaks, this limit often implies extremely low values of β ($\lesssim 1$) and therefore long total desorption sweep times. For such large peaks, however, the minimum errors become very small and are seldom required. Higher values of β, allowing more experiments to be completed may be preferable. In addition to severely restricting the rate of experimentation, very low β values tend to aggravate the unwanted gas desorption from the crystal surroundings (see section 4) because of the large thermal energy deposited.

The above considerations suggest that values of β are likely to lie in the range ~ 1 K s^{-1} to ~ 100 K s^{-1} where the upper limit is determined by sample temperature uniformity requirements. Since the temperature change per channel was shown above to be ~ 5 K, the implied data rates $r = 1/\Delta t = \beta/\Delta T$ are ~ 0.2 s^{-1} to 20 s^{-1}. The pumping time constants τ in the dynamic mode will be ~ 4 sec to 0.04 sec if the optimum condition $\Delta t/\tau \approx \sqrt{2}$ is to be fulfilled.

Although desorption peaks involving as few as 10^8 atoms are sometimes of interest, maximum populations of at least 10^{12} atoms are also encountered. Even for a modest system sensitivity (G = 1 x 10^{-3} A $torr^{-1}$, V = 1 ℓ) the resulting detector ion current is $i^+ \approx 3 \times 10^{-12}$ A or 2×10^7 ions/sec for the dynamic mode, and ~ 2×10^8 ions/sec for the static mode. Counting individual pulses at such rates is impractical. It is necessary either to deliberately reduce G to a much lower (but still accurately known) value, or to measure the multiplier output as a "direct" current. The latter alternative is preferable in principle as long as the detected signal is much larger than the multiplier background current since it leads to the smaller statistical uncertainty. In this mode of measurement, the

electrometer should be followed by a low-pass filter whose cut-off frequency f_c can be adjusted to match the data rate r being used. When $f_c = r/2$ Hz, and the cut-off is sharp, the rms fluctuation in the transmitted signal is within a factor m of that found in pulse counting the same signal with the channel time 1/r. The value of m is dependent on the pulse height distribution ($1.5 \gtrsim m \geq 1$, see paper I). If higher data rates and higher filter frequencies are used in acquiring the data, any desired lower data rate can be extracted by digital filtering techniques[12].

Digitization of a current signal leads to a "bit noise" because of the $\pm \frac{1}{2}$ "bit" uncertainty in the digital approximation to the measured value. Analogous to the derivation of the error in $\frac{\Delta E}{E}$ due to shot noise (i.e. starting at eq. A-14 of paper I) it can be shown that the additional error due to bit noise, assuming that sampling at the minimum rate takes place, for the dynamic mode is

$$\frac{\Delta E}{E} \approx \frac{0.5}{\alpha b}$$

and for the static mode

$$\frac{\Delta E}{E} \approx \frac{5}{\alpha b}$$

where b is the amplitude resolution - the number of levels into which the full scale signal can be subdivided - and α is the fraction of the full-scale signal corresponding to the peak amplitude (dynamic mode) or the total desorbed quantity (static mode). It is not practicable in general to have α larger than about 0.25. Thus, in order to satisfy $\frac{\Delta E}{E} \lesssim x\%$, it is necessary to have $b \gtrsim \frac{200}{x}$ for the dynamic mode, and $b \gtrsim \frac{2000}{x}$ for the static mode. This can be satisfied by a 12-bit A/D conversion ($b = 2^{12} = 4096$), if $x \geq 0.5\%$ for the static mode or $\geq 0.05\%$ for the dynamic mode.

For the crystal temperature measurements, filtering considerations are the same as discussed above. Since thermocouple output voltages are usually not far from proportional to temperature, the amplitude resolution should be at least as good as the calibration accuracy (~ 1000) again suggesting that 12-bit A/D conversion is sufficient. Conversion of the acquired data to temperatures requires either algebraic approximations to the thermocouple calibration curve, or stored tables of the calibration combined with numerical interpolation routines.

6 Treatment of the data

To obtain accurate desorption rate spectra from the output signal of the MS, the following must be kept in mind:

i. the electrometer and analogue filter perturb the signal before it is read by the data system,

ii. the MS may have a sensitivity which varies slightly with pressure,

iii. the desorbed gas does not equilibrate instantaneously in the desorption volume,

iv. there are pumps which continuously remove the desorbing gas.

The corrections that must be applied to the raw data to yield the desorption rate are the subject of this section. If the experimental parameters are properly chosen, the corrections are not large and can be applied with good accuracy.

The electrometer response time constant τ_e should be made small compared to $1/f_c$, where f_c is the cut-off frequency of the analogue filter following the electrometer. Provided the transmission of the filter falls steeply (> 12 db/octave), the result is a delay of $\Delta t \approx 1/2f_c$ for all frequencies below f_c.

Departures from linearity of the MS output current with pressure should be corrected next. A calibration of the MS must be available in the form of values of the sensitivity $G(i^+)$ as a function of i^+. Normalizing to the value $G(i_0^+)$ at some chosen value i_0^+, the currents are then corrected by

$$i_c^+ = i^+ \frac{G(i_0^+)}{G(i^+)}$$

to give values strictly proportional to pressure ($p = i_c^+/G(i_0^+)$).

The effects of gas equilibration and pumping can be corrected via the differential equations describing the system gas dynamics. In general, the desorption volume must be considered as two volumes - the sample volume V_1 in which the desorption actually occurs, and the detector volume V_2 containing the MS. If the two are connected by pipes having a vacuum conductance $C\ \ell\ s^{-1}$, the gas flow equations can be written (see Fig. 3)

$$V_1 \frac{dp_1}{dt} = \frac{\left(\frac{dN}{dt}\right)_+ L}{n_0} - S_1 p_1 - C(p_1 - p_2) \qquad (12)$$

$$V_2 \frac{dp_2}{dt} = C(p_1 - p_2) - S_2 p_2 \qquad (13)$$

where S_1 and S_2 are the pumping speeds ($\ell\ s^{-1}$) in V_1 and V_2 respectively. L is the background rate of gas input and $\frac{dN}{dt}$ is the desorption rate (mol s^{-1}) assumed to be in V_1. Since p_2 is the measurable quantity, it is convenient to express the gas input rate in terms of p_2 and its derivatives.

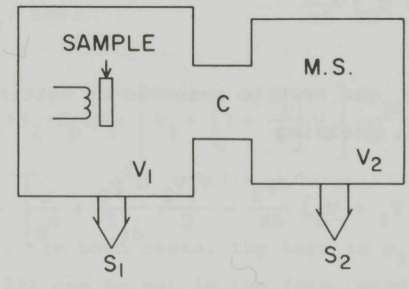

fig. 3 *Sketch of desorption volume, consisting of sample volume V_1 with pump S_1 and mass spectrometer volume V_2 with corresponding pump of speed S_2.*

Rearranging the two equations (12) and (13)

$$\frac{dN}{dt} + L = n_0\left\{\left[S_1 + \frac{S_1 S_2}{C} + S_2\right]p_2 + \left[\left(1 + \frac{S_2}{C}\right)V_1 + \left(1 + \frac{S_1}{C}\right)V_2\right]\frac{dp_2}{dt} + \frac{V_1 V_2}{C}\frac{d^2 p_2}{dt^2}\right\} \qquad (14)$$

For the *static* mode, the pumps of speed S_1 and S_2 are the unavoidable ionic pumping of the crystal bombardment heater and the mass spectrometer, amounting to at most a few hundreths of a $\ell\ s^{-1}$. Since S_1 is proportional to the crystal bombarding current, it will be time dependent during the desorption sweep and is thus best corrected in a separate operation. The conductance C should be made as large as practicable to minimize corrections, and in this case $C >> S_1$ and $C >> S_2$ will always hold. Equation (14) thus becomes

$$\frac{dN}{dt} + L = n_0\left\{(S_1 + S_2)p_2 + (V_1 + V_2)\frac{dp_2}{dt} + \frac{V_1 V_2}{C}\frac{d^2 p_2}{dt^2}\right\} \qquad (15)$$

$$= n_0(V_1 + V_2)\left\{\frac{p_2}{\tau} + \frac{dp_2}{dt} + \tau_c \frac{d^2 p_2}{dt^2}\right\}$$

with $\tau = (V_1 + V_2)/(S_1 + S_2)$ and $\tau_c = V_1V_2/C(V_1 + V_2)$, corresponding to eq. (7) of I with a small correction term. C, V_1 and V_2 can be established to good accuracy from dimension measurements and well known expressions for the conductance. The term in $\frac{dp_2}{dt}$ will predominate in this mode, with the others relatively small corrections to it. The background leak rate L is first established by isolating the desorption volume $(V_1 + V_2)$ from its main pumps and observing the rise of p_2. In this state, $n_0S_2p_2 \ll L$, and so

$$L = n_0 (V_1 + V_2) \frac{dp_2}{dt} \tag{16}$$

The ionic pumping speed S_2 can next be measured by setting up a pressure p_2 so large that $n_0S_2p_2 \gg L$, yielding

$$S_2 = \frac{1}{p_2} \left[-(V_1 + V_2) \frac{dp_2}{dt} - \frac{V_1V_2}{C} \frac{d^2p_2}{dt^2} + \frac{L}{n_0} \right] \ \ell\ s^{-1} \tag{17}$$

Operating the crystal bombarder at a comparable pressure p_2, its time dependent pumping speed is given by

$$S_1(t) = \frac{1}{p_2} \left[-(V_1 + V_2) \frac{dp_2}{dt} - \frac{V_1V_2}{C} \frac{d^2p_2}{dt^2} + \frac{L}{n_0} \right] - S_2 \ \ell\ s^{-1} \tag{18}$$

and from this, the proportionality constant $K_B = S_1(t)/i_B(t)$, where i_B is the bombarding current, can be established. In both (17) and (18), the terms in dp_2/dt predominate.

For the *dynamic* mode, an additional measurement must be made since a relatively large pump with controllable speed S_p is deliberately added to either V_1 or V_2. A total gas inflow rate L_s (including L) is set up with the pump closed off ($S_p = 0$) and measured using eq. (15), with $S_1 = 0$. The valve to the pump is then set to some opening, and p_2 allowed to come to equilibrium, so that

$$L_s = n_0(S_p + S_2)p_2. \tag{19}$$

If the pump is in V_2,

$$S_p = \frac{L_s}{n_0p_2} - S_2 \tag{20}$$

and if in V_1,

$$S_p = \frac{L_s}{n_0p_2} - S_2 \cdot \left(1 + \frac{S_2}{C}\right)^{-1} \tag{21}$$

A series of values of S_p as a function of the valve setting are thus easily obtained. Again noting that $S_1 << C$ and $S_2 << C$, the appropriate forms analogous to eq. (15) are then

$$\frac{dN}{dt} + L = n_0 \left\{ (S_1+S_2+S_p)p_2 + \left[\left(1 + \frac{S_p}{C} \right) V_1 + V_2 \right] \frac{dp_2}{dt} + \frac{V_1 V_2}{C} \frac{d^2 p_2}{dt^2} \right\} \tag{22}$$

if the pump is in V_2, and

$$\frac{dN}{dt} + L = n_0 \left\{ (S_1+S_2+S_p)p_2 + \left[V_1 + \left(1 + \frac{S_p}{C} \right) V_2 \right] \frac{dp_2}{dt} + \frac{V_1 V_2}{C} \frac{d^2 p_2}{dt^2} \right\} \tag{23}$$

if the pump is in V_1. In both cases, the term in p_2 is dominant. As with eq. (15), (22) and (23) can be put in the form used in paper I by substituting

$$\frac{S_1+S_2+S_p}{V_1+V_2} = \frac{1}{\tau} \; ; \text{ and } \; \frac{V_1 V_2}{C(V_1+V_2)} = \tau_c \; .$$

Then

$$\frac{dN}{dt} + L = n_0 (V_1+V_2) \left\{ \frac{p_2}{\tau} + \left(1 + \frac{\tau_c}{\tau_p} \right) \frac{dp_2}{dt} + \tau_c \frac{d^2 p_2}{dt^2} \right\} \tag{24}$$

where $\tau_p = \frac{S_p}{V_1}$ if in V_1, and $\frac{S_p}{V_2}$ if in V_2. Eq. (24) corresponds to eq. (7) of I with small correction terms added.

The evaluation of the desorption rate from equation 15, 22 or 23 (but without the correction for the bombarder pumping) can be carried out most effectively by numerical filtering techniques. The filters take the form of sets of coefficients which are applied to the digital data points to yield smoothed values or smoothed derivatives of any order. In ref. (12), methods for establishing the number of these coefficients and their magnitudes for chosen characteristics of the filter (0^{th}, 1^{st} or 2^{nd} order derivative, cut-off frequency, stop band loss, etc.) are given. Let the coefficients for zeroth order, for first order and for second order differentiation be represented by $a_1 \rightarrow a_{2n+1}$, $b_1 \rightarrow b_{2n+1}$ and $c_1 \rightarrow c_{2n+1}$, respectively. If the equation is written in the form

$$\frac{dN}{dt} + L = dp_2 + e\frac{dp_2}{dt} + f\frac{d^2p_2}{dt^2} \tag{25}$$

then the required *combined* filter coefficients are given by

$$g_i = da_i + eb_i + fc_i \quad . \tag{26}$$

The evaluation then proceeds by replacing each data point $(\frac{dN}{dt} + L)_k$ by

$$\left(\frac{dN}{dt} + L\right)_k = \sum_{j=-n}^{n} g_j \times p_2(k+j) \tag{27}$$

To account for the bombarder pumping speed, a small additional term $n_0 p_2 S_1(t)$ must be added to the values found via eq. (27), using for p_2 a digitally smoothed value (e = f = 0, eq. 26)

$$\frac{dN}{dt} + L = \left(\frac{dN}{dt} + L\right)_k + n_0 p_2 K_B i_B(t) \tag{28}$$

where $i_B(t)$ is obtained from the power vs time used to heat the crystal during the desorption sweep, and K_B as indicated in eq. (18).

Finally, for comparison with theory, the desorption rate spectrum must be adjusted to the form it would have if the temperature rise rate β were exactly constant. If the departures of β from its average value β_0 are small, corrections can be made by multiplying each desorption rate value by β/β_0 and plotting the points as a function of the temperature rather than time:

$$\left.\frac{dN}{dt}\right|_c = \frac{\beta_0}{\beta}\frac{dN}{dt} \tag{29}$$

with the corresponding time scale given by

$$t_c = \frac{T - T_0}{\beta_0} \tag{30}$$

This conversion has the required property of conserving the total number desorbed since $\frac{dt_c}{dt} = \frac{\beta}{\beta_0}$, so $\left.\frac{dN}{dt}\right|_c dt_c = \frac{dN}{dt} dt$.

7 Deconvolution of multipeak spectra

Because the peaks are relatively wide (~ 0.08 T_m for first order, wider for higher orders) they frequently overlap in a spectrum and the problem of extracting their individual kinetic parameters arises. Analysis of the peaks by the "characteristic time" method[13] and quantitative assessment of the errors such as that presented in I are not possible in general for such cases. However, computer optimization of the match between arrays of theoretically generated peaks and the experimental data can yield parameter values and uncertainties in them which are closely related to those obtained by the theoretical method mentioned above.

For a single peak with a specified T_m, $\left.\frac{dN}{dt}\right|_m$ and β, once a value of ν is chosen, the calculation of the theoretical peak shape ($\frac{dN}{dt}$ vs t) is straightforward. Since first order kinetics are found in almost all cases, the discussion will be limited to this order. From the first order desorption equation

$$\frac{dN}{dt} = - N_0 \nu \exp(- \frac{E}{kT}) \tag{31}$$

it can be shown that[13]

$$z_m = \ln(\frac{\nu T_m}{\beta}) - \ln(z_m) \tag{32}$$

where $z_m = E/kT_m$ and E is the binding energy. Equation (32) can be solved by iteration starting with the nominal value $z_m = 30$. The initial population N_0 is very accurately given by[13]

$$N_0 = \left.\frac{dN}{dt}\right|_m \times \nu^{-1} \times \exp(z_m + 0.9920 - 1.620/z_m) \tag{33}$$

and the desorption rate at any value of the temperature T by

$$\frac{dN}{dt} = N_0 \nu \exp[- z - \frac{\nu T}{\beta z}(0.9920 - 1.620/z) \exp(- z)] \tag{34}$$

where $z = E/kT$.

Many approaches, differing in detail, are practicable for the optimization procedure. The objective is to adjust the choices of E, N_0 and ν to minimize the overall difference (e.g. rms) between the calculated $\frac{dN}{dt}$ values from eq. (34) and the measured values of $\frac{dN}{dt}$. The optimization accuracy achieved in practice may be limited by the speed or cost of the available computing facilities. An approach which has been used successfully by the present authors[8,14] is outlined below:

1. Nominal peak temperatures T_{m_i} are found by computer search of the data. (Using the first three derivatives of the data, it is possible to find even peaks appearing as minor shoulders on the major peaks.) The nominal values are revised, if necessary, on the basis of previously available information, or in some cases by visual inspection.
2. Nominal values of the frequency factors υ_i are chosen. These have been found to lie in the range 10^{11} to 10^{16} s^{-1}.
3. Values of the individual peak amplitudes h_i $(=\frac{dN}{dt}\Big|_{m_i})$ are calculated by an iteration procedure which takes into account the contributions of the next lower and the two next higher (in temperature) peaks if they exist. The result is a total amplitude (desorption rate) equal to the experimental value at each T_{m_i}.
4. The difference between the generated amplitude, found using eqs. (32) to (34), and the experimental amplitude is found for a fixed number of selected points over a peak and the rms, Δ, of these differences calculated.
5. One of the three parameters T_{m_i}, ν_i or h_i is incremented by a small amount, steps 3 and 4 repeated, and the new value of Δ compared with the old. The procedure is repeated until the decrease in Δ is less than some chosen value or some maximum permitted parameter variation is exceeded.
6. The procedure of 3, 4 and 5 is repeated for each peak in order of decreasing amplitude h_i.
7. The entire procedure 3, 4, 5 and 6 is repeated for a pre-selected sequence of the parameters T_m, ν and h.
8. Finally, the rms difference Δ of the whole spectrum is calculated to give a "quality of fit" parameter which is printed out along with the values of E, ν and N_0 corresponding to the optimum choices for all the peaks.

The uncertainties in the parameters deduced by such techniques cannot be precisely defined. The closer together the peaks are, the more the parameter choices affect each other until at some small separation no meaningful selection can be made among alternative choices. It should be pointed out, however, that the information avalalable to specify the T_m and ν of peaks is by no means limited to a single spectrum. Most commonly, the same peaks appear in a whole series of spectra when a single experimental parameter is varied, and these are known to arise from the same physical processes. (This was used in ref. 14). It is then justifiable to establish the parameters of a given peak from spectra which show it most clearly and to use these parameters in other spectra to aid in the deduction of other peaks. In this way, an extensive series of spectra can lead to much better values of the kinetic parameters of a set of peaks than can one spectrum alone.

Deconvolution of peaks and the establishment of E, ν and N_0 becomes much more difficult when the peak shapes do not conform accurately to the expected (first order) shape. Such a situation can arise, for example, if a number of atoms bound to a given trap are emitted sequentially rather than in a statistically independent way. It has been shown[15,16] that substantial narrowing and distortion of the peak then occurs.

8 Examples

In this section, three examples are given of thermal desorption spectra measured with an apparatus referred to earlier in this paper and described in more detail in ref. 4. It consists of a desorption chamber with a total volume of 2.27 ℓ divided into a sample chamber (1.67 ℓ) and a mass spectrometer chamber (0.60 ℓ). The gas equilibration time constant between the two chambers is $\tau_c = 0.014\sqrt{M}$ s where M is the mass number of the gas. The system is operated statically, the only pumps being the mass spectrometer (τ = 650 s for He, τ = 70 s for Xe for the particular operating conditions) and the crystal bombarder ($\tau > 1000$ s for He, $\tau \approx 14/i_B$ s for Xe, where i_B is the bombarding current in A). The crystal is heated approximately linearly (≈ 40 K s^{-1}) using a power profile calculated and supplied by the data acquisition system (a Hewlett-Packard 9825A desk-top computer) to a current regulator circuit. The pressure is monitored by a sensitive mass spectrometer ($G(He) \approx 0.01$ A $torr^{-1}$, $G(Xe) \approx 0.10$ A $torr^{-1}$) whose collector signal is amplified by an electron multiplier with a background current equivalent to 2.4×10^{-16} A. The multiplier output is fed into an electrometer, with input time constant set at less than 10 msec. The electrometer output signal is filtered by 2 cascaded 4th order Butterworth filters, yielding a cut-off steeper than 40 dB/oct. The cut-off frequency f_c is adjustable to match the data rate set by the computer (see section 3.2 of I). For the examples to be presented, the data rate was 10^{-1} s and f_c was set to 5 Hz. The data are stored in memory during acquisition and subsequently on floppy disk. The data are processed in a later stage, correcting for the gas equilibration time constant τ_c and pumping time constants using a digital filter as described in section 6.

8.1 Example 1

In the first example, a W(100) crystal was bombarded with 5×10^{12} cm^{-2} 1500 eV Xe^+ ions and annealed to 2150 K. This was followed by injection of 4×10^{12} cm^{-2} of 250 eV He^+ ions. The latter bind to the Xe, with a binding energy dependent on the number of helium atoms already bound[14,15]. The

number of gas phase molecules (10^9 molecules corresponds to 1.3×10^{-11} torr), as measured directly at the output of the analogue filter, is plotted in Fig. 4. In the same figure, the channel-to-channel differences divided by the channel width Δt, are plotted also, yielding a curve that is approximately

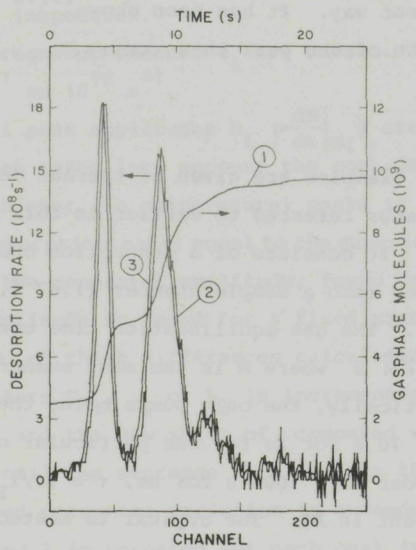

Fig.4 *(1) the number of helium molecules in the gasphase during desorption from W(100) crystal previously implanted with 5×10^{12} cm^{-2} 1500 eV Xe^+ ions, annealed to 2150 K and bombarded with 4×10^{12} cm^{-2} 250 eV He^+ ions; (2) channel to channel differences of (1); (3) numerically filtered signal*

equal to the desorption rate (eq. (15)). The corrections were applied to the integral data using a numerical filter. The parameters of the filter (see Fig. 5) were: a stop-band loss $\varepsilon = 40$ dB, a cut-off frequency $\beta = 0.35$ and a transition band width $\delta = 0.2$. Since about 30 points were taken over the full width at 10% maximum height of the lowest temperature peak, and only about 10 are needed (see paper I, section 3.4), β was chosen at $10/30 \sim 0.35$. The result after applying the filter is shown also in Fig. 4. A shift of 2 channels has taken place too, since this is the time delay invoked by the analogue filter (section 6). The corrections due to the gas equilibration time constant τ_c and the pumping time constant of the MS are small in the case of helium.

Fig. 6 shows the corrected spectrum again, with the horizontal scale converted to temperature (curve 1). Curve 2 results from the automatic analysis program (see section 7), and curve 3 is the difference between them. The positions of the first, second and fourth peaks were found by

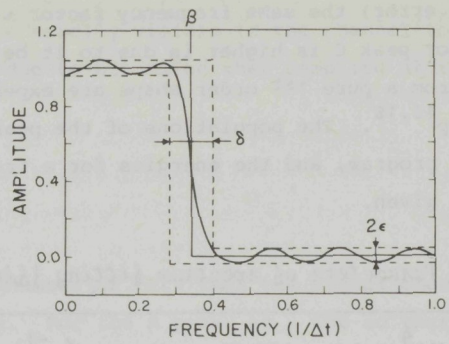

Fig. 5 *Numerical filter parameters: stopband loss ε, cut-off frequency β and transition band width δ. The frequency is in units of the sample frequency 1/Δt.*

the program, and it was supplied with approximate positions for the third and fifth as they were known more accurately from helium dose variation experiments[14]. Nominal values of $\nu = 1 \times 10^{12}\ s^{-1}$ were chosen. The program was instructed to vary the peak temperatures T_{m_i}, the frequency factors ν_i and the peak heights h_i in the order T_{m_i}, ν_i, T_{m_i}, h_i, in such a way as to minimize the rms difference between the theoretical and experimental data. The resulting optimum values are listed in Table I. From the analysis of spectra for other helium doses (ref. 14), it is known that all the peaks have

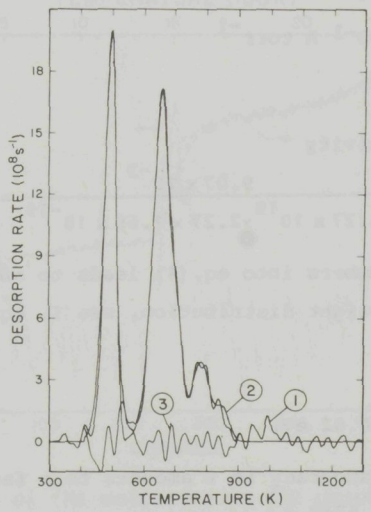

Fig. 6 *(1) corrected spectrum (3) from fig.4; (2) fit from automatic analysis program; (3) difference of (1) and (2).*

(within experimental error) the same frequency factor ν of about 1×10^{12} s^{-1}. That the optimum ν for peak C is higher is due to it being on the shoulder of peak B: deviations from a pure 1st order shape are expected if the peaks substantially overlap[15,16]. The populations of the peaks and their energies as determined by the program, and the energies for a frequency factor $\nu = 1 \times 10^{12}$ s^{-1} are given.

Table I *Parameters of spectrum fitting (fig. 6)*

peak	T_m(K)	N_0(10^9 mol.)	E(eV)	$\nu(s^{-1})$	E(eV)($\nu = 1 \times 10^{12} s^{-1}$)
A	500	2.35	1.16	1.0×10^{12}	1.16
B	658	2.21	1.58	2.0×10^{12}	1.54
C	704	1.13	1.89	6.4×10^{13}	1.65
D	784	0.64	1.80	5.0×10^{11}	1.84
E	850	0.34	2.05	2.0×10^{12}	2.01

The theoretical accuracy with which the energy of the A peak can be extracted, follows from equation 1. The experimental parameters are

$T_m = 400$ K
$N_0 = 2.4 \times 10^9$ molecules
$n_b + Lt_{0.3} \sim 2.5 \times 10^9$ molecules
$\beta = 40$ K s^{-1}
$G = 9.07 \times 10^{-3}$ A $torr^{-1}$
$V = 2.27$ ℓ

making the system sensitivity

$$S = \frac{G}{N_0 Ve} = \frac{9.07 \times 10^{-3}}{3.27 \times 10^{19} \times 2.27 \times 1.60 \times 10^{-19}} = 7.41 \times 10^{-4} \quad *$$

Substitution of these numbers into eq. (1) leads to an accuracy (ignoring the influence of the pulse height distribution, see I, eq. (12)):

$$\frac{\Delta E}{E} \approx 2.2\ \%$$

or $E = 1.15 \pm 0.02$ eV.

Using eq. (25) of I, the accuracy in υ amounts to a factor 2.1, so

$$\upsilon = 1.0 \times 10^{12 \pm 0.3}.$$

* This sensitivity means that one ion/sec arrives at the collector for each 1350 molecules in the gas phase.

The individual bits are readily visible in the channel-to-channel derivative of Fig. 4. The error due to bit noise when sampling at the minimum rate is given by (section 5)

$$\frac{\Delta E}{E} \approx \frac{5}{\alpha b}$$

where αb is the total number of bits that the signal changes during the desorption of the peak. For the A peak, $\alpha b \approx 600$ so that the error due to bit noise based on the minimum rate is about 0.9%. The actual bit noise is smaller by $\sim \sqrt{3}$ since sampling at ~ 3 times the minimum took place. The bit noise error is thus ~ 4 times smaller than the error due to shot noise.

8.2 Example 2

The second example serves to show that very small numbers of particles can indeed be measured making use of ^{3}He. Fig. 7 shows the number of gas phase ^{3}He molecules during the desorption cycle after bombardment of a W(100) crystal with 3×10^{10} cm^{-2} 5000 eV ^{3}He$^+$ ions. The integral curve is filtered using the same procedure as in the previous example. However, the cut-off frequency β was chosen 0.15 since the peak (at 1500 K) now contains about 60 sample points, while only 10 are needed. The peak is the so-called "H peak",

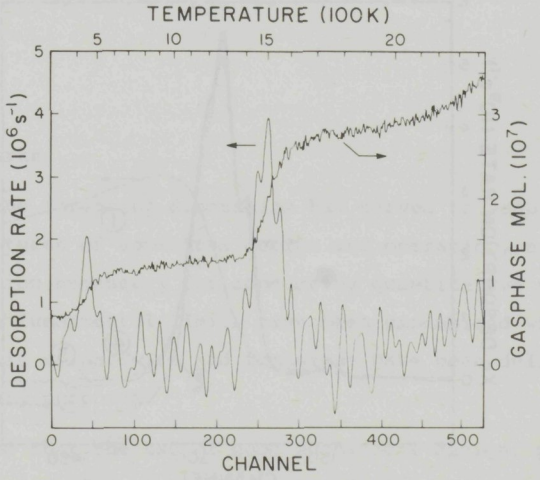

Fig. 7 *Number of ^{3}He molecules in the gasphase during desorption from W(100) crystal, previously bombarded with 3×10^{10} cm^{-2} 5000 eV ^{3}He$^+$ ions. The desorption rate is derived from this data using the numerical filter as described in the text.*

resulting from the desorption of He atoms from singly occupied vacancies[18]. The total number of molecules desorbing in this peak is extremely low: about 1.4×10^7. The background number of molecules just before the desorption of the H peak is $n_b = 1.25 \times 10^7$, of which about 1×10^6 is due to the background current in the electron multiplier (see section 3.3). The leak rate is $L = 1.05 \times 10^5\ s^{-1}$. Based on eq. (1), a relative error $\frac{\Delta E}{E}$ of ~15% is expected for the heating rate $\beta = 40\ K\ s^{-1}$. This is clearly too high to derive E, although the peak population can be easily measured. The accuracy could be increased by lowering β, since $\beta_c \sim 11\ K\ s^{-1}$ (see I, eq. (38)). For $\beta = 0.3 \times \beta_c \simeq 3\ K\ s^{-1}$, $\frac{\Delta E}{E}$ reaches 8%, while for lower values of β, no real improvement is expected ($\frac{\Delta E}{E} \approx 7\%$ for $\beta \to 0$).

8.3 Example 3

In the third example, the thermal desorption of Xe from molybdenum (100) is presented. The incident energy was 600 eV and the dose $1 \times 10^{12}\ cm^{-2}$. The number of Xe atoms in the gas phase is plotted in Fig. 8 as a function of the channel number, again using a channel width Δt of 0.1 sec and a heating rate $\beta = 40\ K\ s^{-1}$. The nominal temperatures are indicated. For the case of Xe, the influence of the mass spectrometer pumping and the pumping of the bombarder is substantial. This is evident from the negative slope of the Xe pressure after the desorption is completed. Also visible is the change in slope when the bombarder is turned off at channel 450. These effects are more clearly visible when the pressure

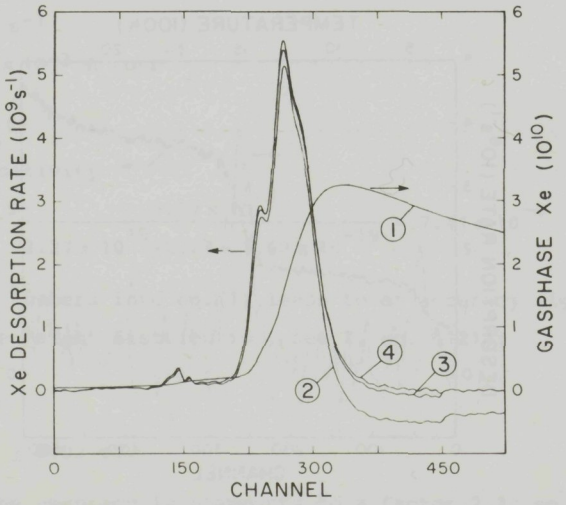

Fig. 8 *Number of molecules in the gasphase (1) during desorption from Mo(100) crystal bombarded with $1 \times 10^{12}\ cm^{-2}$ 600 eV Xe^+ ions; (2) derivative signal without pumping time constants corrections; (3) corrected for MS pumping; (4) corrected for MS and bombarder pumping. The bombarder is turned off at channel 450.*

is differentiated (curve 2). For Xe, the gas equilibration time constant τ_c = 0.16 s, the MS pumping time constant was $\tau_2 = \frac{V_1 + V_2}{S_2} = 70$ s, and the proportionality constant between $S_1(t)$ and the bombarder current $i_B(t)$, $K_B = 7.0 \times 10^{-2} * (V_1 + V_2)$ $\ell\ s^{-1}\ A^{-1}$ for an electron voltage of 1 kV. The total pumping time constant thus becomes

$$\tau^{-1} = \frac{S_1 + S_2}{V_1 + V_2} = \frac{K_B * i_B(t) + (V_1 + V_2)/\tau_2}{V_1 + V_2} = 7.0 \times 10^{-5}\, i_B(t) + \frac{1}{\tau_2}\ .$$

At the end of the sweep the power input is ~ 60 Watt, leading to $i_B = 60$ mA and a bombarder pumping time constant of

$$\tau_B = \frac{1}{7.0 \times 10^{-5} * i_B(t)} \approx 240\ \text{s}.$$

This is about 3.4 times larger than that of the MS, as can be seen also from the change of signal in curve 2 when the bombarder is switched off. Curve 3 shows the signal corrected for the MS pumping alone, and curve 4 shows the final result in which the bombarder pumping has been corrected for, using the bombarder current as a function of time $i_B(t)$. It is thus seen that especially for the heavier gases (lower ionization potential, higher sensitivity of MS) the corrections are substantial. With the availability of a (small) computer system, they can however be applied without major difficulty.

9 Concluding remarks

It is hoped that the foregoing discussion has served to acquaint the reader with the basic features of apparatus design and operation, and of data acquisition and manipulation necessary for conducting quantitative thermal desorption spectrometry. The fundamental limits have been emphasized wherever possible and specific details of hardware and technique have been deliberately omitted except for exemplary purposes.

The authors contend that the use of good mechanical design, good ultrahigh vacuum practice and sound data acquisition and analysis techniques can yield a wealth of high quality data concerning the behaviour of inert gases in solids via thermal desorption spectrometry. A number of recent papers[9,14,15,17] are cited in support of this contention. It is to outline the fundamental and technical requirements for doing such measurements that this and its companion paper[2] were written.

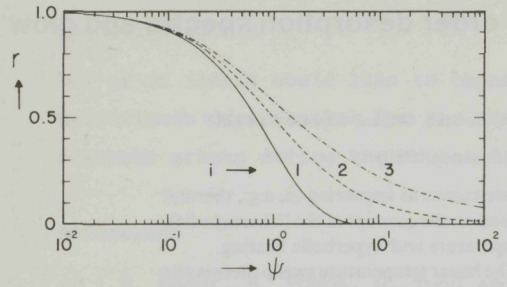

FIG. 1. Relative number of particles r that has not yet reacted as a function of the characteristic time ψ for reaction orders $i = 1,2$, and 3.

If E is independent of r, as is not always true for chemisorption systems,[14] then Eq. (3) is solvable by introducing the "characteristic time" ψ as[15]

$$\psi = \int_0^t K(t)\,dt, \tag{5}$$

reducing Eq. (3) to

$$\frac{dr}{d\psi} = -r^i. \tag{6}$$

The solution of this equation is straightforward:

$$i = 1, \quad r = \exp(-\psi), \quad \text{or } \ln r = -\psi \tag{7}$$

$$i > 1, \quad r^{i-1} = \frac{1}{1+(i-1)\psi},$$

$$\text{or } \ln r = -\frac{1}{i-1}\ln[1+(i-1)\psi]. \tag{8}$$

These functions are given in Fig. 1 for $i = 1$, 2, and 3. They represent the relative number of particles that has not yet reacted (desorbed, emitted) as a function of the characteristic time. It can be seen from Fig. 1 that at the value of $\psi = 1$, about half of the particles have reacted (60% for 1st order to 40% for 3rd order).

B. Evaluation of ψ

ψ will be evaluated for a constant, linear, and hyperbolic heating schedule as follows:

1. Constant ($T = T_0$)

$$\psi = n_0^{i-1}\,st\exp(-E/kT_0), \tag{9}$$

where T_0 is the anneal temperature and t is the anneal time.

2. Linear ($T = T_0 + \beta t$)

$$\psi = n_0^{i-1} s\int_0^t \exp\left(-\frac{E}{k(T_0+\beta t)}\right)dt$$

$$= n_0^{i-1}\frac{s}{\beta}\int_{T_0}^{T}\exp(-E/kT)\,dT. \tag{10}$$

Assuming that T_0 is so low that K is negligible for T_0, i.e., that $n_0^{i-1}\,s\exp(-E/kT_0) \ll 1$, the last integral can be evaluated as follows:

$$\psi = n_0^{i-1}\frac{sE}{\beta k}\int_{E/kT}^{E/kT_0} x^{-2}\exp(-x)\,dx$$

$$\approx n_0^{i-1}\frac{sE}{\beta k}\int_{E/kT}^{\infty} x^{-2}\exp(-x)\,dx$$

$$= n_0^{i-1}\,s\frac{kT^2}{\beta E}\exp(-E/kT)g(E/kT) \tag{11}$$

where

$$g(a) = a^2e^a\int_a^\infty x^{-2}\exp(-x)\,dx = ae^aE_2(a), \tag{12}$$

and $E_2(a)$ is the incomplete Γ function of the second kind.[16] g is plotted in Fig. 2 as a function of E/kT, for $E/kT < 40$. For most practical cases, E/kT_m varies from 20 to 40. Since the FWHM of most desorption peaks is of the order of 10%, E/kT varies by only about 20% over the range of the peak where the desorption rate is greater than 0.1 of the maximum rate. The conclusion is that $g(E/kT)$ is about 1 over twice the FWHM of the DR curves.

The series representation for $g(a)$, that can be found by repeated partial integration of Eq. (12), is

$$g(a) = 1! - \frac{2!}{a} + \frac{3!}{a^2} - \frac{4!}{a^3} + \cdots \tag{13}$$

while a formula accurate to 5×10^{-5} is[16]

$$g(a) = a\left(\frac{0.995\,924a + 1.430\,913}{a^2 + 3.330\,657a + 1.681\,534}\right). \tag{14}$$

For the interesting range of $20 < a < 40$, to within 1×10^{-3},

$$g(a) = 0.9920 - 1.620/a. \tag{15}$$

This function [Eq. (15)] is also drawn in Fig. 2.

3. Hyperbolic ($T^{-1} = T_0^{-1} - bt$)

This case has been studied theoretically and experimentally before.[3,4,17-20] The temperature is given by

$$T(t)^{-1} = T_0^{-1} - bt. \tag{16}$$

The "characteristic time" is equal to

$$\psi = n_0^{i-1}s\int_0^t \exp\left(-\frac{E}{k}(T_0^{-1} - bt)\right)dt. \tag{17}$$

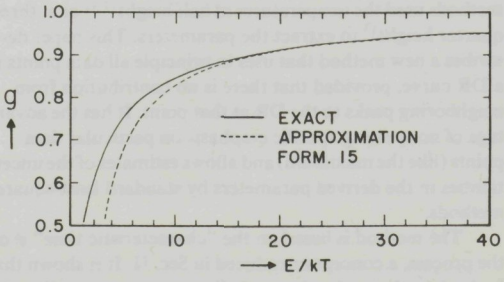

FIG. 2. The function $g(E/kT)$ appearing in the solution for the linear heating schedule [Eq. (12)], together with the approximation according to Eq. (15).

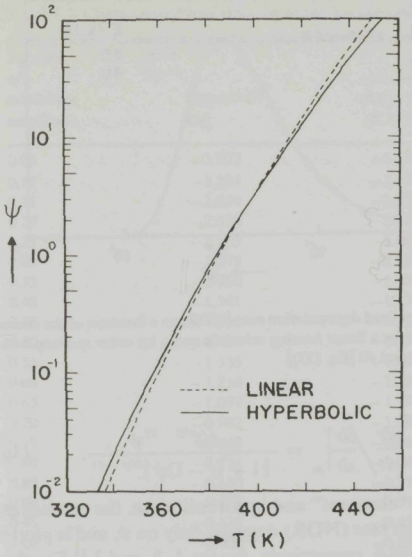

FIG. 3. The characteristic time ψ as a function of temperature for the linear schedule ($\beta = 10$ K s^{-1}) and the hyperbolic schedule ($b = 6.767\times10^{-5}$ K^{-1}) for $E = 1$ eV and $n_0^{i-1}s = 10^{13}$ s^{-1}.

Assuming again that the reaction constant is very low at temperature T_0,

$$\psi = \frac{n_0^{i-1}sk}{Eb}\exp(-E/kT). \tag{18}$$

4. Comparison of ψ for linear and hyperbolic schedules

The relations between ψ and $T(t)$ for a linear and hyperbolic schedule have been plotted in Fig. 3 for the parameters ($E = 1$ eV, $\beta = 10$ K/s, $b = 6.767\times10^{-5}$ K^{-1} s^{-1}, $n_0^{i-1}s = 10^{13}$s^{-1}) as a function of temperature.

The parameter b has been chosen such that the heating rate $dT/dt = 10$ K/s at $T = 384$ K, the peak temperature T_m for both the linear and hyperbolic heating schedules. It can be seen in Fig. 3 that $\log\psi$ as a function of temperature is nearly the same for the two heating profiles. Equations (16) and (18) show that $\log\psi$ is proportional to t for a hyperbolic heating schedule.

C. Maximum in desorption rate

The maximum in the DR for the linear and hyperbolic schedules is given by the condition

$$\left.\frac{d^2r}{dt^2}\right|_m = 0. \tag{19}$$

Using Eqs. (4–6), this can be written as

$$\left(\frac{d\psi}{dt}\right)_m^2 \Big/ \left(\frac{d^2\psi}{dt^2}\right)_m = -\left(\frac{dr}{d\psi}\right)_m \Big/ \left(\frac{d^2r}{d\psi^2}\right)_m. \tag{20}$$

Substituting Eqs. (6–8), we find in terms of ψ

$$\left(\frac{d\psi}{dt}\right)_m^2 \Big/ \left(\frac{d^2\psi}{dt^2}\right)_m = \frac{1+(i-1)\psi_m}{i}. \tag{21}$$

For the *linear* heating case, the left-hand side becomes equal to ψ_m/g_m, leading to

$$\psi_m = \frac{1}{1+i(1/g_m-1)}. \tag{22}$$

For $i = 1$, $\psi_m = g_m$, and since $g_m \approx 1$, $\psi_m \approx 1$. In Fig. 4, ψ_m has been drawn as a function of E/kT_m for $i = 1, 2$, and 3. It is seen that ψ_m is always close to 1, since $25 \lesssim E/kT_m \lesssim 40$. Approximation formulas for $25 < E/kT_m < 40$ with an accuracy of 1×10^{-3} are

$$\begin{aligned} i=1,&\quad \psi_m = 0.9920 - 1.620(kT_m/E),\\ i=2,&\quad \psi_m = 0.9795 - 2.883(kT_m/E),\\ i=3,&\quad \psi_m = 0.9641 - 3.873(kT_m/E). \end{aligned} \tag{23}$$

For the *hyperbolic* heating rate, Eq. (21) reduces to

$$\psi_m = [1+(i-1)\psi_m]/i \tag{24}$$

or

$$\psi_m = 1.$$

The conclusion is that for the linear heating schedule, $\psi_m \approx 1$, while for the hyperbolic heating profile, $\psi_m = 1$ exactly (see Fig. 3).

D. Normalized desorption rates as function of ψ

The desorption rate (DR) dr/dt [Eq. (3)] is in most cases the measured quantity. Equations (7) and (8) for r and Eqs. (9), (11), and (18) are used to generate the following expressions for the DR for a constant, linear, and hyperbolic temperature schedule:

constant:

$$i = 1 \qquad \frac{dr}{dt} = -\frac{\psi}{t}\exp(-\psi), \tag{25}$$

$$i > 1 \qquad \frac{dr}{dt} = -\frac{\psi/t}{[1+(i-1)\psi]^{i/(i-1)}}, \tag{26}$$

linear:

$$i = 1 \qquad \frac{dr}{dt} = -\frac{\beta E}{g(E/kT)kT^2}\psi\exp(-\psi), \tag{27}$$

$$i > 1 \qquad \frac{dr}{dt} = -\frac{\beta E\psi}{g(E/kT)kT^2[1+(i-1)\psi]^{i/(i-1)}}, \tag{28}$$

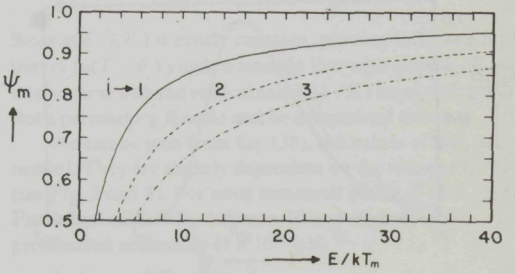

FIG. 4. The value of the characteristic time ψ_m at which the maximum in the depopulation rate occurs for a linear heating schedule and reaction orders $i = 1,2$, and 3 [Eq. (22)].

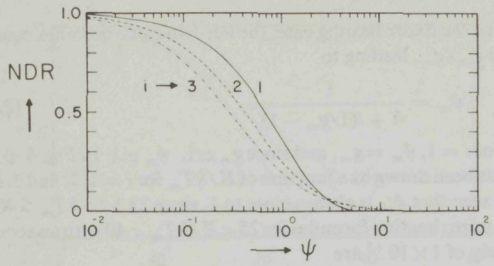

FIG. 5. Normalized depopulation rate (NDR) as a function of the characteristic time ψ for a constant temperature schedule and reaction orders 1,2, and 3 [Eqs. (31) and (32)].

hyperbolic:

$$i=1 \quad \frac{dr}{dt}=-\frac{Eb}{k}\psi\exp(-\psi), \tag{29}$$

$$i>1 \quad \frac{dr}{dt}=-\frac{\psi Eb/k}{[1+(i-1)\psi]^{i/(i-1)}}. \tag{30}$$

These equations for the DR will now be normalized to the starting values in the constant temperature case and to the maximum value for the linear and hyperbolic schedules (to be called the normalized depopulation rate, NDR):

constant:

$$i=1 \quad \frac{dr}{dt}\Big/\frac{dr}{dt}\Big|_0=\exp(-\psi) \tag{31}$$

$$i>1 \quad \frac{dr}{dt}\Big/\frac{dr}{dt}\Big|_0=\frac{1}{[1+(i-1)\psi]^{i/(i-1)}}, \tag{32}$$

linear:

$$i=1 \quad \frac{dr}{dt}\Big/\frac{dr}{dt}\Big|_m=\left(\frac{T_m}{T}\right)^2\frac{\psi}{g}\exp(-\psi+\psi_m), \tag{33}$$

$$i>1 \quad \frac{dr}{dt}\Big/\frac{dr}{dt}\Big|_m=\left(\frac{T_m}{T}\right)^2\frac{\psi}{g}\frac{i[1+(i-1)\psi_m]^{1/(i-1)}}{[1+(i-1)\psi]^{i/(i-1)}}, \tag{34}$$

hyperbolic:

$$i=1 \quad \frac{dr}{dt}\Big/\frac{dr}{dt}\Big|_m=\psi\exp(-\psi+1), \tag{35}$$

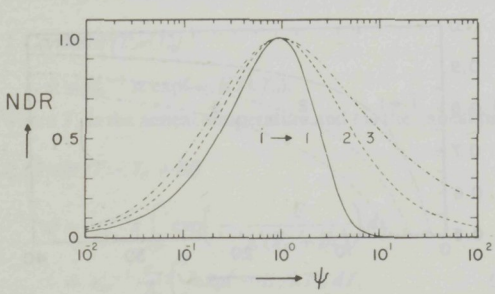

FIG. 6. Normalized depopulation rate (NDR) as a function of the characteristic time ψ for a hyperbolic heating schedule and reaction orders 1,2, and 3 [Eqs. (35) and (36)].

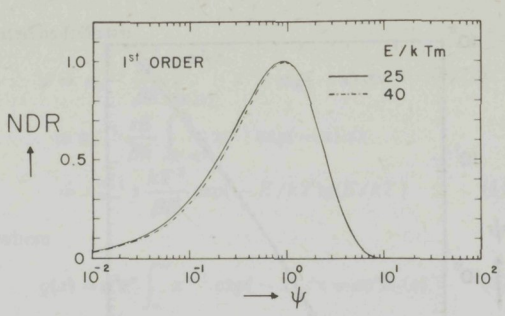

FIG. 7. Normalized depopulation rate (NDR) as a function of the characteristic time ψ for a linear heating schedule and a 1st order reaction with $E/kT_m = 25$ and 40 [Eq. (33)].

$$i>1 \quad \frac{dr}{dt}\Big/\frac{dr}{dt}\Big|_m=\frac{(i)^{i/(i-1)}\psi}{[1+(i-1)\psi]^{i/(i-1)}}. \tag{36}$$

In the "constant" and hyperbolic case, the normalized depopulation rate (NDR) depends only on ψ, and is plotted in Figs. 5 and 6, respectively, for $i = 1$, 2, and 3.[21] For the linear heating schedule, the NDR does not depend on ψ only: both through T and $g(E/kT)$, the kinetic parameters, enter into the equation. It can be shown however that these parameters appear only through the ratio E/kT_m. In Fig. 7 (order = 1) and 8 (order = 2), the NDR has been plotted for $E/kT_m = 25$ and 40, covering a huge range of energy and/or frequency factors. It can be seen that there is only a slight dependence on the ratio E/kT_m. As expected, the maximum is always close to $\psi = 1$. Note also that the NDR curves for the hyperbolic and the linear schedule are very similar. [Compare Fig. 6 ($i = 1$) with Fig. 7, and Fig. 6 ($i = 2$) with Fig. 8]. It can be shown that when $E/kT_m \to \infty$ the linear NDR becomes equal to the hyperbolic one.

III. THE METHOD

In Sec. II, it was shown that the NDR curves plotted as a function of ψ were independent of (for a constant temperature or a hyperbolic heating schedule) or only slightly depen-

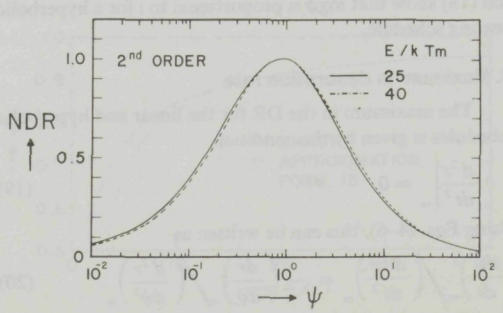

FIG. 8. Normalized depopulation rate (NDR) as a function of the characteristic time ψ for a linear heating schedule and a 2nd order reaction with $E/kT_m = 25$ and 40 [Eq. (34)].

TABLE I. Characteristic time ψ for 1st order reactions for hyperbolic and linear heating schedules.

Fraction of maximum amplitude	Hyperbolic $\ln\psi_j$	Linear $\ln\psi_j$ $(E/kT_m = 30)$	Linear $\ln\psi_j = \gamma(kT_m/E) + \delta$ γ	δ	Fraction
0.05	−3.977	−4.222	−6.717	−3.997	0.05
0.10	−3.264	−3.471	−5.718	−3.280	0.10
0.15	−2.839	−3.023	−5.121	−2.852	0.15
0.20	−2.530	−2.699	−4.703	−2.541	0.20
0.25	−2.285	−2.441	−4.368	−2.295	0.25
0.30	−2.079	−2.226	−4.093	−2.089	0.30
0.35	−1.900	−2.038	−3.862	−1.909	0.35
0.40	−1.741	−1.872	−3.659	−1.749	0.40
0.45	−1.596	−1.720	−3.478	−1.604	0.45
0.50	−1.461	−1.579	−3.315	−1.468	0.50
0.55	−1.335	−1.447	−3.164	−1.341	0.55
0.60	−1.214	−1.321	−3.021	−1.220	0.60
0.65	−1.097	−1.199	−2.887	−1.103	0.65
0.70	−0.982	−1.080	−2.758	−0.988	0.70
0.75	−0.868	−0.961	−2.632	−0.873	0.75
0.80	−0.752	−0.840	−2.507	−0.756	0.80
0.85	−0.630	−0.714	−2.380	−0.634	0.85
0.90	−0.497	−0.576	−2.250	−0.501	0.90
0.95	−0.338	−0.412	−2.097	−0.342	0.95
1.00	0.000	−0.064	−1.732	−0.006	1.00
0.95	0.304	0.250	−1.525	0.301	0.95
0.90	0.426	0.376	−1.426	0.424	0.90
0.85	0.521	0.473	−1.359	0.518	0.85
0.80	0.601	0.555	−1.302	0.599	0.80
0.75	0.674	0.629	−1.256	0.671	0.75
0.70	0.741	0.698	−1.210	0.739	0.70
0.65	0.804	0.763	−1.173	0.802	0.65
0.60	0.866	0.826	−1.132	0.864	0.60
0.55	0.926	0.887	−1.096	0.924	0.55
0.50	0.985	0.948	−1.060	0.984	0.50
0.45	1.045	1.009	−1.025	1.044	0.45
0.40	1.106	1.071	−0.990	1.105	0.40
0.35	1.169	1.136	−0.958	1.168	0.35
0.30	1.235	1.203	−0.920	1.234	0.30
0.25	1.306	1.276	−0.888	1.305	0.25
0.20	1.385	1.356	−0.849	1.384	0.20
0.15	1.475	1.448	−0.800	1.474	0.15
0.10	1.587	1.561	−0.746	1.586	0.10
0.05	1.748	1.725	−0.683	1.748	0.05

dent on (for a linear heating schedule) the kinetic and heating parameters. For a measured DR curve as a function of temperature or time, there is thus a correspondence between ψ and the temperature (or time). Every data point generates a pair of values [ψ_j, T_j (or t_j)] by comparing it with the appropriate NDR curve. From the set of pairs of values [ψ_j, T_j(or t_j)] the kinetic parameters can be extracted.

A. Constant temperature

In the constant temperature case, plotting the values of $\ln t_j$ against $\ln \psi_j$ yields a straight line with slope 1 [see Eq. (9)]:

$$\ln t_j = \ln\psi_j + (E/kT_0) - \ln(n_0^{i-1}s). \tag{37}$$

It is thus possible to determine $(E/kT_0) - \ln(n_0^{i-1}s)$ by standard least-square methods. From the isothermal experiment one cannot derive independently the values of E and s. By repeating the experiment at different temperatures, a series of parallel lines will be found from which E and s can be calculated.

B. Linear heating schedule

For linear heating schedules, Eq. (11) is used:

$$\frac{E}{kT_j} = \ln\left(\frac{T_j^2}{\psi_j}\right) + \ln\left(\frac{n_0^{i-1}sk\,g(E/kT_j)}{\beta E}\right). \tag{38}$$

Since $g(E/kT_j)$ is nearly constant, plotting $1/T_j$ as a function of $\ln(T_j^2/\psi_j)$ yields a straight line with slope k/E and intersection with the vertical axis of $(k/E)\ln(n_0^{i-1}sk\,g/\beta E)$. Both parameters E and s can be determined this way.

As can be seen from Eq. (38), the values of $\ln\psi_j$ are needed. They are slightly dependent on the value of E/kT_m (see Fig. 7 and 8). For most measured peaks, $E/kT_m \approx 30$. For values of E/kT_m between 20 and 40, $\ln\psi_j$ can be approximated accurately (1×10^{-3}) by

$$\ln\psi_j = \gamma_j(kT_m/E) + \delta_j. \tag{39}$$

For convenience both the values of $\ln\psi_j$ for $E/kT_m = 30$ and the γ and δ values are given in Table I for 1st order. They are evaluated for points in steps of 0.05 of the maximum DR.

TABLE II. Characteristic time ψ for 2 [nd] order reactions for hyperbolic and linear heating schedules.

Fraction of maximum amplitude	Hyperbolic $\ln\psi_j$	linear $\ln\psi_j$ $(E/kT_m = 30)$	linear $\ln\psi_j = \gamma(kT_m/E) + \delta$ γ	linear δ	Fraction
0.05	−4.357	−4.624	−7.258	−4.381	0.05
0.10	−3.637	−3.868	−6.306	−3.657	0.10
0.15	−3.204	−3.414	−5.758	−3.221	0.15
0.20	−2.887	−3.083	−5.370	−2.903	0.20
0.25	−2.634	−2.818	−5.074	−2.649	0.25
0.30	−2.420	−2.595	−4.833	−2.434	0.30
0.35	−2.232	−2.401	−4.634	−2.245	0.35
0.40	−2.063	−2.225	−4.467	−2.076	0.40
0.45	−1.908	−2.065	−4.319	−1.920	0.45
0.50	−1.763	−1.914	−4.188	−1.774	0.50
0.55	−1.625	−1.772	−4.070	−1.636	0.55
0.60	−1.491	−1.635	−3.965	−1.502	0.60
0.65	−1.360	−1.500	−3.869	−1.371	0.65
0.70	−1.230	−1.367	−3.781	−1.241	0.70
0.75	−1.099	−1.233	−3.700	−1.109	0.75
0.80	−0.962	−1.094	−3.626	−0.972	0.80
0.85	−0.817	−0.946	−3.556	−0.827	0.85
0.90	−0.655	−0.781	−3.491	−0.664	0.90
0.95	−0.455	−0.579	−3.435	−0.464	0.95
1.00	0.000	−0.125	−3.257	−0.016	1.00
0.95	0.455	0.331	−3.417	0.445	0.95
0.90	0.655	0.529	−3.478	0.645	0.90
0.85	0.817	0.689	−3.538	0.807	0.85
0.80	0.962	0.831	−3.610	0.952	0.80
0.75	1.099	0.965	−3.686	1.088	0.75
0.70	1.230	1.094	−3.768	1.220	0.70
0.65	1.360	1.220	−3.858	1.350	0.65
0.60	1.491	1.348	−3.956	1.480	0.60
0.55	1.625	1.477	−4.066	1.613	0.55
0.50	1.763	1.611	−4.187	1.751	0.50
0.45	1.908	1.751	−4.323	1.896	0.45
0.40	2.063	1.901	−4.479	2.051	0.40
0.35	2.232	2.063	−4.659	2.219	0.35
0.30	2.420	2.243	−4.873	2.407	0.30
0.25	2.634	2.448	−5.133	2.620	0.25
0.20	2.887	2.690	−5.461	2.873	0.20
0.15	3.204	2.991	−5.896	3.188	0.15
0.10	3.637	3.401	−6.542	3.620	0.10
0.05	4.357	4.080	−7.715	4.338	0.05

Table II gives the data for second order. The values of $\ln\psi_j$ for the hyperbolic heating rate have been added. Note that when $E/kT_m \to \infty$, $\ln\psi_j \to \delta_j$ according to Eq. (39). As can be seen from Tables I and II, the values of δ_j are nearly equal to those of $\ln\psi_j$ for the hyperbolic schedule. This is in accordance with an earlier remark that the two curves become identical for $E/kT_m \to \infty$. The small differences between δ_j and ψ_j (hyperbolic) are due to the fact that Eq. (39) is only accurate for $20 < E/kT_m < 40$.

C. Hyperbolic heating schedule

For the hyperbolic heating schedule, $1/T_j$ as a function of $\ln\psi_j$ has to be plotted since [see Eq. (18)]:

$$E/kT_j = -\ln\psi_j + \ln(n_0'^{-1} sk/bE). \tag{40}$$

From the resulting straight line, both E and s can be determined. The values of $\ln\psi_j$ are given in Tables I and II also, and conform to the data published by Smutek.[22]

D. General remarks

In case the wrong assumption about the reaction order i is made, the above-mentioned procedures will not yield a straight line, so that is is possible to determine the reaction order.

It should be noted that for a reaction order i of 1, ψ is not dependent on n_0, the initial number of particles, while for $i > 1$, ψ is linear in $n_0'^{-1}$. By changing n_0 from $(n_0)_1$ to $(n_0)_2$, a different DR curve will in general result. For $i = 1$, the peak temperature will not change[3] so that essentially no new information is obtained: the data points derived from the new pairs (ψ_j, T_j) will lie on the same straight line. For $i > 1$, however, the straight line will be shifted vertically by an amount $(i-1)\ln[(n_0)_1/(n_0)_2]$. If the activation energy for the process is independent of n, the lines should be parallel. Changes in E with n are thus detectable.

Changing the heating parameter β from β_1 to β_2 (linear) (or b for hyperbolic) will also result in a vertical shift of the

straight line, by amounts $\ln(\beta_2/\beta_1)$ and $\ln(b_2/b_1)$, respectively. If E is independent of T, the lines ought to have the same slope. If E is a function of T, the slopes will differ.

IV. EXAMPLES

In this section, two examples will be given demonstrating the new method. The first example is a thermal desorption spectrum (TDS), the second a thermoluminescence spectrum (TLS).

A. Thermal desorption

In Fig. 9, a desorption spectrum is given, measured after injection of energetic (4 keV) helium into a $W(100)$ crystal. The helium occupies some of the created vacancies, and upon heating desorbs in the so-called H peak.[23] The concentrations are chosen low enough to avoid retrapping effects. In this case, the desorption is first order and involves the helium atom leaving the vacancy. The heating rate was 40 K s^{-1}. To obtain the pairs (T_j,ψ_j), the T_j's were chosen where the DR was maximum, 0.9 of the maximum, etc., until 0.1 of the maximum DR. This yielded 19 values of T_j. The corresponding values of ψ_j were taken from Table I, using $E/kT_m = 30$. The values of $1/T_j$ and the corresponding $\ln(T_j^2/\psi_j)$ are plotted in Fig. 10. Nearly all points lie indeed on a straight line, the first three data points from the rising side being slightly off. A least-squares analysis using equal weighting factors gives a straight line through all of the 19 points with $E = 4.40$ eV and $s = 3.6\times10^{14}$ s^{-1}. Leaving out the first three points from the rising side of the peak gives $E = 4.64$ eV, $s = 2.3\times10^{15}$ s^{-1}. When only the points at the falling side of the peak are used (j = 10 to 19), $E = 4.60$ eV, $s = 1.7\times10^{15}$ s^{-1} are found. Using only the central 11 points, the best fit is given by $E = 4.66$ eV, $s = 2.6\times10^{15}$ s^{-1}.

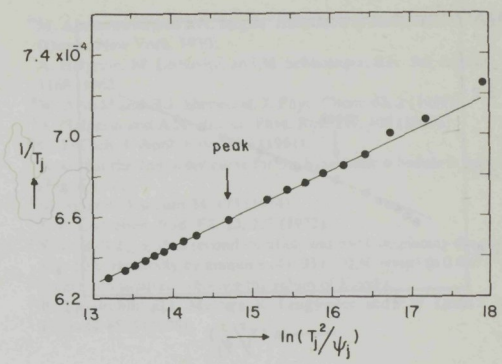

FIG. 10. Analysis plot for the measured thermal desorption peak from Fig. 9. The data point corresponding to the peak maximum is indicated; points to the right are derived from the rising side of the peak, those to the left originate from the falling side.

The conclusions are that this particular peak is very accurately of first order, the energy being 4.64 $\pm$ 0.04 eV and $s = 2.3\times10^{15\pm0.1}$ s^{-1}. Moreover, the rising side of the curve is better fitted by a peak with lower frequency factor, as can be seen by the discrepancy between the best straight line and the data points from the rising side (Fig. 10). These conclusions are confirmed by the theoretical curves drawn in Fig. 9 with frequency factors of 10^{14}, 10^{15}, and 10^{16}, and the energies (4.24, 4.54, and 4.83 eV, respectively) chosen such that the peak maxima coincided with the measured curve.

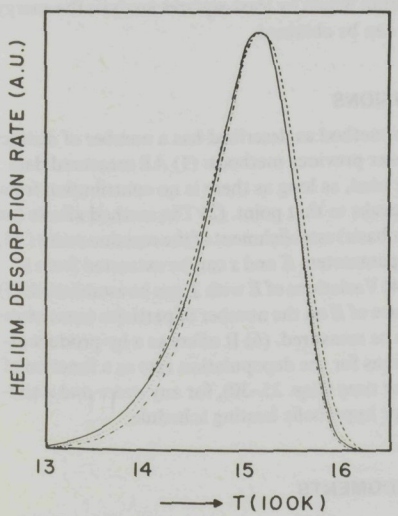

FIG. 9. Measured rate of desorption of helium from vacancies as a function of temperature for a linear heating schedule (β = 40 K s^{-1}) (—); theoretical desorption curves for 1st order reaction with frequency factors of 10^{14} (- - - -), 10^{15} (·····), and 10^{16} (- - - - - -) and energies of 4.24, 4.54, and 4.83 eV, respectively.

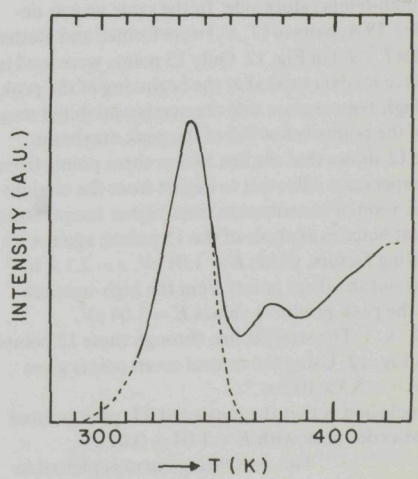

FIG. 11. Part of the thermoluminsecence spectrum of LiF TLD-100 (see Ref. 25), (——). The theoretical curve corresponding to a 1st order reaction with $E = 1.04$ eV and $s = 7.4\times10^{11}$ s^{-1} as found from the analysis plot, Fig. 12 (- - - - - -).

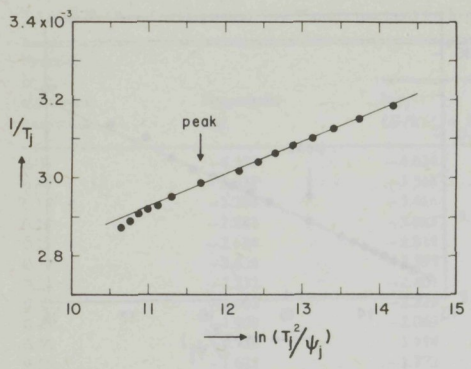

FIG. 12. Analysis plot for the measured thermoluminescence peak from Fig. 11. The data point corresponding to the peak maximum is indicated.

Figure 9 shows that the best overall fit is given by the curve with $E = 4.54$ eV and $s = 10^{15}$ s^{-1}, while the accurate analysis gave 4.64 eV and $s = 2.3 \times 10^{15}$. Also noticeable is the fact that the fit at the start of the peak is better using a lower value of s, in agreement with the conclusion from Fig. 10. The method is thus capable of detecting local departures from the theoretical curve.

B. Thermoluminescence

An example of a TL peak was taken from a recent paper by Fairchild *et al.*[25] who conducted a careful study of the TL spectra of LiF TLD-100. Part of Fig. 3(b) of Ref. 25 is reproduced in Fig. 11, showing a TLD spectrum after an exposure of 10^5 R. The peaks are thought to be first order. Our analysis method will be used for the first peak, that has only overlap on the high-temperature side. In the same way as described in Sec. IVA, pairs of (T_j, ψ_j) were formed and plotted as $1/T_j$ vs $\ln(T_j^2/\psi_j)$ in Fig. 12. Only 15 points were used in this case, since no data existed at the beginning of the peak, and at the high-temperature side the overlap inhibited measurement of the points below 0.3 of the peak maximum.

Figure 12 shows that the last two or three points from the high-temperature side start to depart from the straight line, an indication of contribution from higher temperature peaks. A least-squares analysis of the 15 points, again with equal weighting factors, yields $E = 1.01$ eV, $s = 2.1 \times 10^{13}$ s^{-1}. Leaving out the three points from the high-temperature side of the peak produces values $E = 1.04$ eV, $s = 7.4 \times 10^{13}$ s^{-1}. The straight line through these 12 points is plotted in Fig. 12. Using the central seven points gives $E = 1.03$ eV, $s = 5.5 \times 10^{13}$ s^{-1}.

The conclusion is that the measured TL peak is fitted best by a first-order peak with $E = 1.04 \pm 0.01$ eV, $s = 7.4 \times 10^{13 \pm 0.1}$ s^{-1}. This best fitting curve is plotted in Fig. 11 and shows that an excellent fit is obtained. Fairchild *et al.*[25] found by computer analysis of the total spectrum $E = 1.05$ eV, $s = 1 \times 10^{14}$ s^{-1}, in very good agreement with the present analysis.

V. DISCUSSION

Based on the concept of the "characteristic time" ψ, the presented method has a range of applications: it can be used for any reaction order and for the most common heating schedules (extension to other schedules than the ones discussed is straightforward).

The method can be compared to the "old" one of measuring the peak temperature T_m for a first-order reaction and a linear schedule using various values of the heating rate β. In Sec. IIC, it was shown that for the peak of a first-order DR curve:

$$\psi_m = g_m$$

or using Eq. (6)

$$(skT_m^2/\beta E)\exp(-E/kT_m) = 1, \tag{41}$$

a condition that can be derived directly from differentiating the rate equation (1).
Equivalent to Eq. (41),

$$E/kT_m = \ln(T_m^2/\beta) + \ln(sk/E), \tag{42}$$

so that plotting $1/T_m$ as a function of $\ln(T_m^2/\beta)$ yields a straight line from which E and s can be determined. It is a well-known fact that β has to be varied over several orders of magnitude in order to be able to derive E and s with reasonable accuracy.[3] Comparing Eq. (42) with Eq. (38) shows that ψ fulfills the same "role" as β. Since ψ varies over the 10% width of the peak by over 3 orders of magnitude, this ψ method is as accurate as varying β over 3 orders of magnitude when all data points that have a DR higher than 10% of the maximum are used.

The method by which the width at half height is used[11,12] is embedded in the present method: using the peak maximum and the two temperatures at half height gives three points from which by least-squares analysis the energy E and $n_0'^{-1}s$ can be obtained.

VI. CONCLUSIONS

The new method as described has a number of distinct advantages over previous methods: (1) All measured data points can be used, as long as there is no contribution from neighboring peaks to that point. (2) The method allows (on trial and error basis) establishment of the reaction order i. (3) Both kinetic parameters E and s can be extracted from a single peak. (4) Variations of E with T can be established. (5) The dependence of E on the number of particles (concentration) can also be measured. (6) It offers as a by-product explicit expressions for the depopulation rate as a function of temperature or time (Eqs. 25–30), for any order and a constant, linear, or hyperbolic heating schedule.

ACKNOWLEDGMENTS

The author would like to thank Dr. E.V. Kornelsen for many helpful discussions and Drs. R.A. Armstrong and P.A. Redhead for a critical reading of the manuscript. Diane Dabrowski is greatfully acknowledged for the excellent work of typing this paper.

[1]L. Apker, Ind. Eng. Chem. **40**, 846 (1948).
[2]G. Ehrlich, J. Appl. Phys. **32**, 4 (1961).
[3]P.A. Redhead, Vacuum, **12** 203 (1962).
[4]G. Carter, Vacuum **12**, 245 (1962).
[5]J.J. Randall and M.H.F. Wilkins, Proc. R. Soc. (London) **A184**, 366–390 (1945).
[6]F. Urbach, Wiener Ber. IIa, **139**, 363 (1930).
[7]G.F.J. Garlick and A.F. Gibson, Proc. Phys. Soc. London **60**, 574 (1948).
[8]F.M. Lord and J.S. Kittelberger, Sur. Sci. **43** 173 (1974).
[9]J.L. Falconer and R.J. Madix, Sur. Sci. **48**, 393 (1975).
[10]G. Ehrlich, Adv. Catal. **14**, 255 (1963).
[11]R. Chen, J. Appl. Phys. **40**, 570 (1969).
[12]D. Edwards Jr., Sur. Sci. **54**, 1 (1976).
[13]C.-M. Chan, R. Aris, and W.H. Weinberg, Appl. Surf. Sci. **1** 360 (1978).
[14]For some chemisorption systems, E depends (linear) on surface coverage.
[15]Similar to the concept of "equivalent time" used in electrical resistivity recovery analysis, see e.g., L. Thompson and A. Sosin, Radiat. Eff. **25**, 233 (1975).
[16]M. Abramowitz and I.A. Stegun, *Handbook of Mathematical Functions* (Dover, New York, 1970).
[17]A. Halperin, M. Leibovitz, and M. Schlesinger, Rev. Sci. Instrum. **33**, 1168 (1962).
[18]W. Arnold and H.J. Sherwood, J. Phys. Chem. **63**, 2 (1959).
[19]A. Halperin and A.A. Braner, Phys. Rev. **117**, 408 (1960).
[20]G. Ehrlich, J. Appl. Phys. **32** 4 (1961).
[21]Note that the 2nd order curve for the hyperbolic schedule is symmetric (Fig. 6, $i = 2$).
[22]M. Smutek, Vacuum **24**, 173 (1974).
[23]E.V. Kornelsen, Rad. Eff. **13**, 227 (1972).
[24]Since $E/kT_m \approx 35$, a second iteration was used, displacing the points in Fig. 10 horizontally by amounts of 0.03 (-0.10 point) to 0.003 ($+0.1$ point), too small to influence the values of E and s.
[25]R.G. Fairchild, P.L. Mattern, K. Lengweiler, and P.W. Levy, J. Appl. Phys. **49** 4523 (1978).

Radiation Effects, 1979, Vol. 42, pp. 93–111
0033-7579/79/4201-0093 $04.50/0

ATTACHMENT OF MOBILE PARTICLES TO NON-SATURABLE TRAPS

I. A Theoretical Model

A. A. VAN GORKUM and E. V. KORNELSEN

Division of Electrical Engineering, National Research Council of Canada, Ottawa, Canada K1A 0R8

(*Received March 8, 1979*)

A theory is presented describing the diffusion and trapping of particles near a surface. The starting depth distribution of the injected particles and the depth distribution of the traps are assumed to depend on the dimension normal to the surface. The traps are nonsaturable and their filling is calculated as a function of the dose of injected particles. Both the fraction f of the injected particles trapped and the fraction n_i of the traps that have captured i injected particles are calculated for different distributions of traps and injection distributions of the particles. It is shown that under certain conditions, measurement of f and n_i yields the number of traps and the product of their trapping radius and average injection depth of the particles. The theory is applied to helium thermal desorption experiments in a companion paper.

I INTRODUCTION

This paper was prompted by experimental studies of the thermal desorption of trapped helium from metal crystals previously implanted with heavy inert-gas ions. That injected helium atoms diffuse freely in metals at room temperature has been demonstrated earlier for tungsten,[1] molybdenum[2] and nickel.[3] That implanted inert gas atoms can act as traps for the diffusing helium in tungsten has also been shown,[1] and evidence that these traps are not saturable is presented in a companion paper to this[4] hereafter referred to as II.

Helium thermal desorption is a useful technique for the study of trap filling because:

a) Different kinds of traps generally exhibit different helium binding energies, and thus lead to distinctive peaks in the desorption spectra.

b) Binding energies usually vary with the number of helium atoms occupying a given trap, again leading to distinguishable peaks.

c) The concentration of the traps and the amount of injected helium can both be controlled with good precision over a wide range.

d) The surface can be arranged to be the predominant sink for both the primary diffusing and the thermally released particles.

e) Available experimental sensitivities are such that the low concentration limits can usually be explored, a capability which is important in interpretation of the data.

Mathematical descriptions of the trapping of diffusing particles have been given by e.g. Gaus[5] and Kelly and Matzke.[6] Their treatments are both based on a uniform trap concentration extending to infinite depth, and they consider only the fraction of the diffusing particles trapped. In helium thermal desorption experiments, the traps are not uniformly distributed and extend over only a limited depth. Moreover, as mentioned above, not only the fraction of the helium trapped but also the fractions n_i of the traps occupied by i helium atoms can be measured. The mathematical model requires extension accordingly.

In an earlier paper,[7] a simple model based on the filling of unsaturable traps was presented to describe the attachment of He to Kr impurities in tungsten. Expressions valid for low helium doses and based on the same model were published still earlier.[8] In the present paper, an extended version of the model of Van Veen *et al.*[7] will be developed. It is based on the diffusion equation describing the concentration of mobile particles and a series of first-order rate equations for the concentrations of the multiply-filled traps. These equations are given in Section 2, and their general solution is outlined in Section 3. Section 4 describes some examples that are analytically solvable and show the basic properties of the model. It will be

shown that under certain conditions, which do not depend on the actual distributions of the traps and mobile particles, information can be derived about the number of traps, their average depth and/or the average injection depth of the mobile particles. The necessary conditions will be outlined in Section 5, where applications are given. In Section 6, the influence of a variable trap size will be discussed.

The theory has been applied to experimental data on the trapping of helium at xenon impurities in tungsten presented in paper II. Good agreement was found, allowing a number of trap types to be identified and the binding energy of helium in them to be specified. As a second application, the variation of the average penetration depth of low energy helium ions (≤ 5 keV) as a function of crystallographic angle has been measured.[9]

The theory can be applied to any situation in which mobile particles are being trapped in non-saturable traps in the presence of a surface. An example is the implantation of high energy helium in metals, where the damage created by the helium acts as traps.[10,11] With the present theory it is possible to calculate the early stages of the development of bubbles formed in such experiments.

2 GEOMETRY AND EQUATIONS

2.1 *Geometry*

In ion bombardment experiments, the diameter of the beam (0.1–1 cm) is in most cases much larger than the ion penetration depth (10^{-7}–10^{-4} cm). Consequently only one dimension of the diffusion equation describing the concentration of the mobile particles needs to be considered, namely the dimension perpendicular to the surface. The surface, taken to be at $x = 0$, plays an important role in the diffusion behavior. It is an inexhaustible, and usually dominant sink for the diffusing particles. Moreover, in thermal desorption experiments the measurable quantity is the rate at which particles leave the crystal through this surface.

2.2 *Equations*

The diffusion equation describing the concentration of the mobile particles (MP's) is

$$\frac{\partial c_m(x,t)}{\partial t} = D\frac{\partial^2 c_m(x,t)}{\partial x^2} - Kc_m(x,t)c_T(x) + S(x,t) \tag{1}$$

The quantities are defined in Table I. Equation (1) is Fick's Law, with the third term describing the loss of MP's through trapping and the last term the source function of MP's being injected. The latter is proportional to the range distribution of the MP's and is related to the total injection rate of MP's, J, by

$$J(t) = N_0 \int_0^\infty S(x,t)\mathrm{d}x \ \mathrm{cm}^{-2}\mathrm{s}^{-1}.\dagger \tag{2}$$

The diffusion coefficient D is a constant in Fick's Law, and can be written

$$D = \frac{\nu\lambda_0^2}{6} \tag{3}$$

TABLE I

List of symbols

Symbol	Definition	Units
N_0	concentration of lattice atoms	cm^{-3}
$c_m(x,t)$	concentration of mobile particles (MP's) expressed as a fraction of the lattice atom concentration	
D	diffusion coefficient of MP's	$\mathrm{cm}^{-2}\mathrm{s}^{-1}$
$c_T(x)$	concentration of the traps (T)	
$c_{Ti}(x,t)$	concentration of traps filled with i MP's†	
K	reaction rate coefficient for the reaction MP + $T \rightarrow$ MP · T	s^{-1}
$S(x,t)$	source function of MP's in concentration per second	s^{-1}
J	rate of injection of MP's	$\mathrm{cm}^{-2}\mathrm{s}^{-1}$
ν	jump frequency of MP's	s^{-1}
λ_0	jump distance of MP's	cm
z	geometrical "trap size" factor $= \frac{K}{\nu}$	
$\bar{d}_m$	average starting depth of MP's	cm
$\bar{d}_T$	average depth of traps	cm
L	diffusion length, $(D/KC_T(x))^{1/2}$	cm
C_T	number of traps per cm^2	cm^{-2}
C_{Ti}	number of traps per cm^2 filled with i MP's	cm^{-2}
c_m^*	normalized concentration of MP's $= (DN_0/J\bar{d}_m)c_m$	
x^*	normalized depth $= x/\bar{d}_m$	
S^*	normalized source function of MP's $= N_0\bar{d}_m S(x,t)/J$	
c_T^*	normalized trap concentration $= N_0\bar{d}_m c_T/C_T$	
λ^*	normalized reciprocal diffusion length $= \bar{d}_m/L$	
L^*	normalized diffusion length $= L/\bar{d}_m$	

Other important parameters:

$$\alpha = \frac{K\bar{d}_m C_T}{DN_0} \qquad B = \frac{K\bar{d}_m Jt}{DN_0} = \frac{\alpha Jt}{C_T}$$

† Once trapped, the MP's are of course no longer mobile.

† Note that J is proportional to, but not equal to the incident flux density, since not all the incident particles thermalize in the solid. (See Section 5.)

where λ_0 is the jump distance of the MP's (cm) and ν their jump frequency (s^{-1}).

For the reaction rate coefficient, a useful expression is

$$K = z\nu \tag{4}$$

where z is a geometrical factor related to the size of the traps. The nature of z can be understood in the following way: Replace the trap by an ideal spherical sink of radius r_0. Assuming that all diffusing particles are trapped as soon as they reach the surface of the sink, K is found to be[12]

$$K = 4\pi r_0 N_0 D \tag{5}$$

Comparing Eq. (5) with Eq. (4), and using Eq. (3)

$$z = \frac{r_0}{a} \cdot \left(\frac{2\pi}{3} N_0 \cdot \lambda_0^2 \cdot a \right) \tag{6}$$

in which a is the crystal lattice constant. For helium diffusing interstitially in a *bcc* lattice, the term in brackets is equal to $\pi/3$; in this case z is approximately equal to the radius, expressed in lattice constants, of the ideal spherical sink equivalent to the trap. It has been shown by Monte Carlo computations that $z \approx 1$ for helium being trapped in vacancies.[13]

Since the particles leave the solid at $x = 0$ and the flux of particles is 0 for $x \to \infty$, the boundary conditions for the diffusion Eq. (1) are

$$c_m(0, t) = 0 \tag{7}$$

$$\lim_{x \to \infty} \frac{\partial c_m(x, t)}{\partial x} = 0$$

The rates of change of the trap populations are according to rate theory given by the first order rate equations:

$$\frac{\partial c_{T0}(x, t)}{\partial t} = -K c_m(x, t) c_{T0}(x, t) \tag{8}$$

$$\frac{\partial c_{T1}(x, t)}{\partial t} = -K c_m(x, t) c_{T1}(x, t) + K c_m(x, t) c_{T0}(x, t) \tag{9}$$

$$\vdots$$

$$\frac{\partial c_{Ti}(x, t)}{\partial t} = -K c_m(x, t) c_{Ti}(x, t) + K c_m(x, t) c_{T(i-1)}(x, t) \tag{10}$$

Note that

$$\sum_{i=0}^{\infty} c_{Ti}(x, t) = c_T(x)$$

In Eqs. (8–10) it is assumed that the reaction rate coefficient K does not depend on the number i of MP's in the trap. In Section 6 the case of K varying with i is considered.

3 GENERAL SOLUTIONS

3.1 *Introduction*

In most experimental situations the diffusion of the mobile particles occurs in a time t_D short compared to the bombardment time. (For He in W at 300 K, to $\sim 10^7\, d_m^2$ sec). Assuming that variations in the injection rate $J(t)$ are slow compared to the diffusion time, $S(x, t)$ in Eq. (1), being linearly dependent on $J(t)$, can be considered constant on the time scale of the diffusion. This means that a quasi steady-state concentration c_m exists during most of the bombardment, since c_m follows linearly the variations in $J(t)$ (Eq. 14). The quasi steady-state solution $c_m(x)$ will be derived in Section 3.2. In Section 3.3, the solution of the rate equations is given. It is shown there that the solutions depend only on the time integral of c_m, so that variations in c_m due to variation in injection rate are not important. Therefore a constant injection rate J, equal to the average value of $J(t)$ will be assumed.

3.2 *The Diffusion Equation*

The steady-state concentration c_m of the MP's is the solution of (see Eq. 1):

$$0 = D \frac{\partial^2 c_m(x)}{\partial x^2} - K c_m(x) c_T(x) + S(x) \tag{11}$$

Introducing the normalized parameters c_m^*, x^*, S^* and c_T^* defined in Table I,† the following expressions can be shown to hold:

$$\int_0^{\infty} S^*(x^*) \mathrm{d}x^* = 1 \tag{12}$$

$$\int_0^{\infty} c_T^*(x^*) \mathrm{d}x^* = 1 \tag{13}$$

† Note that normalizations used differ from those used in Ref. 7.

and the normalized steady state diffusion equation can be written

$$\frac{\partial^2 c_m^*}{\partial x^{*2}} - \alpha c_T^* c_m^* + S^* = 0 \tag{14}$$

with

$$\alpha = \frac{K\bar{d}_m C_T}{DN_0} \quad \text{and} \quad c_m^* \equiv c_m^*(x^*) \tag{15}$$

c_m^* now depends only on the one remaining parameter α and the normalized distributions $S^*(x^*)$ and $c_T^*(x^*)$.

Integrating Eq. (14) over x^*, using the boundary conditions Eq. (7) yields

$$\left.\frac{\partial c_m^*}{\partial x^*}\right|_{x^*=0} + \alpha \int_0^\infty c_T^* c_m^* \, \mathrm{d}x^* = 1 \tag{16}$$

One can easily show that the fraction of the MP's trapped is equal to

$$f = \alpha \int_0^\infty c_T^* c_m^* \, \mathrm{d}x^* \tag{17}$$

so that Eq. (16) can be written as

$$\left.\frac{\partial c_m^*}{\partial x^*}\right|_{x^*=0} = 1 - f \tag{18}$$

Equation (17) shows that f is linear in α and dependent on the normalized functions c_T^* and c_m^*.

3.3 *The Rate Equations*

By introducing the function

$$A(x, t) = \int_0^t K c_m(x, t) \mathrm{d}t \tag{19}$$

the solution of the rate Eqs. (8 10) can be written as[7]

$$\frac{c_{Ti}(x, t)}{c_T(x)} = \frac{\{A(x, t)\}^i}{i!} \exp(-A(x, t)) \tag{20}$$

Since c_m is a function of x only,

$$A(x, t) = K c_m(x) \cdot t \tag{21}$$

so that A is linear in time.

Using the normalizations, Eq. (20) becomes

$$\frac{c_{Ti}(x, t)}{c_T(x)} = \frac{\{A^*(x^*, t)\}^i}{i!} \exp(-A^*(x^*, t)) \tag{22}$$

with

$$A^*(x^*, t) = \frac{K\bar{d}_m Jt}{DN_0} c_m^* \tag{23}$$

which will be written as

$$A^*(x^*, t) = B c_m^* \tag{24}$$

where

$$B = \frac{K\bar{d}_m Jt}{DN_0} \tag{25}$$

The last equations show that A^* is linearly dependent on the incident dose of MP's (Jt), their average depth $\bar{d}_m$ and the reaction rate coefficient K. The quantity most directly comparable with experiments is the number of traps per cm^2 containing a specific number of MP's i irrespective of their depth x:

$$C_{Ti}(t) = N_0 \int_0^\infty c_{Ti}(x, t) \mathrm{d}x \ (\mathrm{cm}^{-2}) \tag{26}$$

Inserting Eq. (22)

$$C_{Ti}(t) = C_T \int_0^\infty \frac{\{A^*(x^*, t)\}^i}{i!} \exp\{-A^*(x^*, t)\} \mathrm{d}x^*. \tag{27}$$

The total number of MP's in the traps per cm^2 is equal to

$$\sum_{i=1}^{\infty} i \cdot C_{Ti}(t) \tag{28}$$

Inserting Eq. (27) and interchanging integration and summation yields:

$$\sum_{i=1}^{\infty} i C_{Ti}(t) = \alpha Jt \int_0^\infty c_T^* c_m^* \, \mathrm{d}x^* \tag{29}$$

This result is consistent with expression (17) for the trapped fraction,

$$\sum_{i=1}^{\infty} i C_{Ti}(t) = f \cdot Jt \tag{30}$$

3.4 *Summary of General Solution*

The general solution of the combination of diffusion equation and rate equations is thus given by

$$n_i = \frac{C_{Ti}(t)}{C_T} = \int_0^\infty c_T^* \frac{(A^*)^i}{i!} \exp(-A^*) \mathrm{d}x^* \tag{31}$$

where n_i is the fraction of the traps occupied by i MP's,

$$A^*(x^*, t) = \frac{K\bar{d}_m Jt}{DN_0} c_m^*(x^*) = Bc_m^* \tag{32}$$

and c_m^* is the solution of

$$\frac{\partial^2 c_m^*}{\partial x^{*2}} - \alpha c_T^* c_m^* + S^* = 0 \tag{33}$$

with

$$\alpha = \frac{K\bar{d}_m C_T}{DN_0} \tag{34}$$

The Eqs. (31–34) can be solved once the distributions S^* and c_T^* are known. In general, this has to be done by computer. In the next section a few analytically solvable examples will be discussed which show the basic predictions of the model.

4 ANALYTICALLY SOLVABLE EXAMPLES

4.1 *Introduction*

In this section, five examples of distributions of traps c_T^* and of starting distributions of the MP's S^* that lead to analytical solutions will be given. The examples are chosen to show all of the basic properties of the filling of the traps.

In the first two examples, it is assumed that both c_T^* and S^* are δ distributions. The next three examples show what happens if the traps are distributed in depth.

In each of the five cases, the following quantities are calculated:

a) the fraction of the MP's trapped (f)

b) the fraction of the traps n_i occupied by i MP's in the two limiting cases,

i) when the trapping is negligible†

ii) when the trapping is at its maximum.

The basic results for the five cases, and the numbers of the figures in which they are displayed are summarized in Table II. The quantities represented by the axes of the figures are not the same for all examples, and are therefore indicated in Table II as well.

† It will be shown that $f \ll 1$ is a necessary but not sufficient condition for negligible trapping.

4.2 *Example I*

The distributions are drawn in Figure 1: both c_T^* and S^* are δ distributions and the traps are in front of (i.e. closer to the surface than) the MP's:

$$S^*(x^*) = \delta(x^* - 1) \tag{35}$$

$$c_T^*(x^*) = \delta(x^* - \gamma)$$

in which γ is the depth of the traps relative to the MP's:

$$\gamma = \frac{\bar{d}_T}{\bar{d}_m} < 1. \tag{36}$$

The solution of the diffusion-Eq. (33) is straightforward and indicated in Figure 1. The resulting normalized concentration c_m^* is drawn as a function of normalized depth for the cases of negligible trapping ($\alpha\gamma \ll 1$) and of significant trapping. The trapped fraction is given by Eq. (17)

$$f = \alpha \int_0^\infty c_T^* c_m^* \, dx^* = \alpha c_m^*(\gamma) = \frac{\alpha\gamma}{1 + \alpha\gamma} \tag{37}$$

Figure 2 shows the solution of Eq. (37) where X and Y represent $\alpha\gamma$ and f respectively.

For $\alpha\gamma \ll 1$ ($f < 0.1$),

$$f = \alpha\gamma = \frac{K\bar{d}_T C_T}{DN_0} \tag{38}$$

so f is linear in C_T and in the average depth of the traps, an important fact that will be referred to later.

The fractions of the traps containing i MP's (hereafter called "the fractions n_i") are given by

$$n_i(t) = \int_0^\infty c_T^* \frac{(A^*)^i}{i!} \exp(-A^*) dx^*$$

$$= \frac{\{A^*(\gamma, t)\}^i}{i!} \exp\{-A^*(\gamma, t)\} \tag{39}$$

with

$$A^*(\gamma, t) = \frac{B\gamma}{1 + \alpha\gamma} = \frac{K\bar{d}_m Jt}{DN_0} \cdot \frac{\gamma}{1 + \alpha\gamma} \tag{40}$$

Using Eq. (37) this can be written as

$$A^*(\gamma, t) = \frac{f \cdot Jt}{C_T} \tag{41}$$

showing that $A^*(\gamma, t)$ is the average number of MP's trapped per trap. If $f \ll 1$,

$$A^* = B\gamma = \frac{K\bar{d}_T Jt}{DN_0} \tag{42}$$

TABLE II

Summary of the analytical examples

Example	f	f_{low}	f_{high}	Figure no.	n_i low	Figure no.	n_i high	Figure no.
I 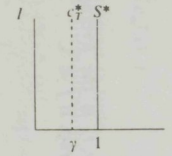	$\frac{\alpha\gamma}{1+\alpha\gamma}$	$\gamma\alpha$	1	2 $X = \alpha\gamma$ $Y = f$	$\frac{(\gamma B)^i}{i!}e^{-\gamma B}$	4 $Q = \gamma B$	$\frac{B/\alpha}{i!}e^{-B/\alpha}$	4 $Q = \frac{B}{\alpha}$
II 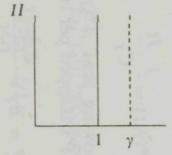	$\frac{\alpha}{1+\alpha\gamma}$	α	$\frac{1}{\gamma}$	2 $X = \alpha\gamma$ $Y = f\gamma$	$\frac{B^i}{i!}e^{-B}$	4 $Q = B$	$\frac{B/\alpha\gamma}{i!}e^{-B/\alpha\gamma}$	4 $Q = \frac{B}{\alpha\gamma}$
III 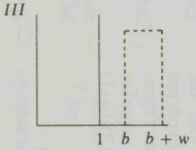	$\frac{\lambda^*}{\tanh\lambda^* w + \lambda^* b}$	α	$\frac{\lambda^*}{1+\lambda^* b}$	7	$\frac{B^i}{i!}e^{-B}$	4 $Q = B$	$\frac{1}{i\lambda^* w}P(i, B)$	8 $Q = B$
IV 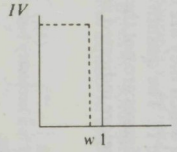	$1 - \frac{1}{\sinh\lambda^* w}$	$\frac{w}{2}\alpha$	1	11 $(w = 1)$ $X = \frac{\alpha w}{2}$	$\frac{1}{wB}P(i+1, Bw)$	12 $Q = Bw$	$\frac{1}{i\lambda^* w}P\left(i, \frac{B}{\lambda^*}\right)$	8 $Q = \frac{B}{\lambda^*}$
V 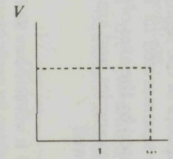	$1 - \frac{\sinh\lambda^*(w-1)}{\sinh\lambda^* w}$	$\left[1 - \frac{1}{2w}\right]\alpha$	$1 - e^{\lambda^*}$	11 $X = \left[1 - \frac{1}{2w}\right]\alpha$	$\frac{1}{wB}P(i+1, B)$ $+\left(1 - \frac{1}{w}\right)\frac{B^i}{i!}e^{-B}$	$w = 1$ 12 $Q = B$ $w = 2$ 13 $Q = B$ $w \gg 1$ 4 $Q = B$	$\frac{1}{i\lambda^* w}P(i, B)$	8 $Q = B$

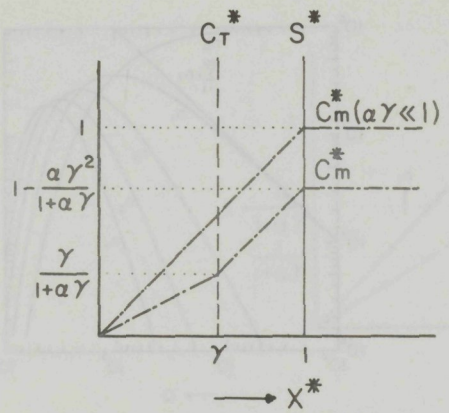

FIGURE 1 The normalized stationary concentration of MP's (c_m^*) as a function of the normalized depth x^* for Example I. The normalized distributions of the traps, c_T^* and MP's, S^* are also shown.

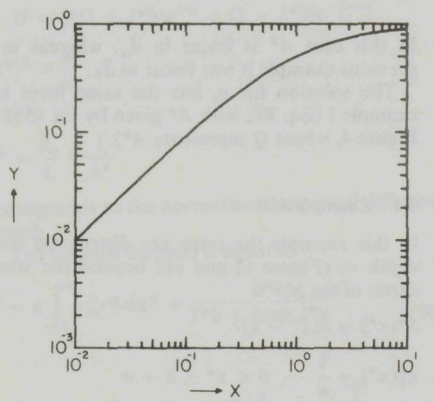

FIGURE 2 Trapped fraction $f(=Y)$ as a function of $\alpha\gamma$ for Example I and $f \cdot \gamma(=Y)$ as a function of $\alpha\gamma$ for Example II.

which is linear in ϑ_T. For $f \approx 1$

$$A^* = \frac{Jt}{C_T} \tag{43}$$

Equation (39) shows that the n_i's form a Poisson distribution in i with A^* as parameter. In Figure 3, the fractions n_i are drawn as a function of i. As can be seen, the maximum in the distribution occurs for $i \approx A^* - \frac{1}{2}$. For $A^* > 10$, the distribution approaches a Gaussian with maximum at $i = A^*$

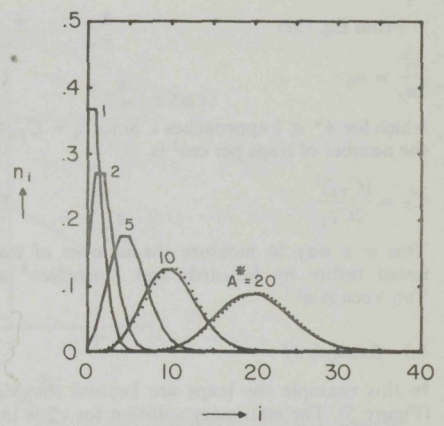

FIGURE 3 Fractions n_i of the traps occupied by i MP's with the average number of MP's per trap A^* as parameter (full lines). The dotted curves are the Gaussian approximations (Eq. (44)).

and standard deviation $\sqrt{A^*}$:

$$n_i = \frac{1}{\sqrt{2\pi A^*}} \exp\left\{\frac{-(i - A^*)^2}{2A^*}\right\} \tag{44}$$

Consequently, if the average number of MP's per trap (A^*) is equal to N, the distribution of the fractions n_i is a Gaussian with maximum at $i = N$ and standard deviation $\sqrt{N}$.†

The fractions n_i as a function of A^* (proportional to the dose of MP's) for $i = 0, 1, 2, 3, 4$, are given in Figure 4, where Q represents A^*. For low values of A^*, the n_i's rise with the ith power of A^*, a well known fact used to study the multiplicity of desorption peaks.[1]

The curves for $i \neq 0$ reach maxima at $A^* = i$ and heights

$$(n_i)_m = \frac{i^i}{i!e^i} \tag{45}$$

a fact noted before.[7]

Also the total number of MP's trapped per trap,

$$\sum_{i=1}^{\infty} i n_i$$

is plotted. Note that it is linear in A^* and equal to 1 for $A^* = 1$, a consequence of Eq. (41).

† This result can be derived also by a continuum interpretation of Eqs. (8–10).

From Eq. (39)

$$\frac{n_1^2}{2n_2} = n_0 \tag{46}$$

which for $A^* \ll 1$ approaches 1. Since $n_i = C_{Ti}/C_T$, the number of traps per cm^2 is

$$C_T = \frac{(C_{T1})^2}{2C_{T2}} \tag{47}$$

This is a way to measure the number of traps, noted before by Edwards and Kornelsen[8] and Van Veen *et al.*[7]

4.3 *Example II*

In this example the traps are beyond the MP's (Figure 5). The stationary solution for c_m^* is indicated. The trapped fraction is given by

$$f = \alpha \int_0^\infty c_T^* c_m^* \, dx^* = \frac{\alpha}{1 + \alpha\gamma} \tag{48}$$

Comparing this result to the previous example shows that f is now a factor γ smaller. The maximum trapped fraction is equal to $1/\gamma$ (<1). We refer to Figure 2 for $f \cdot \gamma$, where X and Y represent $\alpha \cdot \gamma$ and $f \cdot \gamma$ respectively. For $\alpha \cdot \gamma \ll 1$, or $f \cdot \gamma \ll 1$,†

$$f \approx \alpha = \frac{K\bar{d}_m C_T}{DN_0}, \tag{49}$$

In this case f is proportional to the average depth of the MP's and to the number of traps per cm^2, C_T.

The fractions n_i are given by

$$n_i(t) = \frac{\{A^*(\gamma, t)\}^i}{i!} \exp\{-A^*(\gamma, t)\} \tag{50}$$

where

$$A^*(\gamma, t) = B \cdot c_m^*(\gamma) = \frac{B}{1 + \gamma\alpha} = \frac{K\bar{d}_m Jt}{DN_0} \cdot \frac{1}{1 + \gamma\alpha} \tag{51}$$

As in Example I, this can be written

$$A^*(\gamma, t) = \frac{f \cdot Jt}{C_T} \tag{52}$$

For $\gamma \cdot \alpha \ll 1$, or $f \cdot \gamma \ll 1$

$$A^*(\gamma, t) = B = \frac{K\bar{d}_m Jt}{DN_0}. \tag{53}$$

† Note that this may be a very stringent restriction on f if $\gamma \gg 1$.

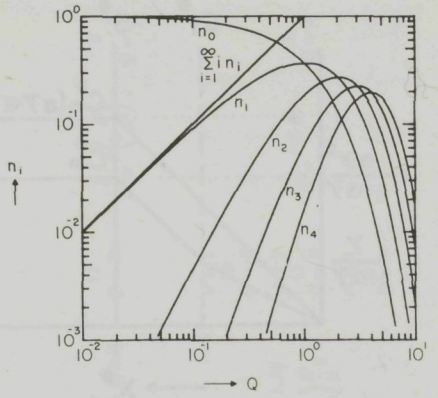

FIGURE 4 The fractions n_i of the traps occupied by i MP's as a function of Q, proportional to the dose of MP's. Also the total number of MP's trapped per trap is plotted. In Example I, Q is equal to $B\gamma/(1 + \alpha\gamma)$, in II, $B/(1 + \alpha\gamma)$, and in III and V equal to B.

In this case A^* is linear in $\bar{d}_m$, whereas in the previous example it was linear in $\bar{d}_T$.

The solution for n_i has the same form as in example I (Eq. 39), with A^* given by Eq. (51), (see Figure 4, where Q represents A^*).

4.4 *Example III*

In this example the traps are distributed over a depth w, (Figure 6) and are beyond the starting depth of the MP's.

$$S^*(x^*) = \delta(x^* - 1) \tag{54}$$

$$c_T^*(x^*) = \frac{1}{w} \qquad b \le x^* \le b + w$$

Solution of the diffusion equation for c_m^* yields for the four regions

$$\begin{aligned} \text{Region} \quad \text{I}: c_m^* &= \left(1 - \frac{\lambda^*}{N} \cosh \lambda^* w\right) x^* \\ \text{II}: c_m^* &= 1 - \frac{\lambda^* x^*}{N} \cosh \lambda^* w \\ \text{III}: c_m^* &= \frac{1}{N} \sinh\{\lambda^*(b + w - x)\} \\ \text{IV}: c_m^* &= \frac{1}{N} \end{aligned} \tag{55}$$

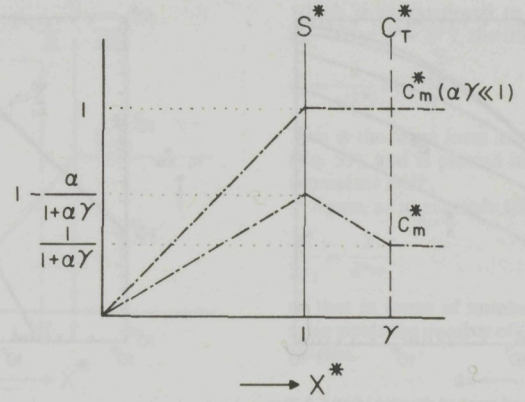

FIGURE 5 Normalized stationary concentration of MP's (c_m^*) as a function of the normalized depth x^* for Example II. The normalized distributions of the traps, c_T^* and MP's, S^* are also shown.

with

$$N = \tfrac{1}{2}\{(1 + \lambda^* b)e^{\lambda^* w} + (1 - \lambda^* b)e^{-\lambda^* w}\}$$

$$(\lambda^*)^2 = \frac{\alpha}{w}$$

where

$$\lambda^* = \frac{d_m}{L} = \frac{1}{L^*}$$

corresponds to the normalized reciprocal diffusion length.

The trapped fraction is equal to

$$f = \alpha \int_0^\infty c_m^* c_T^* \, dx^* = \frac{\lambda^*}{\lambda^* b + \tanh \lambda^* w} \qquad (56)$$

For $\lambda^* w < 0.25$ (diffusion length ≫ width of trap distribution)

$$f = \frac{\alpha}{1 + \alpha\gamma} \qquad (57)$$

where

$$\gamma = b + \frac{w}{2}$$

is the average depth of the traps, the same result as found in the previous example (Eq. 48).

For $\lambda^* w > 2$,

$$f = \frac{\lambda^*}{1 + \lambda^* b}. \qquad (58)$$

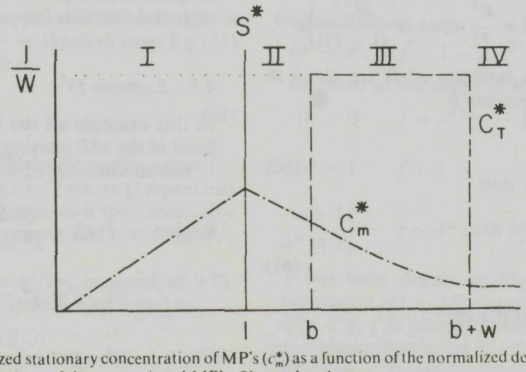

FIGURE 6 Normalized stationary concentration of MP's (c_m^*) as a function of the normalized depth x^* for Example III. The normalized distributions of the traps, c_T^* and MP's, S^* are also shown.

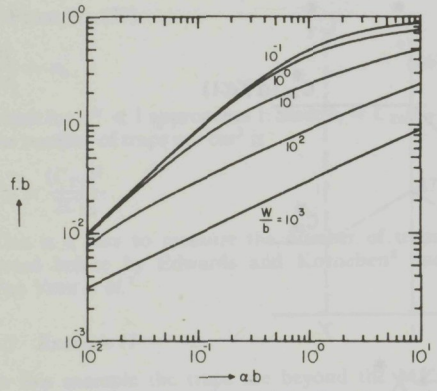

FIGURE 7 The product of trapped fraction f and b (see Figure 6) as a function of $\alpha \cdot b$ with w/b as parameter (Example III).

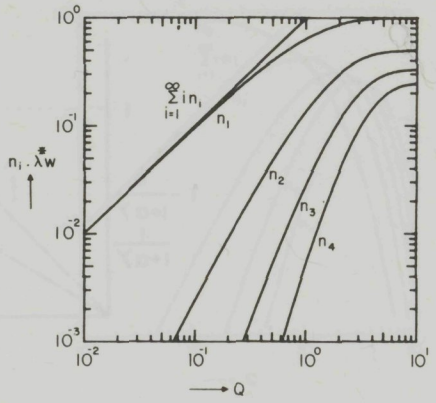

FIGURE 8 The fractions n_i of the traps occupied by i MP's multiplied by $\lambda^* w$, as a function of Q. For Example III and V, Q represents B; for Example IV, Q represents B/λ^*. The total number of MP's trapped per trap is also plotted.

Figure 7 gives $f \cdot b$ as a function of $\alpha \cdot b$ with w/b as parameter. As long as $f \cdot b \ll 1$, a) f is linear in the trap concentration C_T (in α) when $\lambda^* w \ll 1$, and b) f is proportional to $C_T^{1/2}$ (to $\alpha^{1/2}$) when $\lambda^* w \gg 1$.

The fractions n_i for the case $\lambda^* w \ll 1$ ($w \ll L^*$) have the same form as in example II. For $\lambda^* w \gg 1$ ($w \gg L^*$), the solution of Eq. (33) is given in Appendix I. The result is

$$n_i = \frac{1}{i\lambda^* w} P(i, B) \tag{59}$$

where P is the incomplete gamma function. A convenient form for P is[14]

$$P(i, B) = 1 - e_{i-1}(B)e^{-B}$$

$$= 1 - \left(1 + B + \frac{B^2}{2!} + \cdots + \frac{B^{i-1}}{(i-1)!}\right)e^{-B}$$

The values of n_i as a function of B are given in Figure 8 where Q represents B.

For $B \ll 1$,

$$n_i = \frac{B^i}{\lambda^* w i} \tag{60}$$

so the ratio

$$\frac{n_1^2}{2n_2} = \frac{2}{\lambda^* w} \tag{61}$$

or, in numbers of traps per cm^2

$$\frac{(C_{T1})^2}{2C_{T2}} = \frac{2}{\lambda^* w} \cdot C_T \tag{62}$$

Equation (62) shows that, in contrast to the case where $w \ll L^*$, the ratio $(C_{T1})^2/2C_{T2}$ does not yield the number of traps, but rather the number of traps in a layer of thickness equal to two diffusion lengths.

The fractions n_i reach an equilibrium value

$$n_i = \frac{1}{\lambda^* w i} \tag{63}$$

(Note that then $n_1^2/2n_2 = 1/\lambda^* w$)

It can be shown that the n_i's will start to decrease when the average number of MP's per trap at the deepest traps ($x^* = b + w$) becomes about equal to 1, and that this happens for $B \approx e^{\lambda^* w}$ ($\gg 1$).

4.5 *Example IV*

In this example all the traps are assumed to be in front of the MP starting distribution (see Figure 9).

The solution for c_m^* is

$$\text{Region} \quad \text{I: } c_m^* = \frac{\cosh \lambda^* x^*}{\lambda^* \sinh \lambda^* w}$$

$$\text{II: } c_m^* = x^* - w + \frac{\tanh \lambda^* w}{\lambda^*} \tag{64}$$

$$\text{III: } c_m^* = 1 - w + \frac{\tanh \lambda^* w}{\lambda^*}$$

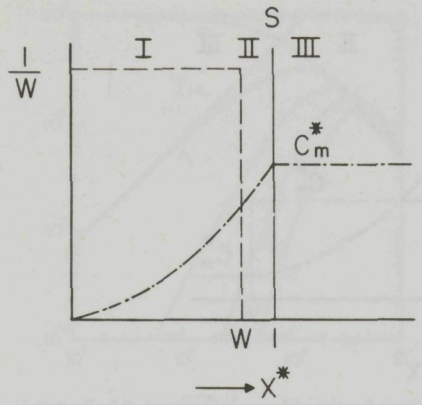

FIGURE 9 Normalized stationary concentration of MP's (c_m^*) as a function of the normalized depth x^* for Example IV. The normalized distribution of the traps, c_T^* and MP's, S^* are also shown.

The trapped fraction is equal to

$$f = \alpha \int_0^\infty c_m^* c_T^* \, dx^* = 1 - \frac{1}{\sinh \lambda^* w} \tag{65}$$

For $\lambda^* w \gg 1$

$$f = 1 - 2e^{-\lambda^* w} \tag{66}$$

while for $\lambda^* w \ll 1$,

$$f = \frac{\alpha w}{2} = \alpha\gamma \tag{67}$$

The trapped fraction f is plotted as the curve $w = 1$ in Figure 11, where X represents $\alpha w/2$.

The fractions n_i when the diffusion length is much greater than w ($\lambda^* w \ll 1$) follow from Eq. (31) using $c_m^* = x^*$. The result is

$$n_i = \frac{1}{wB} P(i + 1, Bw). \tag{68}$$

This is identical to the result in the next example for $w = 1$, and is given in Figure 12 where Q represents Bw. Note that the n_i's all approach the value $1/Bw$ after going through a maximum, and that $n_i \geq n_{i+1}$ throughout.

For $Bw \ll 1$, the ratio $n_1^2/2n_2$ is equal to 0.75. Note that the horizontal scale is now equal to

$$Bw = \frac{K\bar{d}_m Jt}{DN_0} \cdot \frac{2\bar{d}_T}{\bar{d}_m} = 2\frac{K\bar{d}_T Jt}{DN_0} \tag{69}$$

which is proportional to $\bar{d}_T$ and independent of $\bar{d}_m$. When $\lambda^* w \gg 1$, the fractions n_i are given by

$$n_i = \frac{1}{w\lambda^{*i}} P(i, B/\lambda^*) \tag{70}$$

This is the same form as the result of example III (Eq. 59), and is plotted in Figure 8 where Q now represents B/λ^*.

Again, as in example III, for $B/\lambda^* \ll 1$

$$\frac{n_1^2}{2n_2} = \frac{2}{\lambda^* w}, \tag{71}$$

so that in terms of number per cm^2 (Eq. 62), this ratio yields the number of traps within two diffusion lengths.

4.6 *Example V*

The situation considered in this example is drawn in Figure 10. The traps are now assumed to extend to the surface and the MP's start within the trap distribution.

The solution for c_m^* is

$$\text{Region} \quad \text{I: } c_m^* = \frac{\sinh \lambda^*(w-1)}{\lambda^* \sinh \lambda^* w} \cosh \lambda^* x^*$$

$$\text{II: } c_m^* = \frac{\cosh \lambda^*}{\lambda^* \sinh \lambda^* w} \cdot \sinh \lambda^*(w - x^*)$$

$$\text{III: } c_m^* = \frac{\cosh \lambda^*}{\lambda^* \sinh \lambda^* w} \tag{72}$$

The trapped fraction is equal to

$$f = \alpha \int_0^\infty c_m^* c_T^* \, dx^* = 1 - \frac{\sinh \lambda^*(w-1)}{\sinh \lambda^* w} \tag{73}$$

A few limiting cases:

$\lambda w \to \infty, \quad f = 1 - e^{-\lambda^*} \to 1,$

identical to the result of Kelly and Matzke.[6]

$$\lambda w \to 0 \qquad f = \lambda^{*2}(w - \tfrac{1}{2})$$

$$w = 1 \qquad f = 1 - \frac{1}{\sinh \lambda^* w} \tag{74}$$

$$\left.\begin{matrix} w \gg 1 \\ \lambda^* \ll 1 \end{matrix}\right\} \qquad f = \lambda^* \coth \lambda^* w$$

f has been drawn in Figure 11, where X now represents $\alpha(1 - 1/2w)$ and w is a parameter. For $\lambda^* w < 1$, f is proportional to α. For $w > 1$, there is a transition region in which f is proportional to $C_T^{1/2}$ (i.e. $\alpha^{1/2}$) until it saturates at $f = 1$.

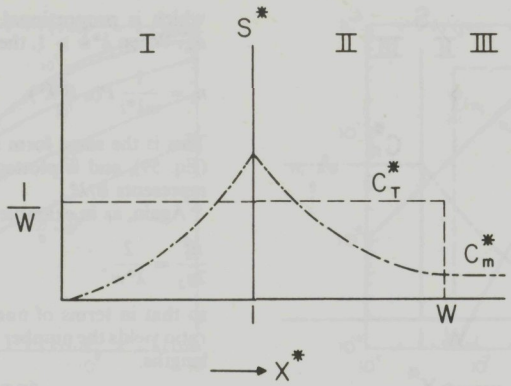

FIGURE 10 Normalized stationary concentration of MP's (c_m^*) as a function of the normalized depth x^* for Example V. The normalized distributions of the traps, c_T^* and MP's, S^* are also shown.

The fractions n_i are calculated for $\lambda^* w \ll 1$. The concentrations c_m^* are then equal to

$$\begin{aligned} &\text{Region} \quad \text{I: } c_m^* = x^* \\ &\qquad\quad \text{II: } c_m^* = 1 \\ &\qquad\quad \text{III: } c_m^* = 1 \end{aligned} \tag{75}$$

The n_i's calculated using Eq. (31), give the result

$$n_i = \frac{1}{wB} P(i+1, B) + \left(1 - \frac{1}{w}\right) \frac{B^i}{i!} \exp(-B) \tag{76}$$

where $P(x, y)$ is the incomplete Γ function.[14] For $w \gg 1$, the second term dominates and the result becomes identical to the one of example III. For $w = 1$, the result is

$$n_i = \frac{1}{B} P(i+1, B) \tag{77}$$

For $w = 1$ and $i = 1$ to 4, the n_i's have been drawn in Figure 12 where Q represents B.

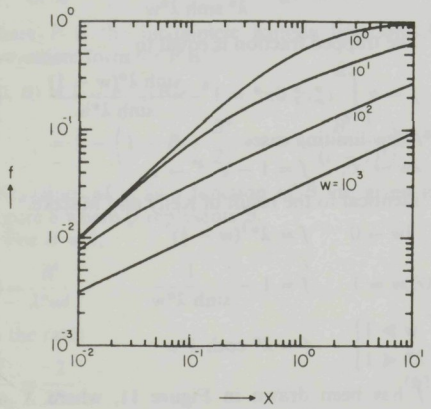

FIGURE 11 Trapped fraction as a function of X with w as a parameter. For Example IV, f is given by the curve $w = 1$ and X replaced by $\alpha w/2$. In Example V, w is a parameter and X is replaced by $\alpha(1 - (1/2w))$.

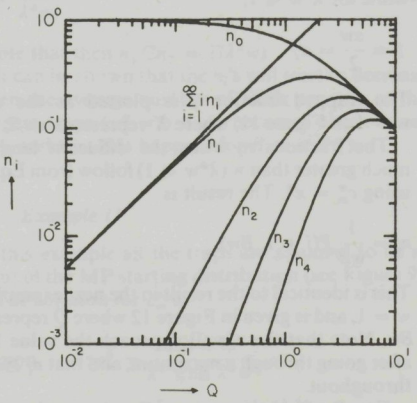

FIGURE 12 The fractions n_i of the traps occupied by i MP's as a function of Q, where Q represents Bw for Example IV. These curves also apply to Example V for $w = 1$, and Q representing B. The total number of MP's trapped per trap is also plotted.

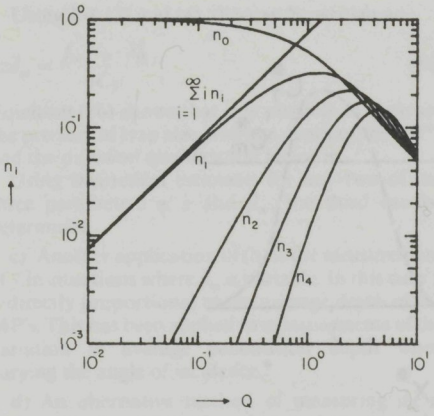

FIGURE 13 The fractions n_i of the traps occupied by i MP's as a function of Q for Example V and $w = 2$, Q representing B. The total number of MP's trapped per trap is also plotted.

For $w = 1$ and $B \ll 1$,

$$\frac{n_1^2}{2n_2} = 0.75, \tag{78}$$

so that in terms of numbers of traps per cm^2

$$\frac{(C_{T1})^2}{2C_{T2}} = 0.75\,C_{T\epsilon} \tag{79}$$

This ratio thus yields 0.75 of the total number of traps.

Figure 13 shows the fractions n_i for $w = 2$. These are sums of the n_i's from Figure 4 and Figure 12. The interesting feature is that the n_i's now cross and then reach an asymptotic value of $1/wB = 1/2B$. In this case, the ratio $n_1^2/2n_2 = 0.85$.

For $w \gg 1$, the result has been given before (see Figure 4). In this case, the n_i's do not approach an asymptotic value, but decrease proportionally at high values of B.

In general, the following conclusion holds: If the concentration c_m^* is constant in the region of the traps, the fractions n_i are given by $(B^i/i!)e^{-B}$. If the concentration c_m^* is not constant in the region of the traps, then

a) the maxima in the n_i's occur later than $B = i$

b) the maximum values of n_i's are lower than $(i^i/i!)e^{-i}$

c) the falling side of the n_i curves is less steep.

For the situation $\lambda^* w \gg 1$, the general solution is rather complicated. However, if $\lambda^* \ll 1$ (this implies $w \gg 1$), being the situation that the MP's start at a depth small compared to the diffusion length, the solution is

$$n_i = \frac{1}{\lambda^* w i} P(i, B) \tag{80}$$

the same result as in example III for the case $\lambda^* w \gg 1$. The same conclusions hold as given there. The n_i's are plotted in Figure 8 with Q representing B.

5 REALISTIC DISTRIBUTIONS AND APPLICATIONS

5.1 *Introduction*

In this section, more realistic distributions of traps and mobile particles will be discussed. The results will be compared to the examples in the previous section.

Two situations will be considered: (1) The traps all beyond, and (2) the traps all in front of the starting distribution of the MP's. It will be shown that these two situations, where there is no overlap between the two distributions, are preferable for experimental investigation. In situation 1, the result is independent of the form of the two distributions, while in situation 2 only overall parameters of the trap distribution ($\bar{d}_T$, $\bar{d}_T^2$, etc.) are important. Only situations in which attenuation effects are negligible will be discussed. This means that the stationary distribution c_m^* does not depend on c_T^* or that the trapping term in the diffusion Eq. (33) is negligible. *It can be shown that this is equivalent to f being linear in c_T^*.* The models in Section 4 showed that a trapped fraction small compared to 1 is a necessary but not sufficient condition for negligible attentuation (see e.g. example III, where $f \cdot b \ll 1$ with $b > 1$). Especially with deep traps ($b \gg 1$), the negligible attentuation condition may require that f be extremely small.

Experimentally, the linearity of f in the trap concentration is a simple criterion for the absence of attenuation. Negligible attenuation has the additional advantage of making the measured desorption spectra easier to analyse since re-trapping effects[21] during the thermal desorption are then also negligible.

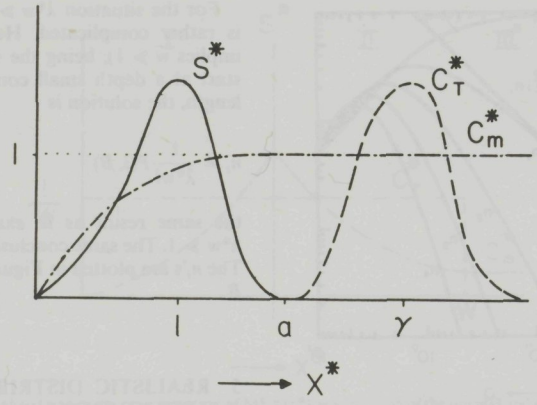

FIGURE 14 Normalized distributions of traps (c_T^*) and MP's (S^*) and the stationary concentration of MP's (c_m^*) as a function of the normalized depth x^* in case all traps are beyond the MP starting distribution S^*.

5.2 *Traps beyond MP's*

The situation is sketched in Figure 14. The stationary concentration c_m^* is found from Eq. (33):

$$\frac{\partial^2 c_m^*}{\partial x^{*2}} - \alpha c_T^* c_m^* + S^* = 0$$

Since the second term is assumed to be negligible, integrating Eq. (33) twice yields

$$c_m^*(x^*) = \int_0^{x^*} \mathrm{d}y \int_y^{\infty} S^*(z)\mathrm{d}z \tag{81}$$

Interchanging the order of integration gives

$$c_m^*(x^*) = \int_0^{x^*} zS^*(z)\mathrm{d}z + x^* \int_{x^*}^{x} S^*(z)\mathrm{d}z \tag{82}$$

For $x^* > a$, where a is the maximum starting depth of the MP's, Eq. (82) reduces to

$$c_m^*(x^*) = \int_0^{x} zS^*(z)\mathrm{d}z = 1 \tag{83}$$

since $S^*(x^*) = 0$ for $x^* > a$. The solution for c_m^* is drawn in Figure 14. Since $c_m^* = 1$ in the region of the traps, the solution is the same as the one found in examples II and III. So,

$$f = \alpha$$

$$n_i = \frac{B^i}{i!} \exp(-B) \tag{84}$$

where

$$\alpha = \frac{K\bar{d}_m C_T}{DN_0}$$

$$B = \frac{K\bar{d}_m Jt}{DN_0}$$

The fractions n_i are given in Figure 4 where Q represents B. Equations (84) can be applied to the following:

a) Measurement of n_i as a function of MP dose (Jt) and fitting to the theoretical curves yields the number of traps C_T. For low values of B, $C_T = (C_{T1})^2/2C_{T2}$.

b) In experiments, f cannot be measured directly since only some fraction η of the incident particles come to rest in the solid and takes part in the diffusion process. The fraction of the incident particles trapped is thus $f_{in} = \eta f$. Since (Eq. 49)

$$f = \frac{K\bar{d}_m C_T}{DN_0}$$

and method (a) above gives the value of C_T, the parameter

$$\frac{\eta K\bar{d}_m}{D} = \frac{f_{in}N_0}{C_T} \tag{85}$$

can be determined.

Using Eq. (3) and (4), this can be written as

$$\eta z \bar{d}_m = \frac{f_{in} N_0 \cdot \lambda_0^2}{6 C_T} \tag{86}$$

Equation (86) shows that it is possible to measure the product of trap size, average depth of the MP's and the diffusion qualification factor η.

Using theoretical estimates for any two of the three parameters η, z and $\bar{d}_m$, the third can be determined.

c) Another application of (b) is the measurement of f in situations where $\bar{d}_m$ is variable. In this case f is directly proportional to the average depth of the MP's. This has been applied to measurements of the variation in average penetration depth when varying the angle of incidence.[9]

d) An alternative method of measuring $\bar{d}_m$ is fitting the experimental peak populations to the theoretical fractions n_i. Expression (81) shows that

$$\frac{K \bar{d}_m}{D N_0} = \frac{B}{Jt} \tag{87}$$

and since Jt is the dose of MP's that took part in the diffusion, the incident MP dose $(Jt)_{in}$ is Jt/η.

So

$$\frac{\eta K \bar{d}_m}{D} = \frac{B N_0}{(Jt)_{in}} \tag{88}$$

which is similar to Eq. (85). Variations in $\bar{d}_m$ can also be measured in this way.

The two methods (b) and (d) are equivalent as long as the assumption of constant K holds. It will be shown in Section 6 that when K is not constant, only the method (d) is applicable.

5.3 *Traps in front of MP's*

This situation is given in Figure 15. The solution of the diffusion Eq. (33) under the same assumption of negligible attenuation is the same as Eq. (82). For $x^* < a$, where a is the minimum depth of the starting distribution $S^*(x^*)$ of the MP's,

$$c_m^*(x^*) = x^* \tag{89}$$

The trapped fraction is equal to

$$f = \alpha \int_0^\infty c_T^* c_m^* \, dx^* = \alpha \int_0^\infty x^* c_T^* \, dx^* = \alpha \gamma$$

or

$$f = \frac{K \bar{d}_T C_T}{D N_0} \tag{90}$$

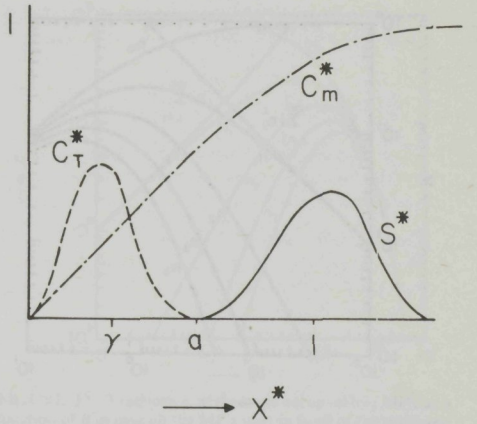

FIGURE 15 Normalized distributions of traps (c_T^*) and MP's (S^*) and the stationary concentration of MP's (c_m^*) as a function of the normalized depth x^* in case MP's start beyond the traps.

This is the same result as in Example IV. The trapped fraction is proportional to the average depth of the traps. The fractions n_i are given by Eq. (31)

$$n_i = \int_0^x c_T^* \frac{(A^*)^i}{i!} \exp(-A^*) dx^*$$

$$= \int_0^x c_T^* \frac{(Bx^*)^i}{i!} \exp(-Bx^*) dx^* \tag{91}$$

This integral cannot be solved in general since it depends on the form of c_T^*. The solution for a uniform distribution of c_T^* has been given in example IV.

For the case c_T^* exponential, Eqs. 92 to 94 are applicable:

$$c_T^* = \frac{1}{\gamma} \exp\left(-\frac{x^*}{\gamma}\right) \tag{92}$$

with

$$\gamma = \frac{\bar{d}_T}{\bar{d}_m}$$

The solution for n_i is (see Appendix 2):

$$n_i = \frac{(B\gamma)^i}{(1 + B\gamma)^{i+1}} \tag{93}$$

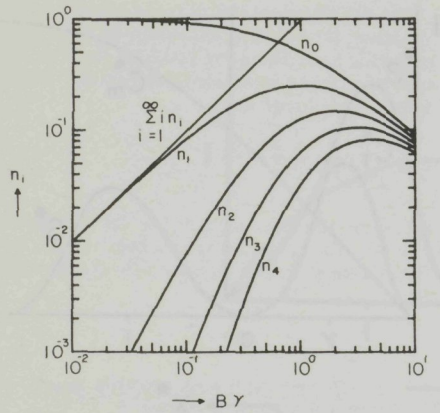

FIGURE 16 Fractions n_i of traps occupied by i MP's as a function of $B\gamma$ for the case that all MP's start beyond the traps and the form of the trap distribution is exponential. The total number of MP's trapped per trap is also plotted.

The curves for n_i are plotted in Figure 16, as a function of

$$B\gamma = \frac{K\bar{d}_T Jt}{DN_0} \tag{94}$$

Note that $C_{T1}^2/2C_{T2}$ for $B\gamma \ll 1$, is equal to $0.5C_T$.

In general, if $A^* \ll 1$, Eq. (91) reduces to

$$n_i = \int_0^\infty c_T^* \frac{(Bx^*)^i}{i!} dx^* = \frac{B^i}{i!} \int_0^\infty x^{*i} c_T^* \, dx^* \tag{95}$$

This result shows that n_i is proportional to the ith moment of the function $c_T^*(x^*)$, or

$$n_i = \frac{1}{i!} \left(\frac{KJt}{DN_0}\right)^i \overline{d_T^i} \tag{96}$$

The ratio

$$\frac{n_1^2}{2n_2} = \frac{(\bar{d}_T)^2}{\overline{d_T^2}} \tag{97}$$

or in general

$$\frac{n_1^i}{i! n_i} = \frac{(\bar{d}_T)^i}{\overline{d_T^i}} \tag{98}$$

For a uniform distribution as in example IV

$$\frac{(\bar{d}_T)^2}{\overline{d_T^2}} = \frac{3}{4}$$

as was found there. If c_T^* is an exponential

$$\frac{(\bar{d}_T)^2}{\overline{d_T^2}} = \frac{1}{2}$$

also consistent with the answer from Appendix 2.

The applications of Eqs. (90), (97) and (98) are,

a) knowing the form of the distribution of traps c_T^* and measuring C_{T1} and C_{T2} at low values of $B\gamma$ (i.e. low average number of MP's trapped per trap), one can calculate the number of traps from Eq. (97):

$$C_T = \frac{\overline{d_T^2}}{(\bar{d}_T)^2} \cdot \frac{C_{T1}^2}{2C_{T2}} \tag{99}$$

b) Using Eq. (90) and the calculated C_T from method (a), one is able to calculate the parameter (see Eq. 85),

$$\frac{\eta K \bar{d}_T}{D} = \frac{f_{in} N_0}{C_T} \tag{100}$$

where η is the fraction of the incident particles that qualifies for diffusion, and f_{in} is the fraction of the incident particles trapped. Analogous to Eq. (86):

$$\eta z \bar{d}_T = \frac{f_{in} N_0 \lambda_0^2}{6C_T} \tag{101}$$

with Eq. (101), estimates of $\bar{d}_T$ can be made.

c) The average depth of the traps is proportional to f, so that relative values of $\bar{d}_T$ can be determined directly by measuring variations in f.

d) The fraction of the incident particles trapped (f_{in}) is equal to ηf, with f independent of $\bar{d}_m$. If any parameter of this mobile particle injection is changed (e.g. energy or crystallographic angle) the resulting variation in η can be determined from the variation of f_{in}. It is only necessary that all of the mobile particles be injected beyond the traps.

6 VARIABLE REACTION RATE COEFFICIENT K

All previous calculations were based on the assumption that K, the reaction rate coefficient for the trapping, did not depend on i, the number of MP's already present in the trap. However, for the experiments described in paper II, it was found that K increases as soon as even one MP occupies a trap.

When K is variable, the general solution found in Section 3 is no longer valid. Since the trapping term $Kc_T c_m$ in the diffusion Eq. (1) is no longer time independent (since K changes in time), the concentration c_m is not constant in time. However when the trapping term is negligible, as assumed in Section 5, the diffusion equation is again stationary.

The solution of the rate equations must now be found from (see Eqs. 8–10)

$$\begin{aligned}
\frac{\partial c_{T0}}{\partial t} &= -K_0 c_m c_{T0} \\
\frac{\partial c_{T1}}{\partial t} &= -K_1 c_m c_{T1} + K_0 c_m c_{T0} \qquad (102) \\
&\vdots \\
\frac{\partial c_{Ti}}{\partial t} &= -K_i c_m c_{Ti} + K_{i-1} c_m c_{T(i-1)}
\end{aligned}$$

The solution of this system of equations is given by

$$\frac{c_{Ti}}{c_T} = \prod_{j=0}^{i} (-k_j) \sum_{l=0}^{i} \frac{\exp(-k_l A^*)}{\prod_{m=0, m\neq l}^{i} (k_l - k_m)} = F_i(k, A^*) \qquad (103)$$

with

$$k_i = \frac{K_i}{K_0}$$

and

$$A^* = \int_0^t K_0 \cdot c_m \cdot \mathrm{d}t = B c_m^*$$

If n of the k's are equal (k_e) in the sum in Eq. (103), these n terms reduce to

$$\frac{(-A^*)^{n-1} \exp(-k_e A^*)}{(n-1)! \prod_{m=0, k_m \neq k_e}^{i} (k_e - k_m)} \qquad (104)$$

The numbers of traps per cm^2 with i helium atoms C_{Ti} are equal to

$$C_{Ti} = N_0 \int_0^{l} c_{Ti}\, \mathrm{d}x = C_T \int_0^{\infty} c_T^* F_i(k, A^*) \mathrm{d}x \qquad (105)$$

For general distributions $c_T^*(x^*)$ and $S^*(x^*)$ the solution requires a computer calculation. For the case of all traps beyond the starting distribution of the MP's, Eq. (105) reduces to

$$n_i = \frac{C_{Ti}}{C_T} = F_i(k, B) \text{ (see Eq. 103)} \qquad (106)$$

and

$$B = \frac{K_0 \cdot d_m J t}{D N_0}$$

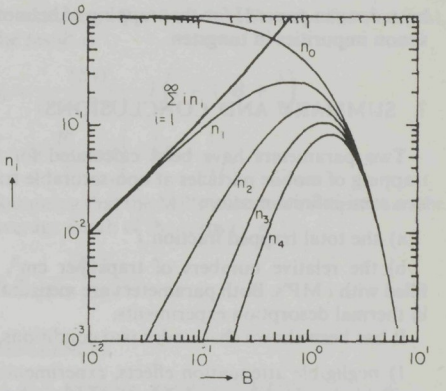

FIGURE 17 Fractions n_i of the traps occupied by i MP's as a function of B in case all the MP's start in front of the traps and the reaction rate coefficient given by $K_i = K_0 \cdot (i+1)$

As an example, assuming $K_i = K_0 \cdot (i+1)$, the solution of Eq. (106) is

$$n_i = \sum_{j=0}^{i} (-1)^j \binom{i}{j} e^{-(j+1)B} \qquad (107)$$

with

$$\binom{i}{j} = \frac{i!}{j!(i-j)!}$$

For $B \ll 1$, this reduces to

$$n_i = B^i \qquad (108)$$

The n_i's are given in Figure 17 as a function of B.

Comparing this to the case where K is constant shows that

1) the maximum values of the fractions n_i are lower and appear earlier.

2) the onset of the n_i's for $i > 1$ occurs earlier

3) the total trapped fraction f is not linear in B and thus not linear in $\bar{d}_m$. However B and $\bar{d}_m$ are proportional (see Eq. 106) so the parameter B can thus be used to measure $\bar{d}_m$ as mentioned in Section 5.2. This has been done in experiments in which the channeling of low energy helium was measured.[9]

Another important application is the actual measurement of the different K_i's by fitting the measured fraction n_i to the theoretical curves. In this way, the size of the traps with increasing number of MP's trapped is measured. This has

been done in paper II for the trapping of helium at xenon impurities in tungsten.

7 SUMMARY AND CONCLUSIONS

Two parameters have been calculated for the trapping of mobile particles at non-saturable traps in a semi-infinite medium:

a) the total trapped fraction f

b) the relative numbers of traps per cm^2, n_i, filled with i MP's. Both parameters are measurable in thermal desorption experiments.

It has been shown that under two conditions,

1) negligible attenuation effects, experimentally verifiable by checking the linearity of f in the trap concentration,

2) no overlap between the trap distribution and the starting distribution of the MP's,

relatively simple expressions result.

If under these conditions the traps are deeper than the starting distribution of the MP's, the quantities which can be derived by measuring f and n_i as a function of the mobile particle dose are

a.1) the number of traps per cm^2, C_T

a.2) the product $\eta \bar{d}_m z$

a.3) the relative values of the rate coefficients K_i.

This enables measurements of the variation in average depth of the MP's as has been done for helium, both as a function of angle and of energy.[9] Estimates of η and $\bar{d}_m$ yield a value of z, giving the radius of the equivalent spherical trap. The values of K_i as a function of i can be used in bubble nucleation theories to calculate the growth of bubbles around traps.[15-19] This phenomenon has been observed experimentally (paper II) for the trapping of helium at xenon impurities in tungsten.

If the traps are in front of the starting distribution of the MP's, measuring f and n_i as a function of the MP dose yields:

b.1) the number of the traps per cm^2, C_T, provided that $\overline{d_T^2}/(\bar{d}_T)^2$ of the trap distribution is known,

b.2) the product $\eta \bar{d}_T z$ when C_T is known,

b.3) relative values of $\bar{d}_T$ even when C_T is not known,

b.4) relative values of η under variation of the injection energy or angle of the MP's.

Estimates of $\overline{d_T^2}/(\bar{d}_T)^2$ can be made by standard range theories.[20] They indicate that this ratio is dependent only on the mass ratio of the trapping particles to the medium. Conversely, if C_T is known by other methods, the range straggling $(\overline{d_T^2})^{1/2}/\bar{d}_T$ can be measured.

Combining a.2) and b.2), the ratio $\bar{d}_m/\bar{d}_T$ can be measured directly.

Since inert gases like Ne, Ar, Kr and Xe act as traps for mobile helium, the channeling of these gases as well as their relative ranges as a function of energy are measurable.

The possibilities mentioned above open a whole new field for the application of helium thermal desorption spectrometry. Besides the binding energy of helium to traps, quantitative information can be derived about both the helium penetration distribution and the trap depth distribution. It also offers interesting possibilities for studying the early stages of nucleation of helium bubbles around impurities in metals.

ACKNOWLEDGEMENTS

One of us, (AAvG) would like to thank the Canada Council for a scholarship and Dr. A. van Veen for discussions during the early part of the work.

APPENDIX 1

The fractions n_i are calculated for example III (Figure 6) and the width of the distribution w much greater than the diffusion length $1/\lambda^*(\lambda^* w \gg 1)$. The solution of c_m^* in region III is then

$$c_m^* = \frac{\exp(\lambda^*(b - x^*))}{1 + \lambda^* b}$$

The fractions n_i are given by

$$n_i(t) = \int_0^\infty c_T^* \frac{(A^*)^i}{i!} \exp(-A^*) \mathrm{d}x^*$$

$$= \int_b^{b+w} \frac{1}{w} \cdot \frac{[B \exp\{\lambda^*(b - x^*)\}]^i}{i!}$$

$$\times \exp[-B \exp\{\lambda^*(b - x^*)\}] \mathrm{d}x^*$$

Substituting $Be^{\lambda^*(b-x^*)} = S$

$$n_i(t) = \frac{-1}{i\lambda^* w}\int_B^{Be^{-\lambda^* w}} \frac{S^{i-1}}{(i-1)!}\exp(-S)\mathrm{d}S$$

$$= \frac{1}{i\lambda^* w}\left\{\int_0^B \frac{S^{i-1}}{(i-1)!}\exp(-S)\mathrm{d}S - \int_0^{Be^{-\lambda^* w}} \frac{S^{i-1}}{(i-1)!}e^{-S}\,\mathrm{d}S\right\}$$

$$= \frac{1}{i\lambda^* w}\{P(i, B) - P(i, Be^{-\lambda^* w})\}$$

in which $P(i, B)$ is the incomplete gamma function (see Ref. 14, 6.5.1). Since $\lambda^* w \gg 1$,

$$n_i(t) = \frac{1}{i\lambda^* w}P(i, B)$$

APPENDIX 2

The fractions n_i are calculated when the trap distribution is exponential with average depth γ:

$$c_T^* = \frac{1}{\gamma}\exp\left(-\frac{x^*}{\gamma}\right)$$

In the no-attenuation approximation, c_m^* is equal to

$$c_m^* = x^* \qquad x^* < 1$$

$$c_m^* = 1 \qquad x^* \geq 1$$

The fractions n_i are calculated from Eq. (31) and (32):

$$n_i = \int_0^\infty c_T^* \frac{(Bc_m^*)^i}{i!}\exp(-Bc_m^*)\mathrm{d}x^*$$

$$= \int_0^1 \frac{1}{\gamma}\exp\left(-\frac{x^*}{\gamma}\right)\cdot\frac{(Bx^*)^i}{i!}\exp(-Bx^*)\mathrm{d}x^* + \int_1^\infty \frac{1}{\gamma}\exp\left(-\frac{x^*}{\gamma}\right)\cdot\frac{B^i}{i!}\exp(-B)\mathrm{d}x^*$$

Substituting $(B + 1/\gamma)x^* = S$ in the first integral, the result is

$$n_i = \frac{(B\gamma)^i}{(1 + B\gamma)^{i+1}}P\left(i + 1, B + \frac{1}{\gamma}\right) + \frac{B^i}{i!}\exp\left\{-\left(B + \frac{1}{\gamma}\right)\right\}$$

Assuming that the MP's start much deeper than the average depth of the traps ($\gamma \ll 1$)

$$n_i = \frac{(B\gamma)^i}{(1 + B\gamma)^{i+1}}$$

REFERENCES

1. E. V. Kornelsen, *Rad. Eff.*, **13**, 227 (1972).
2. L. M. Caspers, A. van Veen, A. A. van Gorkum, A. van den Beukel, and C. M. van Baal, *Phys. Stat. Sol.* (a), **37**, 371 (1976).
3. E. V. Kornelsen and D. E. Edwards, Jr., *Applications of Ion Beams to Metals*, p. 521, eds. S. T. Picreaux, E. P. Eernisse, F. L. Vook, Plenum Press, New York, 1973.
4. E. V. Kornelsen and A. A. van Gorkum, following paper(ch.6)
5. H. Gaus, *Z. Naturforschung*, **20a**, 1298 (1965).
6. R. Kelly, H-J. Matzke, *J. Nucl. Mat.*, **20**, 171 (1966).
7. A. van Veen, L. M. Caspers, E. V. Kornelsen, R. H. J. Fastenau, A. A. van Gorkum, and A. Warnaar, *Phys. Stat. Sol.* (a), **40**, 235 (1977).
8. D. Edwards, Jr., and E. V. Kornelsen, *Rad. Eff.*, **26**, 155 (1975).
9. E. V. Kornelsen and A. A. van Gorkum, to be published(ch.7)
10. M. I. Baskes and W. D. Wilson, *J. Nucl. Mat.*, **63**, 126 (1978).
11. J. Roth, R. Behrisch, B. M. U. Scherzer, and F. Pohl, Proc. 8th Symp. on Fusion Techn., Noordwijkerhout 1974.
12. T. R. Waite, *Phys. Rev.*, **107**, 463 (1957).
13. R. H. J. Fastenau, A. van Veen, P. Penning, and L. M. Caspers, *Phys. Stat. Sol.* (a), **47**, 577 (1978).
14. M. Abramowitz and I. A. Stegun, *Handbook of Mathematical Functions*, Dover Publications, New York, 1970.
15. A. D. Brailsford and R. Bullough, *J. Nucl. Mat.*, **44**, 121 (1972).
16. K. C. Russel, *Scipta Metallurgica*, **6**, 209 (1972).
17. V. F. Sears, *J. Nucl. Mat.*, **39**, 18 (1971).
18. H. Wiedersich, J. J. Burton, and J. L. Katz, *J. Nucl. Mat.*, **51**, 287 (1974).
19. A. D. Brailsford, R. Bullough, and M. R. Hayns, *J. Nucl. Mat.*, **60**, 246 (1976).
20. H. E. Schiøtt, *Rad. Eff.*, **6**, 107 (1970).
21. C. Roodbergen, A. van Veen, and L. M. Caspers, *Delft Prog. Rep. A*, **1**, 107 (1975).

Radiation Effects, 1979, Vol. 42, pp. 113–124
0033-7579/79/4201-0113 $04.50/0

ATTACHMENT OF MOBILE PARTICLES TO NON-SATURABLE TRAPS
II. The Trapping of Helium at Xenon Atoms in Tungsten

E. V. KORNELSEN and A. A. VAN GORKUM

Division of Electrical Engineering, National Research Council of Canada, Ottawa, Canada K1A 0R8

(*Received March 18, 1979*)

Thermal desorption spectra have been measured for helium attached to xenon atoms in a tungsten crystal. The xenon was implanted at 1.5 keV and annealed to 2150 K, and the helium then injected at 250 eV along the ⟨100⟩ direction normal to the crystal surface. The binding energy of the helium was found to increase monotonically with the number of helium atoms occupying the trap, from 1.2 eV for a single atom to ≈2.1 eV for 7 to 10 atoms. At still higher injected doses, the attachment of up to 100 helium atoms to each trap has been observed. The binding energy continues to increase to ≈4 eV for 100 atoms, and the apparent trapping radius increases by a factor of four from the empty trap value of 3.3 Å.

1 INTRODUCTION

It has been shown in earlier papers that helium injected into a metal crystal is mobile as an interstitial at room temperature, but that it can be tightly bound to lattice vacancies and to impurities or defect/impurity complexes. Such phenomena have been observed in some detail for tungsten,[1] molybdenum[2] and nickel,[3] and may be expected in most metals.

For inert gas atoms annealed to >1400 K in tungsten, helium binding states were found which were specific to the atomic number of the gas.[1] An interpretation based on the multiple binding of helium to annealed Kr in tungsten has been given[4] but a good test of the proposed theoretical trap-filling model was not possible at that time because of insufficient experimental sensitivity.

The present paper reports more extensive thermal desorption data for the case of annealed Xe in tungsten. The data was obtained using an apparatus of much higher sensitivity[5] and has been corrected and analyzed using a small computer-based acquisition system. For a specific set of experimental parameters, the results are compared with a more complete theoretical model based on the multiple filling of non-saturable traps. The model is presented in some detail in the preceding paper, which will be referred to as I. It includes the effects of depth distributions and variation of the trap size with the number of helium atoms occupying the trap.

2 EXPERIMENTAL

The ultrahigh vacuum apparatus used for the experiments has been described previously.[5] The (100) tungsten crystal was the same one used earlier in a study of helium trapping at lattice vacancies.[6] The crystal was heated at 40 K/s by 1 kV electron bombardment of the rear face employing a current wave form generated by the acquisition computer system. The crystal temperature was monitored by recording the output of an infra-red pyrometer previously calibrated against an optical pyrometer at temperatures ≥1000 K. Below 1000 K, the crystal temperatures were deduced from the values of the crystal mass (1.22 g), surface area (1.28 cm^2), the thermal conduction loss (4.6×10^{-3} watt/K) and published values of $P_R(T)$, the radiated power per unit surface area. The thermal conduction loss was deduced from $P_R(T)$ and the total power required to maintain various constant temperatures between 1000 K and 2300 K. The maximum temperature during desorption cycles was normally 2300 K. Annealing sequences were carried out by interrupting the temperature sweep at the required time with an appropriate computer instruction.

Bombardment conditions common to all experiments are given in Table I. Xenon ions at 1500 eV are known to produce lattice damage in tungsten, whereas 250 eV helium ions do not.[1] In all cases, the ions irradiated the central 0.36 cm diameter (0.10 cm^2 area) of the 0.70 cm diameter crystal face.

TABLE I

Xenon ion energy	1500 eV
Helium ion energy	250 eV
Crystal temperature	300–350 K
Incident angle	Normal (⟨100⟩ ± 1°)

Beam defocussing in the case of He, and raster scanning in the case of Xe were used to ensure that the beam current density did not vary by more than 15% over the bombardment area.

Details of the computer-based digital acquisition and treatment of the thermal desorption data will appear in a separate paper.[7] Briefly, the helium partial pressure was recorded digitally at 0.1 sec intervals as the crystal was heated in a 2.27 l volume in which the helium pumping speed was low. Corrections were then computed and applied for the vacuum equilibration time constant (0.028 s), the electronic system time constant (0.26 s) and the ionic pumping time constant of the mass spectrometer (650 sec). The data was then smoothed and differentiated to yield the desorption rate spectrum. By supplying the computer with the mass spectrometer sensitivity, the desorption volume and the scale of the sensing electrometer, the spectrum could be plotted directly in absolute units, i.e. atom cm^{-2} sec^{-1}. The spectra shown in this paper were drawn directly by a computer-controlled plotter from the data processed as described above. The populations and binding energies for individual peaks in the spectra were obtained by matching a series of computer-generated first order peaks[8] to the processed data.

Computations by Oen and Robinson[9] predict that 2 keV helium ions would penetrate ~110 Å into "random" tungsten. We measured the ratio of helium trapping for 2 keV randomly incident helium and 250 eV ions incident along ⟨100⟩, (the crystal normal) for the case of the traps much deeper than the helium penetration depth. Using methods described in paper I, and assuming that the chosen random direction gives the same average range as that calculated for random tungsten, we deduced an average range for the 250 eV He^+ along ⟨100⟩ to be ~70 Å. Further assuming that the range straggling is that given by Schiøtt,[10] the form of the helium range distribution is approximately as shown in Figure 1 (S_{He}).

The range distribution of 1500 eV Xe^+ along the ⟨100⟩ channel was estimated from penetration data for 1 keV and 5 keV.[11] According to xenon thermal desorption measurements (see Figure 3)

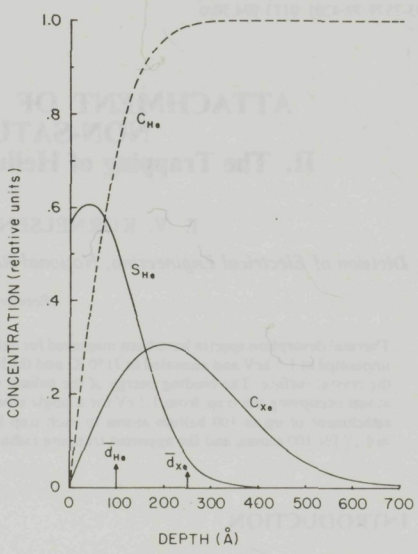

FIGURE 1 The depth distribution of 1500 eV xenon after 2150 K anneal (c_{Xe}), the range distribution of 250 eV helium (S_{He}) and the corresponding stationary distribution of the helium (c_{He}), normalized in amplitude.

all the xenon desorbing below 1600 K does so from near-surface sites with no significant diffusive motion of the more deeply implanted gas. For the 1500 eV implant, heating to 1600 K was found to desorb one third of the implanted xenon, and it was assumed that this was the one third of the distribution closest to the surface. The remaining distribution, which contained 0.38 of the originally incident ions, then had an approximately exponential form and an average depth $\bar{d}_0 = 18$ Å.

The evolution of this remaining distribution as the gas diffused (i.e. as the crystal was heated beyond 1600 K) was calculated analytically from the diffusion equation. It was found that during diffusion, the product of the average depth of the remaining Xe and the fraction left was constant, so that the average depth is given by,

$$\bar{d} = \bar{d}_0\left(\frac{0.38}{f}\right) \tag{1}$$

where f is the fraction of the incident xenon still in the crystal. For the particular case of annealing to 2150 K, used in the main experiments, f was measured to be 0.026, so that $\bar{d}$ was then 260 Å. The

distribution for this case, as obtained from the measured starting distribution[11] and the solution of the diffusion equation, has the form shown as C_{Xe} in Figure 1. As shown in paper I, the conclusion that $\bar{d}$ is substantially greater than the helium range makes the trapping quite insensitive to the details of the depth distributions, a fact verified experimentally in this paper.

3 RESULTS

Helium desorption spectra observed for three anneal temperatures of the implanted xenon are shown in Figure 2. From earlier work[1] and the present experiments, we believe that lattice vacancies singly and doubly occupied by helium give rise to peaks H and G; that vacancies bound to the xenon "impurities" likewise give peaks H' and G'; and that xenon atoms in their high temperature equilibrium state are the traps responsible for peaks A, B, C and D. The latter we denote "type A" traps in what follows. For anneal temperatures $T_A \leq$ 600 K, all three types of traps are present, as in Figure 2a. For $T_A = 1100$ K (Figure 2b) the free-vacancy traps have vanished, and for $T_A = 1400$ K (Figure 2c), only type A traps remain. The helium populations associated with the three kinds of traps as a function of T_A are shown in more detail in Figure 3, where the helium dose was kept constant at 5×10^{12} cm^{-2}, the same as in Figure 2. Two distinct anneal stages can be seen, at $T_A = 800$ K and 1200 K respectively. These stages are similar to those reported previously for krypton,[4] and can be understood as follows. At 800 K, the lattice vacancies become mobile. This is consistent with the Stage III anneal in tungsten.[14] The majority of the vacancies disappear at the surface, but a few attach temselves to xenon atoms, as seen by the rise of the $(H' + G')$ population. At 1200 K, the bound vacancies escape from the xenon atoms and migrate to the surface ($(H' + G')$ decreases to zero). Concurrently, "type A" traps are created either during the vacancy release or coincidently from previously non-trapping xenon atoms.

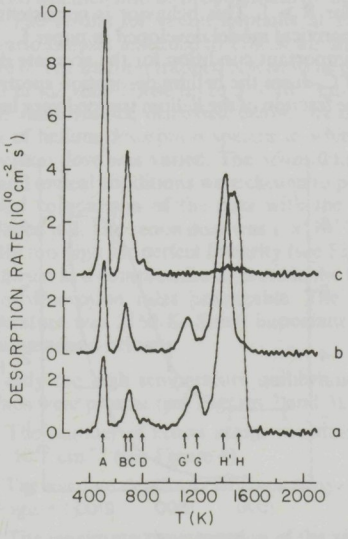

FIGURE 2 Helium desorption spectra for Xe^+-implanted (100)W annealed to different temperatures. Xe implant: 3×10^{12} cm^{-2} at 1500 eV. He injection: 5×10^{12} cm^{-2} at 250 eV. Both at normal incidence (⟨100⟩). Anneal temperatures a) 500 K b) 1100 K c) 1400 K. The temperature rise rate was 40 K/s.

The ration C_{Xe}/C_T is seen to be ≈ 3 for $T_A =$ 1600 K and to gradually decrease, becoming ≈ 1.5 for $T_A \equiv 2400$ K. We conclude that a substantial fraction of the remaining xenon atoms does not

The xenon desorption spectrum for the same implantation conditions (dashed line in Figure 3) shows that neither of these stages is connected with major xenon release peaks, even though two of the three types of traps are associated with the xenon atoms.

For $T_A > 1400$ K, the helium spectra continued to have the basic form of Figure 2c, but decreased in amplitude as the xenon was released. The type A traps thus correspond to the high temperature thermal equilibrium state of xenon atoms in tungsten. After heating the crystal to 2600 K for 30 seconds, the helium trapping was too small to be observable on the scale of Figure 2, and xenon desorption was essentially complete. Heating to 2600 K was therefore used to determine the amount of xenon C_{Xe} remaining in the crystal after implantation and annealing to various lower temperatures. The results for an implanted dose of 1×10^{13} cm^{-2} are shown as the upper curve in Figure 4. The lower curve gives the number of traps per cm^2 C_T remaining in the crystal for the same combinations of implantation and anneal. The deduction of C_T is one of the main results derived from the data of this paper using the model of paper I, and the details are given in Section 4.

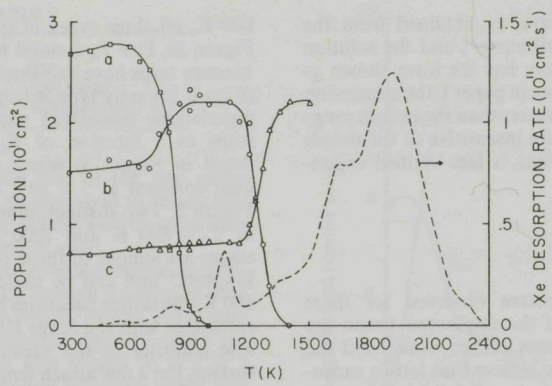

FIGURE 3 Peak populations as a function of anneal temperature. Bombardment parameters as in Figure 2. a) sum of $G + H$, b) sum of $G' + H'$, c) sum of $A + B + C$. The broken curve is the Xe desorption spectrum for the same implantation parameters.

trap helium at the bombardment (room) temperature. As T_A increases, this fraction decreases until at $T_A \geq 2400$ K, about 2/3 of the remaining xenon atoms act as type A traps.

Using the C_T values of Figure 4, the number of helium atoms trapped per trap, $\bar{i}$, can be deduced. For a helium dose of 1×10^{13} cm^{-2}, $\bar{i}$ was found to vary with T_A as shown in Figure 5. From Eq. (1), the remaining fractions f in Figure 4, and the estimated average helium range (70 Å) the ratio R of the average xenon depth $\bar{d}_{Xe}$ to the average helium range $\bar{d}_{He}$ was calculated and is included in Figure 5. The trapped helium per trap is seen to increase with R up to $R \approx 1$, but to become constant for $R \gg 1$. This behavior is consistent with the theoretical model developed in paper I.

An important condition for the accurate deduction of C_T from the helium desorption spectrum is that the fraction of the helium trapped vary linearly

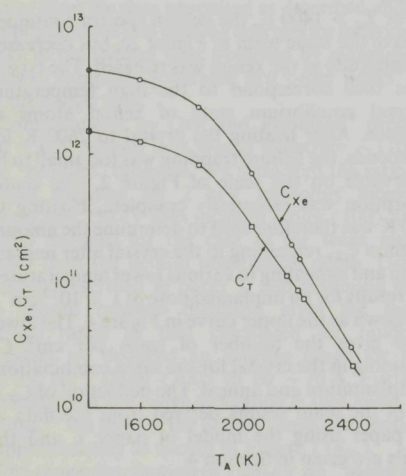

FIGURE 4 The number of xenon atoms per cm^2 (C_{Xe}) and number of traps per cm^2 (C_T) remaining in the crystal as a function of anneal temperature. Xe implant: 1×10^{13} cm^{-2} at 1500 eV, normal incidence.

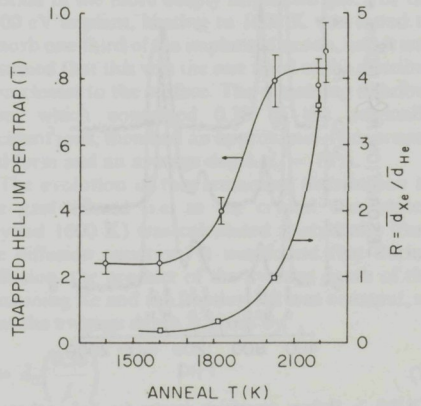

FIGURE 5 The number of helium atoms per trap as a function of anneal temperature for the same Xe implant as in Figure 4. He injection: 1×10^{13} cm^{-2} at 250 eV. Included is the ratio R of the average depth of the remaining Xenon $\bar{d}_{Xe}$ to the average helium penetration $\bar{d}_{He}$.

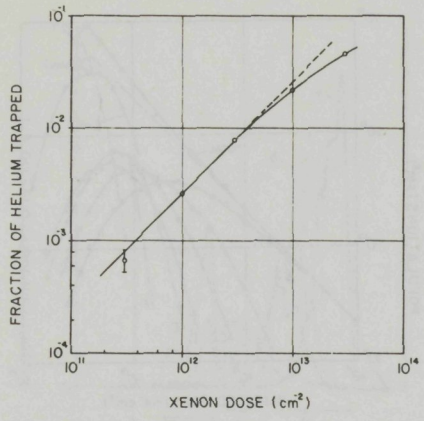

FIGURE 6 The fraction of 250 eV helium ions trapped as a function of Xe dose. The Xe was implanted at 1500 eV at normal incidence and annealed to 2180 K. The helium dose was 4×10^{12} cm^{-2}.

with the xenon dose (see I, Section 5). The C_T values deduced will then also be proportional to the xenon dose. The results for xenon implants at 1500 eV and various doses annealed to 2180 K are shown in Figure 6. The fraction trapped is seen to be proportional to the xenon dose up to 5×10^{12} cm^{-2}.

The main results, discussed below, are a single series of helium desorption spectra in which only the helium dose was varied. The xenon implantation and anneal conditions were chosen to permit a detailed comparison of the data with the theory developed in I. The xenon dose was 1×10^{13} cm^{-2}, slightly too high for perfect linearity (see Figure 6) but chosen as a compromise to provide the highest helium desorption rates practicable. The anneal temperature was 2150 K. Some important points are summarized below:

a) only the high temperature quilibrium "type A" traps were present (see Figures 2 and 3).

b) The number of xenon atoms remaining was 2.6×10^{11} cm^{-2} (see Figure 4).

c) The average depth of the traps was ~ 250 Å (see Figure 1).

d) The maximum concentration of the xenon in atomic fraction was $\sim 1.5 \times 10^{-6}$.

Figures 7 and 8 give desorption spectra for the series of helium doses indicated in the captions, ranging from 6×10^{11} cm^{-2} to 2×10^{13} cm^{-2}.

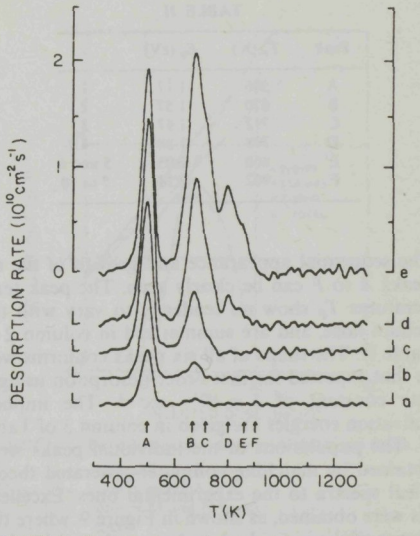

FIGURE 7 Helium desorption spectra as a function of helium dose. The bombardment parameters are those of Table I and $T_A = 2150$ K. The injected helium doses were a) 6×10^{11} cm^{-2}; b) 1×10^{12} cm^{-2}; c) 2×10^{12} cm^{-2}; d) 4×10^{12} cm^{-2}; e) 6×10^{12} cm^{-2}.

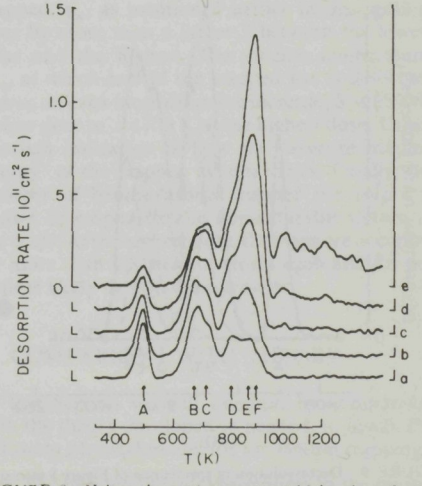

FIGURE 8 Helium desorption spectra at higher doses for the same implant as Figure 7. The helium doses were a) 8×10^{12} cm^{-2}; b) 1×10^{13} cm^{-2}; c) 1.25×10^{13} cm^{-2}; d) 1.5×10^{13} cm^{-2}; e) 2.0×10^{13} cm^{-2}.

TABLE II

Peak	T_P (K)	E_B (eV)	i
A	506	1.17	1
B	670	1.57	2
C	712	1.67	3
D	798	1.88	4
E	860	2.03	5 and 6
F	902	2.13	7 to 10

The sequential appearance and growth of the six peaks *A* to *F* can be clearly seen. The peak temperatures T_P show no tendency to vary with the helium dose, and are summarized in column 2 of Table II. The shape of all six peaks conforms well to that expected for first-order desorption using a rate constant of 1×10^{12} sec^{-1}. The implied activation energies are given in column 3 of Table II. The populations of the individual peaks were obtained by matching computer-generated theoretical spectra to the experimental ones. Excellent fits were obtained, as shown in Figure 9, where the shapes of the individual peaks are plotted (dashed lines) and their sum (dotted line) is compared with the experimental spectrum of Figure 8b. The total quantity of helium desorbed in this case was 2.9×10^{11} cm^{-2}, 2.9% of the incident dose.

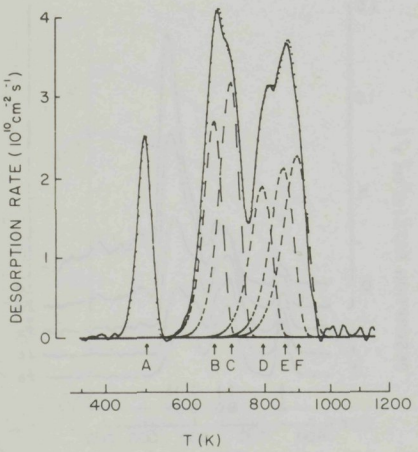

FIGURE 9 Deconvolution of spectrum *b* of Figure 8 into six first-order desorption transients. The rate constant used was 1×10^{12} s^{-1}. The dashed curves are the theoretical component peaks, the dotted curve their sum, and the full curve the experimental spectrum.

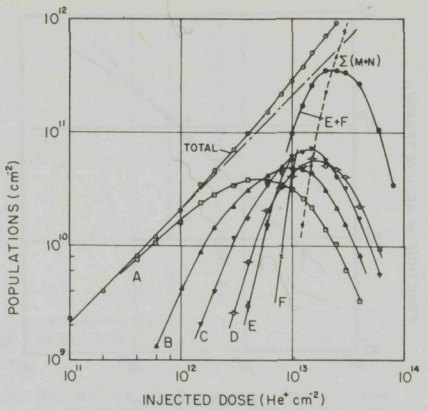

FIGURE 10 Individual peak populations and their sum as a function of helium dose. Bombardment parameters and anneal as in Figure 7

peak A
peak B
peak C
peak D
peak E
peak F
sum of peaks E and F
sum of M and N peaks
total

The broken line is an extension of the constant trapped fraction (2.1 %) found at low dose.

In Figure 10, we have plotted the individual peak populations, obtained in this way, and their sum over a somewhat wider range of helium dose. The peak populations are seen to rise with increasing dose, to reach maxima at gradually increasing values of the dose, and thereafter to decrease rather rapidly. Peak *A* rises linearly in dose, peak *B* approximately as (dose)^2 and the later peaks with still higher and increasing powers of the dose. The total population at first rises linearly, corresponding to a constant trapped fraction of 2.1% (broken line). As soon as the later peaks (*B*, *C*, *D*) become prominent, the trapped fraction is observed to *increase* slowly but steadily, reaching 3.6% at a dose of 2×10^{13} cm^{-2}. For helium doses $\geq 1 \times 10^{13}$ cm^{-2}, the *E* peak and *F* peak populations could not be obtained separately, so that only the sum $E + F$ has been plotted. For doses $\geq 2.5 \times 10^{13}$ cm^{-2}, this sum is dominated by peak *F*. Peaks *A* to *D* have maxima in the range 4 to 7×10^{10} cm^{-2}, while $E + F$ reaches a value about five times larger.

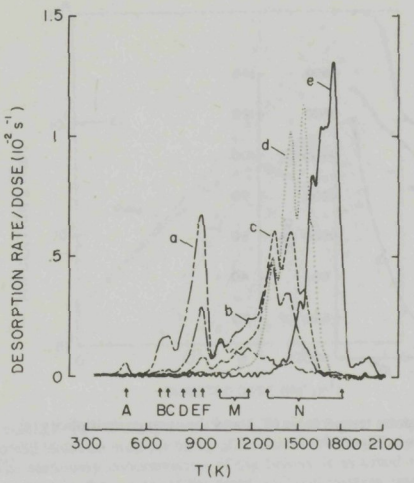

FIGURE 11 Helium desorption spectra at very high doses normalized to the incident dose. Bombardment parameters and anneal as in Figure 7, a) 2×10^{13} cm^{-2}; b) 4×10^{13} cm^{-2}; c) 6×10^{13} cm^{-2}; d) 1×10^{14} cm^{-2}; e) 2×10^{14} cm^{-2}.

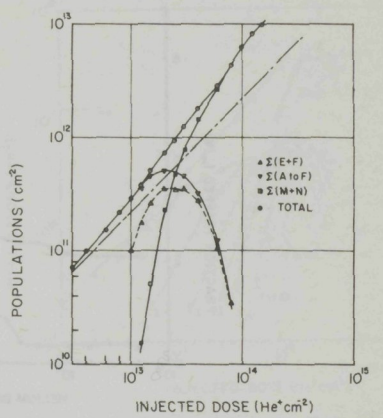

FIGURE 12 Peak populations for very high helium doses.
- △—△ sum of E and F peaks
- ▽—▽ sum of peaks A to F
- ⊡—⊡ sum of M and N peaks
- ⊙—⊙ total

The broken curve is the extension of the low dose trapped fraction (see Figure 10).

As peak *F* approaches its maximum amplitude, an increasing number of additional peaks appear at still higher temperatures as can be seen in Figure 8. First a group of probably 3 peaks, which we have designated "*M*", appear in the temperature band 1000 K to 1300 K. Then at still higher doses, still more peaks (labelled "*N*") appear at successively higher temperatures. Figure 11 shows spectra for this high dose range, with the amplitude scales normalized to the incident dose for easier comparison. The peaks in the *N* region are extremely narrow. They could not be fitted by first order desorption transients for any reasonable values of the rate constant ($\leq 10^{16}$ s^{-1}). No attempt at deconvolution of these peaks has been made. At the highest dose (2×10^{14} cm^{-2}) most of the desorption occurs between 1400 K and 1800 K, whereas at 2×10^{13} cm^{-2} peak *F*, at 900 K, dominates the desorption.

Figure 12 shows the continuation of the trapped population vs dose to the high dose region. The sum of the *M* and *N* peak populations was obtained by integrating the parts of the spectra lying above 1000 K. For doses $>6 \times 10^{13}$ cm^{-2}, essentially all of the trapped helium is seen to desorb in the *M* and *N* peaks, and at the highest dose, the trapped fraction has risen to about 7% from the low dose value (broken line) of 2.1%.

Figure 13 summarizes the variation of three important parameters of the trapped helium as a function of dose. The fraction of the incident ions trapped, f_{in}, as mentioned earlier in this section, rises by more than a factor 3 between the lowest dose and the highest. The median temperature, T_m, at which half of the trapped gas is desorbed, shows an even more dramatic increase; from 500 K at low dose to >1700 K at the highest dose. This is a rough indication of how the "average binding energy" of the trapped helium varies. Finally, the number of helium atoms trapped per trap $\bar{i}$ is shown to emphasize the non-saturable nature of the traps. At the highest dose, the traps are occupied by more than 100 helium atoms each and do not appear likely to stop their growth.

4 COMPARISON WITH THEORY

In this Section we will attempt, by comparison with the theory developed in paper I, to justify the following physical model for the helium trapping:

i) The injected helium thermalizes in the crystal and undergoes rapid interstitial diffusion.

ii) A few percent of the diffusing atoms become bound ("trapped") when they encounter xenon

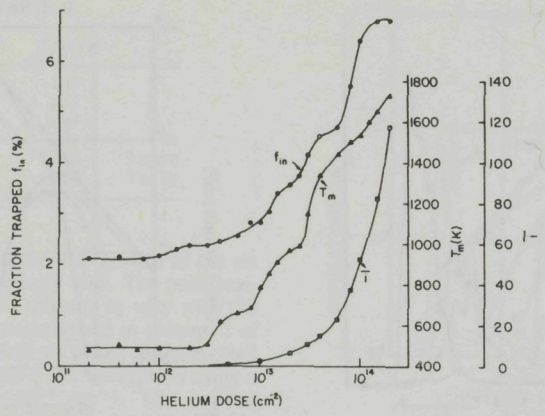

FIGURE 13 The variation of trapped fraction (f_{in}), median desorption temperature (T_m), and the average multiplicity $\bar{i}$ with helium dose. The bombardment parameters and anneal are as in Figure 7.

atoms in the form of "type A" traps, the remainder encounter the surface and escape.

iii) The binding energy of the helium to the trap is determined by the number of helium atoms occupying the trap.

iv) The binding energy of all the helium atoms to the trap is, in general, increased by the addition of the next helium atom.

v) The "size" of the trap increases with increasing number of helium atoms occupying it.

Let the number of helium atoms in the trap be i. During desorption, the helium from traps with $i = 1$ will desorb first (lowest binding energy). For traps with $i = 2$, when one of the two atoms is released, the second will follow in a relatively short time since its binding energy will then be less than when both were present. In this way, the escape of one helium atom from a multiply-filled trap is always the rate limiting step; the remaining helium in the trap is quickly released after its departure. If n_i traps contain i helium atoms each, the amount of helium they contain, the quantity appearing in the desorption peak, is in_i atoms.

To make a quantitative comparison of the data of Figure 10 with the theoretical model of I, we first summarize the experimental parameters in the terms used there:

i) the average of the helium range distribution $\bar{d}_m \approx 70$ Å

ii) the average depth of the traps $\bar{d}_T \approx 250$ Å

iii) the number of implanted xenon atoms per cm^2 left in the crystal, $C_{Xe} = 2.6 \times 10^{11}$ cm^{-2}

iv) the total trapped fraction of the helium at low dose $f_{in} = 2.1 \times 10^{-2}$.

Figure 1 shows that, while most of the xenon is beyond the average helium range, there is a substantial overlap of the two distributions. Nevertheless we first assume that all of the traps lie beyond the helium range. In this case, treated as example III in paper I, the fractions of the traps n_i filled with i helium atoms are given by (see Table I of paper I)

$$n_i = \frac{B^i}{i!} e^{-B} \tag{2}$$

where

$$B = \frac{KJt\bar{d}_m}{DN_0} \tag{3}$$

Note that B is the average number of helium atoms per trap. The curves of n_i vs B are shown in Figure 4 of paper I, where Q represents B. Multiplying each curve by the appropriate values of i gives a set of curves of peak populations in_i vs B. Fitting these curves to the experimental data gives the correspondence shown in Figure 14. Here the data points of Figure 10 have been duplicated, but the joining lines omitted to avoid confusion. The dashed lines are those of in_i vs B, placed at optimum positions along the vertical and horizontal axes.

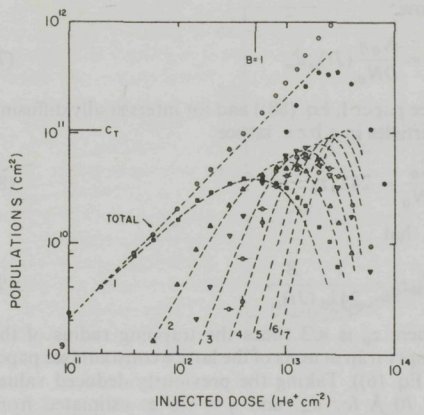

FIGURE 14 A comparison of the data of Figure 10 with a model based on multiple filling of non-saturable traps (paper I). The stationary concentration of the helium is assumed to be constant in the region of the traps and the reaction rate coefficient for trapping K_i to be independent of number of helium atoms occupying the trap. The data point symbols are duplicated from Figure 10. The dashed lines are predicted populations of traps with the indicated multiplicities.

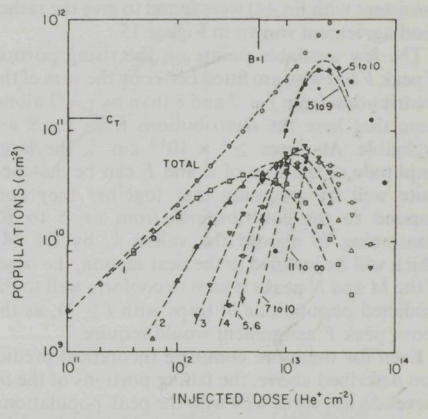

FIGURE 15 Comparison of the data of Figure 10 with a modified multiple filling model in which the depth distributions of the traps and the injected helium are taken into account, and the reaction rate coefficient is allowed to increase with increasing multiplicity. The format is as in Figure 14.

This placement is equivalent to choosing respectively the number of traps C_T (unity on the *Y*-axis of Figure 4 of paper I), and the trap size or reaction rate coefficient as will be discussed in more detail later.

Even with the simple approximations of example III (all the traps beyond the helium range, and the reaction rate coefficient independent of *i*) there is a definite similarity of the form of the curves $i = 1$, 2 and 3 to the populations of the first three desorption peaks *A*, *B* and *C*. Substantial discrepancies can, however, be seen in four areas:

1) the rising portions of the theoretical curves for $i = 2$, 3 and 4 show progressively larger departures from the measured populations of peaks *B*, *C* and *D* if the $i = 1$ curve is fitted to peak *A*.

2) The predicted total trapping, proportional to the dose in this model, lies increasingly far below the experimental points with increasing dose.

3) The theoretical curves decrease more rapidly than the peak populations on the falling side (doses $> 1 \times 10^{13}$ cm^{-2}).

4) The population of peak *F* grossly exceeds that expected of any of the individual values of in_i up to $i = 7$.

A more rigorous comparison with the theory requires that account be taken of the detailed range distributions (see Figure 1) and of the increasing trap size indicated by the non-linear total trapping seen in Figure 10. (See Sections 5 and 6 of paper I). The general Eq. (105) of I was solved numerically for the case of the distributions shown in Figure 1. The values of K_i (see Eq. (102) of paper I) were chosen to optimize the fit of the rising portions (up to their maxima) of the curves for $i = 2$, 3 and 4 to the data points of peaks *B*, *C* and *D*. For

$$k_i = \frac{K_i}{K_0} = 1 + 0.25(1 + i) \qquad (4)$$

($i = 1$, 2, 3) excellent agreement was obtained, as can be seen in Figure 15. The resulting non-linear total trapping was then also found to be in good agreement with the data. It should be noted that the k_i choices were not highly critical, values 10% higher or lower giving almost equally good fits.

No choice of k_4 could be found which would cause the $i = 5$ curve to agree with the rise of peak *E*, particularly its crossing of peak *D* at a dose well below the *D*-peak maximum. If, however, peak *E* was assumed to correspond to the *sum* of $i = 5$ and $i = 6$, then values of $k_4 = 2.25$ and $k_5 = 2.5$,

consistent with Eq. (4) were found to give the rather good agreement shown in Figure 15.

The few available points on the rising portion of peak F likewise are fitted better by the sum of the contribution from $i = 7$ and 8 than by $i = 7$ alone. Note that here the contributions from $i \geq 9$ are negligible. At doses $\geq 1 \times 10^{13}$ cm^{-2}, the large amplitude of the sum of E and F can be matched quite well by assuming that together they correspond to the contributions from $i = 5$ to 10. Continuing to choose the values k_i by Eq. (4), which will be justified in the next section, the onset of the M and N peaks is seen to conform well to the predicted populations of traps with $i \geq 11$, as the above peak F assignment would require.

Even for the more complete theoretical prediction described above, the falling portions of the in_i curves do not agree well with the peak populations. The remaining discrepancies could be caused by the following experimental inadequacy: A small fraction of the traps may be in a zone near the edge of the bombarded area where the helium current density is lower. For these traps, the peaks would reach their maximum amplitude at proportionally higher injected helium doses, and have the effect of making the peak populations decrease more slowly. For example, the discrepancy between the curve for $i = 1$ and the peak A population at a dose of 3×10^{13} cm^{-2} could be accounted for by $\sim 5\%$ of the traps being in a region where the helium current density was 10% of its average value.

We believe that the correspondence between the theoretical curves of Figure 15 and the peak populations firmly justifies the model proposed at the start of this section. The choice of the vertical position of the theoretical curves on Figure 15 corresponds to the choice of $C_T = 1.3 \times 10^{11}$ cm^{-2} for the number of traps. The value found from the simpler model (Figure 14) was 1.05×10^{11} cm^{-2}, showing that the deduced value is quite insensitive to the detailed assumptions regarding the distributions.

The choice of the horizontal position of the theoretical curves corresponds to placing $B = 1$ at an incident dose

$$(Jt)_{in} = 5.6 \times 10^{12} \text{ cm}^{-2} \tag{5}$$

compared with 5.2×10^{12} cm^{-2} found using the simpler model (Figure 14). Thus

$$\frac{B}{(Jt)_{in}} = (5.6 \times 10^{12})^{-1} = 1.78 \times 10^{-13} \text{ cm}^2 \tag{6}$$

Now

$$B = \frac{K_0 \eta}{DN_0} (Jt)_{in} \bar{d}_m \tag{7}$$

(see paper I, Eq. (88)) and for interstitially diffusing particles in a b.c.c. lattice,

$$\frac{K_0}{DN_0} = 24 \lambda_0 z_0 \tag{8}$$

so that

$$\eta \bar{d}_m z_0 = \frac{1}{24 \lambda_0} \frac{B}{(Jt)_{in}} \tag{9}$$

where z_0 is $\pi/3$ times the trapping radius of the empty trap in units of the lattice constant (see paper I, Eq. (6)). Taking the previously deduced values of 70 Å for d_m, and $\eta = 0.6$ as estimated from collision computations[12] Eq. (8) yields $z_0 = 1.1$. Since the lattice constant of tungsten is 3.17 Å, this corresponds to a trapping radius of the empty trap $r_0 = 3.3$ Å, slightly smaller than the distance from a lattice site to the third neighbor interstitial position (3.52 Å). This suggests that the trap is approximately of atomic size.

5 THE HIGH DOSE REGION

The variation of the total helium trapping with dose provides an important insight into the nature of the traps when $i \gg 1$, and into the values of $k_i = K_i/K_0$ in this region. The average value of k is given by

$$\bar{k} = \sum_{i=0}^{\infty} k_i n_i. \tag{10}$$

The differential trapping f', where

$$f' = \frac{\Delta(\text{number of He trapped})}{\Delta(\text{number of He}^+ \text{ incident})} \tag{11}$$

is proportional to the average value of K. At low doses, $f'(= f'_0)$ is equal to the trapped fraction f_{in} and is proportional to K_0. Consequently,

$$\bar{k} = \frac{f'}{f'_0} \tag{12}$$

f' was evaluated at various values of the average multiplicity $\bar{i}$ where

$$\bar{i} = \frac{\text{total He trapped}}{\text{number of traps}} \tag{13}$$

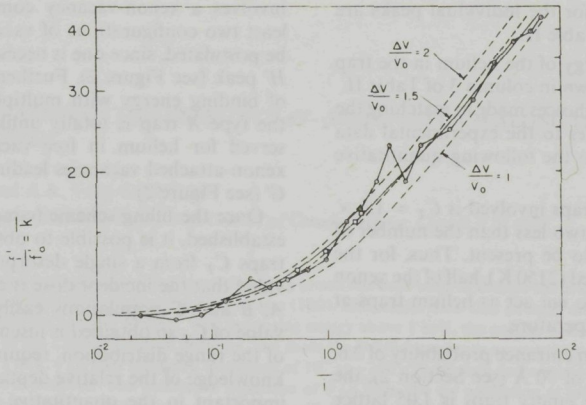

FIGURE 16 Average relative reaction rate coefficient $\bar{k}$ as a function of the average multiplicity $\bar{i}$. Experimental points ○ derived from the total trapping. Average k's (□) according to Eq. (4) and (10) and the measured relative populations. The dashed curves are plots of Eq. (16) for the three indicated values of $\Delta V/V_0$.

from the curve of total helium trapped vs dose, and this gave the points of Figure 16.

The curves of Figure 16 are not inconsistent with the choices of k_1 to k_5 from Eq. (3), as can be shown in the following way. At any given value of i (or of dose), the value of $\bar{k}$ implied by the choices of Eq. (3) was found using Eq. (10) where the fraction n_i of the traps of each multiplicity i was found by dividing the peak population by i. (Note that at low dose, the empty traps n_0 become increasingly important). For doses of 2, 3, 5, 8 and 10×10^{12} cm^{-2}, the resulting values of $\bar{k}$ are plotted as square points in Figure 16, and are seen to be consistent with the curve of $\bar{k}$ generated from the differential trapping (Eq. 12).

It was shown in paper I that K was proportional to the trapping radius of the trap, so that $k = K/K_0 = r/r_0$ where r_0 is the trapping radius of the empty trap. If we assume that each helium atom adds a trapping volume ΔV to the trap, then the average trapping volume is

$$\bar{V} = V_0 + \Delta V \bar{i} \tag{14}$$

Thus

$$\frac{\bar{V}}{V_0} = 1 + \frac{\Delta V}{V_0}\bar{i} \tag{15}$$

and if the traps are assumed to be spherical

$$\bar{k} = \frac{\bar{r}}{r_0} = \overline{\left(\frac{V}{V_0}\right)^{1/3}} \approx \left(1 + \frac{\Delta V}{V_0}\bar{i}\right)^{1/3} \tag{16}$$

where $\bar{r}$ is the average trapping radius and $V_0 = \frac{4}{3}\pi r_0^3$. The broken lines in Figure 16 are curves of Eq. (16) for $\Delta V/V_0 = 1$, 1.5 and 2. They show that agreement with the experimentally deduced values of $\bar{k}$ is obtained for $\Delta V/V_0 \approx 1.5$. We may thus conclude that every arriving helium atom increases the trapping volume by 1.5 V_0 (± 0.5 V_0).

When $\bar{i}$ is 50, the average trapping radius is 4 r_0, or 13 Å. Using the helium covalent radius of 0.93 Å, and assuming close packing, the fifty helium atoms would occupy a sphere of radius 3.8 Å, distinctly smaller than the trapping radius. We conclude that either the helium atoms are not close-packed in the trap or the strain field of the trap extends well beyond the occupied volume.

6 SUMMARY AND CONCLUSIONS

The fact that the model developed in paper I is able to describe the main features of the data of Figure 10 allows the following conclusions:

1) There is only one kind of trap to which the helium is being bound.

2) The trapping radius of the trap is observed to grow monotonically with i, the number of helium atoms it contains, up to at least $i = 100$.

3) The peaks A to F in the thermal desorption spectra correspond to the family of reactions,

$$He_i Xe_A \rightarrow Xe_A + iHe$$

where the values of i for the individual peaks are given in column 4 of Table II.

4) The binding energy of the helium in the trap increases with i as shown in column 3 of Table II.

The two parameter choices made in matching the theoretical filling curves to the experimental data (see Figure 15) lead to the following quantitative conclusions:

5) The number of traps involved is $C_T = 1.3 \times 10^{11}$ cm^{-2} a factor of two less than the number of xenon atoms known to be present. Thus, for the anneal temperature used (2150 K), half of the xenon atoms in the crystal do *not* act as helium traps at the bombardment temperature.

6) With a helium ion entrance probability of 0.6, and an average range of 70 Å (see Section 2), the trapping radius of the empty traps is 1.05 lattice constants or $r_0 = 3.3$ Å. This value is consistent with the trap occupying a single lattice site, and the helium atom being trapped when it arrives at the second-nearest interstitial position to this site.

The trapping radii for $i = 1$ to 4, normalized to that of the empty trap (r_0) are $r_1 = 1.5$, $r_2 = 1.75$, $r_3 = 2.0$, $r_4 = 2.25$. For large values of i, the trapping volume increases by about 1.5 times the empty trapping volume for each helium atom added to the trap. The trapping radius when 50 helium atoms occupy the trap is deduced to be $r = 13$ Å whereas at close-packing, the 50 atoms would occupy a sphere with $r = 3.8$ Å.

The actual atomic configuration of the empty "type A" trap is still an open question. The trapping radius suggests that it occupies one lattice site, and annealing shows it to be the high-temperature equilibrium state of xenon in tungsten. It would seem natural to suggest that it is simply a substitutional atom, as was done for annealed krypton in tungsten in an earlier paper.[4] However, for anneal temperatures up to 2150 K, it appears that at least half of the xenon in the crystal does not trap helium at all. If the type A trap is a substitutional atom, what is the configuration of this "invisible" xenon?

It may be significant that for $T_A \geq 2200$ K, where most of the xenon is in the type A state, thermal vacancies are plentiful. If the type A trap involves a xenon-vacancy complex, however, at least two configurations of vacancy binding must be postulated, since one is necessary to explain the H' peak (see Figure 2). Furthermore, the increase of binding energy with multiplicity observed for the type A trap is totally unlike the binding observed for helium in free vacancies,[1] or in the xenon-attached vacancies leading to peaks H' and G' (see Figure 2).

Once the filling scheme (conclusion 3) is firmly established, it is possible to obtain the number of traps C_T from a single desorption spectrum provided that the incident dose is chosen to make the A, B and C populations easily measurable. The value of C_T so obtained is insensitive to the details of the range distribution, requiring only a general knowledge of the relative depth d_m and d_T. This is important in the quantitative application of the thermal desorption technique.

ACKNOWLEDGEMENT

One of us (AAvG) would like to thank the Canada Council for a scholarship.

REFERENCES

1. E. V. Kornelsen, *Rad. Eff.*, **13**, 227 (1972).
2. L. M. Caspers, A. van Veen, A. A. van Gorkum, A. van den Beukel, and C. M. van Baal, *Phys. Stat. Sol.*, **A37**, 371 (1976).
3. E. V. Kornelsen and D. E. Edwards, Jr., *Application of Ion Beams to Metals*, p. 521, eds. S. T. Picraux, E. P. EerNisse and F. L. Vook, Plenum Press (1974).
4. A. van Veen, L. M. Caspers, E. V. Kornelsen, R. Fastenau, A. A. van Gorkum, and A. Warnaar, *Phys. Stat. Sol.*, **A40**, 235 (1977).
5. E. V. Kornelsen and D. L. Blair, *J.V.S.T.*, **14**, 1299 (1977).
6. E. V. Kornelsen, *Can. J. Phys.*, **48**, 2812 (1970).
7. E. V. Kornelsen and A. A. van Gorkum. To be published(ch. 3)
8. P. A. Redhead, *Vacuum*, **12**, 203 (1962).
9. O. S. Oen and M. T. Robinson, *Int. Phys. Conf.* Series No. 28, 329 (1976).
10. H. E. Schiøtt. *Rad. Eff.*, **6**, 107 (1970).
11. E. V. Kornelsen, F. Brown, J. A. Davies, B. Domeij, and G. R. Piercy, *Phys. Rev. A*, **136**, 849 (1964).
12. O. S. Oen and M. T. Robinson, *Nuclear Instrum. and Methods*, **132**, 647 (1976).
13. M. Abramowitz, I. A. Stegun, *Handbook of Mathematical Functions*, Dover Publications, New York, 1970.
14. R. W. Balluffi, *J. Nucl. Mat.*, **69, 70**, 240 (1978).

Nuclear Instruments and Methods 170 (1980) 161–170

ENHANCED PENETRATION OF LOW ENERGY (25 eV–5000 eV) HELIUM ALONG THE ⟨100⟩ CHANNEL IN TUNGSTEN

E.V. KORNELSEN and A.A. VAN GORKUM

Division of Electrical Engineering, National Resarch Council of Canada, Ottawa, Canada K1A OR8

The trapping of injected helium at annealed xenon impurity atoms has been used to deduce the average penetration of helium ions into tungsten as a function of crystallographic angle near ⟨100⟩. The results show that strongly enhanced penetration occurs along the ⟨100⟩ axis for all ion energies ≥50 eV. With increasing energy above 1 keV, the angular half-widths $\psi_{1/2}$ of the penetration peaks approach 0.8 of the Lindhard critical angle ψ_2, and show the $E^{-1/4}$ dependence expected from channeling theory. With decreasing energy below 1 keV, $\psi_{1/2}$ goes through a maximum of 10° at ~250 eV and then decreases to 8° at 50 eV. At 25 eV, no penetration enhancement is observed. The qualitative departure of $\psi_{1/2}$ from the ψ_2 prediction at low energy is probably associated with the change from channeling primarily via collisions with isolated strings to "proper" channeling in which the particles are confined to individual lattice channels. The ratio of the channeled-to-random values of $\eta\bar{d}_m$ (the product of the diffusion qualification factor and the average penetration) is 5–6 in the region 250–1000 eV and decreases to ~4.5 at 5000 eV. Below 250 eV this ratio falls rapidly as the fraction of the ions channeled decreases and approaches 1 at 25 eV. Comparison of the random values of $\eta\bar{d}_m$ with computations of average penetration and reflection coefficient [18,20] suggests that the apparent radius of the xenon impurity trap is ~3 Å.

1. Introduction

The measurement of directional effects in the penetration of very low energy ions (≤1 keV) into crystals presents some difficulties. Backscattered particles (except for the alkali metals) are primarily neutral and therefore hard to detect. Depth profile measurements require extremely high resolution since total penetrations are typically ≤50 Å, and for the same reason well characterized surfaces free of impurities are essential. Recently depth distributions in this energy range have been measured with single atomic plane resolution using an atom probe FIM technique [1]. However, since characteristic angles are expected to be large, fairly wide ranges of incident angle (±30°) must often be used, and the relationship between the measured distribution and the penetration distribution then becomes uncertain.

At energies between 1 keV and 100 keV, a variety of methods have been used to measure critical channeling angles. These include transmission through thin foils [2,3], backscattering [4–8], induced conductivity [7] and sputtering [9,10]. Although not all directly concerned with penetration, they shed light on the influence of the crystal lattice order on the trajectories of the incident ions.

During studies of the attachment of injected helium to impurity traps in W by means of thermal desorption [11,12], it was found that under certain experimental conditions, relative values of the average helium penetration could be obtained with reasonable accuracy. The basis of the measurement is that after coming to rest in the crystal, injected helium ions (now atoms) undergo random thermal diffusion as interstitials. Their chance of encountering traps situated at large depth (i.e. greater than their own penetration) is then directly proportional to the depth at which the diffusive motion begins.

Making use of this effect, we present in this paper measurements of the variation of average helium penetration with crystallographic angle near the ⟨100⟩ axis normal to a (100) W surface for He^+ energies 25–5000 eV.

2. Theoretical basis

In an earlier paper [11], referred to hereafter as I, a general theory was developed to describe the attachment of mobile particles (MPs) injected into a solid to non-saturable traps which they encounter by random diffusion. For the special conditions that

a) the traps are at an average depth at least as large as the MP injection depth, and

b) the number of traps per cm^2 C_T is low enough that the fraction f of MPs trapped is proportional to C_T, it was shown there [cf. eq. (88) of I] that

$$\eta \bar{d}_m z_0 = \frac{N_0 \lambda_0^2}{6} \frac{B}{(Jt)_{in}}, \quad (1)$$

or, using eq. (5) of I,

$$\eta \bar{d}_m r_0 = \frac{1}{4\pi} \frac{B}{(Jt)_{in}},$$

where

$\bar{d}_m$ = average penetration depth of MPs (cm),
η = diffusion qualification factor (i.e. the probability of an incident MP qualifying for random diffusion),
B = trap sampling density of the MPs (see discussion below),
N_0 = concentration of lattice atoms (cm^{-3}),
λ_0 = jump distance of the MPs (cm),
$(Jt)_{in}$ = incident dose of MPs (cm^{-2}),
r_0 = radius of the ideal spherical sink equivalent to the trap (cm),
z_0 = a geometrical "trap size" factor for the empty traps = $r_0(\frac{2}{3}\pi N_0 \lambda_0^2)$.

For a specific kind of trap and MP in a particular substance z_0, N_0 and λ_0 are all constants. The product $\eta \bar{d}_m$ is then directly proportional to the ratio $B/(Jt)_{in}$.

The nature of B can be understood in the following way: if the trap size were to stay constant at its initial value (z_0), B would be the average number $\bar{i}$ of trapped MPs per trap and BC_T the total trapped. B is in fact simply related to the average number of times Q that an interstitial site in the unperturbed lattice (i.e. far from any trap) is visited by an MP. In particular it can be shown that

$$B = \alpha z_0 Q, \quad (2)$$

where α is the number of interstitial sites per lattice atom. For a bcc lattice, $\alpha = 3$. In practice, the size of the traps may increase when they are occupied by one or more MPs. In this case, $\bar{i}$ would increase more rapidly than B, but the "sampling density" relationship defined by eq. (2) would continue to hold.

In a second paper [12] (II hereafter) we showed that the theory gave a good account of the multiple attachment of injected helium to annealed xenon impurity traps in tungsten. It proved possible there to identify each of a number of helium thermal desorption peaks with release from traps "filled" with a specific number i of helium atoms. The theory in fact yielded a "filling plot" most conveniently presented as a logarithmic plot of the product $i \cdot n_i$ as a function of B, where n_i is the fraction of the traps filled with i helium atoms. In the experiments reported here, the same kind of traps were used, and thermal desorption spectra were measured after injecting helium ions at various incident energies and angles (i.e. at various values of $\bar{d}_m$). As expected from the theory, the relative peak populations could be fitted in every case to the same filling plot, fig. 1, provided that the dose $(Jt)_{in}$ was chosen to give $0.2 \leqslant B \leqslant 2$. Using the detailed procedure described in the appendix, the values of B and C_T (the number of traps per cm^2) were determined for each spectrum.

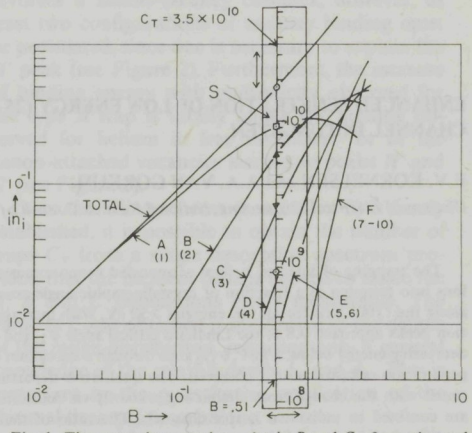

Fig. 1. The procedure used to obtain B and C_T from thermal desorption peak populations is illustrated. The individual peak populations are marked on the logarithmic scale of the transparent strip S. The strip is then moved to optimize the fit between the population points and the filling plot (full lines) and the two quantities read from the scales as indicated.

3. Experimental

To satisfy the criteria of section 2, a separate xenon implant was performed for each helium ion

Table 1
Xenon implant and helium injection parameters. $n_{Xe} = 1 \times 10^{13}$ cm^{-2}, $E_{Xe} = 1500$ eV.

E_{He^+} (eV)	T_A (K)	$\bar{d}_T$ (cm)	n_{He^+} (cm^{-2})	$\bar{d}_T/\bar{d}_{He}$	C_T (cm^{-2})	f_{max}
50	1800	2.8×10^{-7}	1×10^{14}	5.60	8.8×10^{11}	0.0078
100	2000	8.3×10^{-7}	3×10^{13}	4.75	3.4×10^{11}	0.017
250	2210	4.7×10^{-6}	1×10^{13}	7.80	8.5×10^{10}	0.019
1000	2260	6.6×10^{-6}	2×10^{12}	4.25	6.0×10^{10}	0.055
5000	2430	2.5×10^{-5}	5×10^{11}	3.80	2.0×10^{10}	0.066
4000 [a]	random	2.6×10^{-6}	3×10^{12}	0.70	5.7×10^{11}	0.120
4000 [a]	channeled	9.5×10^{-6}	3×10^{12}	0.40	1.15×10^{11}	0.070

[a] No xenon implant. The traps are the vacancies produced by the He^+ bombardment.

energy to be studied. The xenon was introduced by bombarding the crystal surface at normal incidence (⟨100⟩) with 1×10^{13} cm^{-2} 1500 eV Xe^+ ions. An anneal temperature T_A was then chosen sufficient to diffuse the Xe over a depth approximately equal to the expected maximum penetration of the helium ions to be injected. The anneal temperatures used are given in column 2 of table 1. The resulting estimated average depths of the traps, $\bar{d}_T$, based on methods given in II, appear in column 3.

The helium ion dose was chosen to give a maximum B value of about 1.5, which was convenient for the analysis procedure described in the appendix. The choices for the various He^+ energies are given in column 4 of table 1. Helium ions were injected at this dose at a series of incident angles θ lying in a (310) plane (19° from a (100) plane). It was hoped that this azimuth would give reasonable "random" values at large θ. For $\theta > 10°$, a $(\cos\theta)^{-1}$ correction was made to the incident number of ions to ensure that the number per unit area $(Jt)_{in}$ remained constant.

After each injection, the trapped helium was thermally desorbed by heating the crystal at 40 Ks^{-1}. The maximum temperature during these desorption cycles was kept below $0.85T_A$ to avoid any disturbance of the trap distribution. (This was verified by repeating an early value of θ at the end of the experiment.)

One series of experiments was done with 4 keV He^+ ions but with no implanted Xe. In this case the trapping occurred at the lattice vacancies produced by the ions themselves, and the thermal desorption spectra were analyzed using an appropriate vacancy filling plot.

4. Results

A set of helium desorption spectra at a series of incident angles θ for 1000 eV incident ions is shown in fig. 2. The peaks labelled A–F are precisely those reported in II. Note that the total area under the desorption curve, which is roughly proportional to B (see fig. 1) and therefore to the average penetration depth, decreases dramatically with increasing θ. Analysis of such spectra gave a constant value for C_T to within ±10% independent of θ, providing a verification that the method of analysis is correct. The values of B found for 1000 eV ions at various θ are shown in fig. 3 (right hand ordinate). A strong enhancement in B for θ near zero (⟨100⟩ axis) is clearly evident. In drawing the smooth curve through the points, it was assumed that the peak was symmetrical about $\theta = 0$. Evaluating the constants of eq. (1) for tungsten, and using the incident dose $(Jt)_{in} = 2 \times 10^{12}$ cm^{-2} gave the scale of $\eta\bar{d}_m z_0$ shown on the left hand ordinate of fig. 3.

Similar series of helium injections at energies 50 eV, 100 eV, 250 eV and 5000 eV under the conditions specified in table 1 gave the penetration peaks shown in figs. 4a–d. Although an easily measurable fraction of 25 eV ions were trapped ($f \approx 5 \times 10^{-4}$), no significant variation of the trapping (i.e. of B) with θ was observed at this energy. It should be stressed that changes in the penetration probability η cannot be separated from changes in $\bar{d}_m$ using the present data. It is not thought likely that η is strongly dependent on θ, but a minor increase near $\theta = 0$ would not be surprising. The angular half-width at half maximum $\psi_{1/2}$ of the penetration peaks, obtained from

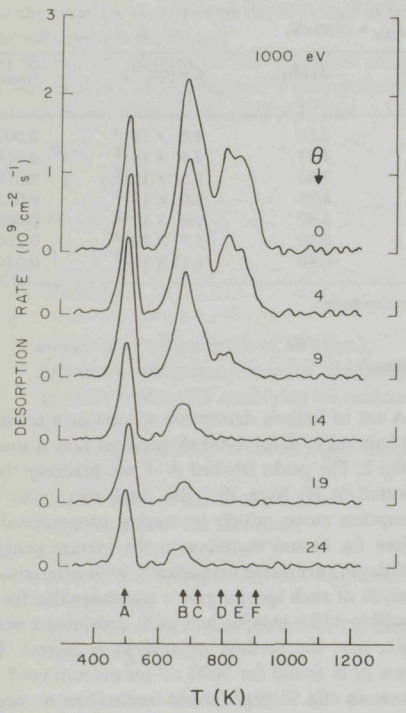

Fig. 2. Thermal desorption spectra following injection of 2×10^{12} cm^{-2} 1000 eV helium ions at various angles θ relative to the ⟨100⟩ crystal normal. The prior xenon implantation conditions are given in table 1.

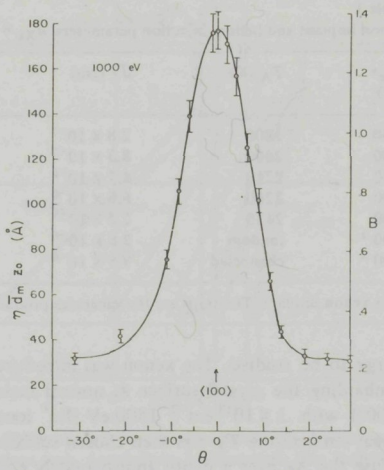

Fig. 3. The variation of B with θ as obtained by the procedure of the appendix from spectra such as those of fig. 2. The error bars indicate the uncertainty of the matching on the horizontal axis of fig. 1. Corresponding depth parameters $\eta\bar{d}_m z_0$, obtained via eq. (1) are given as the left ordinate.

figs. 3 and 4, is shown as a function of the incident energy in fig. 5 (lower panel). The corresponding ratios of the peak to the "random" $\eta\bar{d}_m$ appear in the upper panel of fig. 5.

Fig. 6 summarizes the actual values of $\eta\bar{d}_m z_0$ found for ⟨100⟩ and "random" incidence as a function of ion energy. Data at 500 eV and 2000 eV have been added, although complete peak shapes were not measured at these energies.

The directional effects observed using 4 keV He$^+$ ions alone are somewhat different. Here, the traps to which the helium is bound are the lattice vacancies produced by the helium ions themselves [14]. These vacancies will in general be at an average depth $\bar{d}_v$ less than $\bar{d}_m$, violating the first criterion mentioned in section 2. In this case, however, the observed values of B allow at least an approximate determination of the average trap depth $\bar{d}_v$ (see section 5.3 of I). In addition, any variation in the number of vacancies produced will be observed in the derived values of C_v, again with some uncertainty due to distribution effects. The basic results are shown in fig. 7, where B and C_v are plotted against θ of the 4 keV ions.

5. Discussion

5.1. Penetration depths

Comparison of the present penetration depth results with previous work requires an absolute value for the trap size z_0. Computations by Fastenau et al. [15] suggest that for helium trapped by vacancies in a bcc lattice, $z_0 \approx 1$. We have compared trapping at Xe impurities and at vacancies in our crystal for identical He$^+$ bombardments and found the apparent trap sizes

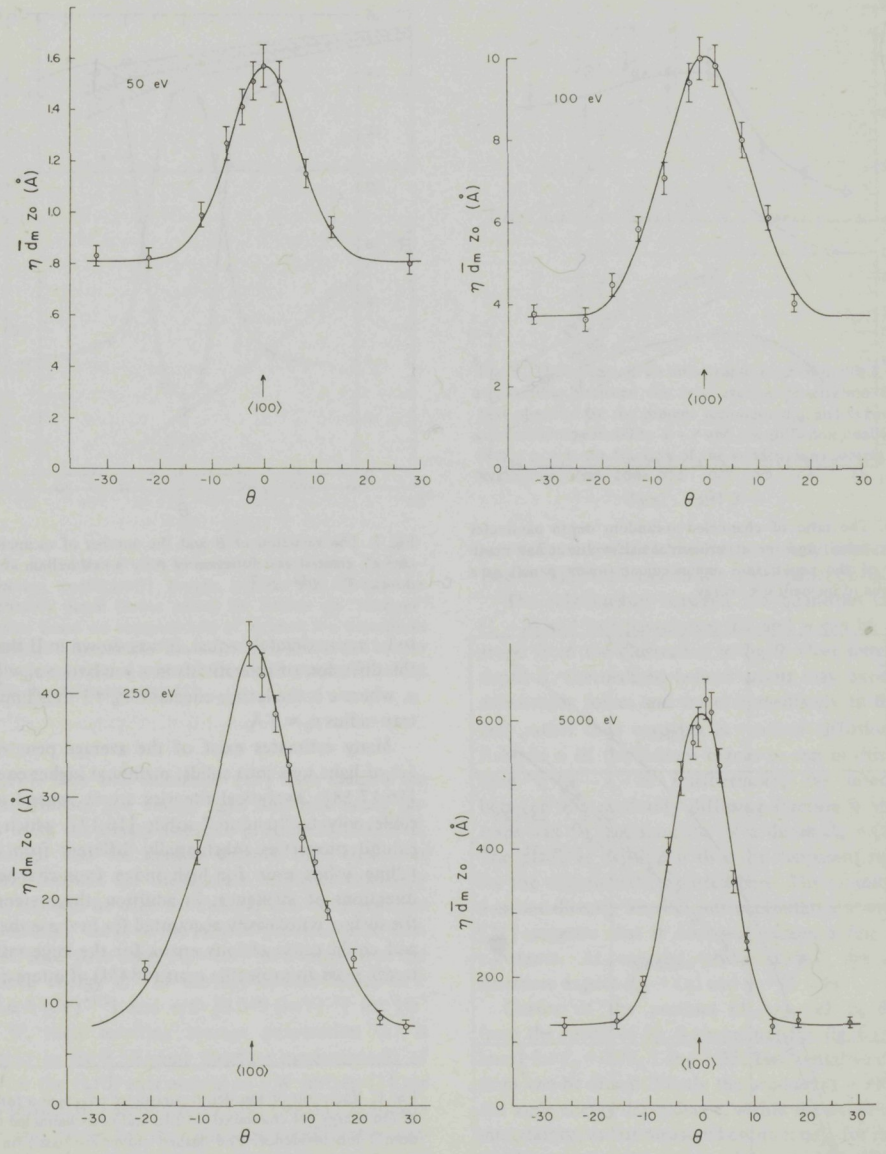

Fig. 4. Depth parameters as a function of incident angle for helium of different energies: (a) 50 eV, (b) 100 eV, (c) 250 eV and (d) 5000 eV. Experimental parameters are summarized in table 1.

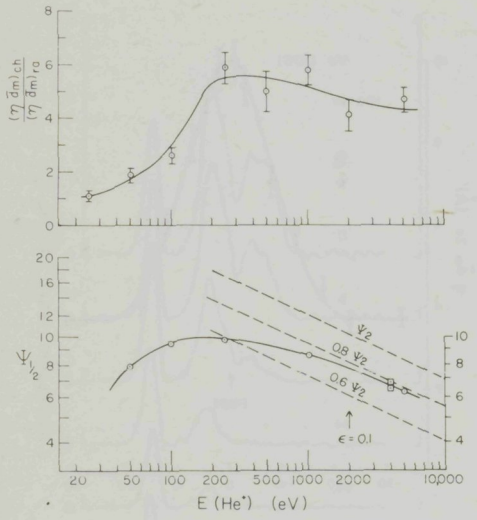

Fig. 5. The ratio of channeled-to-random depth parameter (upper panel) and the experimental half-width at half-maximum of the penetration enhancement (lower panel) as a function of incident ion energy.

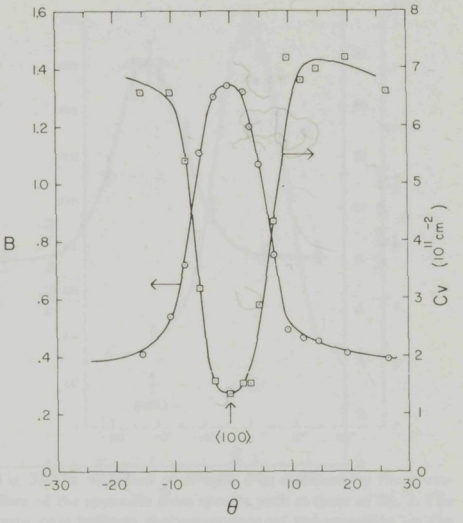

Fig. 7. The variation of B and the number of vacancies per cm^2 C_v created as a function of θ by 4 keV helium ions at a dose of 3×10^{12} cm^{-2}.

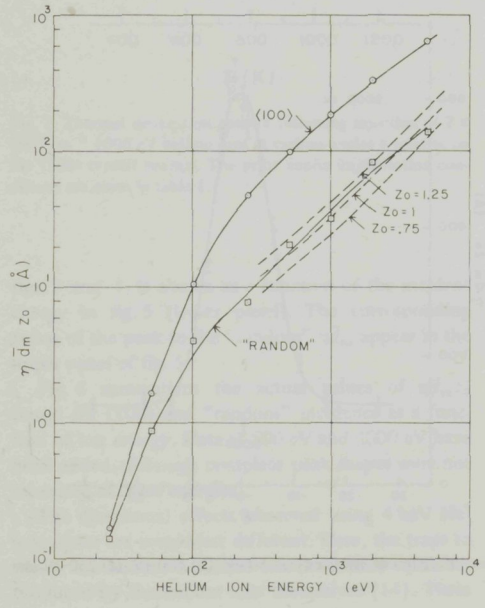

Fig. 6. Variation of the depth parameter $\eta \bar{d}_m z_0$ as a function of ion energy for channeled (⟨100⟩) and non-channeled ("random") ion incidence. The dashed curves are based on computed values [18,20] of the product of the penetrating fraction and the average penetration depth for three assumed values of the trap size factor z_0.

to be approximately equal. It was shown in II that for the diffusion of interstitials in a bcc lattice $z_0 = \frac{1}{3}\pi\, r_0/a$, where a is the lattice constant. $z_0 = 1$ thus implies a trap radius $r_0 \approx 3$ Å.

Many estimates exist of the average penetration $\langle x \rangle$ of light ions into solids, mainly at higher energies [16,17,18]. Analytical theories are in general applicable only to "random" solids [16,17], which may exhibit properties substantially different from crystalline solids even for high index (non-channeling) directions of incidence. In addition, the presence of the surface is not easily accounted for in these theories and could cause serious errors for the large ratio of target mass to projectile mass (184/4) of interest here

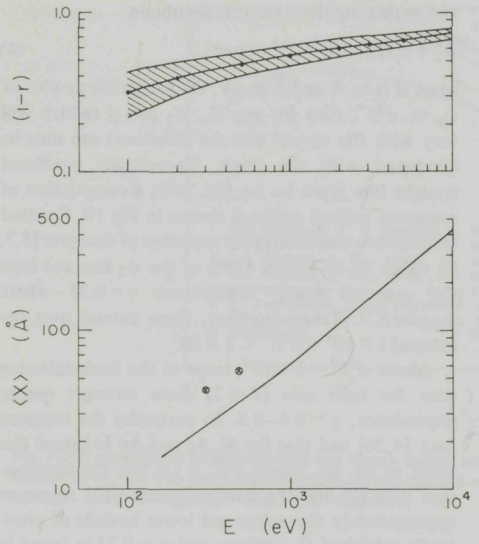

Fig. 8. Estimates of the penetration coefficient [ie. 1 – (reflection coefficient)] (upper panel), and the average penetration depth (lower panel) for helium on "random" tungsten based on computations of incident ion trajectories [18,20] as a function of the ion energy. The circled crosses are absolute measured values of the average penetration along a ⟨110⟩ channel in tungsten [1].

[17,19]. Oen and Robinson [18] have studied the penetration of low energy light ions into heavy targets using the binary collision program MARLOWE. Although also for random targets, their treatment should account for the surface influence relatively well, and will be used for comparison. They generate a "universal" curve of the ratio of penetration to electronic total path range $R_e = cE^{1/2}$ as a function of the reduced energy ϵ. For the appropriate values of c [26.6 Å $(\text{eV})^{-1/2}$] and ϵ/E [0.049 $(\text{keV})^{-1}$] for He^+ on W, their resulting average penetration $\langle x \rangle$ is plotted in fig. 8. Recent absolute measurements of $\langle x \rangle$ for the ⟨110⟩ axis normal to a W surface [1] are also shown. In a second paper [20] Oen and Robinson also give values for the reflection coefficient r computed by the same techniques. Again a universal curve is obtained when plotted against ϵ. For He^+ on heavy targets, their prediction of the fraction $1\text{-}r$ of particles

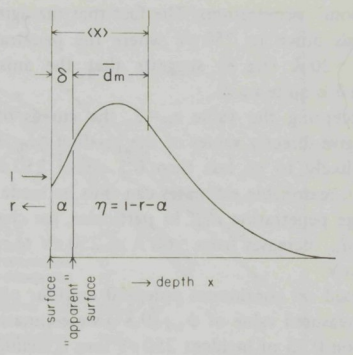

Fig. 9. The effect of an anisotropic zone of depth δ on the relationship between the true average penetration $\langle x \rangle$ and that observed by the present technique $\bar{d}_m$, and between the penetration probability $1 - r$ and the diffusion qualification factor η. α is the fraction of the incident ions coming to rest in the anisotropic zone.

not reflected, which should be closely related to η [see eq. (1)] is plotted in the upper panel of fig. 8.

The relationship between the quantities $\langle x \rangle$ and $(1 - r)$ and our parameters $\bar{d}_m$ and η can be understood from the illustration in fig. 9. Over some small depth δ, thermalized helium atoms may experience anisotropic forces and travel immediately to the surface rather then engaging in random diffusion. If a fraction α of the helium comes to rest in this zone, then $\eta = 1 - r - \alpha$. Furthermore, the interaction between the randomly diffusing fraction η and the traps will be characteristic of a depth $\bar{d}_m = \langle x \rangle - \delta$. The plane at depth δ is thus the "apparent surface" for the experiments reported here. The magnitude of δ is not directly known, but computational evidence [21] suggests that it does not exceed a few lattice constants. At energies where $\langle x \rangle \gg \delta$, we would therefore expect $\bar{d}_m \to \langle x \rangle$ and $\eta \to (1 - r)$.

Curves of the product $(1 - r) \cdot \langle x \rangle \cdot z_0$ derived from the curves of fig. 8 are included in fig. 6 (dashed lines) for $z_0 = 0.75$, 1 and 1.25. Two tentative conclusions can be drawn: Firstly the product $(1 - r)\langle x \rangle$ has the same energy dependence, within the experimental uncertainty, as our measured product $\eta \bar{d}_m$ for random incidence over the energy interval 250–5000 eV. Secondly, the value $z_0 = 1$ gives fairly good quantitative agreement between the computations and our

"random" penetrations. The fact that the agreement extends down to 250 eV where the penetration is only ~20 Å (fig. 8) suggests that the anisotropy depth δ is quite small.

Accepting the value $z_0 = 1$, the curves of fig. 6 then give directly values of the product $\eta\bar{d}_m$. Since η is unlikely to be less than 0.5 above 250 eV (see fig. 8), reasonable estimates can thus be made of the average penetration $\bar{d}_m$. In particular, for channeled ions, $\bar{d}_m$ increases from ~60 Å at 250 eV to ~700 Å at 5 keV.

Based on continuum potential contour plots and the measured value of $\psi_{1/2}$ (9.8°) we estimate that a fraction 0.25 of incident 250 eV ions is channeled. If η is independent of θ, the computed value of 0.5 (see fig. 8) implies that the range of those particles channeled must be ~10 times the random range at this energy.

At the lowest energies, η is expected to become small since $r \to 1$, and this is the most likely cause of the rapid decrease of $\eta\bar{d}_m z_0$ below 100 eV (fig. 6). Conversely, at higher energies (>1 keV) one would expect η to approach 1 for channeled incidence since backscattering then occurs primarily from the first atom in each atomic row. At 1 keV, computations suggest [22] that $r \approx 0.03$, so that $\eta \approx 0.97$, and should be even closer to 1 at higher energies.

5.2. Critical angles

The critical angle ψ_2 for channeling at low energies has been derived by Lindhard [23] [see eq. (3) below]. To compare our data with others, we follow the normalization procedure suggested in refs. 7 and 8. The critical angle at low energies according to Lindhard's theory is

$$\psi_2 = \left[\frac{(Ca)^2}{d^3}\,\frac{Z_1 Z_2 e}{4\pi\epsilon_0 E}\right]^{1/2} \text{rad}\,, \tag{3}$$

where

$C = \sqrt{3}$,

$a = 0.8853 a_0 (Z_1^{2/3} + Z_2^{2/3})^{-1/2}$,

a_0 = Bohr radius,

d = interatom distance along the row.

Defining

$$E^* = E\left(\frac{Z_1^{2/3} + Z_2^{2/3}}{Z_1 Z_2}\right),$$

and evaluating the constants we obtain

$$\psi_2 = 100.5[d^3 E^*]^{-1/4} \text{ degrees}\,, \tag{4}$$

when d is in Å and E in eV. On a logarithmic plot of ψ_2 vs. d^3E^*, data for any Z_1, Z_2 and d (which will vary with the crystal and the direction) can thus be compared with the single theoretically predicted straight line given be eq. (4). Such a compilation of measured critical angles is shown in fig. 10. Omitted (to improve readability) are a number of data sets [5,7, 8] which all lie within ±15% of the ψ_2 line and have the expected energy dependence $\gamma = 0.25$, where $\psi_{1/2} = kE^{-\gamma}$. Taken together, these extend over the interval $1 \times 10^4 < d^3E^* < 2 \times 10^6$.

Above $d^3E^* = 1 \times 10^5$, some of the backscattering data for light ions ($Z \leqslant 2$) show stronger energy dependence, $\gamma \sim 0.4$–0.5. In particular the tungsten data [4,24] and that for Al, Ag and Au [6] show this trend in fig. 10. Below $d^3E^* = 1 \times 10^5$, the transmission data [2] and the sputtering data [10] represent approximately the upper and lower bounds of previously published $\psi_{1/2}$ values, and $\gamma \approx 0.25$ is found in nearly all cases.

The data of this paper are so indicated, and the following features are notable:

a) At $d^3E^* > 4 \times 10^3$, the energy dependence approaches $E^{-1/4}$ at the value $\psi_{1/2} = 0.8\psi_2$, lower than any of the previous data. The low values could be due to the fact that our $\psi_{1/2}$ is related to an integral effect over the whole ion path. Backscattering measurements at $E > 100$ keV show that this has the effect of decreasing the measured $\psi_{1/2}$ [24]. Grahmann et al. [8], however, did not observe such a decrease in Si at energies 10–60 keV.

b) The range of d^3E^* extends about a factor thirty lower than the lowest previous measurements.

c) Unlike any previous data, $\psi_{1/2}$ is observed to go through a maximum and to decrease at the lowest energies.

The theoretical basis for the ψ_2 expression [eq. (3)] is the concept of the continuum potential of a single atomic string. At low energies, however, the critical approach distance of a particle to the string, ρ_{crit}, at which channeling breaks down becomes comparable to the channel radius r_{ch} (1/2 of the distance between strings). When $\rho_{crit} \approx \frac{1}{2} r_{ch}$, the continuum potential is mainly determined by the set of strings (usually 4) surrounding an individual lattice channel.

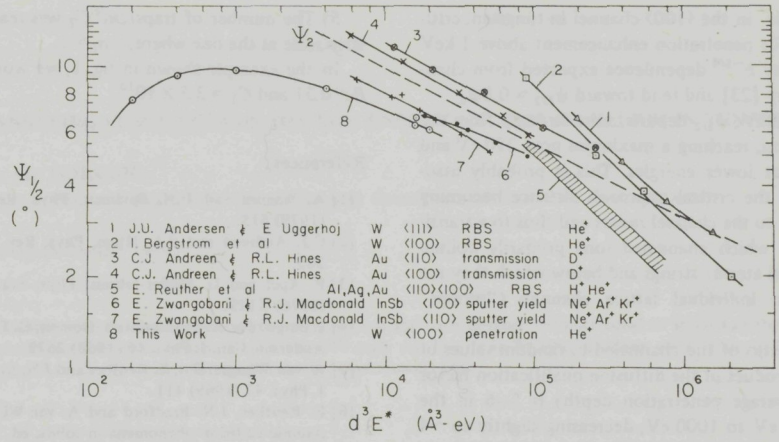

Fig. 10. A compilation of experimental low energy critical angles for channeling as a function of the normalized parameter d^3E^* defined in eq. (4). The experimental details are summarized on the figure. The references are 1 – ref. 23; 2 – ref. 4; 3 – ref. 2; 4 – ref. 2; 5 – ref. 6; 6 – ref. 10; 7 – ref. 10; 8 – this work.

At a still lower energy, E_{min}, where $\rho_{crit} = r_{ch}$, channeling is expected to cease altogether, and $\psi_{1/2}$ to decrease to zero. There must therefore be a transition region in energy from the ψ_2 region where $\psi_{1/2} \sim E^{-1/4}$ to one in which $\psi_{1/2}$ decreases with decreasing energy and finally becomes zero at E_{min} †.

Our measurements establish that for He$^+$ ions in W ⟨100⟩, E_{min} lies between 25 eV and 50 eV. It should be noted that the threshold energy for entry of the ions into the crystal is considerably lower – ~8 eV according to earlier measurements [26]. The transverse energy E_T of an ion of energy E at the critical angle $\psi_{1/2}$ is $E_T = E \sin^2 \psi_{1/2}$. For the present case, E_T = 12.5 eV and 7.4 eV for E = 500 eV and 250 eV respectively. Published two-dimensional continuum potential maps [25] show that at just such values of E_T, $\rho_{crit} \approx \frac{1}{2} r_{ch}$ and below this, the potential contours form closed curves, so that the particles execute "proper" channeling motion confined to a single channel. We may thus identify the energy region 500–250 eV with the transition from the ψ_2 to the proper channeling region mentioned above.

The observed behavior of $\psi_{1/2}$ with energy is thus consistent with the concepts of continuum potential and critical approach distance over the whole energy range from 50 eV up.

Two effects of the channeling of 4 keV He$^+$ ions, both slightly different from the penetration enhancement described above, can be seen in fig. 7. Firstly, the number of vacancies produced C_v decreases by a factor five when channeling occurs demonstrating directly a large decrease in close encounter collisions. Secondly, the average depth of the produced vacancies increases by a factor 3.6, comparable to the increase in $\eta \bar{d}_m$ shown in fig. 6. Striking is the fact that both these effects have $\psi_{1/2}$ values (6.5° and 6.8° respectively) accurately consistent with the penetration enhancement value at the same energy (square points of fig. 5).

6. Conclusions

The main findings of the present work can be summarized as follows:

1) Helium ion trapping studied by thermal desorption has been shown to be a practical method of measuring helium penetration into metals and its crystallographic angle dependence from the penetration threshold to several keV.

† This has been confirmed by computer simulations [27].

2) For He^+ in the ⟨100⟩ channel in tungsten, critical angles for penetration enhancement above 1 keV approach the $E^{-1/4}$ dependence expected from channeling theory [23] and tend toward $\psi_{1/2} \approx 0.8\psi_2$.

Below 1 keV, $\psi_{1/2}$ departs more strongly from the ψ_2 prediction, reaching a maximum near 250 eV and decreasing at lower energies. This is probably associated with the critical approach distance becoming comparable to the channel radius and thus to a transition above which channeled ions primarily collide with isolated atomic strings and below which they are confined to individual lattice channels ("proper" channeling).

4) The ratio of the channeled-to-random values of $\eta\bar{d}_m$ (the product of the diffusion qualification factor and the average penetration depth) is 5–6 in the region 250 eV to 1000 eV, decreasing slightly to ~4 at 5000 eV. Below 250 eV this ratio falls rapidly as the channeled fraction f_c decreases and becomes ~1 near 25 eV where $f_c = 0$.

5) The random value of $\eta\bar{d}_m$ follows computed values of the product $(1-r)\langle x\rangle$ [18,20] fairly well between 500 eV and 5000 eV. The implied trap size factor is $z_0 = 1$ (±0.25) corresponding to a trap radius of 3 Å.

6) By helium trapping and thermal desorption it is also possible to establish both the number and average depth of vacancies produced in crystals by He^+ ions at energies below 10 keV as a function of crystallographic angle.

Appendix

The procedure used to obtain the trap sampling density B and the number of traps per cm^2 C_T from the thermal desorption spectra is as follows:

1) Peak populations were obtained by computer-assisted deconvolution assuming first order kinetics [13].

2) The populations and their sum were plotted on a transparent strip (S in fig. 1) marked with a logarithmic scale matching that of the filling plot.

3) The strip was then overlaid on the filling plot and shifted along the two axes until the fit of the population points to the appropriate lines of the filling plot was optimized.

4) The value of B was then read directly from the filling plot abcissa at the position of the strip scale.

5) The number of traps/cm^2 C_T was read from the strip scale at the line where $i \cdot n_i = 1$.

In the example shown in fig. 1, we would deduce $B = 0.51$ and $C_T = 3.5 \times 10^{10}$.

References

[1] A. Wagner and D.N. Seidman, Phys. Rev. Lett. 42 (1979) 515.
[2] C.J. Andreen and R.L. Hines, Phys. Rev. 159 (1967) 285.
[3] P. Apel and U. Müller-Jahreis, Phys. Stat. Sol. A 33 (1976) K129.
[4] I. Bergström, K. Bjorkqvist, B. Domeij, G. Fladda and S. Andersen, Can. J. Phys. 46 (1968) 2679.
[5] A. van Wijngaarden, E. Reuther and J.N. Bradford, Can. J. Phys. 47 (1969) 411.
[6] E. Reuther, J.N. Bradford and A. van Wijngaarden, in Atomic collision phenomena in solids, ed. D.W. Palmer et al. (North Holland, Amsterdam, 1970) p. 278.
[7] I.A. Abroyan, V.A. Koryukin, N.N. Ushakov and L.A. Tsekhnovicher, Sov. Phys. Sol. Stat. 11 (1970) 2745.
[8] H. Grahmann, A. Feuerstein and S. Kalbitzer, Rad. Effects 29 (1976) 117.
[9] D. Onderdelinden, Can. J. Phys. 46 (1968) 739.
[10] E. Zwangobani and R.J. Macdonald, Rad. Effects 20 (1973) 81.
[11] A.A. van Gorkum and E.V. Kornelsen, Rad. Effects, 42 (1979) 93. (ch.5)
[12] E.V. Kornelsen and A.A. van Gorkum, Rad. Effects, 42 (1979) 113. (ch.6)
[13] E.V. Kornelsen and D. O'Hara, J. Vac. Sci. Technol. 11 (1974) 885.
[14] E.V. Kornelsen, Can. J. Phys. 48 (1970) 2812.
[15] R.H.J. Fasteneau, A. van Veen, P. Penning and L.M. Caspers, Phys. Stat. Sol. A 47 (1978) 577.
[16] H.E. Schiøtt, Rad. Effects 6 (1970) 107.
[17] K.B. Winterbon, Rad. Effects 13 (1972) 215.
[18] O.S. Oen and M.T. Robinson, Conference Series No. 28 (Inst. of Physics, London, 1976) p. 329.
[19] P. Sigmund, Can. J. Phys. 46 (1968) 731.
[20] O.S. Oen and M.T. Robinson, Nucl. Instr. and Meth. 132 (1976) 647.
[21] J.R. Beeler, Jr., in Proc. Int. Conf. on Vacancies and interstials in metals (preprints of Conf. papers) KFA, Julich (1968) p. 598.
[22] M. Pryde, A.G. Smith and G. Carter in Atomic collision phenomena in solids, ed. D.W. Palmer et al. (North Holland, Amsterdam, 1970) p. 573.
[23] J. Lindhard, Mat. Fys. Med. Dan. Vid. Selsk. 34, No. 14 (1965).
[24] J.U. Andersen and E. Uggerhøj, Can. J. Phys. 46 (1968) 517.
[25] D. van Vliet, Rad. Effects 10 (1971) 137.
[26] E.V. Kornelsen, Can. J. Phys. 48 (1970) 2812.
[27] A.A. van Gorkum, Phys. Lett. (in press). (ch.8)

CHANNELING COMPUTATIONS FOR LOW ENERGY (25–2500 eV) HELIUM IN TUNGSTEN

A.A. van GORKUM
Division of Electrical Engineering, National Research Council of Canada, Ottawa, Canada K1A 0R8

Received 18 October 1979

Calculations show that at energies where the critical approach distance becomes equal to about half the channel radius, the channeling half angle deviates from Lindhard's angle ψ_2. For He in W ⟨100⟩ it reaches a maximum at 200 eV and drops to 0 at 35 eV, in accordance with recent measurements [4].

Channeling is a field in which computer simulations have played a very important role in the evolution of theoretical concepts [1]. From the basic theoretical paper by Lindhard [2] follows that there is a critical angle ψ_c between an incoming particle and a row of atoms below which the particle undergoes channeling. The interaction between the particle and the row can be described by a so-called continuum potential, directly related to the impulse approximation to the scattering of the particle from the string of atoms. Using this approach, Lindhard derived that ψ_c is proportional to $E^{-1/2}$ in the so-called high energy range where the distance of closest approach ρ_{min} to the string is of the order of or less than the screening radius a [2]; in the low energy range, ψ_c is proportional to $E^{-1/4}$ and ρ_{min} is greater than a. Many experiments have confirmed this energy dependence in both energy regions.

In this letter, calculations are reported of the channeling behavior at extremely low energies where ρ_{min} is comparable to the channel radius. In this case the injected particles interact with more than one atom simultaneously and the impulse approximation is no longer valid. It will be shown however that the concept of a continuum potential is still useful in this energy range. The calculations were prompted by recent work by means of the helium thermal desorption (HTD) technique [3] on directional effects in tungsten at energies as low as 25 eV [4]. Until this work [4], no observations of channeling at energies below 5 keV for He in W had been made. Using HTD, variation with angle of the average range of the injected helium atoms was measured for incident energies from 5 keV down to 25 eV, at which no directional effects were observed [‡1]. The half angle ($\psi_{1/2}$ thus measured approaches the predicted $E^{-1/4}$ behavior above 1 keV. Below 1 keV however, $\psi_{1/2}$ starts to depart from the $E^{-1/4}$ dependence, reaching a maximum at 250 eV and decreasing below this energy (see fig. 2).

Since this effect is not predicted by Lindhard's

[‡1] The threshold energy for penetration was measured to be 8 ± 1 eV.

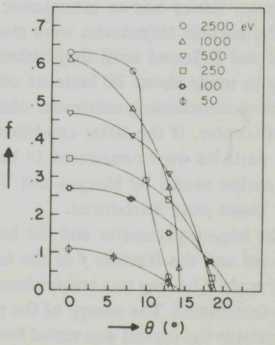

Fig. 1. Channeled fraction f as a function of angle of incidence θ for different incident energies.

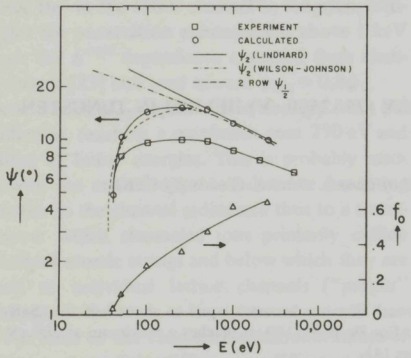

Fig. 2. Experimental half angles (□) [4], half angles $\psi_{1/2}$ based on present calculations (○) (fig. 1), Lindhard's angle ψ_2 (—), critical angle based on Wilson–Johnson potential (–·–·–), critical angle based on the W–J potential for 2 rows (– – –) and the channeled fraction f_0 for normal incidence as a function of energy.

theory, computer calculations were done to simulate the experimental conditions. Earlier Morgan and Van Vliet [5–7] did computer simulations at low energies using a two-dimensional rigid lattice. The lowest energy used was 1 keV since the applied binary collision model in the momentum approximation loses its validity below about 1 keV for He in W.

In our model simultaneous interactions with all neighbouring atoms were considered. The interaction potential was taken from Wilson and Johnson [8]. The 2D square lattice had an interatomic distance of 3.16 Å. The particle trajectories were started outside the crystal and followed until they either led to dechanneling or made about 10 bounces off the two strings with non-increasing maximum distance from the channel centre. If the latter condition was fulfilled, the particles were considered to be channeled. As in the earlier model by Morgan and Van Vliet [5], no energy losses were introduced.

Both the impact parameter and the incident angle θ were varied and the fraction f of the impact parameters at an angle θ leading to a stable channeling trajectory were determined. The energy of the particles starting from outside the crystal was varied from 25 eV to 2500 eV. The fraction f as a function of θ for different energies is plotted in fig. 1. First of all, it is noted that f in the channel direction (f_0) decreases sharply for energies below 1000 eV. f_0 is plotted in fig. 2, together with the angle $\psi_{1/2}$ at which the channeled fraction is reduced to $\frac{1}{2} f_0$. It shows that $\psi_{1/2}$ reaches a maximum at about 200 eV and then drops until it reaches 0 at about 35 eV, in qualitative agreement with the measured data.

At energies above 1 keV, the half angle is within 3% of the Lindhard critical angle ψ_2, although the Lindhard standard potential in this energy region is not very accurate. If instead of the Lindhard potential, the continuum potential derived from the helium–tungsten potential [8] is substituted in the expression [2]

$$U(\psi_c d) = E\psi_c^2 , \qquad (1)$$

in which d is the atom spacing along the row, the result as drawn in fig. 2 is found. It shows excellent agreement with the calculated half angles above 1 keV.

In fig. 3, the critical approach distance ρ_{crit} derived from the computer simulations is plotted. ρ_{crit} is seen to approach half the channel radius r_{ch} at about 500 eV. It becomes equal to r_{ch} at $E \approx 35$ eV, below which no channeling occurs. Comparing figs. 3 and 2 one concludes that the departure of $\psi_{1/2}$ from ψ_2 arises when ρ_{crit} becomes equal to about $\frac{1}{2} r_{ch}$. Within the framework of Lindhard' theory, $\rho_{crit} = \psi_c d$, so that the angle ψ_d at which the departure from ψ_2 occurs is equal to about $\frac{1}{2} r_{ch}/d$. For our computer simulations, $r_{ch} = \frac{1}{2} d$ so that $\psi_d \approx 14°$, in accordance with fig. 2.

The energy dependence of ρ_{crit} was fitted with an expression of the form

$$U''(\rho_{crit}) = nE/d^2 , \qquad (2)$$

as suggested by Lindhard for $n = 8$ [2] in the case of a

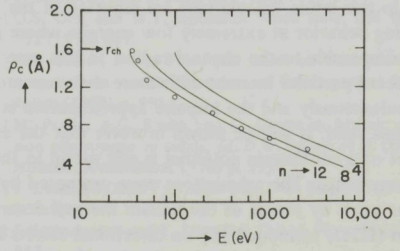

Fig. 3. Critical approach distance ρ_c (⊙) as a function of energy. Full lines are based on form [2], for $n = 12$, 8, 4. r_{ch} is the channel radius.

single string. Using for $U(\rho)$ the two-row continuum potential, with $U(\frac{1}{2}d) = 0$, it is shown in fig. 3 that for energies below 500 eV, $n = 12$ forms a good fit to the computed values of ρ_{crit}. At higher energies the fit tends toward the value $n = 5$, as found by Morgan and van Vliet [5]. Using the ρ_{crit} values obtained from eq. (2), the corresponding critical angles ψ_c were calculated from [2]

$$U(\rho_{crit}) = E\psi_c^2 . \quad (3)$$

The dotted curve in fig. 2 gives the resulting values and shows a rather good fit to the $\psi_{1/2}$ values derived from the trajectory calculations.

The conclusion is that at energies below which the critical approach distance becomes comparable to the channel radius, ψ_c will depart from the ψ_2 behavior and fall to 0 where ρ_{crit} reaches half the channel width. Extending the concept of a continuum potential to these low energies, taking into account the neighbouring strings, ρ_{crit} can approximately be found from

$$U''(\rho_{crit}) \approx 12E/d^2$$

and ψ_c accordingly from eq. (3).

The values of $\psi_{1/2}$ computed on this basis are in qualitative agreement with the measured data for the half-angle for penetration of He in W⟨100⟩. Since these angles are based on an integral effect over the whole trajectory [4], no one-to-one correspondence between the calculated and measured $\psi_{1/2}$ is expected.

I would like to thank Dr. E.V. Kornelsen for stimulating discussions and critical reading of the manuscript.

References

[1] M.T. Robinson and O.S. Oen, Appl. Phys. Lett. 2 (1963) 30.
[2] J. Lindhard, K. Dan. Vidensk. Selsk. Mat. Fys. Medd. 34 (14) (1965).
[3] E.V. Kornelsen, Radiat. Eff. 13 (1972) 227.
[4] E.V. Kornelsen and A.A. van Gorkum, Proc. 8th Intern. Conf. Atomic collisions in solids (Hamilton, 1979), to be published. (ch. 7)
[5] D.V. Morgan and D. van Vliet, Can. J. Phys. 46 (1968) 503.
[6] D.V. Morgan and D. van Vliet, Atomic collision phenomena in solids, eds. D.W. Palmer, M.W. Thompson and P.D. Townsend (North-Holland, Amsterdam, 1970) p. 746.
[7] D.V. Morgan and D. van Vliet, Radiat. Eff. 8 (1971) 51.
[8] W.D. Wilson and R.A. Johnson, Proc. Conf. Interatomic potentials and simulation of lattice defects, eds. P.C. Gehlen, J.R. Beeler Jr. and R.I. Jaffee (Plenum Press, New York, 1972) p. 375.

Radiation Effects, 1980, Vol. 52, pp. 25–34
0033-7579/80/5202-0025$04.50/0

THE ENTRANCE PROBABILITY AND RANGE OF HELIUM IN W(100) FOR ENERGIES 8 eV TO 5000 eV AS MEASURED BY THERMAL DESORPTION SPECTROMETRY

A. A. van GORKUM AND E. V. KORNELSEN

Division of Electrical Engineering, National Research Council of Canada, Ottawa, Canada K1A OR8.

(Received February 28, 1980)

Measurements have been made using thermal desorption spectrometry of the entrance probability η of He^+ ions incident on a W(100) surface at energies 8 eV to 5000 eV. For energies above 250 eV, η for normal incidence, η_n, is within 20% of unity, while for "random" incidence $\eta_r = 0.6 \pm 0.1$. Below 250 eV, both decrease and become equal for $E \leq 25$ eV. At 25 eV, $\eta = 0.2$ and at 8 eV, $\eta \approx 0.01$.

The measured values of η were used to obtain values for the average penetration $\bar{d}$ of the helium ions from previously measured values of the product $\eta\bar{d}$ for the same two directions of incidence. Above ~150 eV, the range for random incidence was found to be $0.12\ E^{0.9}$ Å (E in eV) while for normal incidence, the range is larger by a factor of about 3. Below 150 eV, both decrease rapidly and become equal (≈ 1 Å) at 25 eV.

The fraction of the normally incident ions channeled f_c was derived from the measured η_r and η_n. It was found to be > 0.8 for $E \geq 1000$ eV, and < 0.5 for $E < 200$ eV.

1 INTRODUCTION

The range and entrance probability of energetic ions incident on metals have been measured for many combinations of ions, metals and energies.[1] In addition to being of fundamental interest, these parameters for the case of low energy helium (< 20 keV) are of technical interest because such particles are expected to form an important component of the flux onto the "first wall" of fusion reactors. Since at these low energies small depths are involved, a high depth resolution is needed to measure ranges. Recently, a few measurements of the range of low energy helium in tungsten using the atom-probe FIM technique have become available.[2] Reflection coefficients (1-entrance probability) at these low energies ($\varepsilon < 1$) are scarce.[1] Measurements were reported earlier[3] of the product of the entrance probability η and the average penetration depth $\bar{d}$† for helium on tungsten (100) using thermal desorption spectrometry (TDS). This paper reports measurements of the entrance probability η using the same technique. Traps were implanted close to the surface and the fraction of the incident helium ions trapped was measured as a function of energy. The theoretical basis is explained in Section 2, while the production of the appropriate near-surface traps is described in Section 3. Section 4 contains the actual η measurements, and these are combined in Section 5 with the previous $\eta\bar{d}$ measurements to yield the average range $\bar{d}$ for energies from 8 to 5000 eV.

2 THEORY

It was shown in our basic theoretical paper[4] that the fraction f of the incident helium trapped in traps implanted beyond the maximum helium range is proportional to $\eta\bar{d}$,‡ where $\bar{d}$ is the average range of the helium and η the "diffusion qualification factor," representing the fraction of the incident helium that thermalizes inside the solid and subsequently takes part in the random diffusion process.

The basis for the measurement of η was also given in Ref. 4: if traps are implanted at a *smaller*

† Referred to as $\bar{d}_m$ in our earlier papers.

‡ Provided that $f \cdot \bar{d}_T/\bar{d} \ll 1$, with $\bar{d}_T$ = average trap depth, and that the trapping radius is constant (see Ref. 4).

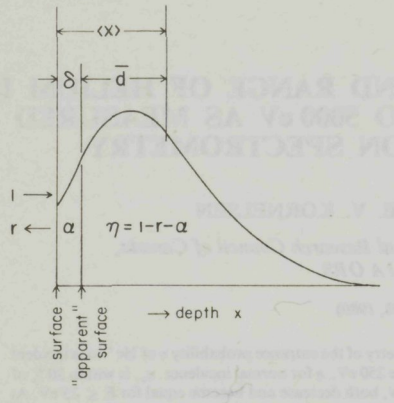

FIGURE 1 A sketch showing the effect of an anisotropic zone of thickness δ on the relationship (a) between the true average penetration $\langle x \rangle$ and that deduced by trapping measurements $\bar{d}$, and (b) between the diffusion qualification factor η and the reflection coefficient r. α is the fraction of the incident particles coming to rest in the anisotropic zone.

depth than the helium range then provided the trapping radius of the traps is constant, f is proportional to η and independent of $\bar{d}$. By measuring f as a function of the helium energy, relative values of η can be derived. Since the range of low energy helium is extremely small ($\sim$ 10 Å for 100 eV He), the traps must be implanted at extremely shallow depth.

As was pointed out previously,[3] there might be a non-isotropic surface zone of thickness δ in which the thermal motion of the helium is preferentially towards the surface (Figure 1). In this case η is equal to $1 - r - \alpha$, where r is the reflection coefficient and α is the fraction of the incident particles that thermalizes in the non-isotropic region. The measured f is proportional to η only if the (shallow) traps are at the depth δ. If the traps are within the layer δ ($\bar{d}_T < \delta$), the measured trapped fraction f will be proportional to the fraction of the helium coming to rest beyond $\bar{d}_T$, slightly larger than if the traps were at $\bar{d}_T = \delta$. If the traps are beyond the depth δ ($\bar{d}_T > \delta$), the trapping of helium coming to rest between δ and $\bar{d}_T$ will be less effective than if they had started beyond $\bar{d}_T$, thus underestimating η at the lowest helium energies. Evidence will be given that 1) δ, if it exists at all, cannot be more than a few angstroms, and 2) the traps used are not in the layer δ. This means that f will be proportional to η down to the lowest energies.

3 NEAR SURFACE TRAPS

It was shown previously[5] that all inert gases, when implanted in tungsten, can act as traps for diffusing helium. In particular, the inert gases left behind after high temperature (2150 K) anneal were studied extensively.

Argon was chosen to provide the traps close to the surface for the present experiments. To optimize the choice of the implantation parameters, desorption spectra for argon were measured for various incident energies, similar to those measured earlier,[6] but with a factor 10 improvement in sensitivity[7] and computer-based data acquisition and analysis.[8] Figure 2 shows the desorption spectra for incident energies from 80 to 5000 eV. For ion energies up to 250 eV, the desorption is dominated by five first order desorption peaks, corresponding to five different argon states labelled 1 to 5 in Figure 2. These were shown earlier to be specific to the (100) crystal surface orientation,[9] and thus seem likely to be associated with specific atomic configurations, and by implication with specific small "depths" below the crystal surface. At higher energies, a 6th peak, first visible at 200 eV, becomes prominent in the spectra (Figure 2b).

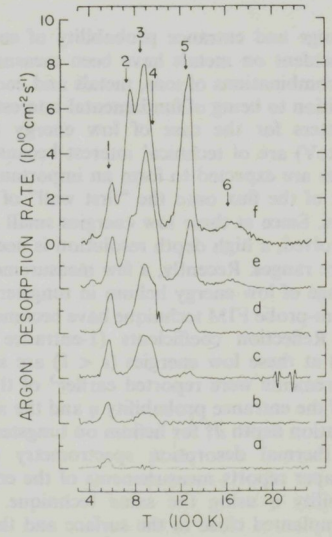

FIGURE 2a Argon thermal desorption spectra from W(100) for various energies. The ions were incident along the surface normal and the dose was 1×10^{13} cm^{-2}. (a) 80 eV; (b) 100 eV; (c) 125 eV; (d) 150 eV; (e) 200 eV; (f) 250 eV.

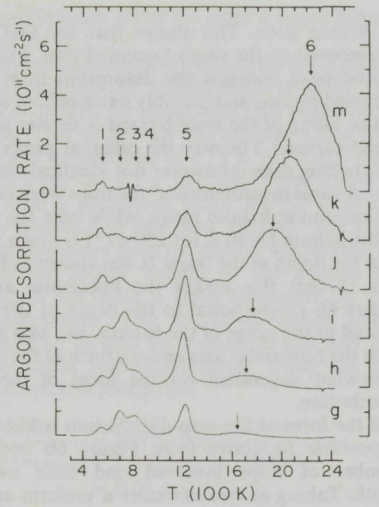

FIGURE 2b As in 2a, incident energies (g) 300 eV; (h) 400 eV; (i) 500 eV; (j) 1000 eV; (k) 2000 eV; (m) 5000 eV. For $E > 500$ eV, the incident dose was reduced to 1×10^{12} cm^{-2} and the amplitudes multiplied by 10.

It shows the shape, the increasing temperature with ion energy, and the independence of crystal surface orientation, characteristic of argon escaping by random-walk diffusion.

Figure 3 shows the fractions trapped in the different states as a function of argon ion energy. The sequential rise and fall with increasing energy suggests that state 6 is deeper than state 5 which in turn is deeper than the states 1–4. State 5 was chosen as the near-surface trap since it can be isolated from the other surface related peaks by annealing to 1150 K. An argon energy of 250 eV was chosen since at this energy peak 5 is nearly at its maximum amplitude.

Spectrum 1 of Figure 4 shows the helium desorption spectrum after a pre-bombardment with 250 eV argon and an anneal of 1150 K to remove the near surface states 1 to 4 as well as the empty vacancies.[10] Four peaks (S_2, S_1, B_1 and B_2) are seen below 1100 K.† Annealing to 1500 K after argon bombardment leaves only state 6, and subsequent helium injection results in the desorption spectrum 2 of Figure 4: the peaks S_1 and S_2 are absent, while

† The peaks at higher temperatures originate from argon-vacancy-helium complexes.

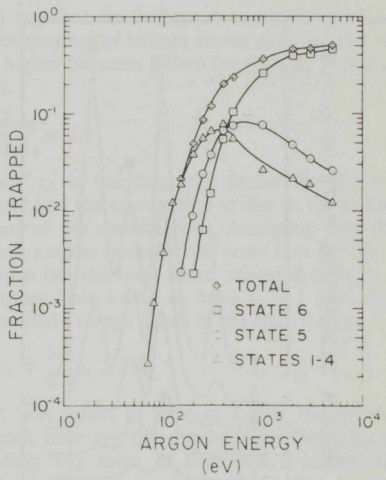

FIGURE 3 The fraction of incident Ar^+ ions trapped for normal incidence on W(100), showing the contributions of the individual states identified in Figure 2.

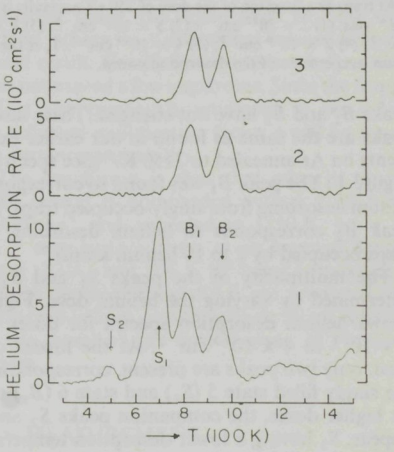

FIGURE 4 Helium desorption spectra from the argon state 5 and 6 traps (see Figures 2 and 3) in W(100). The argon was implanted at 250 eV at normal incidence and the dose was 5×10^{13} cm^{-2}. Helium injection was at 250 eV and normal incidence in all cases. (1) After 1150K anneal to remove Ar states 1–4, leaving states 5 and 6. Dose was 5×10^{13} cm^{-2}. (2) After 1500K anneal to remove Ar state 5, leaving only state 6. Dose was 5×10^{13} cm^{-2}. (3) Spectrum from deeply trapped argon ($\bar{d} \approx 250$ Å) annealed to 2150K to show correspondence with the state 6 trapping of (2). Dose was 1×10^{13} cm^{-2}

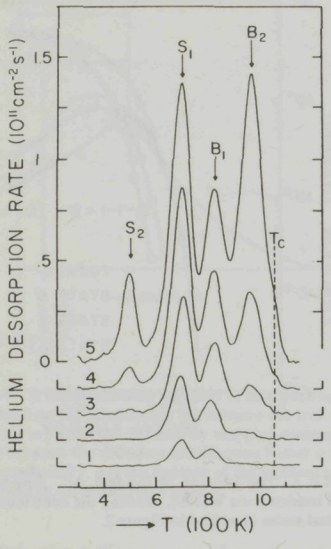

FIGURE 5 Helium desorption spectra from state 5 and state 6 Ar traps as a function of the dose of 250 eV normally incident He^+ ions. (1) 2×10^{12} cm^{-2}; (2) 5×10^{12} cm^{-2}; (3) 1×10^{13} cm^{-2}; (4) 2×10^{13} cm^{-2}; (5) 4×10^{13} cm^{-2}. T_c is the maximum temperature of the desorption sweep.

peaks B_1 and B_2 have not changed. These last two peaks are the same as found in our earlier experiments on Ar annealed to 2150 K.[5] (See spectrum 3 Figure 4.) The peak B_1 was found to correspond to helium desorbing from singly-occupied traps, while peak B_2 corresponds to helium desorbing from traps occupied by 2 to 10 helium atoms.[5]

The multiplicity of the peaks S_1 and S_2 was determined by varying the helium dose. Figure 5 shows helium desorption spectra for doses from 2×10^{12} to 4×10^{13} cm^{-2}. At the lowest doses used, only two peaks are present, corresponding to the singly filled state 5 (S_1) and state 6 (B_1) traps. At higher doses, the companion peaks S_2 and B_2 appear, S_2 having a lower desorption temperature than S_1, similar to the result found for trapping at vacancies,[10] while B_2 appears at a higher temperature then B_1.

The spectra of Figure 5 were deconvoluted, and the resulting peak populations plotted in Figures 6a for the state 5 traps, and 6b for the state 6 traps. In each case, the first peak (B_1, S_1) rises linearly with dose at low doses, while the second peak (B_2, S_2) has quadratic dependence on helium dose. This shows that the first peak corresponds to the singly occupied trap, while the second peak contains the desorption from traps occupied by two and possibly more helium atoms.

The filling of the state 6 traps is similar to that found earlier.[5] The way the different peaks grow with helium dose is however not identical since in the previous measurements[5] the traps were beyond the maximum helium range, while here the range of the helium (≈ 60 Å for 250 eV[3]) is much larger than the depth of the traps. It was shown in Refs. 4 and 11 that this makes the horizontal axis in Figure 6b proportional to the depth of the traps instead of the range of the helium, and also makes both the horizontal axis and the form of the curves somewhat dependent on the form of the trap distribution.

If the form of the trap distribution is known, it is possible to derive from Figure 6b both the number of traps involved and their average depth. Taking as two extremes a uniform and an exponential trap distribution, the number of traps is found to be

$$(n_T)_6 = (3.6 \pm 0.4) \times 10^{11} \text{ cm}^{-2}.$$

The actual number of argon atoms in state 6 was measured as (Figure 3)

$$(n_{Ar})_6 = (3.2 \pm 0.3) \times 10^{11} \text{ cm}^{-2}$$

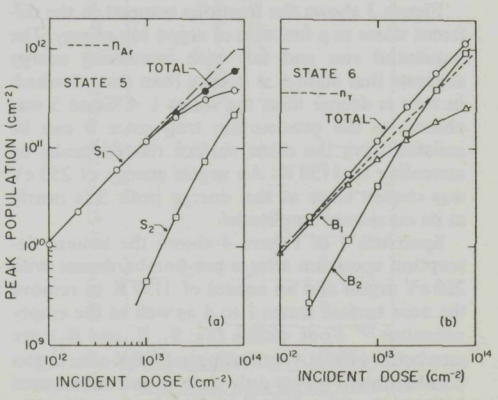

FIGURE 6 Peak populations vs dose for the state 5 traps (a) and the state 6 traps (b) derived from the spectra of Figure 5. The number of state 5 Ar atoms is indicated in (a) and the number of traps deduced from the filling behavior of the state 6 traps in (b). The peaks S_1, S_2, B_1 and B_2 are identified in Figure 5. The dashed lines are linear extrapolations of the trapping at low dose.

suggesting that all of the state 6 argon atoms act as traps.

The average depth of the state 6 traps is estimated by comparing the helium doses at which the B_1 and B_2 peaks are equal with that found for deep traps. This occurs for the shallow traps (Figure 6b) at a helium dose of 1.75×10^{13} cm^{-2} and for deep traps[5] at 2.2×10^{12} cm^{-2} (see also Figure 4). After a correction factor for the form of the trap distribution has been applied,[4] the ratio of these two doses gives the ratio of the average range $\bar{d}$ of the 250 eV helium to the average depth $(\bar{d}_T)_6$ of the state 6 traps produced by 250 eV bombardment. This correction factor was calculated to be 0.80 for a uniform and 0.61 for an exponential trap distribution. Using the above numbers, it is found that

$$\frac{(\bar{d}_T)_6}{(\bar{d})_{\text{helium, 250 eV}}} = (0.7 \pm 0.1) \times \frac{2.2 \times 10^{12}}{1.75 \times 10^{13}}$$

$$= 0.09 \pm 0.01.$$

Since $\bar{d}$ for 250 eV helium for normal incidence was estimated to be ≈ 60 Å,[3] (see also Section 5), the average depth of the state 6 traps resulting from the 250 eV Ar implant is

$$(\bar{d}_T)_6 \approx 5.3 \pm 0.6 \text{ Å}.$$

The argon in state 6 is thus very shallow indeed. Since all the near-surface states 1–5 are shallower, the conclusion is that the depths associated with states 1–5 do not exceed 5 Å.

The filling curve for the state 5 argon (see Figure 6a) cannot be fitted with a simple model in which the reaction rate constant K for trapping is independent of the number i of helium atoms in the trap. Unlike the case of state 6, where K was found to increase with i,[5] a much better fit to the S_1 and S_2 populations was obtained by using a value of K for $i = 1$ smaller by a factor ~ 3 than that for the empty trap ($i = 0$).† The number of traps in this case cannot be deduced from the filling curves of Figure 6a by the method used above for state 6. Instead, the number of state 5 traps was assumed to be equal to the number of state 5 argon atoms desorbing (1.1×10^{12} cm^{-2}) as was found above for state 6. By comparing the number of helium atoms trapped per trap at low helium doses, where the fraction of doubly-occupied traps is still small, it is found (Figure 6a and 6b) that the helium dose needed to reach a given number of helium atoms per trap is a factor 2.3 higher for state 5 than for state 6. This implies that

$$\frac{(z_0 \bar{d}_T)_6}{(z_0 \bar{d}_T)_5} \approx 2.3$$

where z_0 is the trap size factor for the empty traps‡ and the uncertainty is due to the unknown forms of the distributions. Assuming that the z_0 values are the same for the state 6 as for the state 5 traps (all the inert gases annealed to high temperature were found to have $z_0 \approx 1$ (Ref. 5)) the estimated average depth of the state 5 traps is

$$(\bar{d}_T)_5 \approx \frac{5.3}{2.3} = 2.3 \text{ Å}.$$

It was noted in Section 2 that the depths $\bar{d}_T$ quoted here are the depths from the surface excluding any layer of thickness δ in which the helium diffusion is non-isotropic (see Figure 1). That δ is very small may be concluded from the fact that all argon peaks 1 to 5 appear at energies within a factor 2 of the threshold energy for penetration.[9] Moreover, since all peaks 1 to 5 have a first-order shape, the argon must be close to the surface, otherwise a diffusional release behaviour would result. For these reasons we believe that δ does not exceed a few angstroms. Since the trapping radius was previously estimated to be ≈ 3 Å,[11] the diffusion qualification factor η will be equal to the entrance probability.

The conclusion is thus that when a tungsten (100) crystal is bombarded with 5×10^{13} cm^{-2} 250 eV Ar$^+$ and annealed to 1150 K, 1.1×10^{12} cm^{-2} near-surface states at an average depth of about 2.3 Å, and 3.6×10^{11} cm^{-2} states at an average depth of about 5.3 Å are produced. Both states trap helium, and their basic filling behaviour for low numbers per trap is given in Figures 6a and 6b.

4 η MEASUREMENT

For the entrance probability experiments, Ar traps were implanted in W(100) as described in the previous section and the surface then bombarded with He$^+$ ions of selected energies and doses. The maximum fraction of the helium trapped

† Consistent with the less than linear total trapping (Figure 6a).

‡ z_0 is approximately equal to the trapping radius r_0 in lattice constants for helium in a bcc crystal.[11]

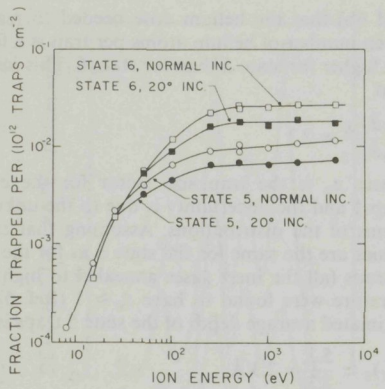

FIGURE 7 The fraction f_n of incident He^+ trapped at the state 5 and state 6 Ar traps normalized to 1×10^{12} traps cm^{-2} as a function of ion energy. The open points were measured at normal incidence and the filled points at 20° from the normal in a (013) plane. Small corrections have been applied to give the values characteristic of the low He^+ dose limit (see Figure 6).

was $\approx 1\%$ and the average number of trapped helium atoms per trap, i, was ≤ 0.2. Two directions of incidence were used: Normal to the surface and 20° from the normal in a (013) plane. The latter is expected to represent a "random" direction (see Ref. 3).

Figure 7 shows the normalized fraction of the incident helium trapped, $f_n = f * (10^{12}/n_T)$, for normal and random incidence, for both the state 5 and the state 6 traps, where f is the fraction trapped in the low dose limit ($i < 0.1$). It is seen that at higher energies ($\gtrsim 250$ eV), the state 6 and state 5 values of f_n are proportional at the same angle of incidence, the proportionality constant being the trap depth ratio 2.3 mentioned earlier (Section 3). Above this energy, both curves thus represent relative values of η. The ratio between normal and random values of η is nearly constant for $E > 250$ eV, being 1.6 ± 0.1.

For energies below 150 eV, f_n drops more rapidly for state 6 than for state 5, indicating that at these energies a significant fraction of the helium has a range less than the depth of the state 6 traps. As pointed out in Section 2, f_n is only proportional to η if all the helium starts to diffuse at depths greater than the depth of the traps. Since the state 5 traps are shallower, this condition will continue to hold to a lower helium energy than for the state 6 traps. It is not known a priori however at what energy it will cease to be true for the state 5 traps. From Figure 7 it is seen that for energies below 25 eV, f_n is equal for the two types of traps. This indicates firstly that the helium starts to diffuse either in the same plane as the state 5 traps or in front of them. Secondly, it is implied that the state 5 traps are not inside the possible non-isotropic layer (Figure 1), since if they were, a higher f_n would be found for state 5 than for state 6.

The trapping radius has been estimated to be ~ 3 Å. Since this is larger than the estimate depth of the state 5 traps, it will be assumed that the state 5 traps are indeed in the first plane in which random diffusion of the helium occurs. The measured values of f_n are then proportional to η down to the lowest energies, and are given by the data for the state 5 traps. η thus drops for $E < 250$ eV, becomes equal for random and normal incidence at 25 eV, and decreases sharply below this energy.

Since f_n is nearly constant for normal incidence above 500 eV, the 5000 eV point on the normal incidence curve is assumed to correspond to $\eta = 1$. The resulting curves of η vs energy are shown in Figure 8. The following points are notable:

1) For the "random" incidence, η_r is $\sim 0.6 \pm 0.1$ over the whole energy range from 250 eV to 5000 eV.

2) Even at 8 eV, about 1% of the ions thermalize in the crystal and no dependence on incidence direction is observed.

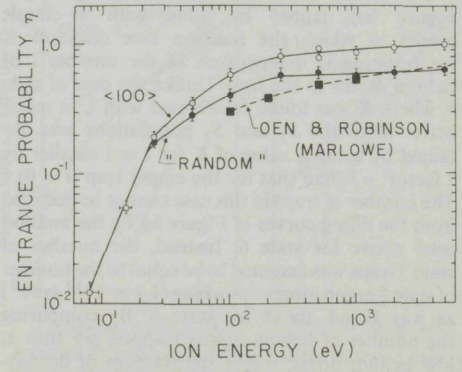

FIGURE 8 The entrance probability as a function of ion energy for He^+ on W(100). The channeled value (⟨100⟩) has been assumed to approach unity at 5000 eV. The filled square points are values of $1-r$, where r is the reflection coefficient computed for "random" material (Ref. 13).

The LSS theory[12] of the penetration of low energy ions predicts that the relative straggling $\Delta R_p/R_p$ is nearly independent of the energy. For helium in tungsten, $\Delta R_p R_p \approx 2.5$. If the range distribution is assumed to be a Gaussian, the fraction f of the distribution lying inside the surface is $\frac{1}{2}[1 + \text{erf}\{\sqrt{2}(\Delta R_p/R_p)\}^{-1}] = 0.65$, close to the nearly constant value of η_r above 250 eV.

Reflection computations[13] using the collision program MARLOWE predict for "random" tungsten the curve so marked in Figure 8. Although the agreement is reasonable, the computed values lie significantly below the experimental ones between 100 eV and 1 keV.

Attempts have been made[14,15] to calculate the entrance probability of He on W (100), based on the assumptions that (1) the probability of passing through the first two planes is a good approximation to η, and (2) this probability can be derived from transparency arguments. The first assumption is questionable since the energy loss per collision for He in W is small (8.4% maximum), making the relative range straggling large, as mentioned above. The second assumption breaks down at low energies where collision diameters become comparable to interatomic distances.

If one assumes (1) that the incident ions are separated into a channeled fraction f_c and a random (unchanneled) fraction $1-f_c$, and (2) that the channeled fraction has $\eta = 1$, while the random fraction has η equal to that measured for random incidence at the same energy, then

$$f_c = \frac{\eta_n - \eta_r}{1 - \eta_r} \qquad (1)$$

where η_n and η_r are the values measured for normal and random incidence. This allows f_c to be deduced from the η measurements. The experimental data of Figure 8 used in Eq. (1) yield the curve for f_c so labeled in Figure 9. The error bars indicate the relatively large uncertainty in the measured differences $\eta_n - \eta_r$. This uncertainty is somewhat smaller than that indicated by the error bars in Figure 8 which refer to uncertainties in the absolute values of η. The dashed curve in Figure 9 was derived from computations of the critical approach distance ρ_c for channeling,[16] assuming that all particles entering the crystal within ρ_c of an atomic row do not channel. The good correspondence between the curves suggests that the above assumptions are reasonable.

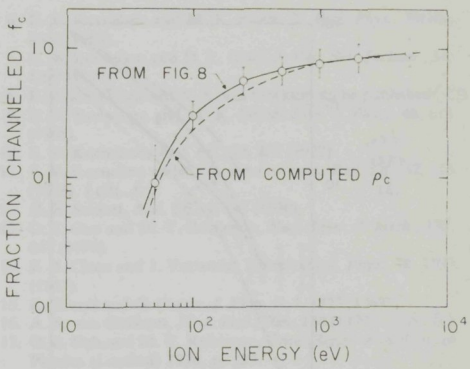

FIGURE 9 The fraction of helium ions channeled as a function of energy for normal incidence on a W(100) surface, derived from the η values of Figure 8, using Eq. (1). The dashed curve is derived from computed values of the critical approach distance for channeling (see Ref. 16)

5 RANGE DATA

Previously we published values of the product $\eta\bar{d}z_0$ for helium energies from 25 to 5000 eV for normal and random incidence.[3] This data is reproduced in Figure 10 as the dotted and dashed curves respectively. Values of $\eta\bar{d}z_0$ for energies below 25 eV have been added, based on the data from Figure 7: Since the state 6 traps are mainly beyond the maximum helium range for helium energies below 25 eV, f_n for these traps is proportional to $\eta\bar{d}$.[4]

Using the η data from Figure 8, values of the product of the average range $\bar{d}$ and z_0 have been derived and are plotted in Figure 10. For energies above 250 eV, the average ranges for normal and random incidence are nearly parallel, with a ratio of about 3. Below 250 eV, they converge and become equal at about 25 eV. Below this energy, $\bar{d}z_0$ has a constant value of ≈ 1 Å, since $\eta\bar{d}z_0$ and η are proportional. It is interesting to note that below 25 eV there is no angular dependence of $\eta\bar{d}z_0$ nor η, and the average range is approximately the interplanar spacing (1.58 Å).

The values of $\bar{d}z_0$ are based on the η curve from Figure 8 using the assumption that the traps were in the first plane where isotropic helium diffusion occurs. Figure 10 shows that the minimum value of $\bar{d}z_0$ is equal to ≈ 1 Å, smaller than the estimated value of 2.3 Å for the depth of the state 5 traps. However, since the trapping radius is ~ 3 Å

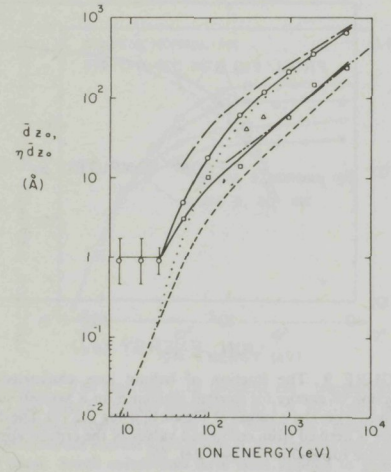

FIGURE 10 Average depths as a function of energy for He^+ ions incident on W(100). – – – – – – – $(\eta\bar{d})_r z_0$, ... $(\eta\bar{d})_n z_0$, —□—□— $\bar{d}_r z_0$, —○—○— $\bar{d}_n z_0$, —— —— $\bar{d}_c z_0$, —— —— —— $\bar{d}_t z_0$, $z_0 = 1$, Oen and Robinson. The triangle points are absolute range measurements on W(110).[2] η is the entrance probability, $\bar{d}$ the average range and z_0 the trap size factor ($z_0 \approx 1$). The subscripts: r = random incidence, n = normal incidence (⟨100⟩). $\bar{d}_c$ is the deduced average range of the fraction of the particles that channeled. The curve of Oen and Robinson was computed for a random solid using the program MARLOWE. (Ref. 13).

($z_0 \approx 1$), the above assumption is satisfied to a good approximation. The estimated range at energies below 25 eV depends critically on the energy at which f_n (Figure 7) becomes the same for state 5 and state 6 traps. (If the energy were 35 eV instead of 25 eV, this range would be ~2 Å instead of ~1 Å.) This is the main contribution to the large error bars below 50 eV.

In Figure 10, a comparison is made with the values of the helium range in "random" tungsten computed by Oen and Robinson.[17] As found previously,[3] the energy dependence of the computed range and $\bar{d}$ agree well and the choice $z_0 = 1$ gives a close correspondence with all measured values. Two absolute values of the helium range in the ⟨110⟩ direction in W measured using FIM atom-probe techniques[2] are included in Figure 10. It is reassuring that they lie between our random and ⟨100⟩ channeled values since the ⟨110⟩ is a less open channel than the ⟨100⟩.

By arguments similar to those used in connection with Figure 8, it is possible to estimate the product of z_0 and the average range $\bar{d}_c$ of the particles that channel. One obtains

$$\bar{d}_c z_0 = \frac{\bar{d}_n z_0 - (1 - f_c)\bar{d}_r z_0}{f_c}$$

where $\bar{d}_r$ is the average range for random incidence, and $\bar{d}_n$ is the average range for normal (channeling) incidence (see Figure 10).

Using the channeled fraction f_c from Figure 9, the results are shown in Figure 10. The ratio of the channeled to random penetrations $\bar{d}_c/\bar{d}_r$ is about 5 for 50 eV $\leq E \leq$ 1 keV, and decreases to ~3 at 5 keV. Above 1 keV, the channeled penetration approaches the $E^{1/2}$ dependence characteristic of pure electronic loss, expected to be the dominant loss for channeling ions.

6 SUMMARY AND CONCLUSIONS

Thermal desorption spectrometry has been used to determine average ranges $\bar{d}$ and entrance probabilities η for helium incident on a W (100) surface, for energies from 8 to 5000 eV. The experiments were done by implanting Ar ions at a small depth (~2.3 Å), and measuring the fraction of the incident helium trapped at the implanted atoms. This fraction is proportional to the entrance probability. For energies above 250 eV, the entrance probability for normal incidence (η_n) is within 20% of unity, and is 0.6 ± 0.1 for random incidence (η_r). Below 250 eV, both η_n and η_r drop sharply, become equal at 25 eV, and reach 1.2×10^{-2} at 8 eV.

The channeled fraction has been derived from the random and channeled values of η, and found to be in good agreement with predictions based on computed critical approach distances for channeling.[16]

The values of η are also used to obtain values of $\bar{d}z_0$ as a function of energy for normal and "random" incidence from previously published $\eta\bar{d}z_0$ data. Comparison with computed values of average penetration for random material[13] show that the energy dependences agree well above 250 eV, and that the trap size factor z_0 is ~1, corresponding to a trapping radius of ≈3 Å.

Above 250 eV, the range for random incidence is equal to $0.12E^{0.9}$ Å, with E in eV, and that for normal incidence is higher by about a factor of 3. Below 250 eV, both decrease rapidly, and become equal (~1 Å) at 25 eV.

The range of the channeled component is deduced using the channeled fraction. The ratio of the channeled to the random range is ~5 from 50 eV to 1 keV and decreases to ~3 at 5 keV.

REFERENCES

1. G. M. McCracken, *Proc. Int. Symp. Plasma Wall Interaction*, Jülich, October 1976, Pergamon Press, p. 339.
2. A. Wagner and D. N. Seidman, *Phys. Rev. Lett.*, **42**, 515 (1979).
3. E. V. Kornelsen and A. A. van Gorkum, Proc. 8th Int. Conf. At. Coll. Solids, Hamilton, *Nucl. Instr. & Meth.* **170**, 161 (1980). (ch. 7)
4. A. A. van Gorkum and E. V. Kornelsen, *Rad. Eff.*, **42**, 93 (1979). (ch. 5)
5. E. V. Kornelsen and A. A. van Gorkum, to be published in *J. Nucl. Mat.* (ch. 10)
6. E. V. Kornelsen and M. K. Sinha, *J. Appl. Phys.*, **39**(10), 4546 (1968).
7. E. V. Kornelsen and D. L. Blair, *J. Vac. Sci. Technol.*, **14**, 1299 (1977).
8. E. V. Kornelsen and A. A. van Gorkum, to be published (ch. 3)
9. E. V. Kornelsen and M. K. Sinha, *Can. J. Phys.*, **46**, 613 (1968).
10. E. V. Kornelsen, *Rad. Eff.*, **13**, 227 (1972).
11. E. V. Kornelsen and A. A. van Gorkum, *Rad. Eff.*, **42**, 113 (1979). (ch. 6)
12. H. E. Schiøtt, *Rad. Eff.*, **6**, 107 (1970).
13. O. S. Oen and M. T. Robinson, *Nucl. Instr. & Meth.*, **132**, 647 (1976).
14. K. J. Close and J. Yarwood, *Brit. J. Appl. Phys.*, **18**, 1593 (1967).
15. K. Erents and G. Carter, *J. Phys. D*, **1**, 1323 (1968).
16. A. A. van Gorkum, *Phys. Lett.*, **75A**, 134 (1979). (ch. 8)
17. O. S. Oen and M. T. Robinson, Conf. Series #28, Inst. of Physics (London) 1976, p. 329.

Journal of Nuclear Materials 92 (1980) 79–88

A STUDY OF BUBBLE NUCLEATION IN TUNGSTEN USING THERMAL DESORPTION SPECTROMETRY: CLUSTERS OF 2 TO 100 HELIUM ATOMS

E.V. KORNELSEN and A.A. VAN GORKUM
Division of Electrical Engineering, National Research Council of Canada, Ottawa K1A 0R8, Canada

Received 9 January 1980

The attachment of helium to annealed inert gas impurity atom traps in tungsten has been measured by thermal desorption spectrometry. For the first helium atom trapped, all five impurities (the substitutional He atom HeV, Ne, Ar, Kr and Xe) were found to have approximately the same trapping radius (≈2.8 Å). The binding energy, however, decreased monotonically with increasing impurity mass from 3.1 eV for HeV to 1.2 eV for Xe. All were found able to trap at least $i = 100$ helium atoms with no evidence of saturation. On the contrary, for $i > 10$ the trapping characteristics, essentially the same for all five traps, were a gradual increase in binding energy from ~2.2 eV at $i = 10$ to ~4.5 eV at $i = 100$, and an increase in the average trapping radius to ~12.5 Å when the average number of trapped He atoms per trap was 62. The results thus describe the first stages of helium bubble formation in tungsten at room temperature.

1. Introduction

Helium and the other inert gases introduced into solids are known to agglomerate because of their extremely low solubility. When the amounts introduced are sufficiently high, quite large bubbles may be formed and the resulting swelling [1], structural weakening [2] and blistering [3] is of major significance in a number of areas of engineering design. Such effects have in particular been the subject of extensive investigation in connection with research on nuclear fusion [4]. The nucleation and the earliest stages of growth of clusters is difficult to study because of their extremely small size. The smallest features observable by electron microscopy (15–20 Å diameter) probably already contain 10^2 to 10^3 gas atoms [5], at which stage the primary mechanisms and parameters cannot be directly determined.

The present paper reports a study, based on the technique of thermal desorption spectrometry (TDS) of just this initial stage of nucleation and cluster growth for the case of helium in tungsten. Specifically, the vacancy occupied by a single He atom (HeV), and Ne, Ar, Kr and Xe impurity atoms annealed to 2150 K have been used as nucleation centers for the trapping of helium injected into the tungsten as 250 eV ions. Relevant aspects of the TDS technique, described in detail in two earlier papers [6, 7] are outlined in section 2. Details concerning the production of the nucleation centers ("traps") and the helium injections are given in section 3. The helium desorption spectra observed for the different traps over a range of the injected He^+ dose and their interpretation in terms of the helium cluster properties are presented in section 4.

2. Theoretical basis of the method

Consider the near-surface region of a metal crystal containing a low concentration ($\leqslant 10^{-6}$) of traps distributed over a depth of a few hundred Angstroms. Helium ions injected into the crystal at room temperature and at an energy too low to cause atomic displacements first thermalize and then undergo rapid interstitial diffusion [8]. Most of them escape through the surface but a small fraction become attached to the traps. In an earlier paper [7], a general theory was developed which predicts the fraction n_i of the traps which would be occupied by i helium atoms as a function of the injected dose n^+ in such an experiment. The theory is based on the iso-

tropic diffusion of particles from a specified distribution of starting depths in the presence of the surface and a specified distribution in depth of non-saturable traps. In the accompanying experimental paper [6] (II hereafter), it was shown that the theory gave an excellent account of the trapping of helium at Xe impurity atoms annealed to 2150 K in tungsten. It proved possible to identify particular peaks in thermal desorption spectra of the trapped helium with release from traps occupied by specific numbers i of helium atoms and to measure the trapped populations p_i and binding energies E_i.

It was shown in the same theoretical paper [7] that provided

(a) the trapping occurring when no traps are deliberately introduced is negligible,

(b) the traps are situated at a depth greater than the maximum helium range,

(c) the trap concentration C_T is sufficiently low that the fraction of the helium trapped is small and proportional to C_T,

then the trapping is independent of the details of the trap depth distribution. As will be outlined below, two important parameters can then be derived:

(1) the trap concentration, i.e. number of traps per cm^2, C_T;

(2) the product $\eta\bar{d}_m r_0$, where η = entrance probability of the He^+ ions, $\bar{d}_m$ = average range of the ions, and r_i = trapping radius of the ideal spherical sink yielding the same trapping rate as the real trap when it is occupied by i helium atoms [9].

The derivation of C_T and $\eta\bar{d}_m r_0$ can be illustrated most easily when r is assumed to be independent of i ($r_i = r_0$). The fractions n_i are then given by [7]

$$n_i = \frac{B^i}{i!} e^{-B}, \tag{1}$$

in which

$$B = 4\pi\eta\bar{d}_m r_0 n^+, \tag{2}$$

where n^+ is the incident ion dose (cm^{-2}). We have called the parameter B the "trap sampling density". As long as $B \leqslant 1$, it is equal to the average number of helium atoms that become trapped per trap, $\bar{i}$.

The number of traps occupied by i helium atoms ($n_i C_T$) can be derived from the peak populations p_i (cm^{-2}). For some traps, such as Xe, the binding energy increases with increasing i, and $(n_i C_T) = p_i/i$ since i helium atoms are released from each trap when desorption occurs. (See section 4 for a more detailed discussion.) If E_i decreases with i, as is true for lattice vacancies [8], then $(n_i C_T) = p_i - p_{i+1}$. From a single desorption spectrum for a known dose n^+, the values of B and C_T can then be derived using eqs. (1) and (2) and the $(n_i C_T)$ for any two values of i. For example, using p_1 and p_2, from eqs. (1) and (2)

$$B = 2\frac{(n_2 C_T)}{(n_1 C_T)},$$

$$\eta\bar{d}_m r_0 = \frac{1}{2\pi n^+}\frac{(n_2 C_T)}{(n_1 C_T)}, \tag{3}$$

and

$$C_T = \frac{(n_1 C_T)^2}{2(n_2 C_T)} \exp\left(\frac{2(n_2 C_T)}{(n_1 C_T)}\right), \tag{4}$$

where the right-hand sides of eq. (3) and (4) contain only measurable quantities.

The procedure used in II is equivalent to evaluating eqs. (3) and (4) (and parallel ones for other values of i) for desorption spectra at a number of doses n^+. The fact that the values of C_T and $\eta\bar{d}_m r_0$ derived in this way are independent of n^+ and i is the basis of the conclusion drawn in II that the theory and the data are in good agreement.

Slight modifications to the expressions are required to take account of the variation of the trapping radius r_i with i and of the fact that not all of the traps are at a depth greater than the maximum helium range. These, however, result in only minor corrections as long as $B \leqslant 2$.

3. Experimental

Distributions of traps appropriate for such experiments were obtained by combinations of low energy (0.5–1.5 keV) ion implantation and annealing. The final concentrations and average depths were kept comparable even though, as mentioned above, this is not expected to be critical. Details of the five implantations and anneal temperatures are given in table 1. The average depth of the traps was ~250 Å in each case as estimated by a method described in II. The trap concentrations, C_T, derived as outlined in the previous section, are seen to vary from 2.6 to 7.2 ×

Table 1
Implantation parameters

	E_i (eV)	n^+ b) ($\times 10^{13}$)	T_A (K)	n_g c) ($\times 10^{10}$)	C_T d) ($\times 10^{10}$)	C_T/n_g	f_0 e) (%)
He a)	5000	0.05	1320	2.7	2.6	~1	0.43
Ne	500	1.0	2150	11.5	7.0	0.61	1.4
Ar	750	1.0	2150	10.3	7.0	0.68	1.4
Kr	1200	0.5	2150	9.1	6.1	0.67	1.1
Xe	1500	0.5	2150	11.5	7.2	0.63	1.3

a) The trap (HeV) in this case dissociates at ~1520 K [8]. The implantation was performed at 7° from ⟨100⟩ to produce and simultaneously fill the lattice vacancies at the desired depth (~250 Å). The anneal in this case served to remove unfilled vacancies and to desorb second and third He atoms from those multiply filled.
b) n^+ = incident ion dose (cm^{-2}).
c) n_g = amount of gas remaining trapped after anneal (cm^{-2}).
d) C_T = deduced number of traps (cm^{-2}).
e) f_0 = fraction of injected He trapped at low dose ($\leqslant 1 \times 10^{12}/cm^2$).

$10^{10}/cm^2$, corresponding to atomic fraction concentrations of ~1.5 to 4.0×10^{-7}.

The helium injections were done under exactly the same conditions as described in II, namely as 250 eV ions incident along the ⟨100⟩ normal to the surface of the (100) tungsten crystal. At this energy, helium ions create no atomic displacements in the crystal, and are estimated to have an average range $\bar{d}_m$ of ~60 Å (see discussion in section 4). The fraction f_0 of the incident helium trapped at low dose varied from 0.4 to 1.4% (column 8, table 1). When no traps were introduced, $f_0 \leqslant 0.02\%$.

Five series of thermal desorption spectra were measured, one for each kind of trap. In each series, the injected He dose was varied from $\sim 3 \times 10^{11}$ to $1.2 \times 10^{14}/cm^2$ in about 10 steps. The desorption was carried out by heating the crystal linearly at $\beta = dT/dt = 40$ K/s by electron bombardment and measuring the rate of helium release with a sensitive mass spectrometer [10].

4. Results and discussion

To make comparison easier, the five spectra at a single value of the helium dose, (one for each trap), have been collected into one figure. These collections are shown for five helium doses in figs. 1–4 and 6. The doses are given in the captions, and also appear in table 2. Usually such spectra are plotted as desorption rate (atoms/$cm^2 \cdot s$) as a function of temperature. Here they have been normalized by dividing by the number of traps per cm^2 (column 5 of table 1) to give the indicated ordinate atoms/s · trap. Integration of these normalized spectra, making use of $dT = \beta\, dt$, gives the average number of trapped helium atoms per trap $\bar{i}$. Nominal values of $\bar{i}$, which can be seen by inspection to be roughly the same for all the traps, are given for each figure in the caption and in column 3 of table 2. Since $B = \bar{i}$ at low dose ($B \leqslant 1$), it can be seen from eq. (2) that for identical bombardments (η, $\bar{d}_m$ and n^+ fixed) $\bar{i}$ is proportional to r_0. Measurements of $\bar{i}$ thus give *relative* values of r_0 for different traps even when η and $\bar{d}_m$ are not known.

Fig. 1 shows spectra for a dose of $1 \times 10^{12}/cm^2$, where $\bar{i} \approx 0.17$ so that most of the traps are still unoccupied. The largest peaks in the spectra for the Xe, Kr and Ar traps correspond to the release of helium from singly-occupied traps. The shape of all

Table 2
Helium doses and average multiplicities

Figure	n^+ (cm^{-2})	$\bar{i}$
1	1×10^{12}	0.17
2	4×10^{12}	0.77
3	2×10^{13}	5.6
4	6×10^{13}	21.5
6	1.2×10^{14}	62

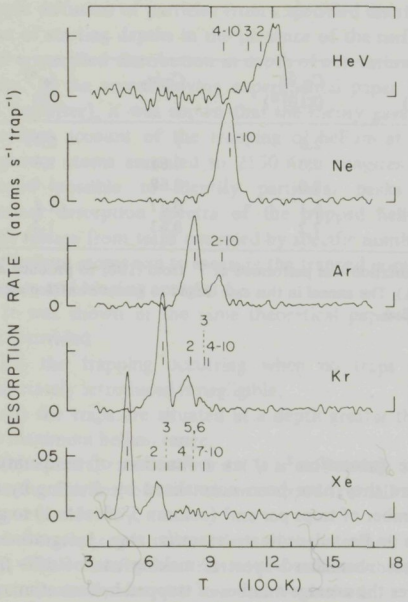

Fig. 1. Desorption spectra from five different trap nuclei. The incident He dose $n^+ = 1 \times 10^{12}/cm^2$, and the average number of trapped He atoms per trap ($\bar{i}$) was about 0.17. The vertical marks on the individual spectra indicate the peak temperatures and the deduced values of the multiplicity i.

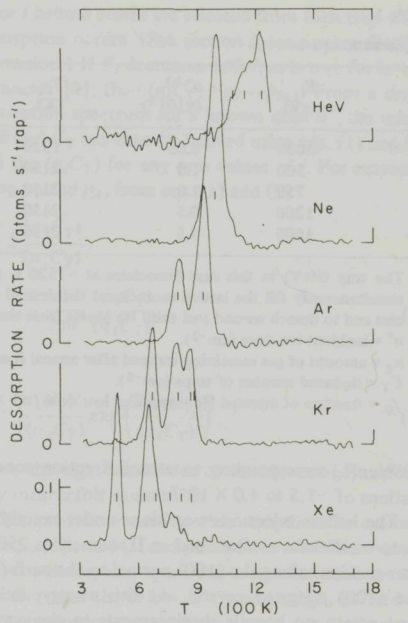

Fig. 2. Desorption spectra for the same five nuclei when $n^+ = 4.0 \times 10^{12}/cm^2$, $\bar{i} \approx 0.77$.

the peaks is consistent with first order kinetics as is expected if release from the traps is the rate-limiting step:

$$HeT \rightarrow He + T\,, \qquad (i = 1)\,, \tag{5}$$

where T represents the trap. In each of these cases a second peak about 20% of the first in amplitude can be seen ~150 K higher in temperature. These correspond to the release of both helium atoms from doubly-occupied traps

$$He_2T \rightarrow 2\,He + T\,, \qquad (i = 2)\,, \tag{6}$$

as can be shown by methods described in II.

The spectrum for the HeV trap in fact also contains a second peak, but in this case it is ~80 K lower in temperature than the major peak at 1220 K. Its presence is more convincingly illustrated in fig. 2. The desorption reactions leading to these peaks

$$He_3V \xrightarrow{1130\,K} He + He_2V\,, \qquad (i = 2)\,, \tag{7}$$

$$He_2V \xrightarrow{1220\,K} He + HeV\,, \qquad (i = 1)\,, \tag{8}$$

were identified in an earlier publication [8]. The neon trap gives rise to only one observable peak, at 1000 K in fig. 1. For reasons to be presented later, we believe that doubly-occupied traps exist in this case also, but that the resulting desorption peak is coincident with the first, i.e. that the reactions of eqs. (5) and (6) are "degenerate" in temperature:

$$HeT(Ne) \xrightarrow{1000\,K} He + T(Ne)\,, \tag{9}$$

$$He_2T(Ne) \xrightarrow{1000\,K} 2\,He + T(Ne) \tag{10}$$

where T(Ne) signifies the annealed Ne atom trap.

The most remarkable feature of fig. 1 is the nearly perfect regularity of the primary peak temperature

with the size (or mass) of the trap. In fact a sixth trap could be added to this figure: the singly-occupied vacancy was shown earlier [8] to lead to a peak at 1520 K. In this case, of course, the doubly-occupied counterpart is identical to the singly-occupied peak for the HeV trap (1220 K) by definition (see eq. (8)). If included, these peaks would nicely extend the regularity of fig. 1.

In fig. 2, the helium dose has been increased to $4 \times 10^{12}/\mathrm{cm}^2$, and $\bar{i} \approx 0.77$. Detailed analysis of the xenon case, reported in II, shows that under these conditions peaks corresponding to multiplicities (i.e. to numbers of helium atoms occupying a trap) up to $i = 4$ can be distinguished. Using the same method of analysis, the multiplicities of the peaks for the other traps were determined. These multiplicities and the peak positions are indicated on the corresponding spectra of fig. 1. The position marks are duplicated on figs. 2–4 and 6 but the values of i omitted. The notation "m–n is meant to indicate that the peak is degenerate and contains contributions from traps occupied by $i = m$ to $i = n$ helium atoms.

Note that the traps depopulate quite differently depending on whether the peak temperature (i.e. binding energy) increases (as for the Xe trap) or decreases (as for the HeV trap) with increasing multiplicity i. In the former case, when one He escapes from a trap with $i > 1$, the cluster left behind is less stable than before, and all the helium leaves in a time short compared to the peak width. In the latter case, when one He escapes, the resulting cluster is more stable, and a further increase in temperature must occur before the next He can desorb. As a result, the Xe_3 peak, for example, contains a contribution of 3 He atoms from each trap with $i = 3$ (i.e. that had 3 trapped He's at the start of the heating) and none from any other i, while the $(HeV)_3$ peak contains a contribution of one He from each trap which had $i \geq 3$.

A further increase in helium dose to $2 \times 10^{13}/\mathrm{cm}^2$ leads to the spectra of fig. 3, where $\bar{i} \approx 5.6$. Analysis indicates that the largest peak in each spectrum is degenerate, involving the release from traps containing j to 10 He atoms, where j depends on the kind of trap. Following the notation begun in II for the Xe trap, these will be referred to as the "F-peaks '. They lie in the relatively narrow temperature interval 870 to 1000 K, in contrast to the 500–1220 K interval of the single-occupation peaks (fig. 1).

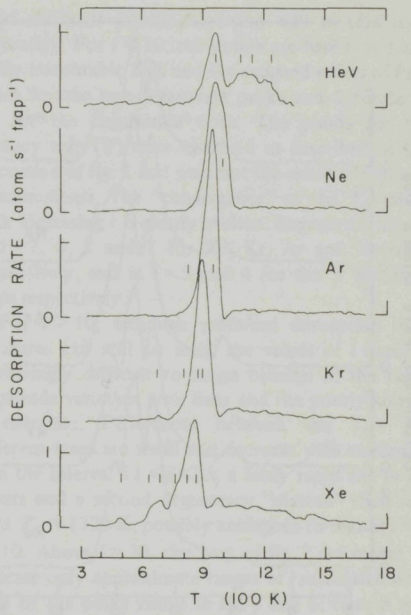

Fig. 3. Desorption spectra for the same five nuclei when $n^+ = 2 \times 10^{13}/\mathrm{cm}^2$, $\bar{i} \approx 5.6$.

Visible above the F-peaks in fig. 3 is a relatively broad desorption extending to ~1500 K, which increases rapidly in amplitude with He dose. At this dose, it is most prominent for the Xe case, where some indication of individual peaks can be seen, and least prominent for the Ne case. For the HeV trap, the $i = 1$, 2 and 3 peaks lie in this temperature interval and could obscure a small desorption of the same form. This desorption indicates a departure from the degeneracy observed for $i \leq 10$, to a relatively rapid increase of binding energy with i.

For a helium dose of $6 \times 10^{13}/\mathrm{cm}^2$, yielding $\bar{i} \approx 21.5$, the spectra are shown in fig. 4. At this dose, no sign remains of the original single-occupation peaks (fig. 1) and even the F-peaks, corresponding to clusters with $i \leq 10$, are minor components of the spectra. The main desorption now occurs between 1200 and 1600 K and consists of five or six peaks in a pattern strikingly similar for all the different traps.

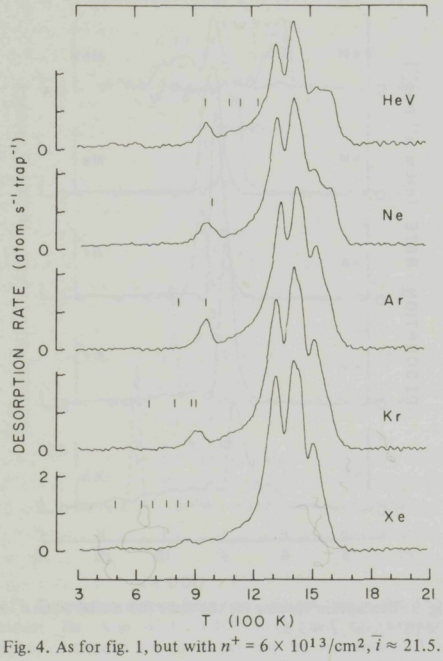

Fig. 4. As for fig. 1, but with $n^+ = 6 \times 10^{13}/\text{cm}^2$, $\bar{i} \approx 21.5$.

The nature of the original nucleus is now clearly of little importance. As will be discussed later, the trapping rate has by this dose increased to ~2.5 to 3 times its original value. It can be shown by trap-filling calculations that this has the effect of making the distribution in i (i.e. the fraction n_i of traps containing i He's as a function of i) much broader than the Gaussian with width $(\bar{i})^{1/2}$ which would be expected if the size were constant (see ref. [7]). It thus seems likely that the major peaks of fig. 4 are all degenerate, although the ranges of i involved in each one cannot be established with any precision.

In deconvoluting the peaks of fig. 4, assuming first-order kinetics, it was found that the best fits were obtained using rate constants of $\sim 10^{21}$, almost certain to be physically unrealistic. Such very narrow peaks are consistent with peak degeneracy if one imposes the additional condition that the helium atoms in the trap "cooperate" in the release of one of their number, equivalent to requiring that they be

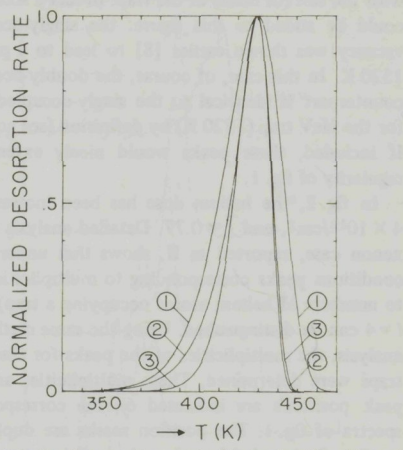

Fig. 5. Calculated desorption peaks illustrating the effect of degeneracy. Curves 1 and 3 are first order peaks, curve 2 is for a 10-fold degenerate state with first order kinetics for the individual reactions. See table 3 for peak parameters.

emitted sequentially †. Computed desorption transients for such sequential release, assuming first-order kinetics, show that peak widths can be reduced from ~0.08 to ~0.05Tp when degeneracies are large ($\geqslant$10), equivalent to increasing the frequency factor exponent by a factor ~8/5. This is illustrated in fig. 5 where a ten-fold degenerate peak (peak 2) is compared with two first-order peaks (1 and 3) having frequency factors ν of 1×10^{13} and 1×10^{22}. The amplitudes are normalized and the activation energies chosen to make the peak temperatures equal. The peak parameters are given in table 3.

Increasing the helium dose by another factor of two to $1.2 \times 10^{14}/\text{cm}^2$ ($\bar{i} \approx 62$) gave the spectra of fig. 6. The peak patterns are qualitatively similar to those of fig. 4, but the most prominent peaks are now at 1550 and 1600 K as compared to 1300 and 1400 K in fig. 4. In II, this trend was observed, for the Xe trap, to continue to a dose of $2 \times 10^{14}/\text{cm}^2$ ($\bar{i} \approx 120$) where the most prominent peak occurred at ~1770 K. Again no significant dependence on the nature of the original nucleus can be seen in fig. 6,

† This concept was originally suggested to us by A. van Veen in private discussions.

Table 3
Parameters of fig. 5

Peak	E (eV)	ν (s^{-1})	n_0 (rel.) [a]	$\Delta T_{1/2}/T_m$ [b]
1	1.07	1×10^{13}	1.000	0.0807
2	1.00	1×10^{13}	0.674	0.0495
3	1.82	1×10^{22}	0.603	0.0484

a) n_0 is the relative initital population required to achieve the amplitude normalization.
b) $\Delta T_{1/2}$ is the full width of the peak at half maximum.

and the spectra for all traps are expected to show the trend mentioned above for Xe.

The temperature T_p of all the observed peaks have been collected together in fig. 7 where they are plotted as a function of the multiplicity i. This provides an overall view of the thermal stability of the nucleated helium clusters as a function of the number of helium atoms they contain. The parts of the figure below $i = 10$ and above $i = 10$ have somewhat different significances and will be discussed separately. For $i \leqslant 10$, the points are based on fairly easily measurable T_p's and the assigned values of i are exact for the non-degenerate peaks and accurate to ± 1 for the degenerate ones. The points for the vacancy trap (V) were obtained as described in the discussion of fig. 1 and were not the result of separate measurements. The "convergence" of the T_p values with increasing i is clearly evident. Degeneracy sets in at $i = 7$, 4, 2 and 1 for Xe, Kr, Ar and Ne traps respectively, and at $i = 5$ and 4 for the V and HeV traps respectively.

For $i > 10$, although preferred desorption temperatures can still be seen, the values of i become increasingly difficult to assign because of the rapid amplitude variation with dose and the poorly known degeneracies. Differences between the T_p's for different traps are small and decrease with increasing i. In the interval $11 \leqslant i \leqslant 15$, a fairly rapid rise in T_p occurs and a second degeneracy "plateau" then sets in at $T_p \approx 1320$ K, possibly analogous to that at $i = 6$ to 10. Above $i = 20$, the bars of fig. 7 are meant to indicate only approximate ranges of i associated with each of the peaks visible in fig. 4 and 6. Here it was assumed, with no direct evidence, that the degree of

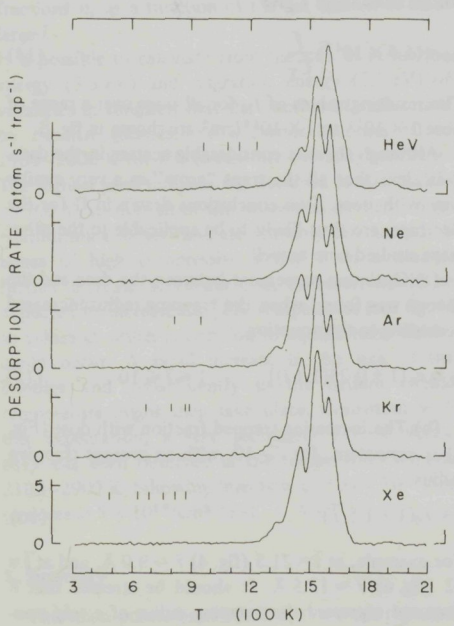

Fig. 6. As for fig. 1, but with $n^+ = 1.2 \times 10^{14}/cm^2$, $\bar{i} \approx 62$.

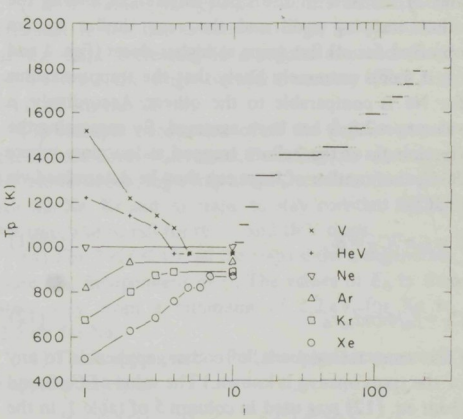

Fig. 7. Peak temperatures for the six trap nuclei as a function of the number i of helium atoms they contain. Above $i = 10$, the bars indicate approximate ranges of the multiplicity i involved in peaks at the indicated temperatures which are the same for all the nuclei.

degeneracy of all the peaks was the same. In support of this assumption, estimates of $\bar{i}$ from combining the average values of i indicated in fig. 7 with the peak amplitudes of figs. 4 and 6 are in rough agreement with the measured values given in table 2.

Measurements of the entrance probability η and the deduction of the average range $\bar{d}_m$ of the He^+ ions incident on this same tungsten surface have been reported in a separate publication [11]. For the normally-incident 250 eV ions used here, it was found that $\eta = 0.80 \pm 0.10$ and $\bar{d}_m = 60 \pm 9$ Å. (The value given for $\bar{d}_m$ is based on measurements of η and *computed* average ranges of 1 to 5 keV He^+ in "random" tungsten by a Monte Carlo method [12].) From the above values and the peak populations measured from spectra with $B < 2$ (such as those in figs. 1 and 2), the trapping radii r_0 of four of the five traps were determined via eq. (3). The average values obtained were 2.5, 3.0, 2.8 and 2.9 Å for the HeV, Ar, Kr and Xe traps respectively. Relative values of the radii have uncertainties of about ±5% since they do not depend on the values of η and $\bar{d}_m$. The uncertainties in the absolute values of r_0 are estimated to be ±0.6 Å.

The trapping radius of the Ne trap cannot be determined by the present method because only a single desorption peak is seen at low dose (see figs. 1 and 2). In view of the small differences among the other trapping radii and the very similar spectra observed for all five traps at higher doses (figs. 4 and 6), it seems extremely likely that the trapping radius for Ne is comparable to the others. Accordingly, a value $r_0 = 2.8$ Å has been assumed. By measuring the fraction f_0 of the helium trapped at low dose where $B = \bar{i}$, the number of traps can then be determined via eq. (2):

$$\bar{i} = f_0 n^+ / C_T = B \,, \tag{11}$$

so

$$C_T = f_0 / 4\pi\eta \bar{d}_m r_0 \tag{12}$$

(The same technique is, of course, applicable to any of the traps once r_0 is known.) The value of C_T found from eq. (12) was used in column 5 of table 1, in the normalizations of the appropriate spectra in figs. 1–4 and 6, and in the construction of fig. 7.

The trapping radii measured by the present technique apply to the traps or clusters as they exist at the injection temperature. The binding states, however, are those that exist at the temperature at which the desorption occurs. It should be kept in mind that these two states could be different if the configuration of the clusters changes during heating.

The fraction f of the incident helium trapped can be obtained by integrating the un-normalized desorption spectrum (to obtain the number of He atoms desorbed) and dividing by the incident ion dose n^+. f is found to increase considerably for all the traps with increasing dose indicating an increase of the trapping radii with i. To show the similarity of this effect for the five traps, it is convenient to normalize the data to a constant number of traps ($f_0 \propto C_T$ from eq. (12)) and to set the low dose fraction f_0 for this number of one of the traps (chosen arbitrarily) to be unity. This procedure has been carried out using the Xe case for normalization, i.e.

$$f_N = \left(\frac{C_T}{f_0}\right)_{Xe} \frac{f}{C_T} \,. \tag{13}$$

The values $f_0 = 1.3 \times 10^{-2}$ and $C_T = 7.2 \times 10^{10}/\text{cm}^2$ for Xe from table 1 give

$$f_N = (5.5 \times 10^{12}) \frac{f}{C_T} \,. \tag{14}$$

The resulting values of f_N for all traps over a range of dose 1×10^{11} to $1 \times 10^{14}/\text{cm}^2$ are shown in fig. 8.

Although there is considerable scatter in the data, it is clear that all the traps "grow" in a very similar way with dose. Two conclusions drawn in II for the Xe traps, are thus likely to be applicable to the other traps studied here as well:

(a) Optimum agreement between the data and the theory was found when the trapping radius increased according to the equation

$$r_i \approx r_0[1 + 0.25(1 + i)] \,, \qquad 1 \leqslant i \leqslant 10 \,. \tag{15}$$

(b) The increasing trapped fraction with dose (Fig. 8) is consistent, for $\bar{i} \geqslant 10$, with an *average* trapping radius

$$\bar{r} \approx r_0(1 + 1.5\,\bar{i})^{1/3} \,. \tag{16}$$

For example, at $\bar{i} = 21.5$ (fig. 4) $\bar{r} \approx 9.0$ Å, and at $\bar{i} = 62$ (fig. 6) $\bar{r} \approx 12.5$ Å. It should be stressed that $\bar{r}$ does not represent the trapping radius of a trap containing $\bar{i}$ helium atoms since the distribution of the

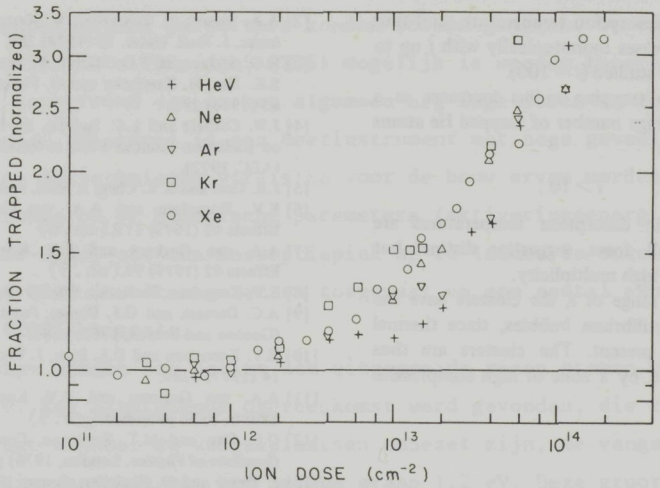

Fig. 8. The fraction of the incident helium trapped as a function of the helium dose, normalized in such a way that the value at low dose for the Xe trap is unity and the concentration of all the traps is the same.

fractions n_i as a function of i is not known at these large $\bar{i}$.

It is possible to calculate from the sum of formation energy (3.3 eV) and migration energy (1.7 eV) of vacancies in tungsten that the number of visits made by thermal vacancies to a cluster becomes ~1 at 1900–2000 K for the sweep rate (40 K/s) used here. The highest peak temperature observed in this work is ~1700 K, so that all of the clusters studied are "non-equilibrium bubbles" and are probably surrounded by zones of high compressive strain. Even a modest further increase in cluster size, however, would be expected to increase the peak temperature (see fig. 7) to values at which conversion to equilibrium bubbles could occur. A rapid increase in the size of the bubbles and consequently in the helium release temperature might then take place. Consistent with this expectation, a very prominent helium release peak has been observed in the temperature interval 2100–2900 K following injection of 1 keV He^+ ions to doses $\geqslant 5 \times 10^{14}/cm^2$ [13].

5. Summary

The main points established in the work reported here are the following:

(1) Helium trapping occurs at room temperature at all of the nuclei studied (HeV, Ne, Ar, Kr, Xe). All have approximately the same size, corresponding to a trapping radius of ~2.8 Å for capture of the first He atom.

(2) The binding energy E_b of the first helium atom attached to the trap depends strongly on the nature of the trap, decreasing in a regular sequence from ~3.1 eV for the singly-occupied vacancy (HeV) to ~1.2 eV for the Xe trap.

(3) Multiple occupation of all the traps occurs as the helium dose is increased. Denoting the number of He atoms occupying a trap as i, E_b tends to rise with i for the Xe, Kr and Ar traps, to stay constant for the Ne trap, and to fall for the V and HeV traps.

(4) For $7 \leqslant i \leqslant 10$, all the traps show a degenerate state (E_b independent of i). The values of E_b in this state vary from a minimum of 2.2 eV for Xe to 2.5 eV for Ne.

(5) The trapping radii of all the traps increase with i approximately as

$$r_i \approx r_0[1 + 0.25(1 + i)] , \qquad 1 \leqslant i \leqslant 10 .$$

For $i > 10$, all the traps show basically the same behaviour and the following conclusions apply to them all:

(6) The helium desorption temperature, and thus very likely E_b, increases monotonically with i up to the end of the range studied ($i \approx 100$).

(7) The average trapping radius increases as a function of the average number of trapped He atoms per trap $\bar{i}$ roughly as

$$\bar{r} \approx r_0(1 + 1.5\,\bar{i})^{1/3}, \qquad \bar{i} > 10 .$$

(8) Characteristic desorption temperatures are clearly visible at all doses, suggesting distinct but degenerate states of high multiplicity.

Over the whole range of i, the clusters have the character if non-equilibrium bubbles, since thermal vacancies are not present. The clusters are thus probably surrounded by a zone of high compressive strain.

References

[1] J.L. Brimhall and E.P. Simonen, Nucl. Technol. 29 (1975) 378.

[2] A.A. Sagues, H. Schraeder, W. Kesternich and H. Ullmaier, J. Nucl. Mater. 78 (1978) 289.

[3] R.G. St-Jacques, J.G. Martel, B. Terrault, G. Veilleux, S.K. Das, M. Kaminsky and G. Fenske, J. Nucl. Mater. 63 (1976) 273.

[4] J.W. Corbett and L.C. Ianiello, in: Proc. Intern. Conf. on Radiation Induced Voids in Metals, Ed. L.C. Ianiello (AEC, 1972).

[5] J.R. Cost and K.R. Chen, J. Nucl. Mater. 67 (1977) 67.

[6] E.V. Kornelsen and A.A. van Gorkum, Radiation Effects 42 (1979) 113. (ch. 6)

[7] A.A. van Gorkum and E.V. Kornelsen, Radiation Effects 42 (1979) 93. (ch. 5)

[8] E.V. Kornelsen, Radiation Effects 13 (1972) 227.

[9] A.C. Damask and G.J. Dienes, Point Defects in Metals (Gordon and Breach, 1963) p. 80.

[10] E.V. Kornelsen and D.L. Blair, J. Vacuum Sci. Technol. 14 (1977) 1299.

[11] A.A. van Gorkum and E.V. Kornelsen, Radiation Effects, to be published. (ch. 9)

[12] O.S. Oen and M.T. Robinson, Conference Series 28 (Institute of Physics, London, 1976) p. 329.

[13] J. Pierre and D. Paulmier, Compt. Rend. (Paris) B280 (1975) 275.

SAMENVATTING

Thermische desorptie spektrometrie (TDS) werd ontwikkeld tot een kwantitatieve techniek, waardoor nieuwe parameters konden worden gemeten. De voorwaarden waaronder kwantitatieve TDS (zgn. QTDS) mogelijk is worden theoretisch afgeleid, waarbij wordt aangetoond dat in het algemeen erg lage doses en concentraties noodzakelijk zijn. Hierdoor is een meetinstrument met hoge gevoeligheid noodzakelijk en de technische vereisten voor de bouw ervan worden aangegeven. Een nieuwe methode om de kinetische parameters (aktiveringsenergie, frekwentiefaktor, reaktie-orde) uit een desorptiepiek af te leiden is ontwikkeld.
De theorie van QTDS is uiteengezet en toegepast op een aantal experimenten met een wolfraam (100) kristal:
- De meervoudige vangst van helium aan uitgegoeide xenon atomen wordt vergeleken met de theorie. Een uitstekende overeenkomst werd gevonden, die resulteerde in de konklusie dat wanneer de vangstplaatsen onbezet zijn, de vangststraal ca. 3 Å is, en de bindingsenergie van het helium eraan 1,2 eV. Deze grootheden nemen toe tot ca. 12 Å resp. 4 eV wanneer er zich 60 atomen op de vangstplaats bevinden. Het aantal vangstplaatsen kon ook uit de experimenten worden afgeleid.
- Het produkt van intreekans en gemiddelde dracht van het geinjekteerde helium werd gemeten als funktie van de invalshoek en energie. Een sterke toename werd gevonden voor loodrechte inval, en de halfwaardehoek werd gemeten voor energieën van 25 tot 5000 eV. De waargenomen afwijking van de theorie van Lindhard beneden 1000 eV werd bevestigd door computersimulaties van het 'channeling'-effekt bij deze lage energieën.
- De intreekans van helium voor loodrechte en 'willekeurige' inval werd afgeleid uit experimenten waarbij argonatomen dicht bij het oppervlak als vangstplaatsen werden gebruikt. Voor energieën boven 250 eV heeft deze intreekans een bijna konstante waarde van ca. 0.6 voor 'willekeurige' en ca. 0.8 voor loodrechte invalshoek. Beneden 250 eV nemen beide af en worden aan elkaar gelijk voor energieën beneden 25 eV. Voor 25 eV bedraagt de waarde van de intreekans 0,2 en deze daalt tot 0,01 bij 8 eV.
- Van de uitgegloeide verontreinigingen He, Ne, Ar, Kr, Xe en de vakature V werd aangetoond dat ze evenals eerder voor Xe werd aangetoond, heliumatomen kunnen invangen. Daarbij hebben ze alle ongeveer dezelfde vangststraal van ca. 3 Å. De bindingsenergie van helium aan de lege vangstplaats neemt monotoon af met de massa van de verontreiniging, en wel van 3,1 eV voor He tot 1,2 eV voor Xe. Zoals al eerder voor Xe werd gevonden, konden alle vangstplaatsen tenminste 100 heliumatomen opnemen zonder dat er verzadiging optrad. Wanneer het aantal ingevangen heliumatomen groter is dan ongeveer 10, zijn alle vangstplaatsen

qua heliumvangstgedrag identiek geworden. Deze resultaten beschrijven dus de nucleatie van heliumbellen bij kamertemperatuur, van groot belang voor materiaalschadeproblemen in fusiereaktoren.

SUMMARY

Thermal desorption spectrometry (TDS) of noble gases in solids was developed into a quantitative technique, enabling the measurement of new parameters. The conditions under which quantitative TDS (QTDS) is possible are derived theoretically, and it is shown that in general very low doses and concentrations are needed. This makes a measuring apparatus of high sensitivity necessary and the technical requirements to build it are given.

A new method to extract the kinetic parameters (activation energy, frequency factor, reaction order) from a desorption peak has been developed.

The theory of QTDS is outlined, and has been applied to a series of experiments using a W(100) crystal:

- The multiple trapping of helium at annealed xenon atoms has been compared to the theory. An excellent agreement was found, resulting in the conclusions that when the traps are empty, the trapping radius is about 3 Å and the binding energy of the helium to it 1.2 eV. These quantities increase to 12 Å and 4 eV when there are 60 atoms in the trap. The number of traps could also be derived from the experiments.
- The product of entrance probability and average range of injected helium has been measured as a function of energy and incident angle. Strong enhancement was found for normal incidence and the half angle was measured for energies from 25 to 5000 eV. The observed departure from the Lindhard theory below 1000 eV was confirmed by computer simulations of the channeling effect at these low energies.
- The entrance probability of helium for normal and random incidence was deduced from experiments using argon atoms as traps close to the surface. For energies above 250 eV, it has a nearly constant value of 0.6 for random and 0.8 for normal incidence. Below 250 eV, both decrease and become equal for energies below 25 eV. At this energy the value is 0.2, decreasing to 0.01 at 8 eV.
- The annealed impurities He, Ne, Ar, Kr and Xe and the vacancy V were shown to trap helium atoms all with about the same trapping radius as was found for Xe (about 3 Å). The binding energy of helium to the empty trap however decreased monotonically with impurity mass from 3.1 eV for He to 1.2 eV for Xe. As was found already for Xe, all were able to trap at least 100 helium atoms with no sign of saturation. When the number trapped is greater than about 10, the nature of the original trap is lost. These results thus describe the first stages of bubble nucleation at room temperature, of great importance for 'first wall' problems in fusion reactors.

CURRICULUM VITAE

In Hazerswoude stonden zowel mijn wieg, de lagere school als de MULO. De eerste bezocht ik voor korte tijd vanaf 28 april 1952, de laatste verliet ik in juni 1968 met het MULO-B diploma. Van september 1968 tot juni 1970 fietste ik naar de HBS in Alphen aan den Rijn, waar ik het HBS-B diploma (be)haalde. Mijn studie aan de Technische Hogeschool te Delft, afdeling Technische Natuurkunde, volgde aangsluitend. In januari 1977 beeindigde ik deze met het ingenieurs-examen. Kandidaats- zowel als ingenieursonderzoek verrichtte ik in de vakgroep Reaktorfysika o.l.v. prof.dr.ir. H. van Dam, in de subgroep Stralingsschade van dr.ir. L.M. Caspers en dr. A. van Veen. De laatste twee jaar werkte ik tevens als studentassistent bij de Stralingsbeschermingsdienst op het Interuniversitair Reaktor Instituut, waar ook de vakgroep Reaktorfysika was gevestigd. Van januari 1977 tot september 1977 werkte ik als ingenieursassistent bij zowel de Stralingsbeschermingsdienst als de Reaktorfysikagroep. Van september 1977 tot maart 1980 verbleef ik aan de National Research Council in Ottawa, Canada, waar ik met dr. E. V. Kornelsen heb samengewerkt. Het eerste jaar werd mij een beurs toegekend door de Canada Council op grond van het cultureel uitwisselingsverdrag, aangevuld met een beurs/lening van het Ministerie van Onderwijs en Wetenschappen, het tweede jaar werkte ik als Research Associate bij de NRC en het laatste half jaar als gast. De resultaten van het werk verricht in die $2\frac{1}{2}$ jaar in samenwerking met dr. Kornelsen zijn voor een balangrijk deel in dit proefschrift beschreven.
Van juni tot oktober 1980 keerde ik terug naar Ottawa om een onderzoek te doen naar het channelinggedrag van zware edelgasionen bij lage energie. Dit onderzoek werd gefinancierd door een studiereisbeurs toegekend door ZWO.
Per november ben ik gaan werken op het Natuurkundig Laboratorium van Philips in Eindhoven.

STELLINGEN

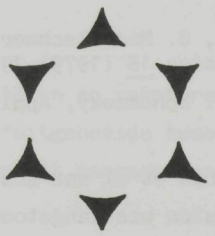

AART VAN GORKUM

1 De door Kornblit gehanteerde methode voor het berekenen van migratie-energieën van vakatures in bcc metalen is onjuist aangezien deze energie wordt gelijkgesteld aan de som van de individuele aktiveringsenergieën van het tweestapsproces leidend tot migratie.

L. Kornblit, Physical Review B 17 (1978) 575

2 Isomorfismen in de natuurkunde, zich uitend in een identiek wiskundig model, worden nog te weinig uitgebuit. Thermische-desorptiespektrometrie (TDS), thermische-stroomgeneratie (TSC) en thermoluminescentie (TL) vormen daarop geen uitzondering.

Dit proefschrift, hoofdstuk 4

3 Computersimulatie van het sputteringsproces van lichte ionen op metalen ter berekening van de sputteropbrengst zal alleen dan een juiste simulatie van het eksperiment opleveren indien ook ionbotsingen met reeds ingevangen ionen worden inbegrepen in het rekenmodel.

R. Behrisch, G. Maderlechner, B.M.U. Scherzer, M.T. Robinson, Applied Physics 18 (1979) 391

H.L. Bay, J. Bohdansky, Applied Physics 19 (1979) 421

4 De bewering van Chen et al dat eksperimenteel nooit tevoren een hoge heliummobiliteit in metalen was aangetoond geeft blijk van het niet op de hoogte zijn van de resultaten van thermische-desorptiespektrometrie.

C.G. Chen, H.K. Birnbaum, A.B. Johnson Jr., Journal of Nuclear Materials 79 (1979) 128

E.V. Kornelsen, Radiation Effects 13 (1972) 227

5 Temperatuurgradienten over het oppervlak van aan de achterzijde verhitte metaalkristallen kunnen grote invloed uitoefenen op eksperimenten waarbij deze temperatuur als belangrijke parameter optreedt. Speciaal bij eksperimenten waarbij de temperatuur wordt gevarieerd in de tijd, is dit effekt groot en tot nu toe onterecht verwaarloosd.

Dit proefschrift, hoofdstuk 3

6 De beschrijving van het diffusionele ontgassingsproces door Stals is ten onjuiste gebaseerd op de levensloop van het gemiddelde deeltje en leidt daardoor tot verkeerde konklusies.

L.M. Stals in: Site characterization and aggregation of implanted atoms in materials, eds. A. Perez and R. Coussement, Plenum Press, New York 1980

7 De door Carter gevonden uitdrukking voor het oplossend vermogen van thermische desorptiespektrometrie voldoet niet aan de dimensie-analyse test en is dan ook onjuist. De korrekte uitdrukking geeft een bijna drie keer lagere waarde voor het oplossend vermogen.

G. Carter, Vacuum 12 (1962) 245

8 Bij de berekeningen van kritieke hoeken voor oppervlaktechanneling moeten dezelfde afwijkingen van Lindhard's theorie optreden bij lage energie als gevonden voor channeling in de bulk. Deze afwijkingen kunnen ook van belang zijn voor het vermijden van channeling bij implantatie van laag energetische ionen in halfgeleiders.

I.N. Evdokimov, Physics Letters 73A (1979) 417

D.R. Myers, R.G. Wilson, J. Comas, Journal of Vacuum Science and Technology 16 (1979) 1893

Dit proefschrift, hoofdstuk 8

9 Het rekombinatievolume voor zelfinterstitiëlen en vakatures van 10^5 atomaire volumina in het door Schüle voorgestelde "uitgebreide twee interstitiëlen model" is fysisch moeilijk voorstelbaar en het aangedragen argument niet steekhoudend.

W. Schüle, Radiation Effects Letters 50 (1980) 93

10 Het is niet duidelijk of het tegenwoordig achterwege blijven van kwalifikaties van instrumenten als "never put in the hands of students" te danken is aan een verbetering van de instrumenten of de studenten.

D.L. Webster, A.E. Hennings, Physical Review 21 (1923) 312

11 De stelling dat Modulated Beam Relaxation Spectrometry (MBRS) wèl en thermische desorptiespektrometrie niet ondubbelzinnige uitkomsten voor aktiverings-energieën en frekwentiefaktoren levert voldoet niet aan de toets van juiste reklame.

G. Ertl, Surface Science 89 (1979) 525

12 Bij de interpretatie van diepteprofielmetingen van helium in wolfraam met behulp van de FIM-Atom-probe techniek is ten onrechte geen rekening gehouden met helium-helium botsingen die het profiel kunnen verstoren.

A. Wagner, D.N. Seidman, Physical Review Letters 42 (1979) 515

13 De bewering van Carter, herhaald door Donnelly et al, dat bij thermische desorptiespektrometrie een lagere opwarmsnelheid een hogere gevoeligheid van de massaspektrometer noodzakelijk maakt om de nauwkeurigheid te handhaven is onjuist. De nauwkeurigheid kan bij afnemende opwarmsnelheid en een konstante gevoeligheid van de massaspektrometer zelfs toenemen.

G. Carter, Vacuum 12 (1962) 245
S.E. Donnelly, D.C. Ingram, R.P. Webb, D.G. Armour, Vacuum 29 (1979) 303
Dit proefschrift, hoofstuk 2

14 De draairichting van diafragmaringen op kameralenzen zou gestandaardiseerd moeten worden.

15 Het gebruik van de benaming Eskimo voor de Inuit is te vergelijken met dat van Kaaskop in het geval van een Nederlander en zou daarom achterwege dienen te blijven.

16 Dat de biologische tijdklok van de mens zich volgens de relativiteitswetten laat transformeren wordt in vele "Gedanken"-eksperimenten aangenomen maar is nooit sterk beargumenteerd noch eksperimenteel aangetoond.

17 Op het gebied van de ontmannelijking van de taal loopt Nederland (weer?) achter op de USA en Canada.

Delft, 12 februari 1981